MICROCOPY RESOLUTION TEST CHART

1.0

1.1

1.25   1.4   1.6

2.8   2.

3.2   2.2

3.6

4.0   2.0

1.8

AD-A193 109

AFWAL-TR-87-2077

AD· A/93   /09
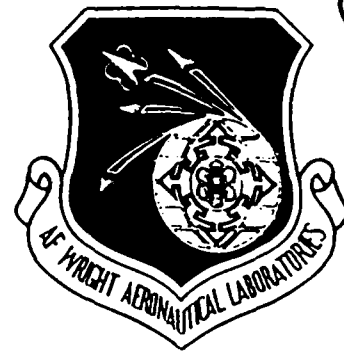
A NAVIER-STOKES STUDY OF CASCADE FLOW FIELDS
INCLUDING INLET DISTORTION AND ROTATING STALL

F. Davoudzadeh, N. S. Liu, S.J. Shamroth, S.J. Thoren

Scientific Research Associates, Inc.
50 Nye Road, P.O. Box 1058
Glastonbury, Connecticut 06033

DTIC
ELECTE
APR 1 9 1988
S
D

December 1987
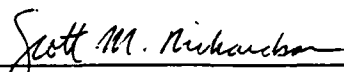
Final Report for Period September 1984 – August 1987
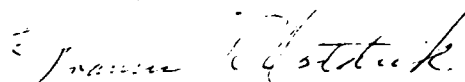
88 4 13 018

NOTICE

When Government drawings, specifications, or other data are used for any purpose other than in connection with a definitely Government-related procurement, the United States Government incurs no responsibility or any obligation whatsoever. The fact that the Government may have formulated or in any way supplied the said drawings, specifications, or other data, is not to be regarded by implication, or otherwise in any manner construed, as licensing the holder, or any other person or corporation; or as conveying any rights or permission to manufacture, use, or sell any patented invention that may in any way be related thereto.

This report has been reviewed by the Office of Public Affairs (ASD/PA) and is releasable to the National Technical Information Service (NTIS). At NTIS, it will be available to the general public, including foreign nations.

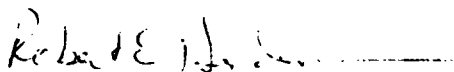This technical report has been reviewed and is approved for publication.

SCOTT M. RICHARDSON, 1Lt, USAF
Compressor Research Group
Technology Branch
Turbine Engine Division

FRANCIS R. OSTDIEK
Chief, Technology Branch
Turbine Engine Division
Aero Propulsion Laboratory

FOR THE COMMANDER

ROBERT E. HENDERSON
Deputy for Technology
Turbine Engine Division
Aero Propulsion Laboratory

REPORT DOCUMENTATION PAGE

1a. REPORT SECURITY CLASSIFICATION		1b. RESTRICTIVE MARKINGS		
Unclassified				
2a. SECURITY CLASSIFICATION AUTHORITY		3. DISTRIBUTION/AVAILABILITY OF REPORT		
		Approved for public release; distribution unlimited.		
2b. DECLASSIFICATION/DOWNGRADING SCHEDULE				
4. PERFORMING ORGANIZATION REPORT NUMBER(S)		5. MONITORING ORGANIZATION REPORT NUMBER(S)		
		AFWAL-TR-87-2077		

6a. NAME OF PERFORMING ORGANIZATION	6b. OFFICE SYMBOL (If applicable)	7a. NAME OF MONITORING ORGANIZATION
Scientific Research Associates, Inc.		Air Force Wright Aeronautical Laboratories Aero Propulsion Laboratory (AFWAL/POTX)
6c. ADDRESS (City, State and ZIP Code)		7b. ADDRESS (City, State and ZIP Code)
50 Nye Road, P.O. Box 1058 Glastonbury, Connecticut 06033		Wright-Patterson Air Force Base, Ohio 45433-6563

8a. NAME OF FUNDING/SPONSORING ORGANIZATION	8b. OFFICE SYMBOL (If applicable)	9. PROCUREMENT INSTRUMENT IDENTIFICATION NUMBER		
		F33615-84-C-2479		
8c. ADDRESS (City, State and ZIP Code)		10. SOURCE OF FUNDING NOS.		
		PROGRAM ELEMENT NO.	PROJECT NO.	TASK NO. / WORK UNIT NO.
		65502F	3005	20 / 20

11. TITLE (Include Security Classification) A Navier-Stokes study of Cascade Flow Fields including Inlet Distortion and Rotating Stall

12. PERSONAL AUTHOR(S) Davoudzadeh, F., Liu, N.S., Shamroth, S.J., Thoren, S.J.

13a. TYPE OF REPORT	13b. TIME COVERED	14. DATE OF REPORT (Yr., Mo., Day)	15. PAGE COUNT
Final Report	FROM Sep 84 TO Aug 87	December 1987	158

16. SUPPLEMENTARY NOTATION

This is a Small Business Innovation Research Program Report.

17. COSATI CODES			18. SUBJECT TERMS (Continue on reverse if necessary and identify by block number)
FIELD	GROUP	SUB. GR.	Navier-Stokes equations, numerical simulation, inlet distortion, rotating stall
21	05		
21	01		

19. ABSTRACT (Continue on reverse if necessary and identify by block number)

A two-dimensional, unsteady, Navier-Stokes computer code has been developed and applied to general cascade problems including inlet distortion and rotating stall. The code allows an arbitrary number of passages with periodicity conditions applied below the first and above the last passage, thus allowing flows in the computational domain to differ on a passage-by-passage basis. Calculations were performed for both C-grid and H-grid coordinate systems for single passage steady flows, multiple passage flows with steady and time-dependent inlet distortions and for multiple passage flows with a disturbance first imposed and then removed. This latter set of calculations demonstrated the ability of the procedure to simulate rotating stall flow fields. Calculations for conditions of incipient rotating stall showed good agreement with data for a J-79 stator set.

20. DISTRIBUTION/AVAILABILITY OF ABSTRACT	21. ABSTRACT SECURITY CLASSIFICATION	
UNCLASSIFIED/UNLIMITED ☐ SAME AS RPT. ☒ DTIC USERS ☐	UNCLASSIFIED	
22a. NAME OF RESPONSIBLE INDIVIDUAL	22b. TELEPHONE NUMBER (Include Area Code)	22c. OFFICE SYMBOL
Scott M. Richardson	(513) 255-4780	AFWAL/POTX

DD FORM 1473, 83 APR   EDITION OF 1 JAN 73 IS OBSOLETE

PREFACE (FOREWARD)

This report details technical work performed in the development of a
rotating stall analysis based upon solution of the unsteady, two-dimensional,
Navier-Stokes equations. The work was funded under Contract F33615-84-C-2479
with Mr. Marvin A. Stibich (AFWAL/POTX) as Project Engineer. Technical
coordination was provided by 1st Lt. Scott Richardson.

Publication of this report does not constitute Air Force approval of the
findings or conclusions presented. It is published only for the exchange and
stimulation of ideas.

ACKNOWLEDGEMENT

TABLE OF CONTENTS

Page

LIST OF ILLUSTRATIONS

LIST OF ILLUSTRATIONS (Continued)

LIST OF ILLUSTRATIONS (Continued)

INTRODUCTION

The phenomena of rotating stall represents a potentially serious problem which must be recognized during the design and operation of a compression system. In general, gas turbine systems are at optimum performance when the compressor is operating at or near its maximum attainable pressure ratio. However, as the pressure ratio increases, the danger of perturbations driving the compressor into the stall regime also increases. Therefore, the operating pressure ratios are generally kept below some specified margin to prevent the compressor from penetrating into the stall region.

If the compressor does penetrate into the stall region, stall may manifest itself in one of several ways. In the first mode, all blade passages show separation and both the mass flow and pressure ratio across the blade passage show a marked decrease. Although separation surely does have an unsteady aspect, the effects of this stall mode can be modeled via a steady analysis. A second mode of stalled behavior is that of rotating stall. In rotating stall, a major separation region appears in one or more adjacent passages and this separation zone then propagates circumferentially with time. As the zone propagates to an adjacent passage, an original passage 'unstalls' and the process continues. Stall may appear as a single propagating cell or multiple propagating cells. When rotating stall is present, the average mass flow over the annulus remains essentially constant, as does the pressure rise, although both the mass flux and pressure rise are at values for lower than the normal operating point values. However, on a passage-by-passage basis, the flow is unsteady. For passages containing a stall zone, the pressure ratio and mass flux show significant decreases from those values in an unstalled passage. As the zone progresses from passage to passage, each individual passage experiences a significantly unsteady process.

The final mode of stall is termed surge. In surge, the annulus averaged mass flux and pressure rise undergo large amplitude oscillation. This is in contrast to rotating stall where the annulus averaged quantities do not exhibit a significant amount of unsteadiness. Whereas, in rotating stall the majority of the passages are operating in an unstalled mode, surge affects the annulus as a whole as all passages continuously exhibit these unsteady effects.

The focus of the present investigation is rotating or propagating stall. Based upon flow processes associated with it, rotating stall is obviously a flow situation to be avoided if possible. Rotating stall is associated with

-1-

decreased compressor performance which, in itself, is a significant problem. However, the large unsteady effects associated with rotating stall can be a factor in blade fatigue and can be a precursor to destructive failure of the component. Therefore, analyses and experiments which shed further light on rotating stall phenomena represent important additions to the knowledge base.

The problem of rotating (or propagating) stall is a very difficult one containing considerable complexity. Since rotating stall is initiated from separated flow, viscous effects which lead to and then control separation are important. As previously discussed, rotating stall is an unsteady process when viewed on a passage-by-passage basis. The unstalled passages are fully flowing whereas those passages which are stalled contain relatively large separation zones. Therefore, large scale unsteady separation is a basic feature of the process. Since stall may occur at significantly off-design conditions, the oncoming flow may be at significant flow incidence relative to the design condition. Three-dimensional effects may be important; in particular, part span stall in which a stall cell occurs over only a portion of the blade passage, as well as full span stall, are both observed. Finally, in actual operation stall may be a multi-blade row phenomena in which the presence of additional blade rows significantly affects the observed flow patterns, with the interaction effect being dependent upon blade spacing.

The work discussed in the present report details a study of the propagating stall problem via the unsteady two-dimensional Navier-Stokes equations. In this work, the Navier-Stokes equations are applied to a multi-passage configuration. Periodic conditions are applied over N passages, which allows the flow from passage to passage to differ. A disturbance is initiated in one of the passages and the resulting behavior is observed.

BACKGROUND

Since its recognition in the early 1950's, rotating stall has been the subject of a large number of analytical, numerical and experimental investigations. Two early works discussing this problem are given in Refs. 1 and 2, which considered the basic mechanisms of rotating stall. Based upon simplified models, Refs. 1 and 2 considered procedures which deduce the features of stall propagation in single blade rows, such as the dependence of the extent of the stalled region upon operating conditions and the stall propagation speed. Reference 2, in particular, reviews several of these early

approaches. In general, these approaches require steady state blade row characteristics which must be obtained from experimental data or an alternate analysis. The required features include flow exit angle and flow loss characteristics as a function of inflow conditions. The flow upstream of the blade row is modeled as a potential flow and that downstream of the blade row is modeled as a rotational inviscid flow using linearized equations. The blade row is considered to be an actuator disk with specified loss and flow turning characteristics. The flows upstream and downstream of the blade row are joined by the actuator disk characteristics. As discussed in Ref. 2, these models give a boundary equation at the actuator disk. In general, this boundary equation is both unsteady and nonlinear. If the boundary equation is linearized, the solution may be expressed as a series of waves of wave number k, and complex frequency ω; the real portion of ω represents the growth or decay with time. The ratio of the imaginary portion of ω to k is the propagation velocity, V_p. The linearized approach gives a curve in (k, ω) space which marks the boundary between stable and unstable waves. For the linearized theory there is no mechanism to limit growth and, therefore, no way of determining which of the unstable waves the nonlinear system will select. Also, as discussed in Ref. 2, if the nonlinear equation is chosen for analysis, wave length, wave shape and wave amplitude can be calculated subject to specific assumptions.

A later analysis with the same basic type of model which considered a nonlinear flow was performed by Takata and Nagano (Ref. 3). Takata and Nagano again divided the flow into two distinct regions separated by the cascade actuator disk. Upstream of the disk the flow was assumed irrotational. Downstream, a rotational inviscid analysis based upon numerical solution of the vorticity transport equations was used. Again, the two regions were connected by specific cascade loss and flow turning characteristics. This approach included nonlinear effects in the downstream region, as well as in the cascade characteristics. A time marching solution was then used to investigate stability characteristics. In Refs. 1-3, as well as other efforts of this type, the major focus was prediction of propagation speed, number of stall cells, wave form, etc.

Another early effort including nonlinear effects is that of Adamczyk (Ref. 4) who considered the result of a specified inlet plane disturbance upon a cascade flow field. Vorticity transport equations were used both upstream

and downstream of the cascade and, as in Refs. 1-3, the regions were connected by equations expressing the blade passage characteristics. A series of calculations were made with specified streamwise disturbances and it was shown that under certain conditions a propagating velocity disturbance at the rotor inlet plane appeared. This approach which solves the governing differential equations in both the upstream and downstream regions has the potential to treat arbitrary inlet distortion effects.

An early effort concentrating upon rotating stall inception was that of Nenni and Ludwig (Ref. 5). In Ref. 5, time-dependent small disturbances were superimposed on a steady mean flow through a blade row and the growth of the disturbances with time was determined for various flow configurations. The theory was developed for both an isolated blade row and a two blade row configuration. In contrast to Refs. 1-3, this utilized a two-dimensional finite thickness actuator sheet. The method of analysis determined solutions for disturbance velocities upstream and downstream of the actuator based upon the linearized Euler equations. These solutions contain three unknown constants that are determined by boundary conditions. The boundary conditions are imposed via matching conditions across the actuator disk which embody the blade row aerodynamic characteristics. Substitution of the general solutions for velocity components into the matching conditions yields a set of three homogeneous equations at the cascade inlet boundary which in turn yields a neutral stability condition. Provided accurate blade row loss and turning characteristics were known, this approach gave reasonable results for incipient stall for a series of calculations. This approach was extended to compressible subsonic flow for single blade rows in Refs. 6 and 7 and to compressible flow with two blade rows in Ref. 8.

While the works of Refs. 1-8 and other work of this type demonstrate some of the important features of rotating stall, the common approach is an inviscid one with empirical cascade turning and loss characteristics. Although inviscid flow is a reasonable assumption upstream of the blade row, it is not downstream of the blade row where nonuniform flows associated with wakes and stall cells are important. A second drawback of this common approach is the use of an empirical cascade model. It is in the blade passage region where the stall process is initiated and use of an actuator disk model here requires a specific data base. Furthermore, these approaches do not consider the basic process within the cascade and, therefore, do not give clear guidance as to how the rotating stall process may be suppressed.

-4-

More recently, the emphasis has been on two somewhat different approaches. The first approach, followed by Greitzer, Moore, Cumpsty and their colleagues, is based upon a combination of empirical observation, compressor characteristics and flow modeling (e.g., Refs. 9-13). Ref. 9 presents a comprehensive review of a variety of approaches to the rotating stall problem.

A different approach which has been pursued recently is based upon a solution of the Navier-Stokes equations via the vortex method (Refs. 14 and 15). In brief, these techniques are based upon the random vortex method (e.g., Refs. 16 and 17). These approaches considered incompressible flow governed by the Euler equations. Viscous effects near the blade surface are modeled by creating a chain of vortices at the blade surface so as to produce the correct total circulation and to satisfy the no-slip wall boundary condition. The vortices created at the walls were released into the main flow at locations downstream of the flow separation point which were determined by an integral boundary layer technique. Vortices in the flow were moved in time in accordance with the local velocity field. In these simulations, a disturbance was introduced into the steady flow field and the calculation was then allowed to proceed in time. Three different types of flow patterns were noted. In the first case, no instability was noted; the flow either remained attached or showed slight separation. The second pattern gave a propagating region of reversed flow with one or two passages reversed and the other passages full flowing. As the calculation proceeded with time, the 'stall zone' propagated through the computational domain. The final pattern showed all passages stalled. Calculations were made to assess the influence of stagger, incidence, blade camber, etc. on the flow pattern.

The work described in the present report details the application of a two-dimensional, unsteady Navier-Stokes analysis to the rotating stall problem. Prior to discussing the work in detail, it is useful to discuss both the potential and the limitations of such an analysis. Regarding first the limitations, it is clear that a two-dimensional simulation does not contain all the relevant flow physics. A variety of experiments indicate the presence of strong radial flows when a stall cell is present; a two-dimensional analysis cannot model these three-dimensional effects. However, in many cases of practical interest, much of the flow is essentially two-dimensional. In the early stages of rotating stall, or for conditions at which rotating stall first occurs, the propagating stall zone is expected to be relatively weak and the flow is expected to remain essentially two-dimensional. Therefore, a

two-dimensional approach to the early stages of this process or to conditions
at which this process first occurs, i.e., incipient rotating, is a reasonable
one. A second major limitation of a Navier-Stokes procedure is that of
turbulence modeling. Appropriate turbulence modeling for highly three-
dimensional, unsteady flows, such as those found in a fully developed rotating
stall cell, is still a significant problem. However, as in the case of the
two-dimensional limitation, the turbulence model is not a major problem for
calculation during the inception period. A final limitation is that of
computer run time. In this regard, significant progress has been made over the
last few years in hardware, software and algorithm technology and cost per
calculation is expected to continue to decrease.

In regard to the benefits of the present approach, the present approach
considers a simulation based upon solution of the Navier-Stokes equations.
When combined with a suitable turbulence model, these equations represent the
actual flow physics. Although two-dimensional and turbulence model
assumptions, along with grid resolution questions, still must be addressed, the
present Navier-Stokes approach represents an initiation of a basic study of
this very complex problem. Whereas actuator disk type approaches (e.g., Refs.
1-8) require cascade turning and loss correlations as a function of flow
conditions, the present approach models these properties via a solution of the
governing partial differential equations. In this manner, the present
Navier-Stokes approach has the potential for assessing the effect of geometric
and flow condition details. Although the vortex method approach of Refs. 14
and 15 does not require cascade loss and turning data, it also has
limitations. As applied in Refs. 14 and 15, in the absence of separation the
vortex sheet representing viscous effects is confined to an infinitesimal sheet
at the wall; vortices are only allowed to enter the passage flow downstream of
separation. In many cases of practical interest much, if not all, of the
cascade passage contains viscous effects and therefore, vorticity is contained
throughout the passage flow field. Furthermore, it is not clear how to extend
the vortex method to turbulent flow without having shed vortices represent the
entire length scale of turbulence, thus forming a 'two-dimensional direct
simulation'. Finally, it is not clear how to extend the vortex method to three
dimensions. The Navier-Stokes approach can include inlet distortion and large
amplitude disturbance effects and has the potential for extension to three
dimensions. Clearly, the Navier-Stokes approach has considerable potential
advantage over more approximate approaches.

-6-

The work presented herein represents a first application of the Navier-Stokes equations to the rotating stall problem. Details of the equations, analysis, numerical method, grid and results are given in the following sections.

ANALYSIS

General

The analysis used in the present effort is based upon a solution of the unsteady Navier-Stokes equations in conjunction with an appropriate turbulence model. The basic code has been used for a variety of applications such as cascade flow simulation (e.g., Refs. 18-21). The code solves the full ensemble averaged Navier-Stokes equations with high near wall resolution; typically the first grid point off a solid surface is placed within the viscous sublayer. Versions of the code are available both for two- and three-dimensional flows. When steady solutions are sought, the procedure utilizes a matrix preconditioning technique to accelerate convergence to steady state (e.g., Refs. 22 and 23). Use of this technique has allowed convergence to be obtained for engineering purposes within eighty to two hundred time steps, depending upon flow configuration and conditions. For unsteady flows the time step must resolve the transients of interest. As will be discussed, the code was vectorized for efficient CRAY operation under the present contract effort. Two-dimensional cascade flows in which a mixing length model is used and a constant total temperature assumption is invoked require approximately 0.4 seconds of CRAY CPU time per time step for a grid of 3500 points. Details of the equations, analysis, boundary conditions, etc., follow.

Governing Equations

The equations used are the ensemble-averaged, time-dependent Navier-Stokes equations which can be written in vector form as

$$\frac{\partial \rho}{\partial t} + \nabla \cdot \rho \vec{U} = 0 \qquad (1)$$

$$\frac{\partial \rho \vec{U}}{\partial t} + \nabla \cdot (\rho \vec{U} \vec{U}) = -\nabla P + \nabla \cdot (\overset{\leftrightarrow}{\pi} + \overset{\leftrightarrow}{\pi}^T) \qquad (2)$$

-7-

$$\frac{\partial \rho h}{\partial t} + \nabla \cdot (\rho \vec{U} h) = -\nabla \cdot (\vec{Q} + \vec{Q}^T) + \frac{DP}{Dt} + \phi + \rho \epsilon \qquad (3)$$

where ρ is density, $\vec{U}$ is velocity, P is pressure, $\overset{\leftrightarrow}{\pi}$ is the molecular stress tensor, $\overset{\leftrightarrow}{\pi}^T$ is the turbulent stress tensor, h is enthalpy, $\vec{Q}$ is the mean heat flux vector, $\vec{Q}^T$ is the turbulent heat flux vector, ϕ is the mean flow dissipation rate and ϵ is the turbulence energy dissipation rate. If the flow is assumed as having a constant total temperature, the energy equation is replaced by

$$T_t = T + \frac{q^2}{2C_p} = \text{constant} \qquad (4)$$

where T_t is the stagnation temperature, q is the magnitude of the velocity and C_p is the specific heat at constant pressure. In most cases considered in this work, the total temperature has been assumed constant. This assumption was made to reduce computer run time when the constant T_t assumption was warranted. A number of terms appearing in Equations (1-3) require definition. The stress tensor appearing in Equation (2) is defined as

$$\overset{\leftrightarrow}{\pi} = 2\mu \overset{\leftrightarrow}{D} - \left(\frac{2}{3}\mu - K_B\right) \nabla \cdot \vec{U} \overset{\leftrightarrow}{I} \qquad (5)$$

where K_B is the bulk viscosity coefficient, $\overset{\leftrightarrow}{I}$ is the identity tensor and $\overset{\leftrightarrow}{D}$ is the deformation tensor, defined by

$$\overset{\leftrightarrow}{D} = \frac{1}{2} \left((\nabla \vec{U}) + (\nabla \vec{U})^T \right) \qquad (6)$$

In addition, the turbulent stress tensor has been modeled using an isotropic eddy viscosity such that

$$\overset{\leftrightarrow}{\pi}^T = -\overline{\rho u' u'} = 2\mu_T \overset{\leftrightarrow}{D} - \frac{2}{3} (\mu_T \nabla \cdot \vec{U}) \overset{\leftrightarrow}{I} \qquad (7)$$

where μ_T, the turbulent viscosity, is determined by a suitable turbulence model. Turbulence modeling is described in the next section.

Equation (3) contains a mean heat flux vector defined as follows:

$$\vec{Q} = -\kappa \nabla T \tag{8}$$

and a turbulent heat flux vector defined as

$$\vec{Q}^T = -\kappa^T \nabla T \tag{9}$$

where κ and κ^T are the mean and turbulent thermal conductivities, respectively.

Also appearing in Equation (3) is the mean flow dissipation term Φ.

$$\Phi = 2\mu \vec{\vec{D}}:\vec{\vec{D}} - \left(\frac{2}{3} \mu - K_B\right)(\nabla \cdot \vec{U})^2 \tag{10}$$

The equation of state for a perfect gas

$$P = \rho RT \tag{11}$$

where R is the specific gas constant, the caloric equation of state

$$e = C_v T \tag{12}$$

and the definition of static enthalpy

$$h = C_p T \tag{13}$$

supplement the equations of motion.

Numerical Method

In regard to the numerical method, the basic method used is that of Briley and McDonald (Refs. 24-26) which is a Linearized Block Implicit ADI procedure. This method has been the focus of considerable intensive improvement over the

last several years. Since its original introduction, the method has been generalized so as to apply in an effective and robust manner to highly stretched grids, as well as to grids having regions of significant nonorthogonality. Particular attention has been placed upon convergence acceleration with highly stretched grids, as well as to matrix preconditioning for low Mach numbers. In addition, considerable effort has focused upon CRAY vectorization.

The method can be outlined as follows: the governing equations are replaced by an implicit time difference approximation, optionally a backward difference or Crank-Nicolson scheme. Terms involving nonlinearities at the implicit time level are linearized by Taylor series expansion about the solution at the known time level, and spatial difference approximations are introduced. The result is a system of multidimensional coupled (but linear) difference equations for the dependent variables at the unknown or implicit time level. To solve these difference equations, the Douglas-Gunn procedure for generating alternating-direction implicit (ADI) splitting schemes as perturbations of fundamental implicit difference schemes is introduced in its natural extension to systems of partial differential equations. This ADI splitting technique leads to systems of coupled linear difference equations having narrow block-banded matrix structures which can be solved efficiently by standard block-elimination methods.

The method centers around the use of a formal linearization technique adapted for the integration of initial-value problems. The linearization technique, which requires an implicit solution procedure, permits the solution of coupled nonlinear equations in one space dimension (to the requisite degree of accuracy) by a one-step noniterative scheme. Since no iteration is required to compute the solution for a single time step, and since only moderate effort is required for solution of the implicit difference equations, the method is computationally efficient; this efficiency is retained for multidimensional problems by using ADI matrix splitting techniques. The method is also economical in terms of computer storage, in its present form requiring only two time levels of storage for each dependent variable. Furthermore, the splitting technique reduces multidimensional problems to sequences of calculations which are one-dimensional in the sense that easily-solved narrow block-banded matrices associated with one-dimensional rows of grid points are produced. Consequently, only these one-dimensional problems require rapid access storage at any given stage of the solution procedure, and the remaining flow variables

can be saved on auxiliary storage devices if desired. Since each one-dimensional split of the matrix produces a consistent approximation to the original system of partial differential equations, the scheme is termed a consistently split linearized block implicit scheme. Consistent splitting has been shown by a number of authors to considerably simplify the application of the intermediate split boundary conditions. Further details of the procedure are given in Refs. 24-26.

Boundary Conditions

Boundary conditions play a major role in obtaining accurate solutions and rapid numerical convergence. The boundary conditions used are based upon the suggestion of Briley and McDonald (Ref. 27). For situations having a subsonic inflow such as those considered in the current effort, total pressure, total temperature and flow angle are specified on the upstream boundary as boundary conditions. Since a fourth numerical condition is required, the second derivative of pressure is usually set to zero. For subsonic outflow conditions, static pressure is set as a boundary condition and second derivatives of temperature and velocity components are set to zero. The periodic boundaries are treated implicitly, i.e., the values of corresponding grid points on the boundaries are set to be equal during the solution process. At solid boundaries, i.e., the blade surface, no slip conditions are enforced and the blade wall temperature is specified. It should be noted that the present approach utilizes very high grid resolution near the blade surface to allow adequate specification of this important region. In general, at least one grid point falls within the viscous sublayer, $y^+ < 10$. This allows rigorous specification of no slip conditions without resorting to wall function formulations. Although wall function formulations may be viable in some cases, such as attached, two-dimensional flow, their application to three-dimensional, unsteady and/or separated flows is much more questionable. As a final wall condition, the normal pressure gradient is set to zero. Both the upstream and downstream boundaries have boundary conditions associated with them which are nonlinear functions of the dependent variables. These are the specification of total pressure on the upstream boundary and static pressure on the downstream boundary. These nonlinear boundary conditions are linearized in the same manner as the govering equations (via a Taylor expansion of the dependent

variables in time), and then solved implicitly along with the interior point equations.

Dependent Variables and Coordinate Transformation

The governing equations, Equations (1-3), are written in general vector form and prior to their application to specific problems it is necessary to decide upon both a set of dependent variables and a proper coordinate transformation. The specific scalar momentum equations solved are the x and z Cartesian momentum equations. The dependent variables chosen are the physical Cartesian velocities, u, w and the density ρ. If the energy equation is solved, enthalpy is added to the set of dependent variables.

The equations are then transformed to a general coordinate system in which the general coordinates, y^j, are related to the Cartesian coordinates x_1, x_2 and x_3 by

$$y^j = y^j(x_1, x_2, x_3, t); \quad j = 1, 2, 3 \tag{14}$$

$$\tau = t$$

As implied by Equation (14), the general coordinate y^j may be a function of both the Cartesian coordinates and time. The governing equations can be expressed in terms of the new independent variables y^j as

$$
\frac{\partial W}{\partial \tau} + \xi_t \frac{\partial W}{\partial \xi} + \xi_x \frac{\partial F}{\partial \xi} + \xi_z \frac{\partial H}{\partial \xi}
$$

$$
+ n_t \frac{\partial W}{\partial \eta} + n_x \frac{\partial F}{\partial \eta} + n_z \frac{\partial H}{\partial \eta} \tag{15}
$$

$$
= \frac{1}{Re} \left[\xi_x \frac{\partial F_1}{\partial \xi} + n_x \frac{\partial F_1}{\partial \eta} + \xi_z \frac{\partial H_1}{\partial \xi} + n_z \frac{\partial P_1}{\partial \eta} \right]
$$

through a straightforward application of chain rule differention. In Equation (15)

$$\xi = y^1 \qquad \eta = y^2$$

and

$$W = \begin{pmatrix} \rho \\ \rho u \\ \rho w \end{pmatrix}, \quad F = \begin{pmatrix} \rho u \\ \rho u^2 + p \\ \rho u w \end{pmatrix},$$

$$H = \begin{pmatrix} \rho u w \\ \rho w \\ \rho w^2 + p \end{pmatrix}, \quad F_1 = \begin{pmatrix} 0 \\ \tau_{xx} \\ \tau_{xz} \end{pmatrix}, \quad H_1 = \begin{pmatrix} 0 \\ \tau_{xz} \\ \tau_{zz} \end{pmatrix} \qquad (16)$$

Notice that the metric coefficients $(\xi, \eta)_{x_1}$ appear outside the derivatives. Experience of Ref. 19 shows the results obtained via the so-called 'semi-strong' conservation form given above are less sensitive to the method used to evaluate the metric coefficients than are results obtained via the so-called 'strong' conservation form, since less differentiation of the metric occurs with the semi-strong form. Both forms can return uniform flow in a nonuniform mesh, but to achieve this the strong form requires that a further 'conservation' condition on the metric coefficients be satisfied. In the current applications, the computational coordinates, ξ, η, are independent of time.

Turbulence Models

As discussed in the Background section, turbulence modeling for complex flows still remains an important issue. Although versions of the existing SRA Navier-Stokes code contain both mixing length and two equation turbulence models, the present effort used a simple mixing length model. The model was divided into wall and wake regions. In both regions the turbulent viscosity was related to the mean flow field via

$$\mu_T = \rho \ell^2 \left(\left(\frac{\partial u_i}{\partial x_j} + \frac{\partial u_j}{\partial x_i} \right) \frac{\partial u_i}{\partial x_j} \right)^{1/2} \tag{17}$$

where μ_T is the turbulent viscosity, ρ is the density, ℓ is the mixing length, u_i is the ith velocity component and x_i is the ith Cartesian direction. Summation is implied for the repeated indices. The question now arises as to specification of ℓ. For the region upstream of the trailing edge, the mixing length is specified in the usual boundary layer manner; i.e.,

$$\ell = \kappa_z (1-e^{-z^+/27}) \qquad \ell \leq \ell_{max} \tag{18}$$

where κ is the von Karman constant and z^+ is the dimensionless normal coordinate, $z u_\tau / \nu$. In boundary layer analysis, ℓ_{max} is usually taken as 0.09δ where δ is the boundary layer thickness taken as the location where $u/u_e = 0.99$. However, this definition of δ assumes the existence of an outer flow where the velocity u_e is independent of distance from the wall at a given streamwise station, i.e., it assumes u_e is only a function of the streamwise coordinate. Although a boundary layer calculation will yield solutions in which u approaches u_e asymptotically at distances far from the solid no-slip surface, Navier-Stokes solutions for cascade flow fields do not in general predict a region where u asymptotes to a constant value. Furthermore, measurements of the flow also show no such region to exist in general. Obviously, a proper choice of δ for the Navier-Stokes cascade analysis is not straightforward. The present formulation is based upon previous efforts at SRA which have given good results for boundary layer velocity profiles and skin friction coefficient for a variety of configurations. This formulation sets the boundary layer thickness by first determining u_{max}, the maximum streamwise velocity at a given station and then setting δ via

$$\delta = 2.0 \, z_{(u/u_{max} = k_1)} \tag{19}$$

i.e., δ was taken as twice the distance for which $u/u_{max} = k_1$ where k_1 was taken as 0.90.

-14-

The region downstream of the blade trailing edge follows the model of Rudy and Bushnell (Ref. 28). In brief, this approach calculates two mixing lengths; one of which is appropriate for the far wake and one of which is appropriate for the near wake. At each station both are calculated and the minimum of the two values used. Results shown in Ref. 28 as well as unpublished results obtained at SRA indicate this is a viable engineering approach for a variety of cases considered to date.

Obviously, the use of a mixing length is not appropriate for the fully developed rotating stall simulation. However, it is a reasonable approach prior to formation of the major fully developed stall cell.

Numerical Dissipation

The final item to be considered is numerical or artificial dissipation. To the authors' best knowledge, all Navier-Stokes numerical analyses which are applied to the high Reynolds number problems typical of turbomachinery application require some artificial dissipation to suppress nonphysical spatial oscillations. Such artificial dissipation could be added via the spatial differencing formulation (e.g., one-sided difference approximations for first derivatives) or by explicitly adding an additional dissipative type term. The present authors favor the latter approach since, when an additional term is explicitly added, the physical approximation being made is usually clearer than when dissipative mechanisms are contained within numerical truncation errors, and further, explicit addition of an artificial dissipation term allows greater control over the amount of nonphysical dissipation being added. Obviously, the most desirable technique would add only enough dissipative mechanisms to suppress oscillations without deteriorating solution accuracy.

The approach used in the present effort is based upon use of a second order anisotropic artificial dissipation term. This approach has given quantitatively accurate predictions for a series of cascade and isolated airfoil calculations for surface pressure, boundary layer velocity profile, surface heat transfer, etc. (e.g., Refs. 19, 20, as well as yet unpublished SRA comparisons).

In this formulation, the terms

$$\rho^{n-1} d_x \frac{\partial^2 \phi}{\partial x^2} , \qquad \rho^{n-1} d_z \frac{\partial^2 \phi}{\partial z^2}$$

are added to the governing equations where $\phi = u$, v and ρ for the x-momentum, z-momentum and continuity equations, respectively. The exponent, n, is zero for the continuity equation and unity for the momenta equations. The dissipation coefficient, d_x, is determined as follows. The general equation has an x-direction convective term of the form $a\partial\phi/\partial x$ and an x-direction diffusion term of the form $\partial(b\partial\phi/\partial x)/\partial x$. The diffusive term is expanded

$$\partial(b\partial\phi/\partial x)/\partial x = b\partial^2\phi/\partial x^2 + \partial b/\partial x \, \partial\phi/\partial x \qquad (20)$$

and then a local cell Reynolds number $Re_{\Delta x}$ is defined for the x-direction by

$$Re_{\Delta x} = \left| a - \partial b/\partial x \right| \Delta x/b \qquad (21)$$

where b is the total or effective viscosity, including both laminar and turbulent contributions, and Δx is the grid spacing. The *dissipation* coefficient, d_x, is nonnegative and is chosen as the larger of zero and the local quantity $\mu_e(\sigma_x Re_{\Delta x} - 1)$. The dissipation parameter, σ_x is a specified constant and represents the inverse of the cell Reynolds number below which no artificial dissipation is added. The dissipation coefficient, d_z, is evaluated in an analogous manner and is based on the local cell Reynolds number $Re_{\Delta z}$, grid spacing Δz for the z-direction, and the specified parameter σ_z. It should be noted that calculations have been run with artificial dissipation added in the conservative form $\partial(\rho^{n-1} d_x \, \partial\phi/\partial x)/\partial x$, and no significant difference between the forms was noted.

In regard to the choice of constants σ_x and σ_z, a variety of parametric studies have indicated that once σ_x and σ_z are set to values between 0.1 and 0.05, a further decrease does not significantly affect the results. As will be discussed, most calculations were run with the constants σ_x, σ_z in this range. However, in the compressor cascade chosen, a higher value was required in the immediate vicinity of the leading edge stagnation point; i.e., $x/c < 0.02$. A variety of computations performed at SRA in Refs. 19-21, as well

as unpublished results under Navy contract N00014-85-C-0499 show this choice to give results which compare very well with experimental data even in the leading edge stagnation region.

CODE VECTORIZATION AND MODIFICATION

A major task under this contract effort was vectorization and modification of the single passage cascade Navier-Stokes code. The basic code used was originally developed as a research code with the major concern on code flexibility and generality (Ref. 29). The code was rewritten for specific application to the cascade problem but without vectorization (Ref. 30). The revised code still retained considerable generality as a cascade code and the run time for a grid of 3500 points was reduced from approximately 20 CRAY-1 CPU seconds per time step to 5 CRAY-1 CPU seconds per time step. The present effort envisioned a series of unsteady, multiple passage simulations. Since the calculations required temporal accuracy, the matrix preconditioning techniques of Refs. 22 and 23 could not be used. Therefore, in order to utilize computer time efficiently, the first step in the present program was to extend the code to allow a multiple passage capability and vectorize the revised code for efficient CRAY operation. In addition, an axial velocity density ratio (AVDR) was incorporated into the code to include converged endwall effects on the stream surface being analyzed. These items are now outlined in brief.

Multiple Passage Capabilty

Prior to the present effort, the cascade code had been restricted to a single passage configuration, such as that shown in Fig. 1. Figure 1 shows a 'C-grid' although both 'C-grid' and 'H-grid' capabilities are currently available. As shown in Fig. 1, the grid consists of two sets of lines; the first being pseudo-azimuthal lines such as JLK and the second being pseudo-radial lines such as FG. A description of the grid generation procedure is given in Ref. 19. It should be noted that for purposes of clarity, not all points have been included in this figure.

Under the present effort the code was first extended to allow calculation for multiple passage configurations, such as that shown in Fig. 2. In this
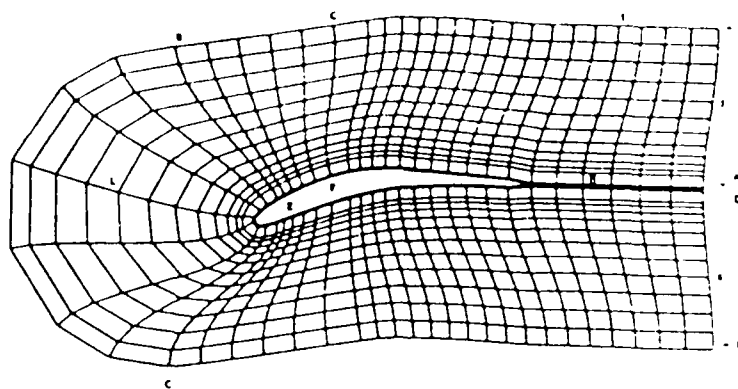
Fig. 1 - Cascade Coordinate Grid - All Grid Points Not Included
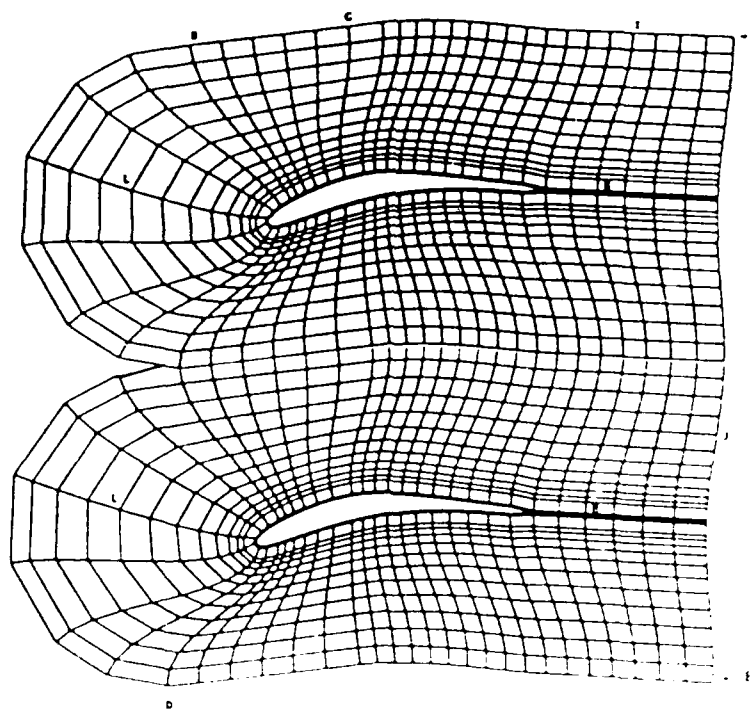
Fig. 2 - Cascade Coordinate Grid - Multiple Passage

case the periodicity condition is imposed on line segments AGB and DE. The passages need not have identical flow fields. However, if initial conditions and boundary conditions for each passage are set to be identical, an identically periodic flow field should emerge.

A calculation demonstrating the multiple passage capability is presented in Fig. 3. This calculation represents a converged solution for the subsonic compressor cascade of Hobbs, Wagner, Dannenhoffer and Dring (Ref. 31); this case was used as a base case in Refs. 19 and 30, where it was shown that the surface pressure calculation by the SRA Navier-Stokes code was in good agreement wih experimental data. Figure 3a shows the grids used. In brief, the grid is a 'C' type grid for each passage. A total number of 3390 grid points were used for each passage with a highly stretched grid having very strong resolution both near the blade and in the vicinity of the blade leading edge. For example, the first point off the surface is a distance of 0.8×10^{-4} chords from the surface, and in the leading edge region grid points along the blade are spaced at a distance of 0.0023 chords apart.

The calculation was run as a low Mach number calculation at Reynolds number based upon chord of approximately 0.6×10^5. The flow field contours are plotted in Figs. 3b-3d. As can be seen, the flow is identical from passage to passage and, although not shown, is also identical to the single passage calculation within truncation error. The pressure coefficient at the leading edge stagnation point, is calculated to be 1.01, which gives a pressure at the stagnation point very close to the freestream stagnation pressure. The surface pressure distribution corresponds to that of Ref. 19, which is in good agreement with data. The velocity vector plot is given in Fig. 3e. These results demonstrate the developed multiple passage capability as the computed flow fields were identical from passage to passage. As will be shown later, passage-to-passage identical flows have been obtained for up to five pasages.

Code Vectorization

As previously discussed, a significant portion of the present effort consisted of restructuring and recoding the existing SRA Navier-Stokes computer code for effective operation on the CRAY family of computers. The code vectorization consisted of several distinct parts. First, all DO loops throughout the code were rearranged for effective vectorization; this often required changing the order of inner and outer loops. Secondly, the basic code

-19-
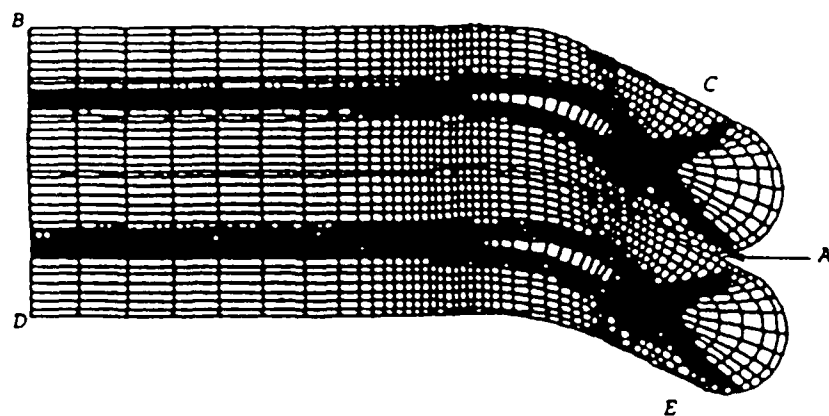
Fig. 3a. Semi-circular Frontal Cap Grid - Two Passages.
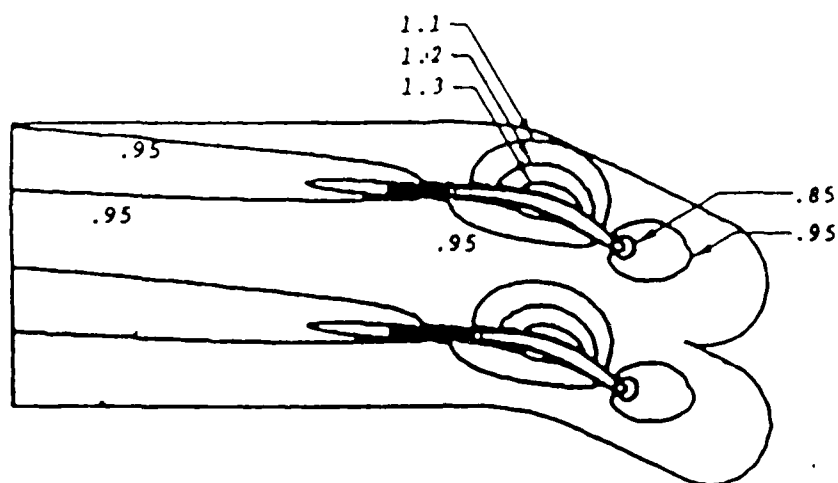
Fig. 3b.   U-Velocity Contours.
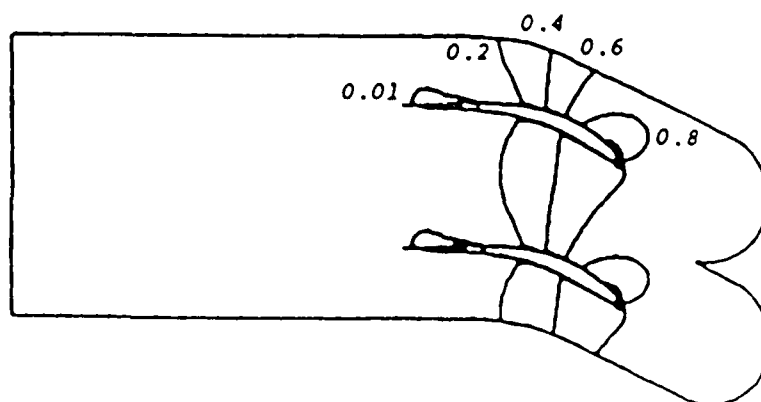
Fig. 3c.   W-Velocity Contours.
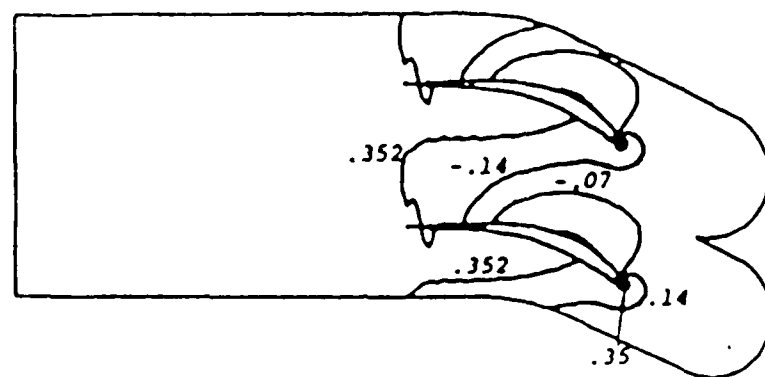
Fig. 3d. Pressure Coefficient Contours.
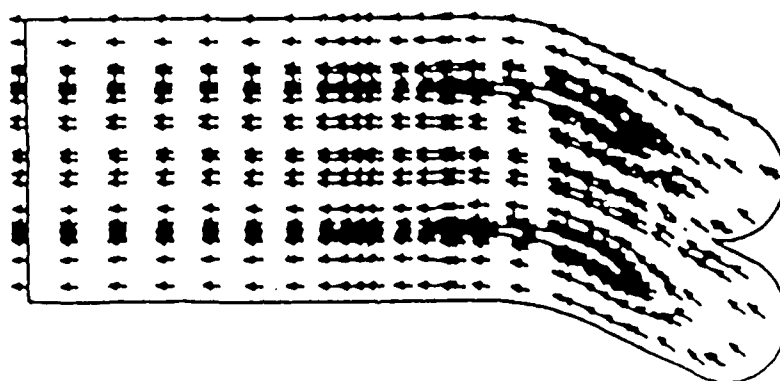
Fig. 3e. Velocity Vector Plot.

was restructured so that in each ADI sweep, the coefficients for the linear equations, which represented the governing equations, were computed in a vector manner. In other words, the coefficients for multiple lines were computed simultaneously. Finally, vectorized matrix inverters which could solve a set of multiple lines simultaneously were developed. As a result of vectorization, run time was reduced by approximately a factor of ten. The multiple passage capability of the vectorized code has been validated by computing the flow about the Stephens-Hobbs (Ref. 31) cascade using an H-grid coordinate system. A computer sketch of the grid for a five passage configuration is given in Fig. 4. In order to demonstrate the passage-to-passage repeatability, two five-passage calculations were carried out. In one case, the flow condition was the design condition (i.e., inflow angle = 38.0°) while in the other case, the flow condition was severely off-design (i.e., inflow angle = 57.7°). The grid geometry for five-passage cascade is shown in Fig. 4. The grid geometry and upstream and downstream boundary conditions for all passages are identical to one-another. The u-velocity contours and w-velocity contours for design flow conditions and severely off-design flow conditions are shown in Figs. 5 and 6, respectively. The contour plots for both conditions illustrate identical flow characteristics from passage to passage, indicating the effects of computational error to be insignificant. The u-w vector plot of the off-design calculation case is shown in Fig. 6c.

AVDR Effects

The present analysis considers a two-dimensional flow field which essentially consists of flow in an assumed stream surface extending between two or more blades. In general, three-dimensional effects are present and one method which includes one of the important three-dimensional effects occurring in cascades or blade rows is based upon the axial velocity density ratio (AVDR) concept. A description of this approach as well as derivation of the basic equation is given in Ref. 32. In brief, this technique includes the effect of flow acceleration or deceleration through the passage due to endwall contraction or expansion and endwall boundary layer growth by adding a term of the form $\frac{\rho u}{b}\frac{db}{dx}$ to the continuity equation, where b represents the thickness of the stream surface under consideration. If an axisymmetric stream surface is
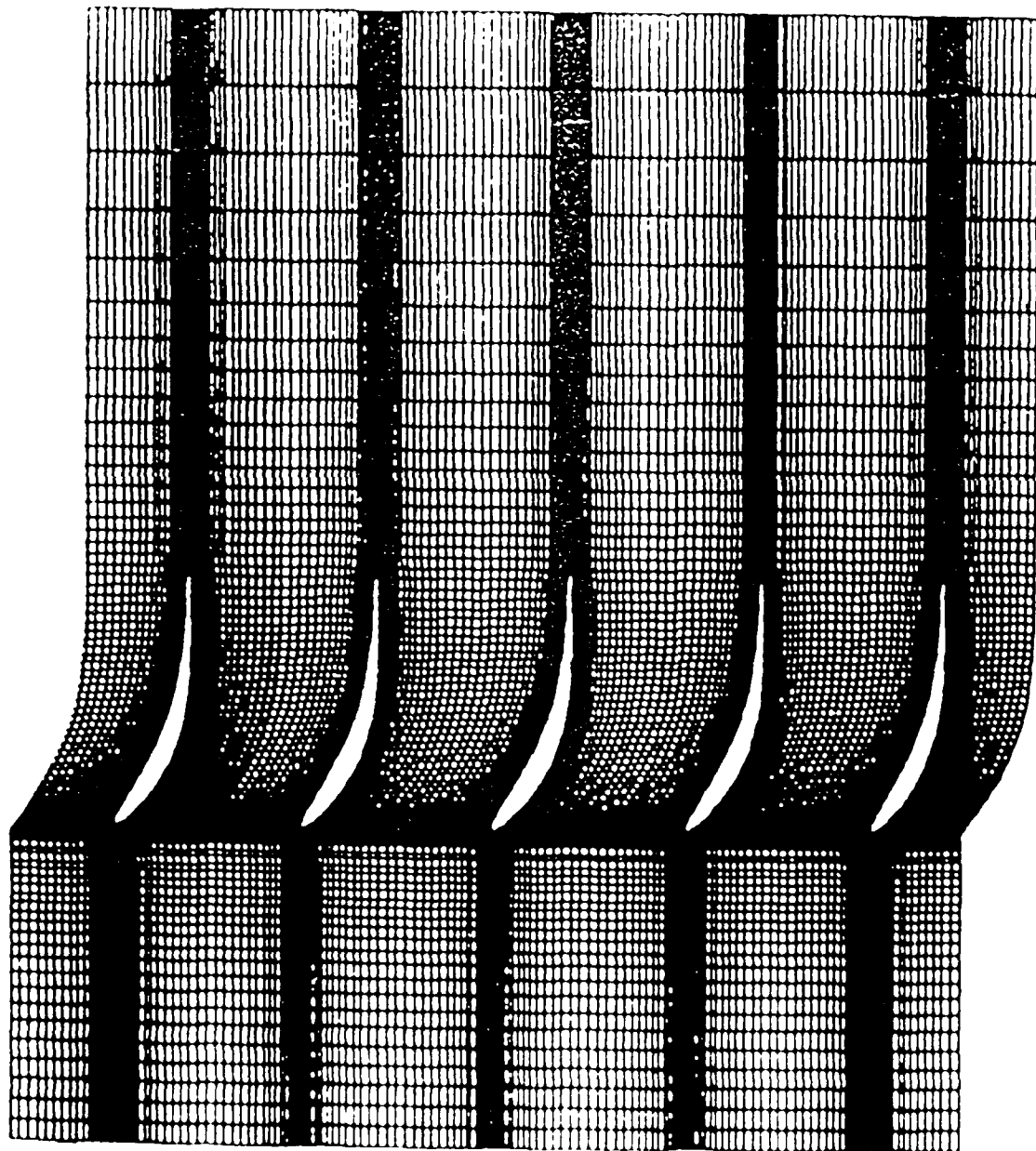
Fig. 4 - H-Grid Distribution for Five-Passage Cascade
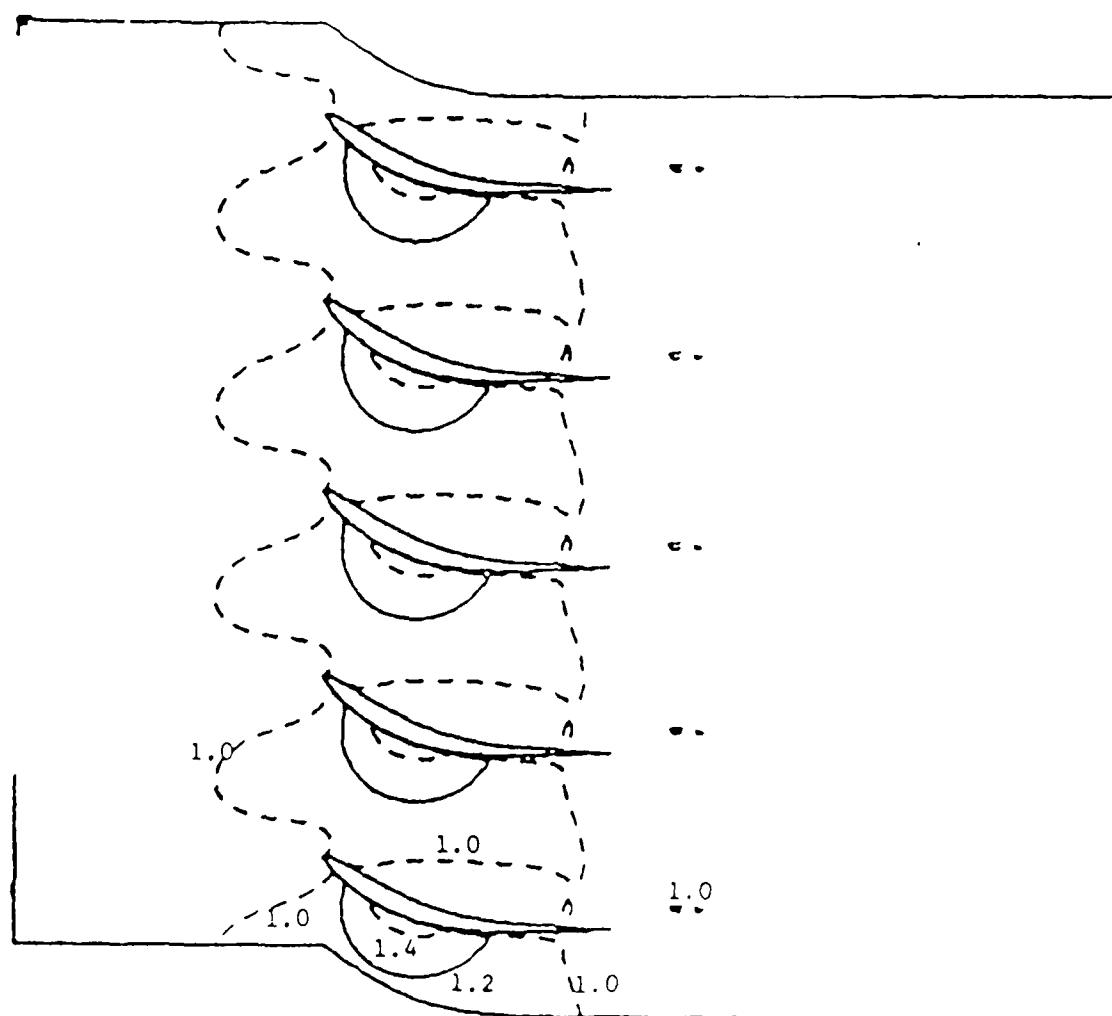
Fig. 5a. U-Velocity Contours, $u_j = $
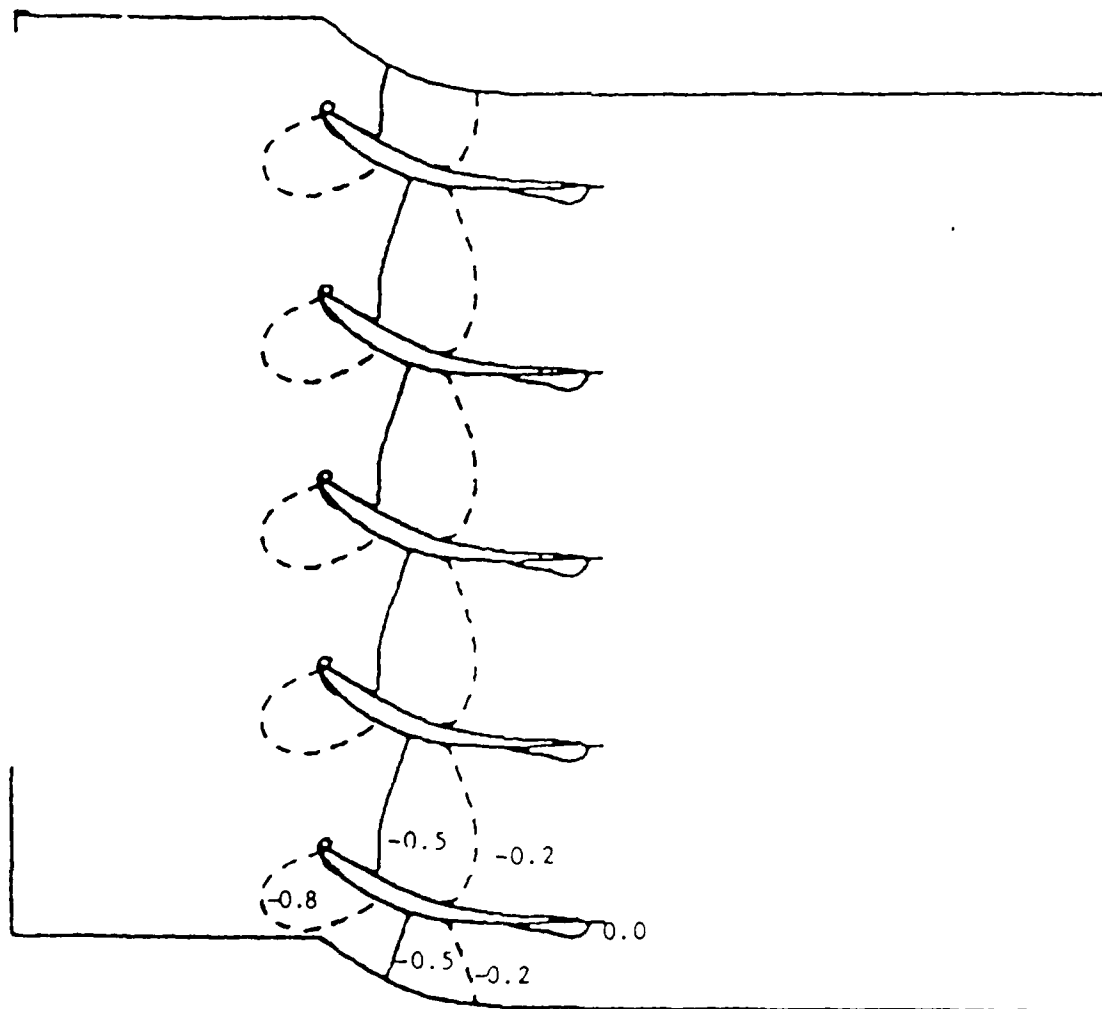
Fig. 5b. W-Velocity Contours, $\alpha_i = 55°$
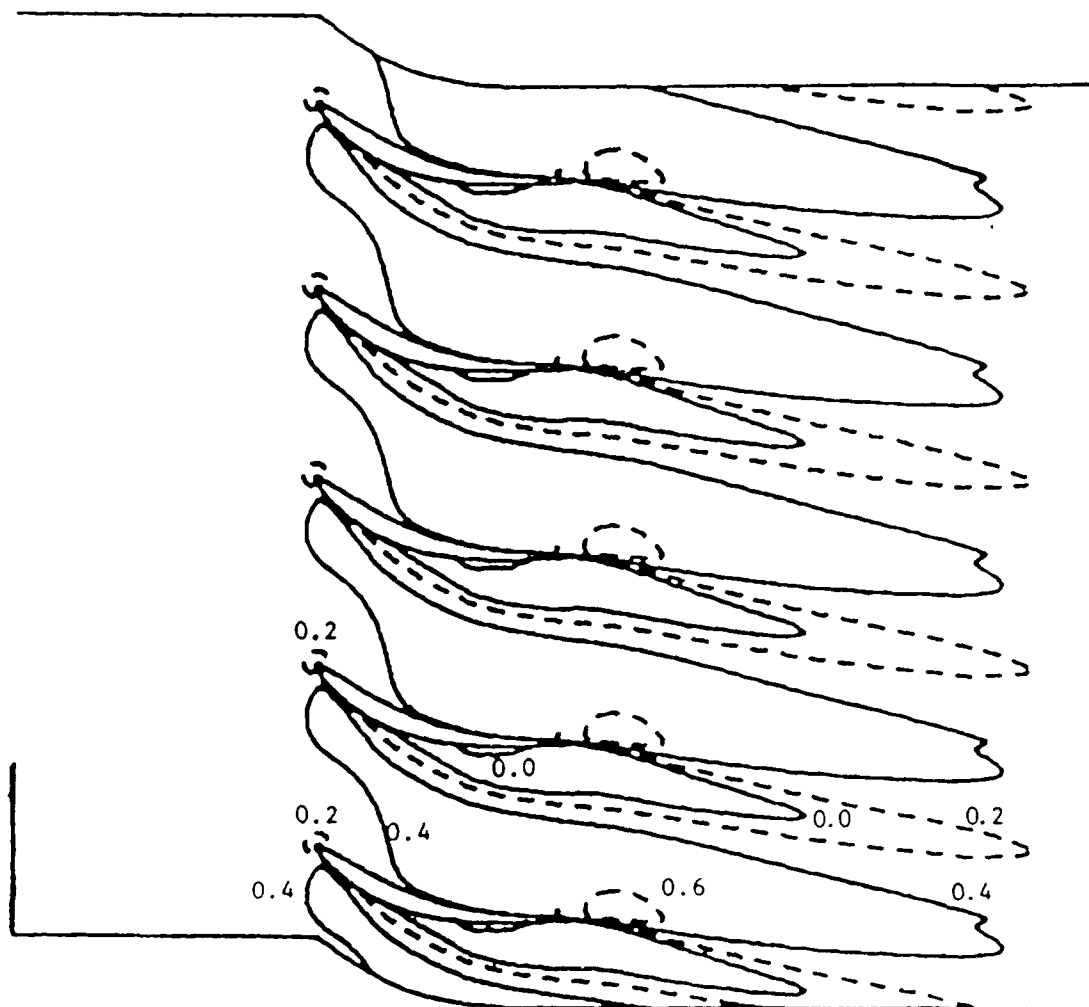
Fig. 6a. U-Velocity Contours, α_i - 57.7°.
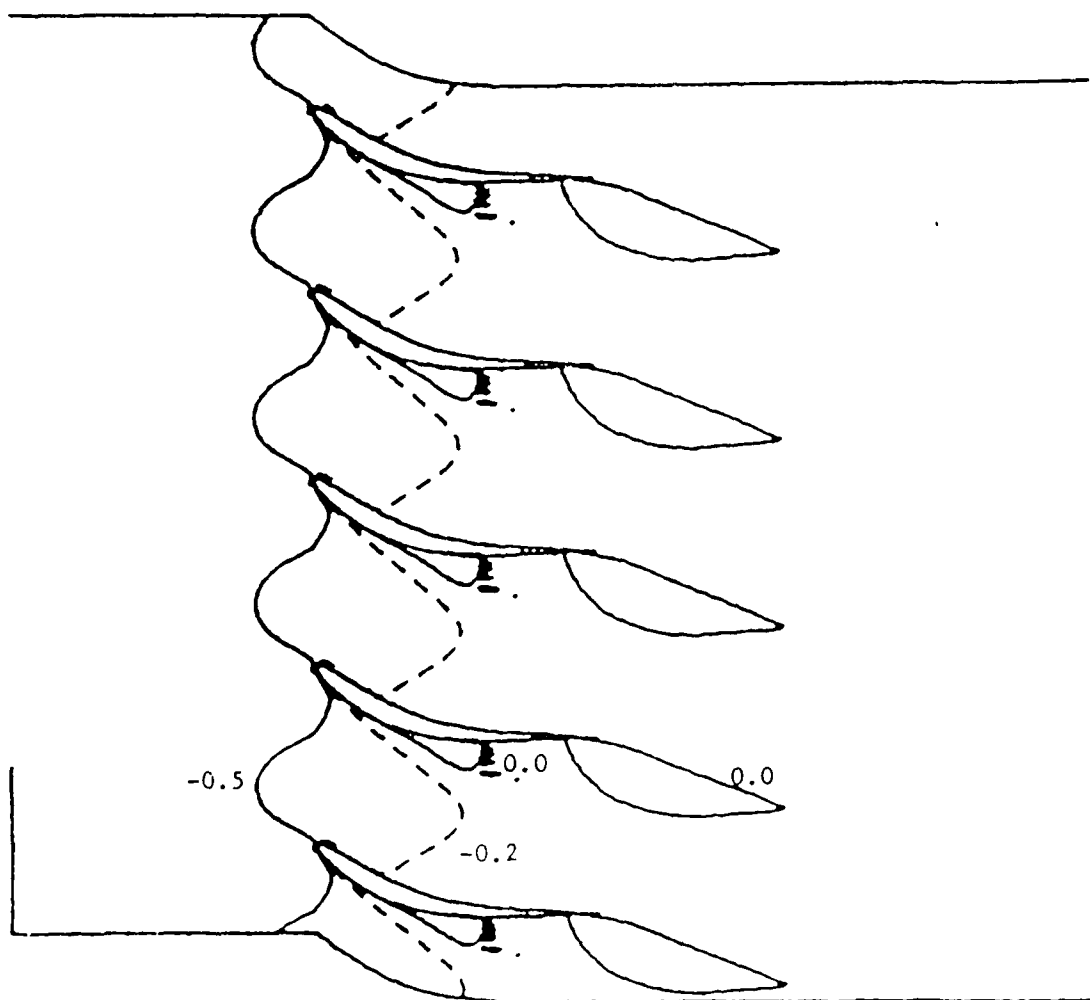
Fig. 6b. W-Velocity Contours, $\alpha_i - 57.7°$.
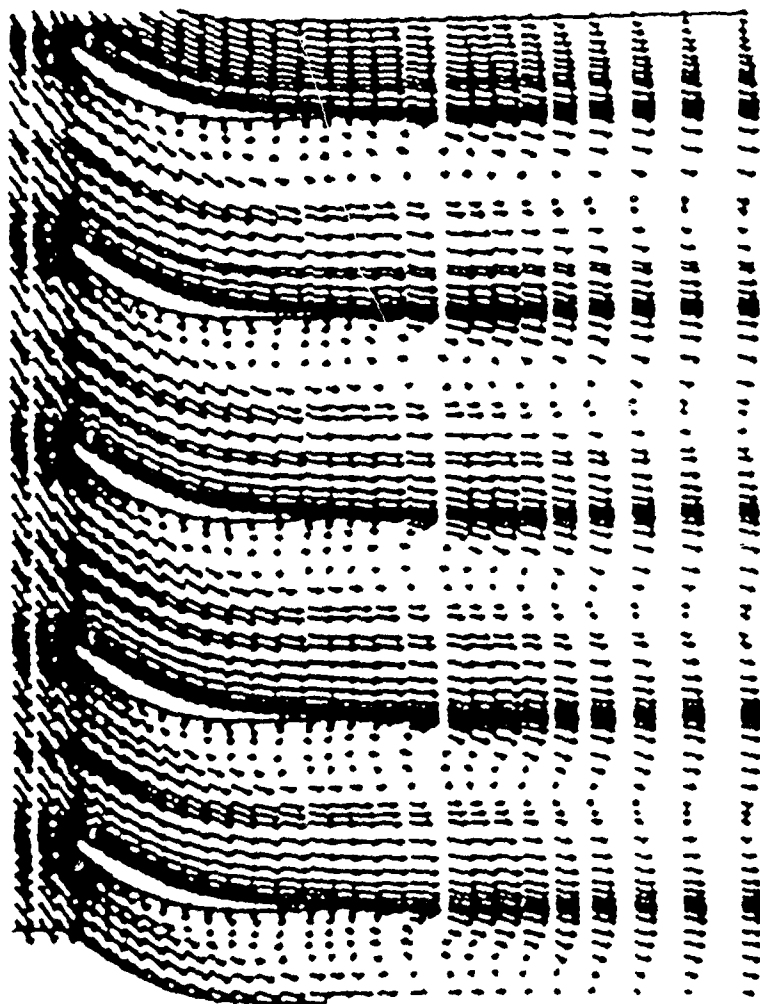
Fig. 6c. Velocity Vector Plot, $\alpha_1 = 57.7°$.

considered, the added term has the form $\frac{\rho u}{br}\frac{dbr}{dx}$, where r is the radial location

of the stream surface. In addition, terms corresponding to components of

centrifugal and Coriolis accelerations in the stream surface can be included.

As discussed in Ref. 32, this additional term in the continuity equation leads

to additional terms in the momenta and energy equations when they are written

in conservation form. The existing code now allows specification of a stream

sheet thickness, b, as a function of axial location to include this effect.

The effects of the addition of the Axial Velocity Density Ratio (AVDR)

terms to the code are shown in Figs. 7-8. Pressure coefficient (C_p) against

axial distance from leading edge for design calculations with AVDR terms and

without AVDR terms is shown in Fig. 7 for the Stephens-Hobbs on design H-grid

calculation. As the axial velocity density ratio is raised, the contraction

effects of thickening side-wall boundary layers are manifested as a gradual

decrease in suction surface pressure. The pressure rise attained at the

trailing edge by the diffusing suction surface flow governs the pressure levels

on the pressure surface, which tends to fall uniformly with increase in axial

velocity density ratio. Comparison of the averaged mass flux for two steady

state calculations, one with AVDR terms and the other one without AVDR terms,

along a single-passage cascade is shown in Fig. 8. In the axial direction

regions where db/dx = 0 (i.e., entrance and discharge regions), the averaged

mass flux was constant. For the case where AVDR terms were set to zero within

the passage, mass flux varied within the passage due to blockage effect of the

blades. However, upstream and downstream of the blades mass flux was constant

with the upstream and downstream values being equal. For the case where AVDR

terms were non-zero, these terms were still set to zero both upstream and

downstream of the passage but were non-zero within the passage. In this case,

the mass flux upstream of the passage differed from that downstream.

In viewing the computed surface pressure distribution, the distribution is

very similar to that obtained with the 'C-grid' and which compared favorably

with data (Ref. 19). A major difference occurs in the immediate vicinity of

the leading edge, where the stagnation computed with the 'H-grid' is

approximately 1.21; this is considerably higher than the expected value of 1.04

based upon the inflow Mach number of 0.4. In this regard, it should be noted

that the pressure coefficient, C_p, is defined as $(p-p\infty)/\frac{1}{2}\rho\infty V\infty^2$. Although

this unrealistically high value of stagnation point pressure coefficient is

confined to the immediate vicinity of the leading edge stagnation point and

CP ON BLADE SURFACE
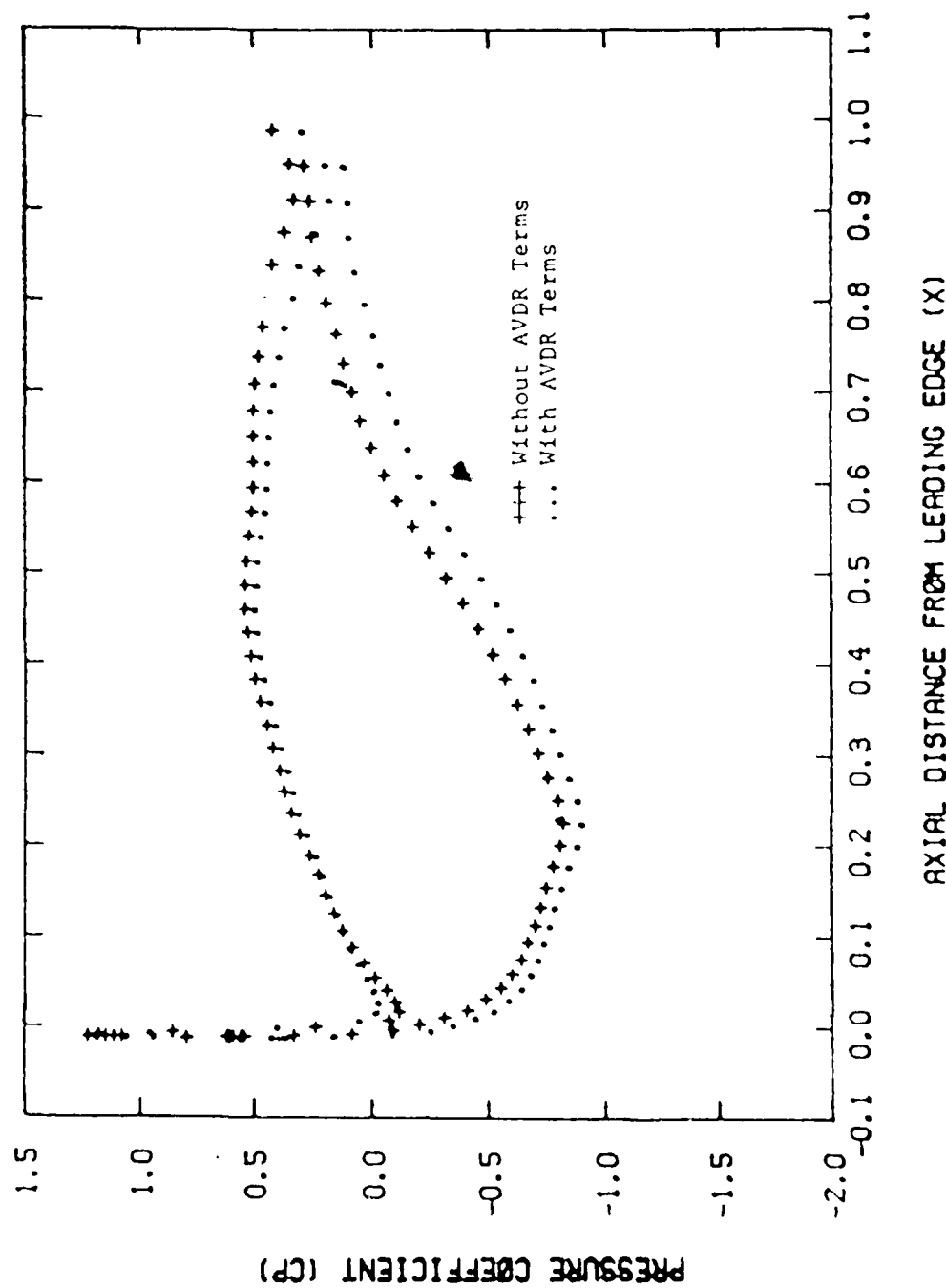
Fig. 7 – Effects of AVDR Terms on Blade Surface Pressure
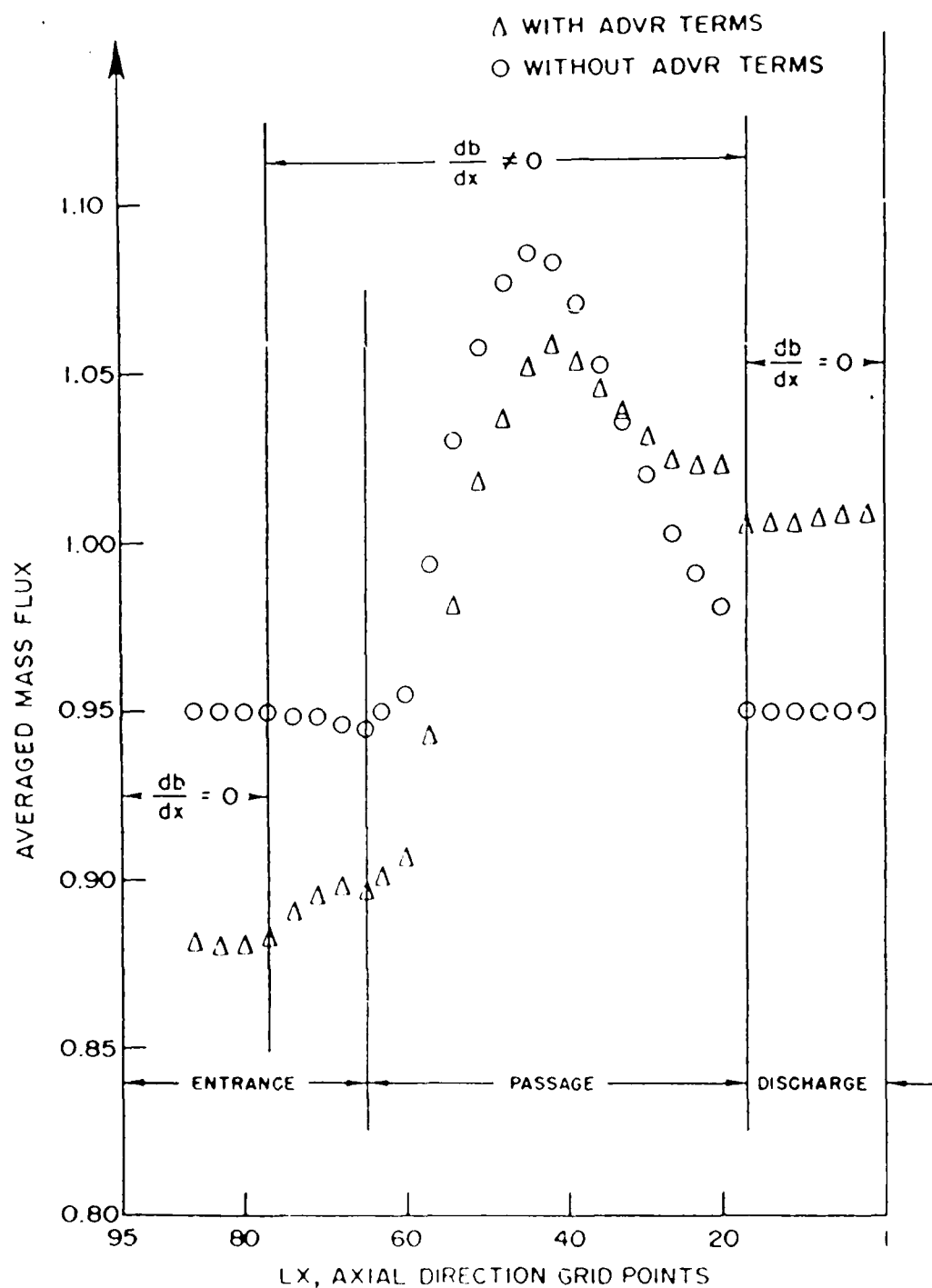
Fig. 8. – Effects of AVDR Terms on Averaged Mass Flux

drops very rapidly as one proceeds away from the stagnation point, this has been characteristic of the present experience with the 'H-grid' calculations. Previous experience with 'C-grids' indicates very close agreement between computed stagnation point pressure and that expected from inviscid considerations.

PRELIMINARY RESULTS

Results obtained under the present effort fall into three categories. These are (i) general results obtained during the course of deck development, modification, etc., (ii) inlet distortion, and (iii) the rotating stall study. In regard to the first of these, several cases have been discussed previously. These include the multiple passage capability (Figs. 3-6) and the AVDR capability (Figs. 7 and 8). In addition, a series of calculations were performed to demonstrate calculations including the energy equation and comparison between 'H'-grid and 'C'-grid results. The energy equation showed expected temperature contours in the flow field and inclusion of wall heat transfer did not show any significant effect on the wall pressure distribution. The cases considered were purely demonstration cases and therefore are not presented here. However, a comparison with data for the C3X turbine cascade is given in Ref. 20.

INLET DISTORTION RESULTS

Inlet distortion calculations were performed in the current program for two reasons. First of all, inlet distortion and its effect upon cascade performance is a subject of interest in its own right. Although most cascade analyses have assumed flow to be periodic on a passage-to-passage basis and also assume uniform inflow conditions, this is clearly not the case often found in practice. In practical situations, upstream obstructions such as struts, upstream flow nonuniformities, downstream pressure nonuniformities, etc., clearly provide nonuniform inflow conditions and negate single passage periodicity. Therefore, the inlet distortion problem is one of considerable interest which has received relatively little attention to date. A second reason for investigating the inlet distortion problem under the current effort is to consider a possible mechanism for introducing a disturbance to initiate

rotating stall and to assess relevant time scales. As will be discussed, both steady and unsteady inlet distortion flows were considered under the present study.

A sample inlet distortion calculation was performed for a two passage Stephens/Hobbs configuration in which the undistorted flow was at design, $\alpha_1 = 38°$. To demonstrate the inlet distortion capability, a total pressure deficit of one-half the inlet head was introduced on the inflow boundary of the upper passage while the inflow condition on the inlet boundary of the lower passage was kept uniform. The effects of this inlet total pressure distortion are illustrated in Fig. 9, which shows the distribution of the total pressure coefficient contours for the flows with and without inlet distortion. The effects of the inlet total pressure distortion on the blade surface pressure distribution are illustrated in Figs. 10a and 10b. As can be seen, although no distortion has been imposed along the inlet of the first passage, both blades are affected. Further indications of the effects of the inlet distortion on the passage flows are given in Figs. 11a-c, which are the contours of the static pressure coefficient, the u-velocity component and the w-velocity component. It appears that the transverse (i.e., w) velocity component is least sensitive to the total pressure distortion.

The previous case concerned inlet distortion applied to a design case condition. The next case considered was the off-design case, again with a time-independent inlet distortion. In this case, a stationary inlet distortion was introduced in terms of a combination of total pressure and flow angle along the inlet section. Figure 12 is a schematic of the imposed distortions in inflow angle and total pressure. This distortion covers a circumferential length of two and one-half passages. The inlet distortion calculation was initiated from an asymptotic steady state solution of a highly loaded case without distortion ($\alpha_{inflow} = 50°$ where design inflow is $38°$). Under these flow conditions, the cascade does not operate effectively and the generated static pressure recovery is considerably less than that obtained at design. Then, the distortion was imposed and the calculation proceeded until a new steady-state was reached. The effects of the inlet distortion on the blade surface pressure distribution are illustrated in Fig. 13. It can be seen that, although the inlet distortion was applied to only one-half of the total inlet circumferential length, the surface pressure of all the blades is affected. It should also be noted that the maximum effect of distortion occurs at blade
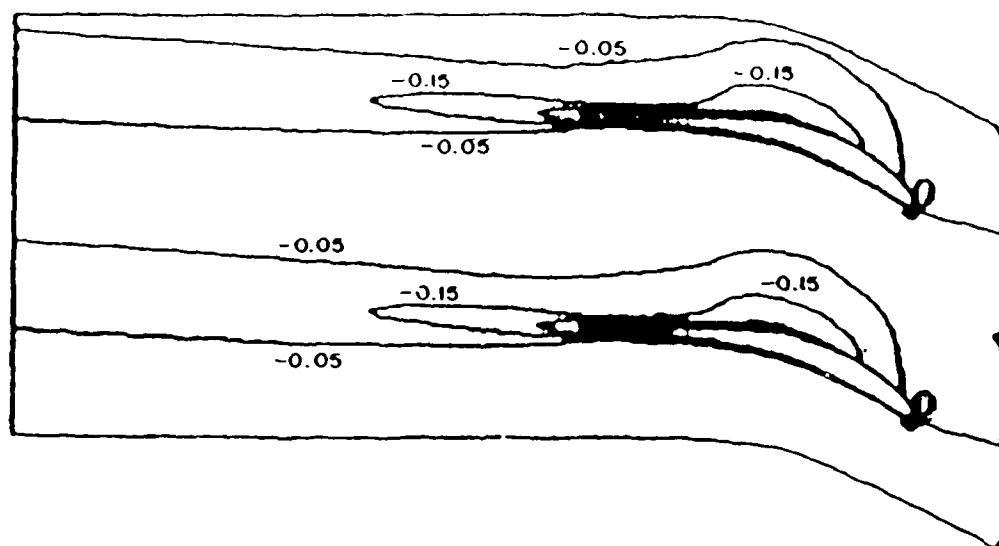
a.   No Inlet Distortion
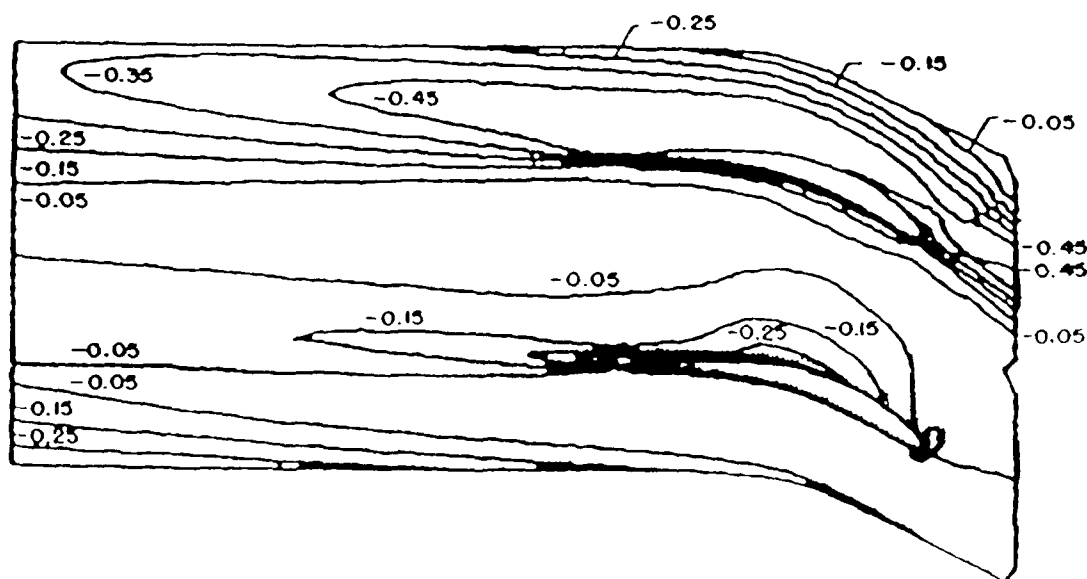
b.   Inlet Distortion

Fig. 9 — Total Pressure Coefficient Contours for Inlet Distortion Case
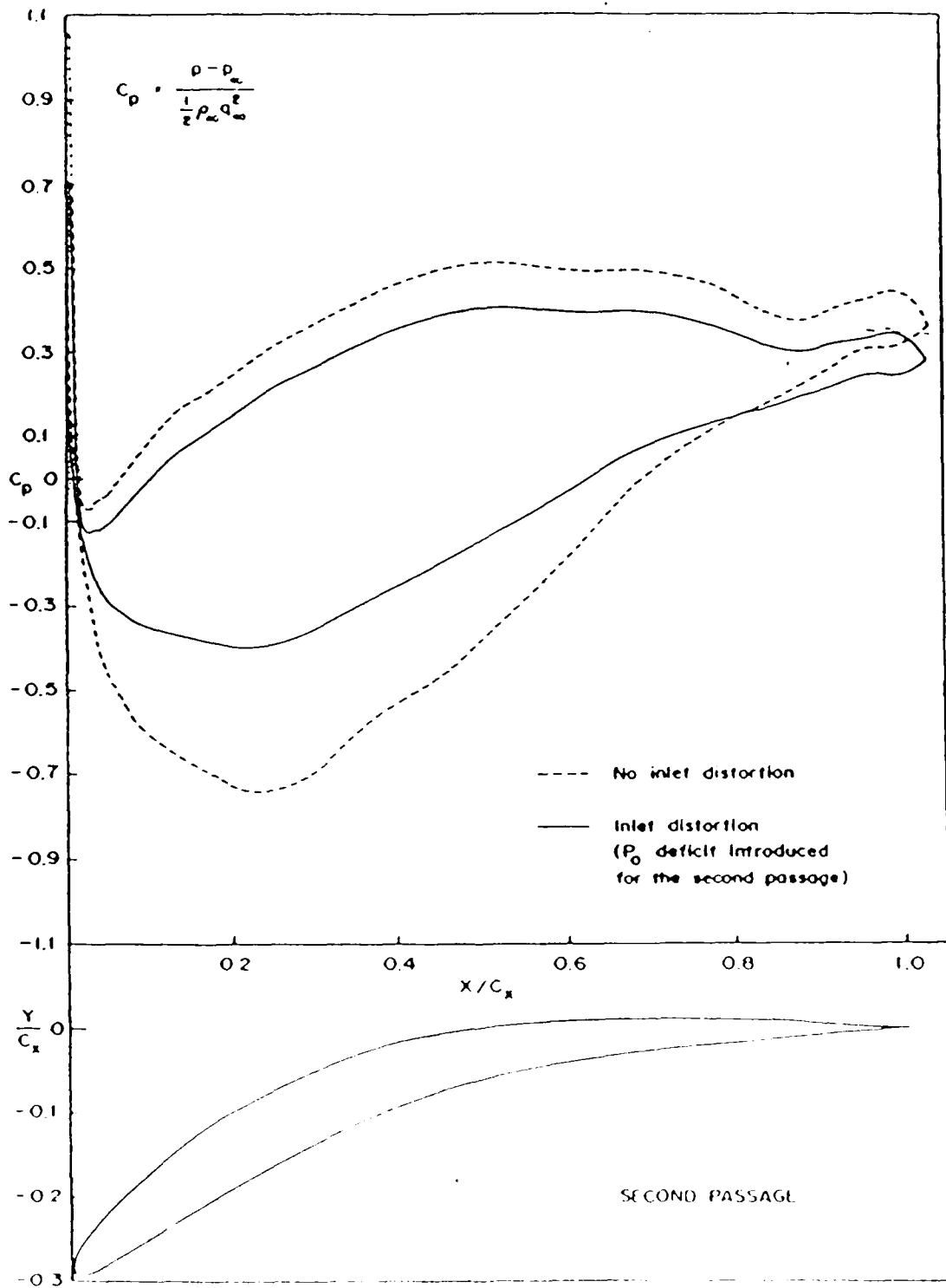
Fig. 10a — Surface Pressure Distribution, Inlet Distortion

$$C_p = \frac{p - p_\infty}{\frac{1}{2}\rho_\infty q_\infty^2}$$

---- No inlet distortion

Inlet distortion
(P$_o$ deficit introduced
for the second passage)

FIRST PASSAGE
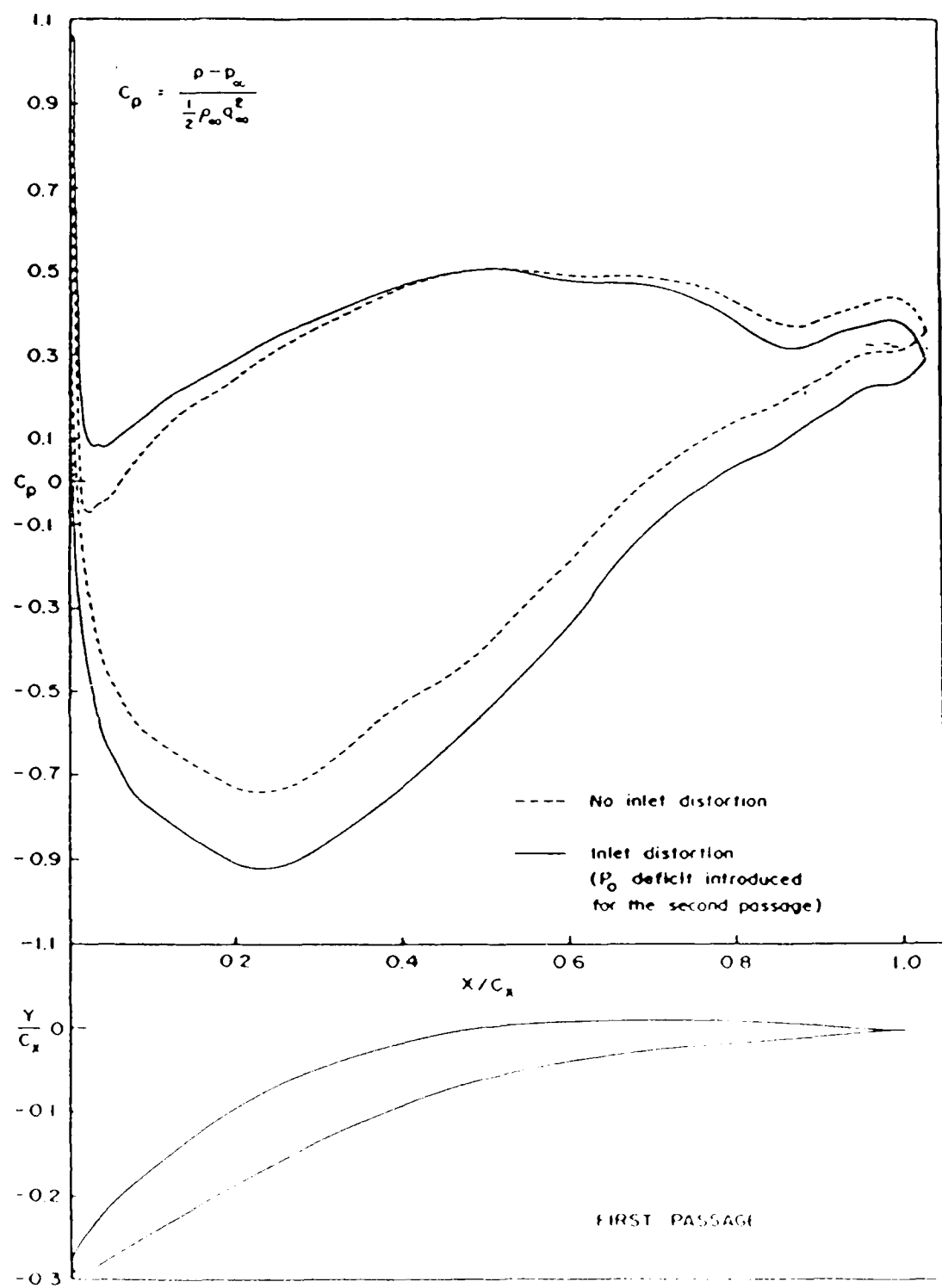
Fig. 10b – Surface Pressure distribution – Inlet distortion

-52-
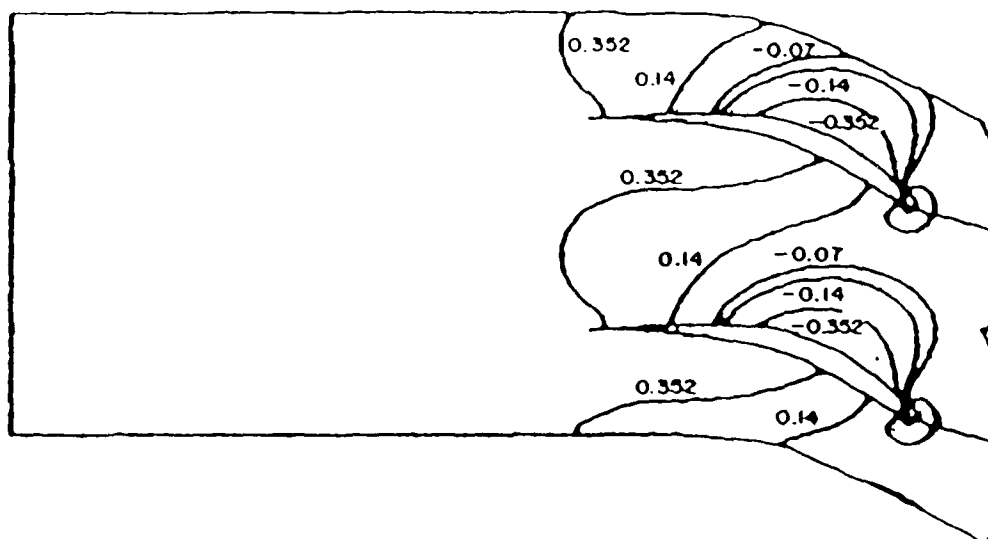
a. No Inlet Distortion
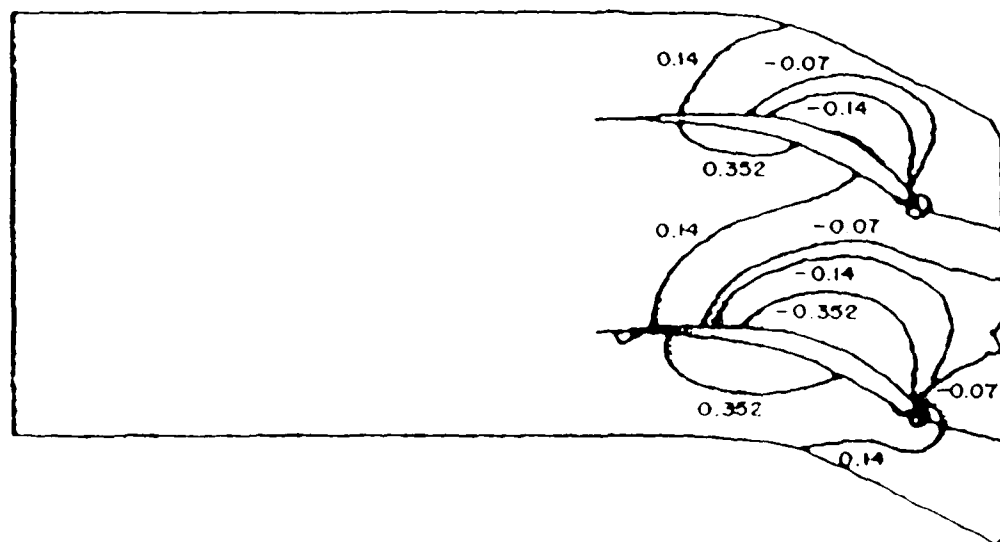
b. Inlet Distortion

Fig. 11a — Static pressure coefficient contours.
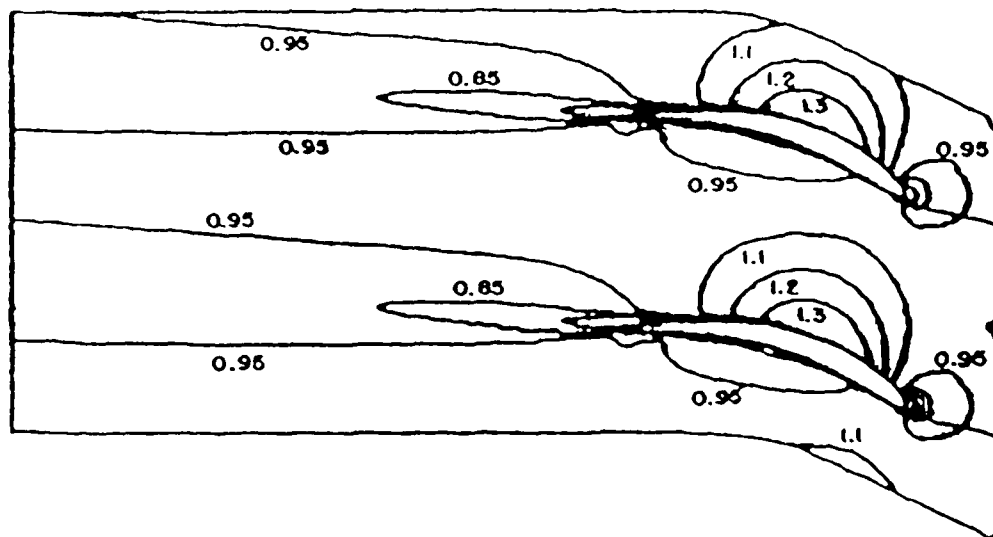
a. No Inlet Distortion

b. Inlet Distortion

Fig. 23. - U-Velocity contour

-54-
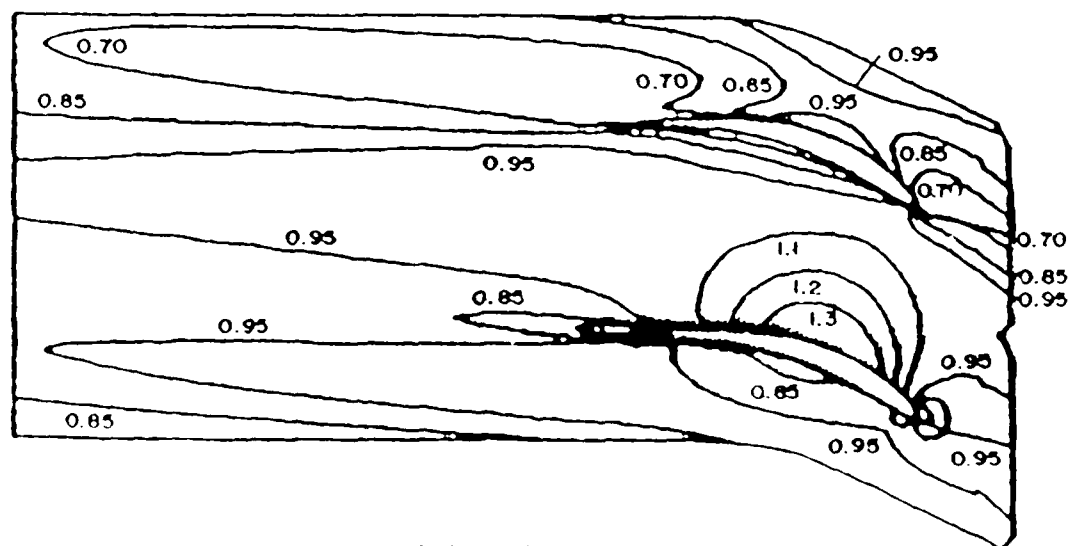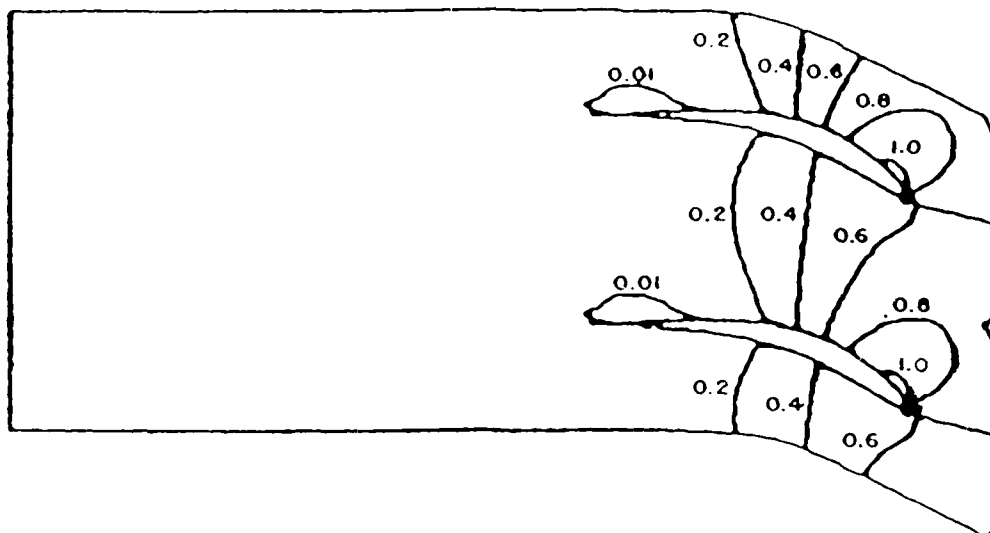
a. No Inlet Distortion
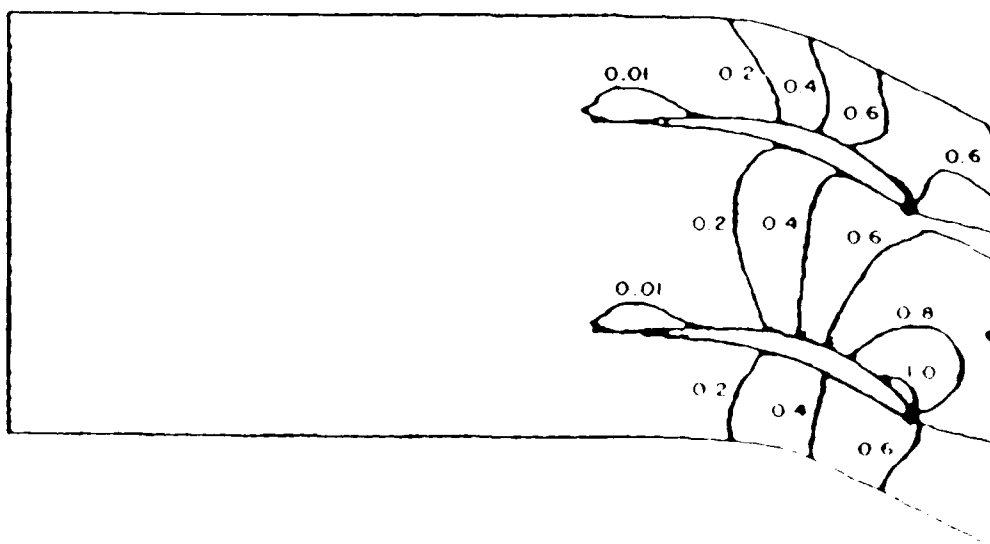
b. Inlet Distortion

Fig. 11c - w-velocity contour
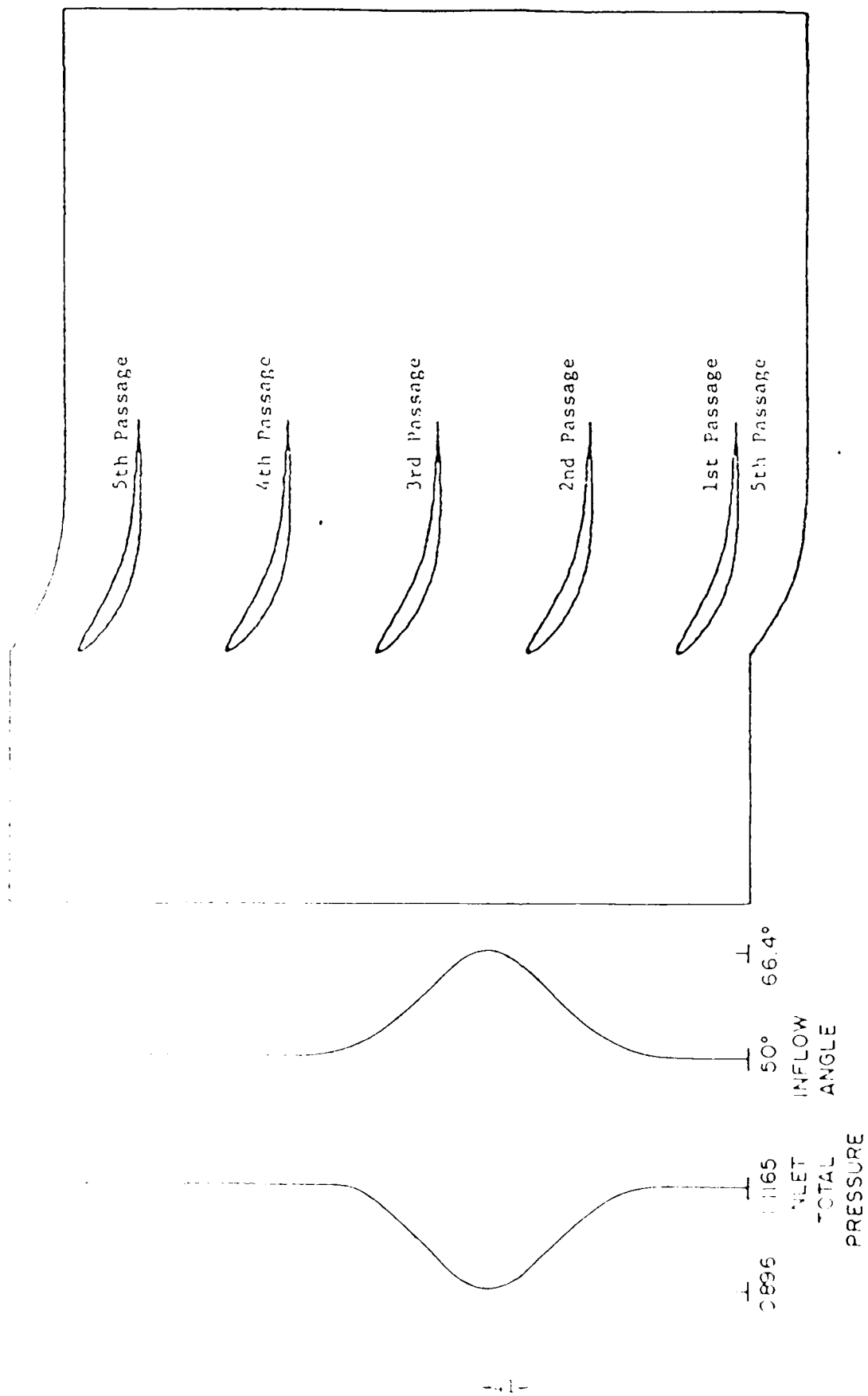
Fig. 12 - Stationary Distortion Along the Inlet Boundary

5th Passage

4th Passage

3rd Passage

2nd Passage

1st Passage

5th Passage

66.4°

50° INFLOW
ANGLE

.1165
INLET TOTAL
PRESSURE

.0896

-54-
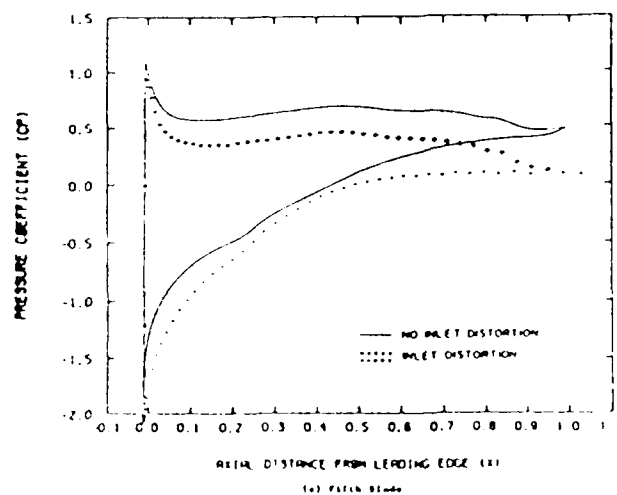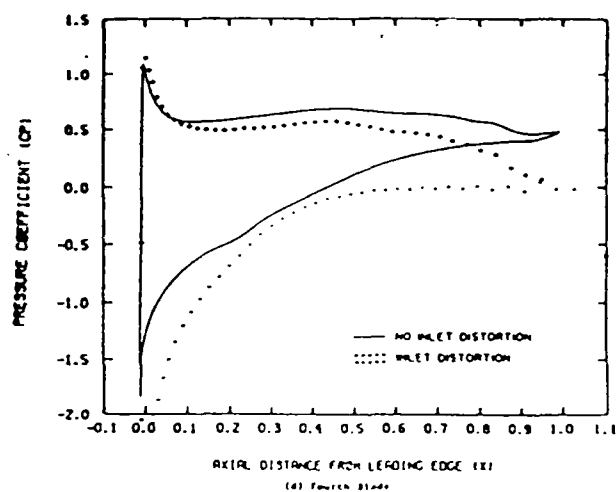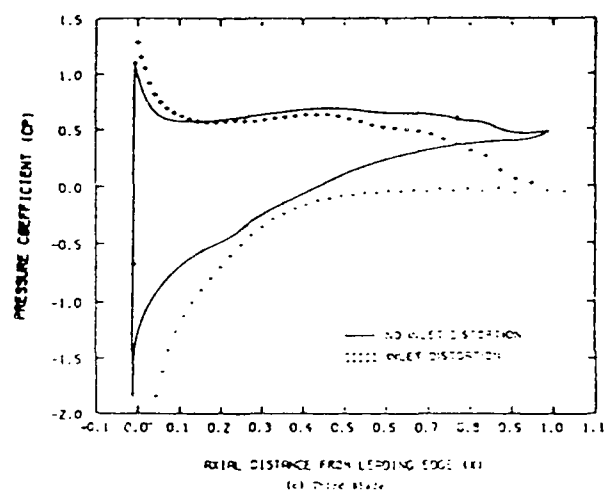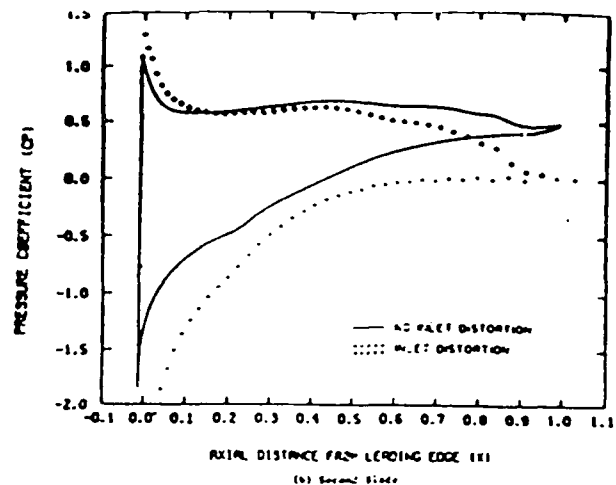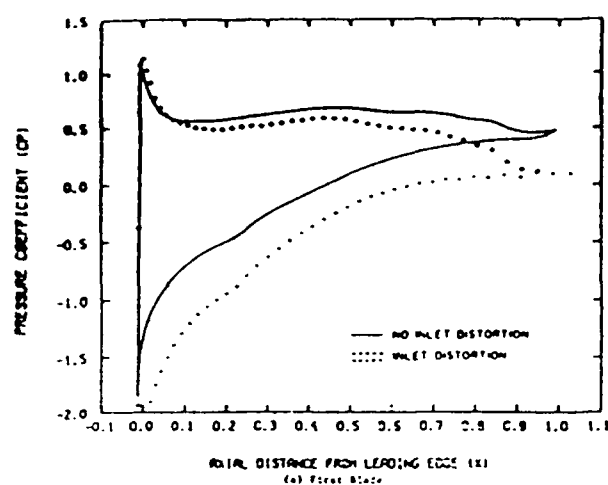
Fig. 15 — Surface Pressure Distribution on
Cascade Blades

passages four and five, which are the locations to which the upstream distortion is convected by the mean flow, as shown in Fig. 14. This is more clearly shown in the velocity plots of Figs. 15a-15c. For the purpose of comparison, both the no-distortion and with-distortion cases are given in Figs. 15a-15c. These figures indicate that the most salient feature of the distorted flow field is the appearance of larger separation zones on the suction sides of the trailing edges of all blades. The separation bubbles in passages two and three are relatively larger, covering approximately 50 percent of the chord and elongating into the wake.

The final inlet distortion case focused upon unsteady response of a cascade subject to change in inflow conditions. A single passage cascade subject to a total pressure distortion on its inlet boundary was used for this test case. The initial condition for the single passage case is shown in Fig. 16b. This is the steady-state solution of a single-passage cascade subject to an inlet distortion. Subsequently, this upstream disturbance is removed over a short period of time and the relaxation of the flow is followed up to t = 7.2. For purposes of comparison, the eventual steady-state is also given in Fig. 16a. The relaxation process of the reversed flow zone is illustrated by the time history of the contours of axial velocity (Fig. 17), circumferential velocity (Figs. 18 and 19), velocity vector field (Figs. 20 and 21) and pressure coefficients on the blade surface (Figs. 22a and 22b). From these figures, it can be seen that following the removal of the inlet distortion, the large separation region on the suction side is shrinking (t = 1.4, 3.2), subsequently, the flow becomes essentially attached to the blade, however, a zone of reversed flow appears in the near wake region (t = 4.0) and eventually disappears (t = 4.8, 7.2). It can be seen from Fig. 21 that the revolving sense of the apparent vortex for t = 3.2 (separation zone on suction surface) is opposite to that of the vortex for t = 4.0 (reversed-flow zone in near wake). Based on this investigation, the relaxation time is estimated to be at least 7 dimensionless time units (the axial chord length is 1 and the inflow axial velocity is 1), which should give an estimate of the time required for a passage to recover to full flow after the rotating stall cell has passed.

ROTATING STALL RESULTS

The major focus of the present program is the application of the Navier-Stokes analysis to the rotating stall problem. As has been discussed in
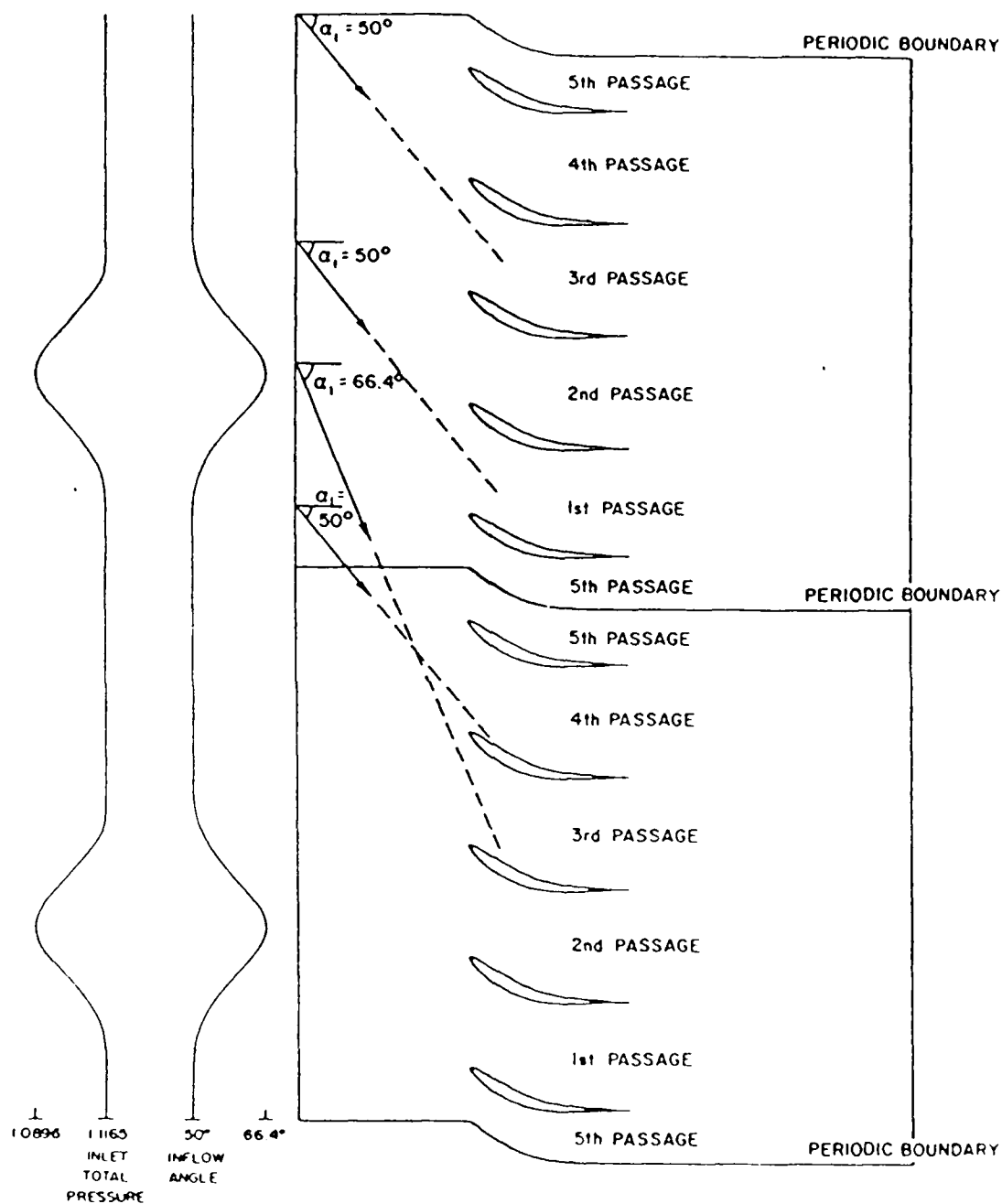
Fig. 14 — Inlet Distortion.

-44-

b. With Inlet Distortion

a. No Inlet Distortion ($\alpha_1 = 50°$)
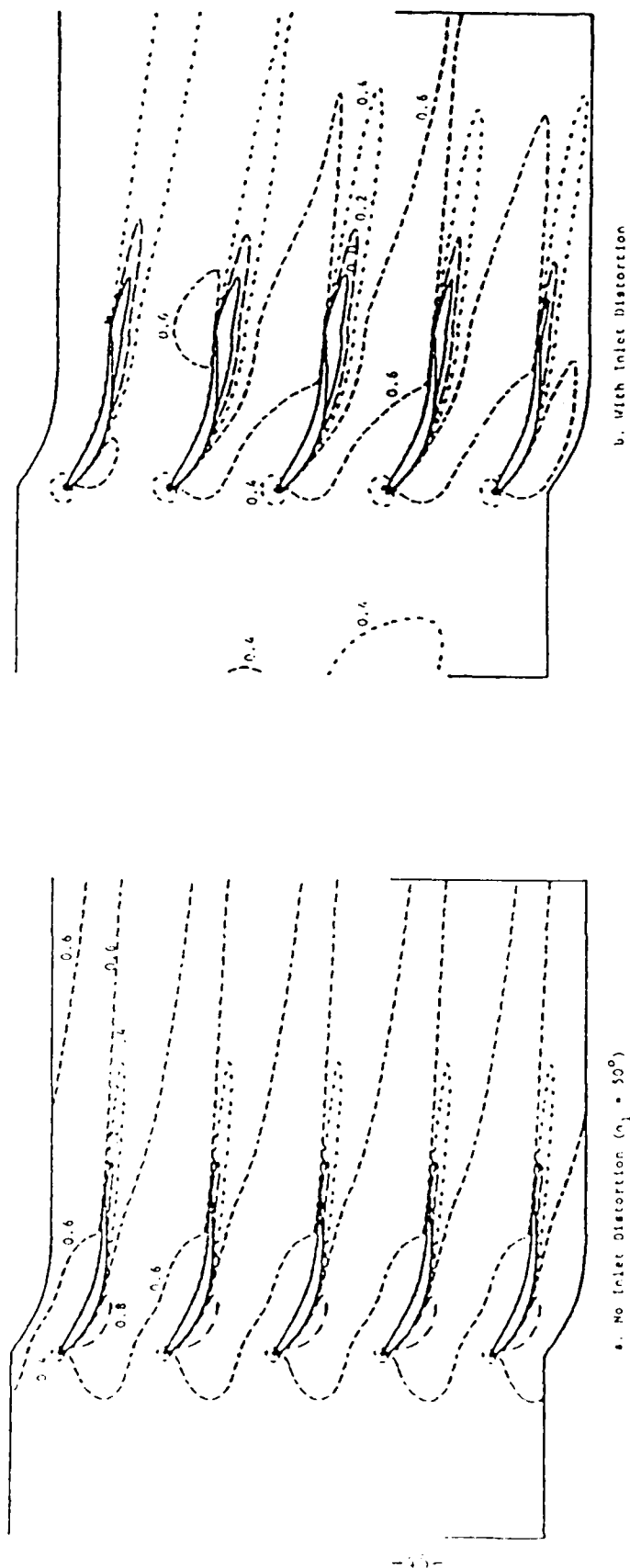
Fig. 15a — Contours of Axial Velocity Component

b. With Inlet Distortion
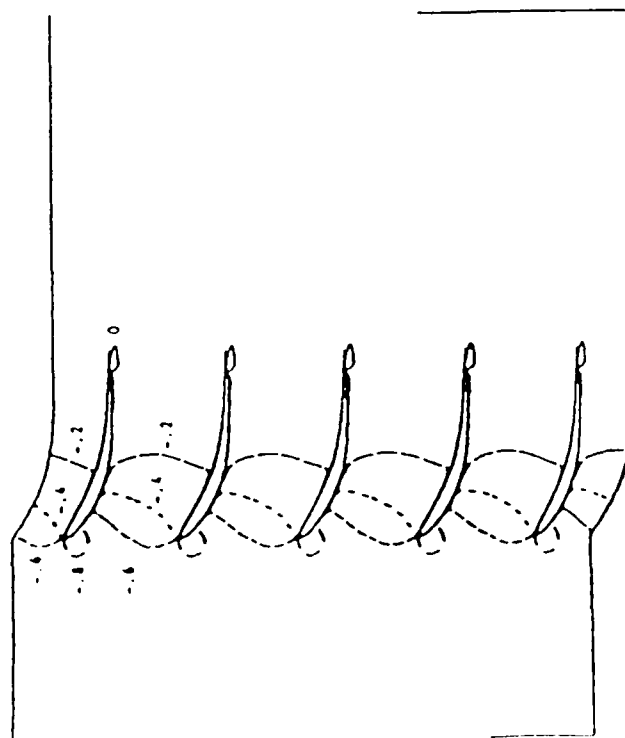
a. No Inlet Distortion, $\alpha_1 = 30°$
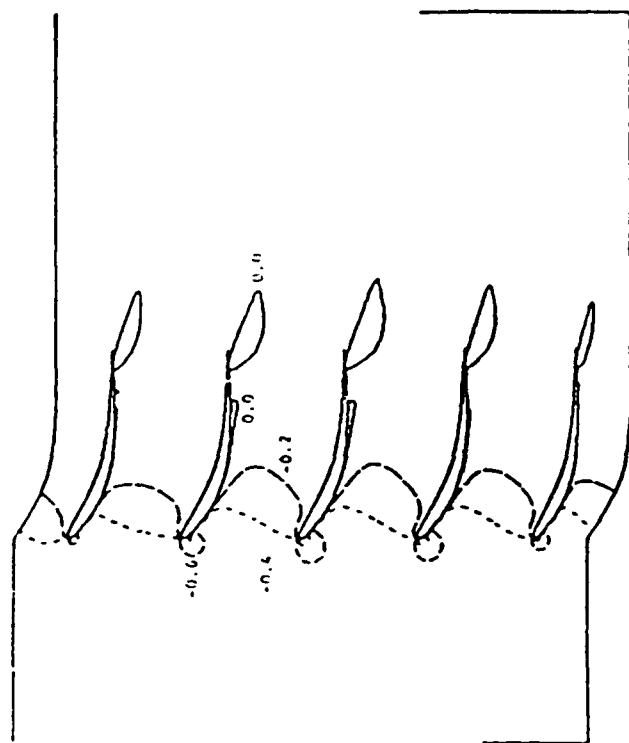
Fig. 15b – Contours of Circumferential Velocity Component

VECTOR SCALE - VM 1.356
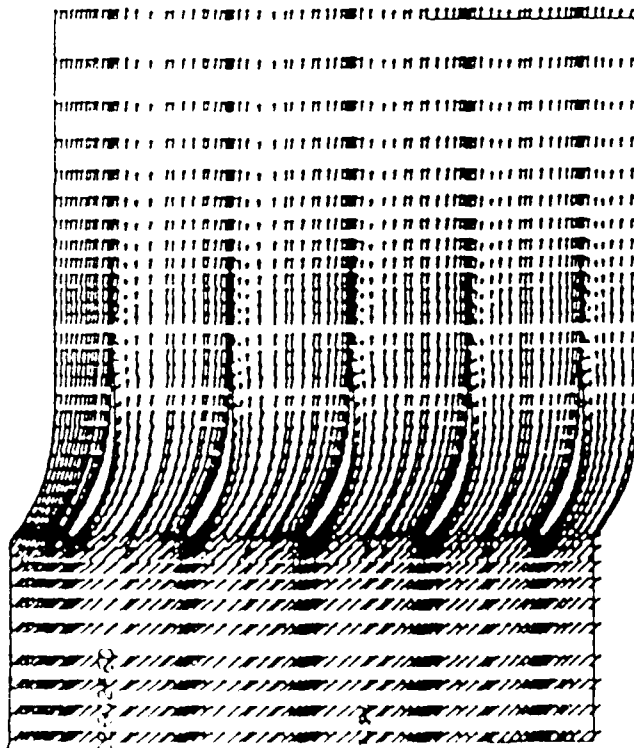
b. With Inlet Distortion

VECTOR SCALE - VM 1.910

a. No Inlet Distortion, $\alpha_1 = 50°$
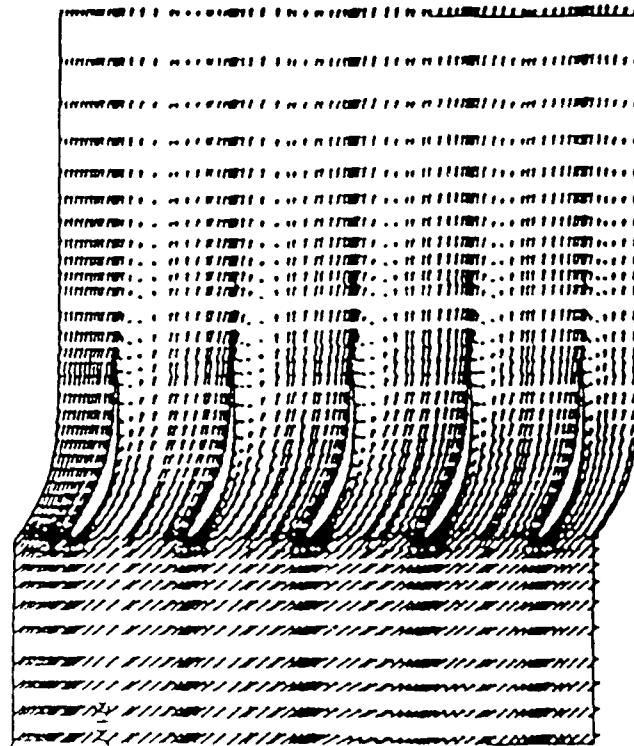
Fig. 15c – Velocity Vector Field
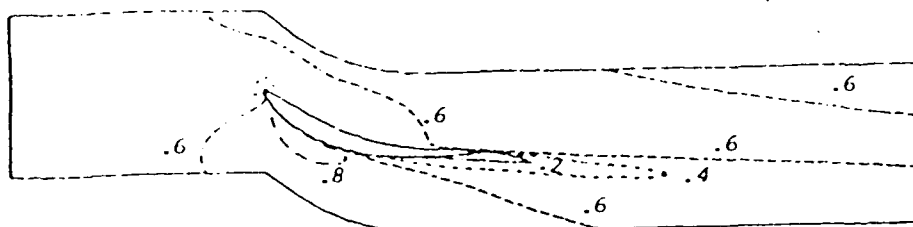
a. No Inlet Distortion
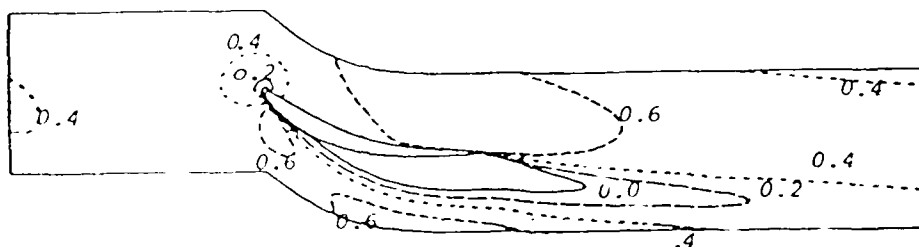
b. With Inlet Distortion t = 0

Fig. 16 — Contours of Axial Velocity Component
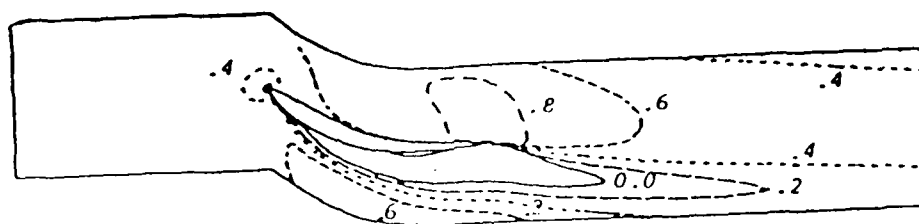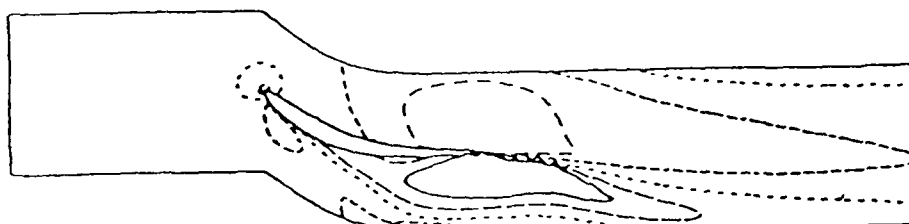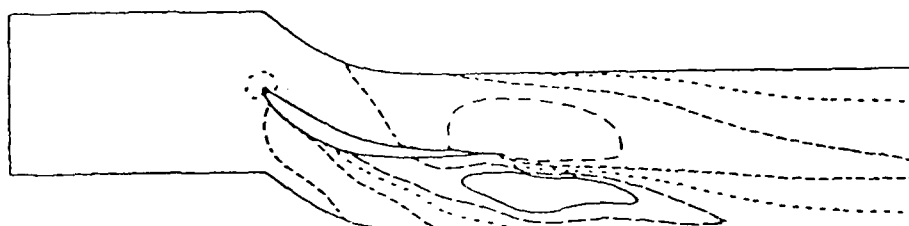
(a) t = 1.4

(b) t = 3.2

(c) t = 4.0
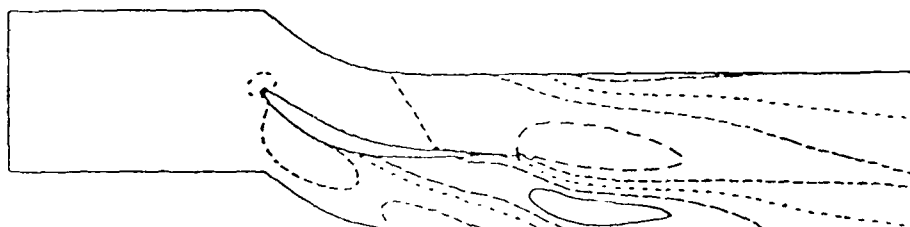
(d) t = 4.8
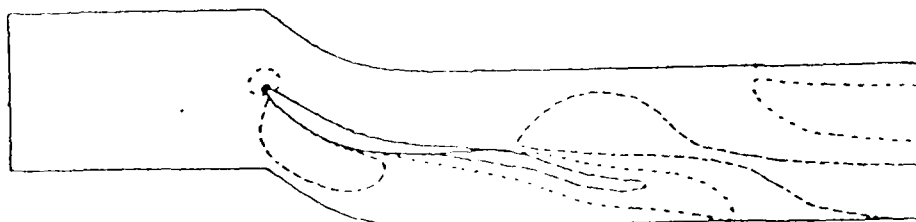
(e) t = 7.2

Fig. 17 — Contours of Axial Velocity Component at Different
Times with Inlet Distortion Removed
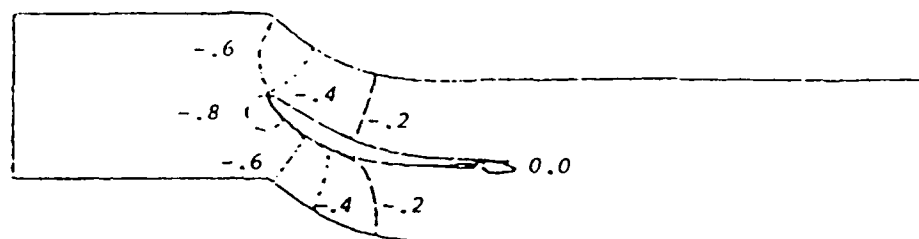
a. No Inlet Distortion, $\alpha_1 = 50°$
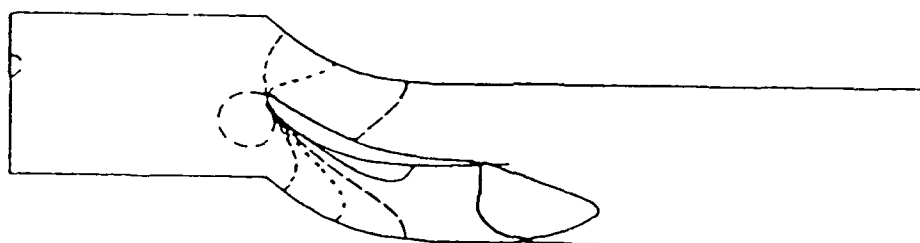
b. With Inlet Distortion, t = 0

Fig. 18 - Contours of Circumferential Velocity Component
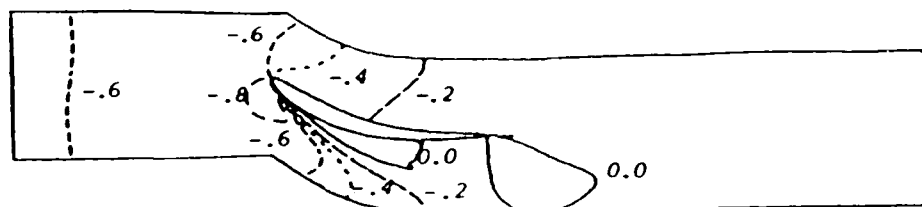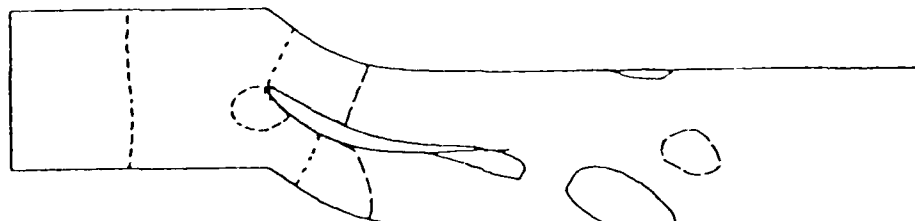
(a) t = 1.4

(b) t = 3.2

(c) t = 4.8
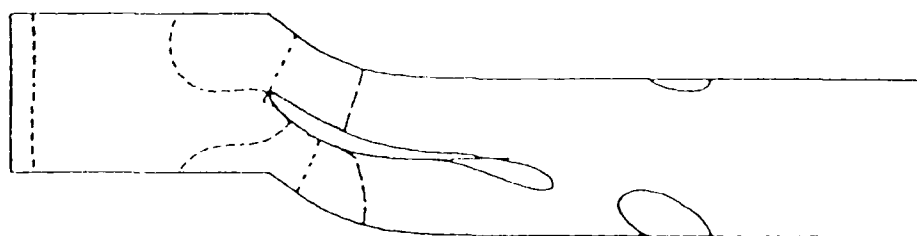
(d) t = 6.0

(e) t = 7.2

Fig. 4-7. Contours of Circumferential Velocity Component at
Different Times With Inlet Distortion Removed
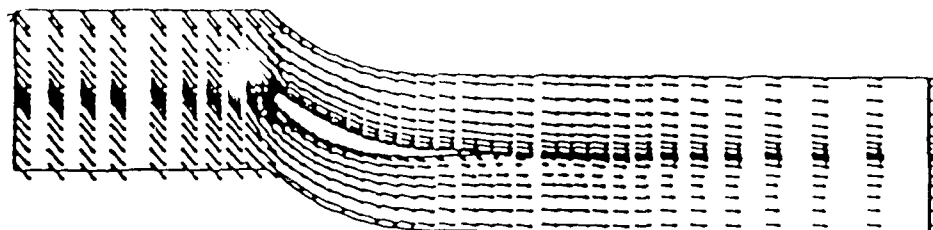
a. No Inlet Distortion
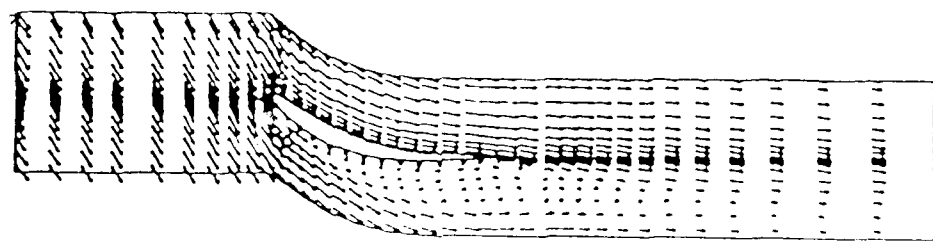
b. With Inlet Distortion, t = 0

Fig. 20 — Velocity Vector Field
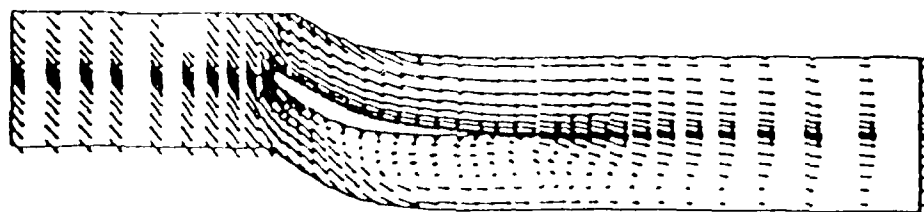
(a) t = 2.4
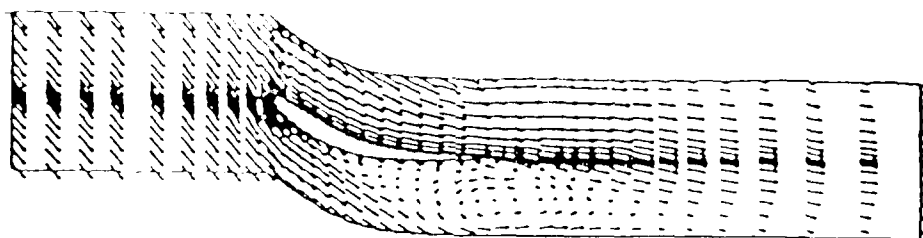
(b) t = 3.2
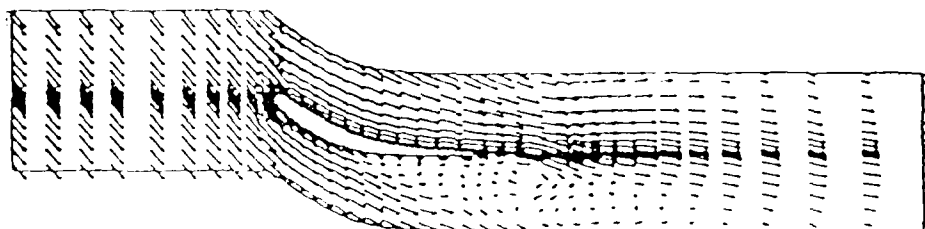
(c) t = 4.0
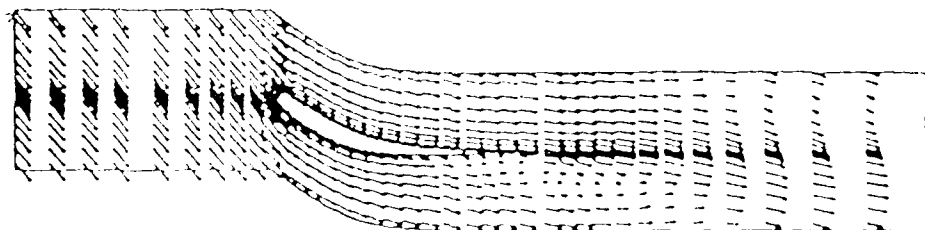
(d) t = 6.6
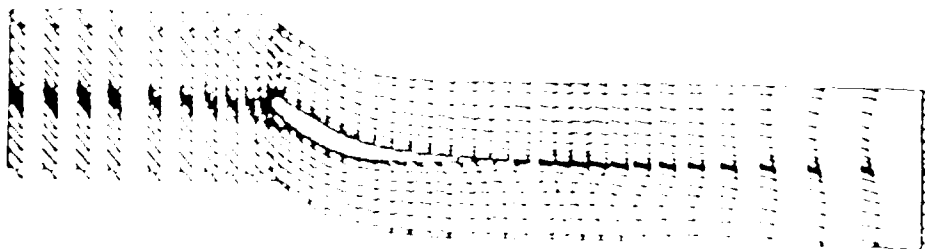
(e) t = 7.2
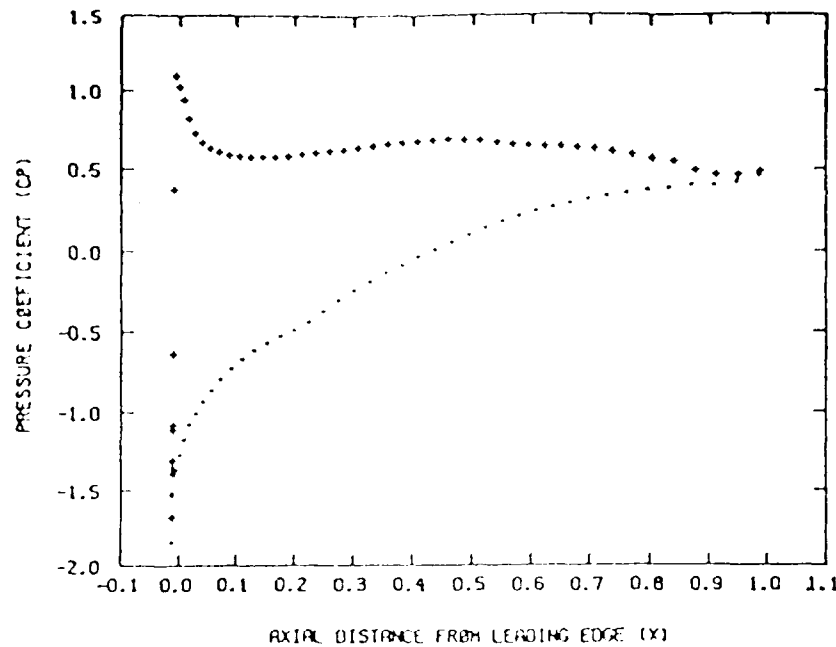
CP ON BLADE SURFACE

a. No Inlet Distortion

CP ON BLADE SURFACE   IPAS = 1   IOT = 1601 - 1700
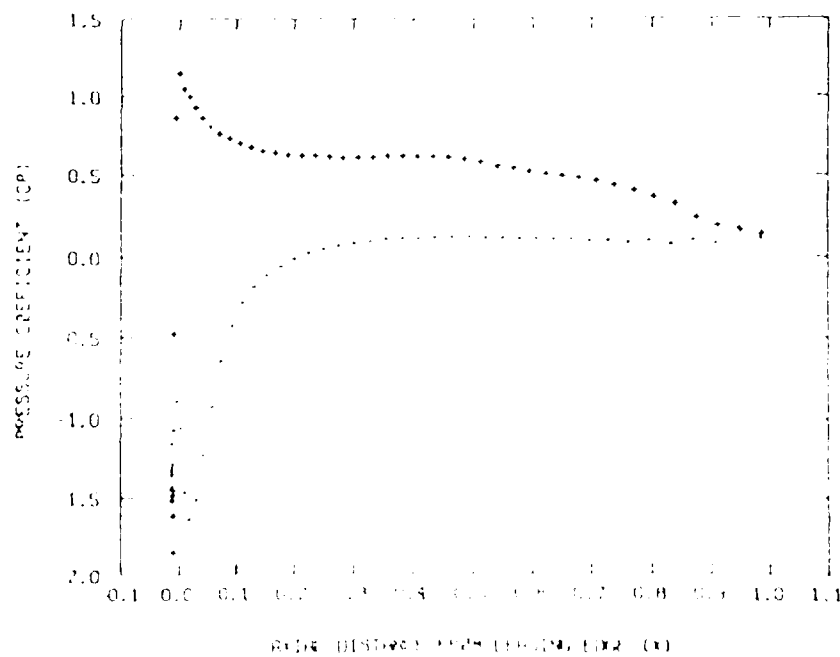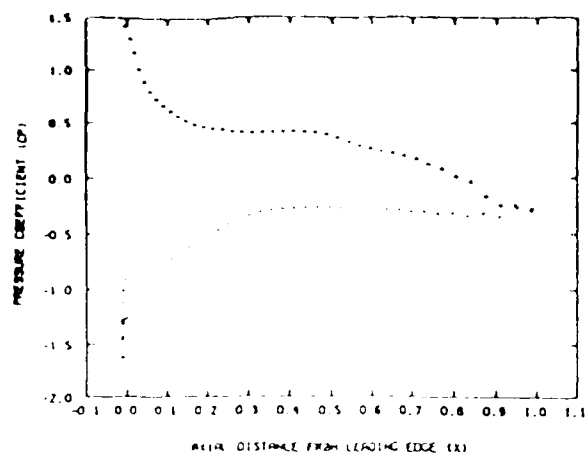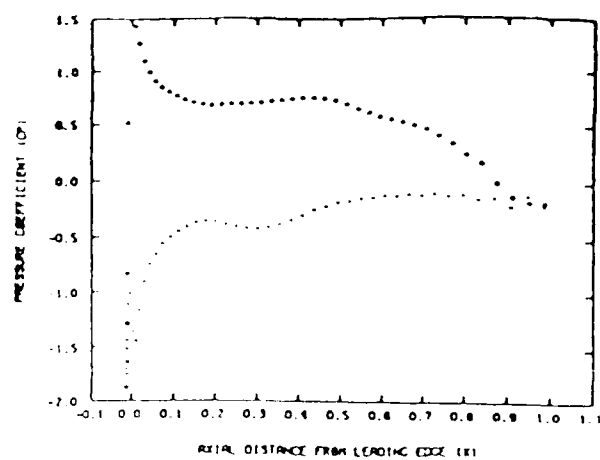
(a) t = 1.0

(b) t = 1.4
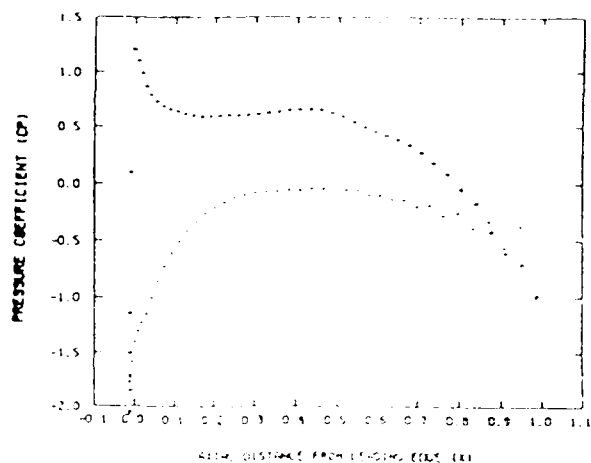
(c) t = 3.0
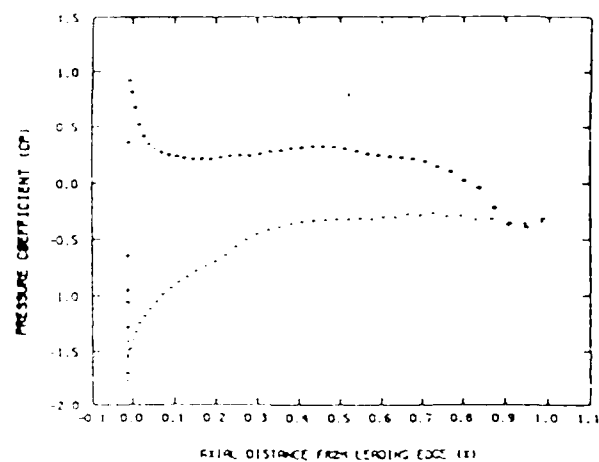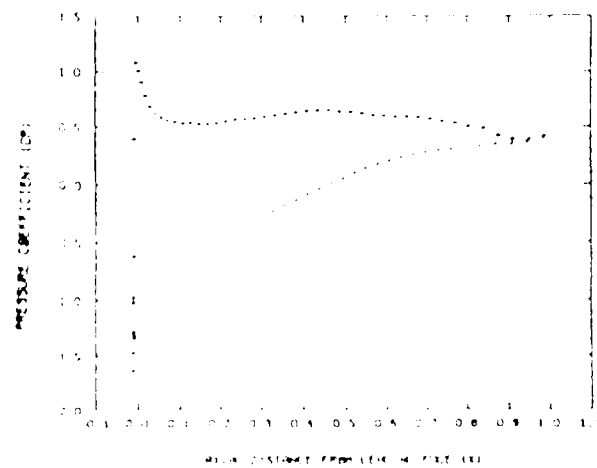
(d) t = 4.0

the previous sections, considerable effort was required prior to addressing the rotating stall problem. This preliminary effort consisted of code vectorization, extension to multiple passages, inlet distortion and inlet relaxation time. The present report section details the application of the Navier-Stokes analysis to the rotating stall problem.

In applying the Navier-Stokes equations to the rotating stall problem, it is necessary to decide whether to use the energy equation, Eq. (3), or to make a constant total temperature assumption. Although including an energy equation does relieve an approximation, it also considerably increases computer run time, perhaps by an additional fifty percent. When written in terms of total temperature, the energy equation becomes

$$\rho \frac{D C_p T^0}{Dt} = \frac{\partial p}{\partial t} + \frac{\partial \tau_{ij} u_i}{\partial x_j} + \frac{\partial}{\partial x_i} \left(\frac{k \partial T}{\partial x_i} \right) \tag{22}$$

Considering the term for the time derivative of pressure, Briley, McDonald and Shamroth (Ref. 23) have shown that when appropriately nondimensionalized, the term has the form $(\gamma - 1) M_r^2 \rho \, \partial \hat{C}_p / \partial t$ where M_r is an appropriate reference Mach number and $\hat{C}_p$ is a pressure coefficient. For the relatively low Mach flows where the time rate of change pressure is small, as is true in the cases of rotating stall initiation considered here, the total temperature approximation should still be reasonable and it is used here to conserve computer time. However, the option to solve for the energy equation is included in the code and can be invoked. It is expected that for calculations which lead to stronger stall, the constant total temperature assumption may become inappropriate and an energy conservation equation would need to be included.

The rotating stall problem is a very complex one; most previous efforts have approached the problem via linearized inviscid equations with the blade row represented by an actuator disc (e.g., Refs. 1-8), approaches based upon component modeling (e.g., Refs. 9-13) and approaches based upon vortex method simulation (Refs. 14 and 15). The present approach is based upon a Navier-Stokes simulation. Advantages and limitations of the present approach have been discussed in the Background section and will not be repeated here.

The case considered is that of Ludwig, Nenni and Arendt (Ref. 33) which is stator set No. 1 from a J-79 jet engine. The coordinate for the midspan geometry was furnished by L. Smith and M. Suo of General Electric Company

-56-

(Ref. 34). Prior to considering a multipassage calculation, a series of
calculations were performed with a single passage configuration. The stagger
angle was 40° and solidity was 0.85. The grid used in both the single and
multiple passage configuration is shown in Fig. 23.

In regard to the type of grid to be used, previous results have been
obtained with both a C grid and an H grid. The advantage of an H grid is that
it allows the upstream grid boundary to be placed at an arbitrary distance
upstream of the cascade entrance plane. In contrast, as the upstream boundary
of the C grid is moved further from the entrance plane, the grid becomes
increasingly non-orthogonal, thus effectively limiting placement of the
upstream boundary. Allowing the boundary to be placed far upstream allows the
flow upstream of the cascade entrance plane to react to individual separated
passages. The disadvantage of the H grid is the rapidly changing coordinate
metric coefficients in the blade leading edge region and the metric singularity
at the leading edge branch point. These may affect both numerical stability
and accuracy. Since the rotating stall study is a study of an instability
leading to a propagating stall cell, the decision was made to utilize a C grid
but to place the inflow boundary as far upstream as possible without having the
grid become unacceptably non-orthogonal.

The grid contains 149 pseudo radial lines and 35 pseudo azimuthal lines,
giving a total number of 5215 grid points per passage. As can be seen, very
high resolution in the pseudo-radial direction is obtained in the vicinity of
the blade, with the first point from the blade being approximately 0.1×10^{-3}
chords from the blade. High streamwise resolution is found in the leading and
trailing edge regions.

In order to qualitatively assess the performance of the numerical
simulation, five different cases were carried out for a single passage flow:
(1) $\alpha_1 = 57°$, (2) $\alpha_1 = 58.5°$, (3) $\alpha_1 = 59°$, (4) $\alpha_1 = 60°$, and (5) $\alpha_1 = 61°$,
where α_1 is the inflow angle at the inflow boundary. The relationship between
α_1 and the rotating stall inception boundary is illustrated in Fig. 24, which
is taken from the CALSPAN report (AFAPL-TR-73-45). The parametric locations of
simulated cases are also indicated in this figure. The goal of the current
simulations is to assess the qualitative consistency between the experimental
results and the numerical results insofar as the inception of unsteady stall is
concerned. As will be demonstrated in the following results, although only a
single passage was considered, the results indicated by the numerical
simulation closely follow the trend indicated by the experiments.
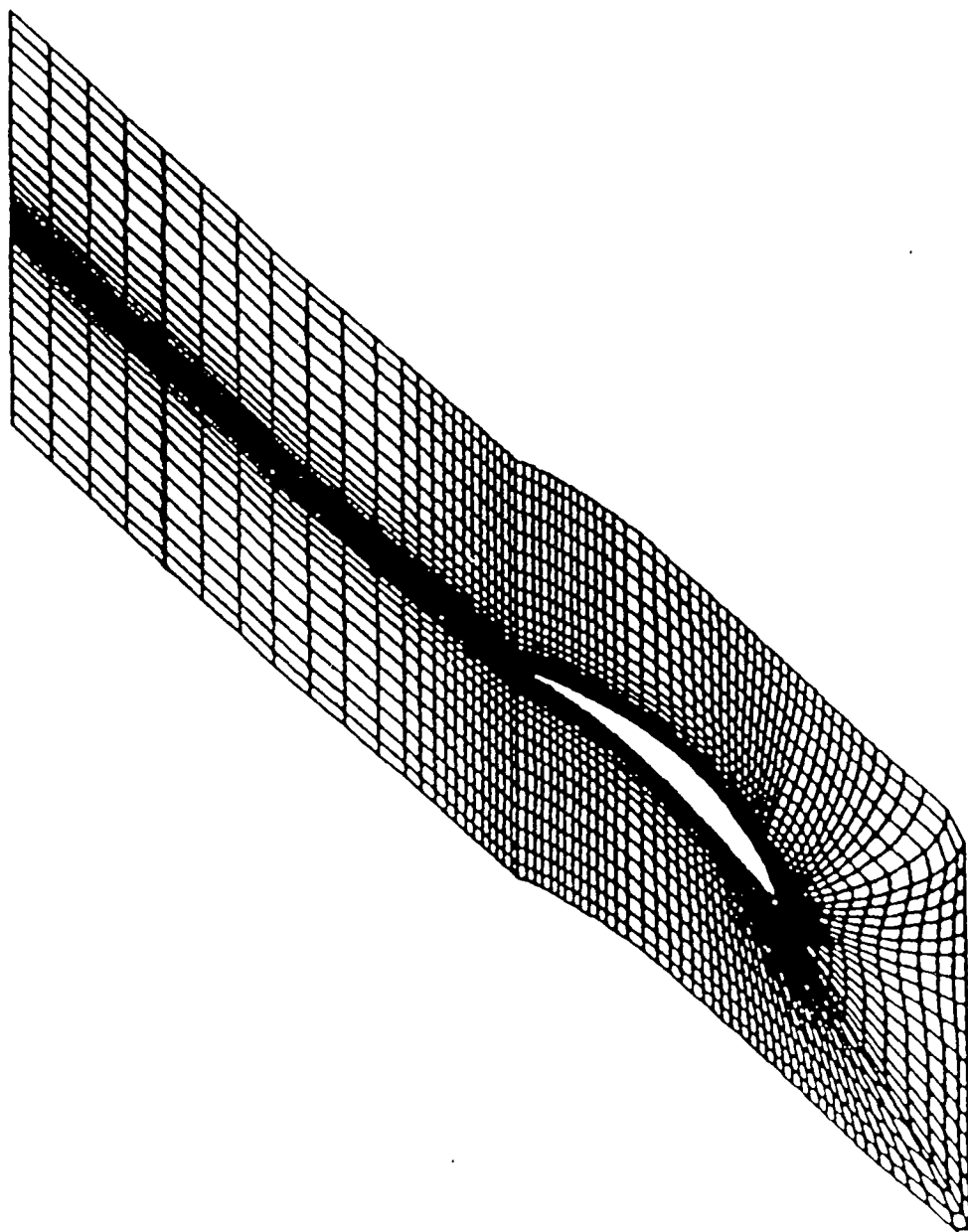
Fig. 23 - Grid Distribution

PT. NO.	INFLOW ANGLE (Inferred from Fig 6 of AFAPL-TR-73-45)
1	57
2	58.5
3	59
4	60
5	61
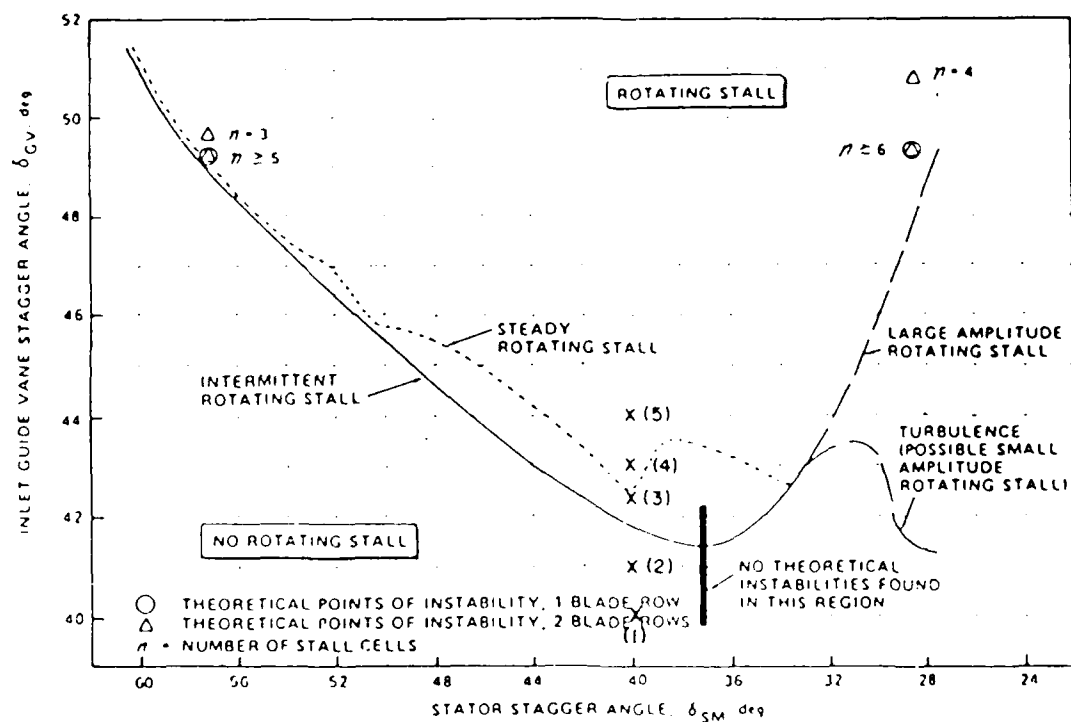
Fig. 24 - Rotating Stall Boundary for J-79 Stator Set No. 1 (Ref. 34)

For cases (1)-(4), the numerical simulations all reach asymptotic steady state. The surface pressure distribution, the contours of axial velocity and the contours of transverse velocity are shown in Figs. 25-27, respectively. It should be noted that the present calculations were run at a low subsonic Mach number, $M = 0.4$, to allow transient accuracy without unrealistically limiting the allowable time step. For $M = 0.4$, the stagnation point C_p, which is defined as $(P_{STAG} - P_\infty)/(1/2 \rho_\infty q^2)$ should be approximately 1.045. The computed C_p is slightly above this value. As the inflow angle increases, a small recirculation region starts to develop on the suction side of the trailing edge. The recirculation zone is indicated by the zero-value contour line (a solid line) in Figs. 26 and 27. The scale of the wake also increases with increasing inflow. Although cases (1)-(4) clearly converge to a steady state solution, in case 5, $\alpha_1 = 61°$, the numerical simulation does not lead to an asymptotic steady state, in fact, the monitored flow quantities exhibit significant unsteadiness. Fig. 28 shows the surface pressure distribution at various times over a non-dimensional time span of 18.35. The time station at $t = 0$ is arbitrarily chosen. It should be noted, by comparing Fig. 28 ($\alpha_1 = 61°$) and Fig. 25d ($\alpha_1 = 60°$), that the lift at $\alpha_1 = 61°$ is smaller than the lift at $\alpha_1 = 60°$. A clear indication of the existence of the unsteady flow at $\alpha_1 = 61°$ is given in Figs. 29 and 30. Again, the recirculation regions are indicated by zero-value contour lines in axial and transverse velocity contour plots. At $t = 0$ there is a large separation zone attached to the suction side of the trailing edge region. Subsequently, it breaks away from the trailing edge so that a relatively smaller separation region still attaches to the trailing edge while a recirculating zone of significant size appears in the near wake region. The flow situation at $t = 14.35$ is further illustrated in Fig. 31, which is a velocity-vector field. Three recirculation zones are clearly discernable. This set of simulations indicate that the inception boundary of unsteady stall for a flow with single passage periodicity, which may or may not be related to rotating stall, is approximately at $\alpha_1 = 60°$. It is of interest to note that this is the approximate inflow of the rotating stall boundary as given by the experimental results depicted in Fig. 24.

Single Passage Calculation with Injection

Following the single passage calculation, attention shifted to single passage calculations with wall transpiration. In initiating a rotating stall
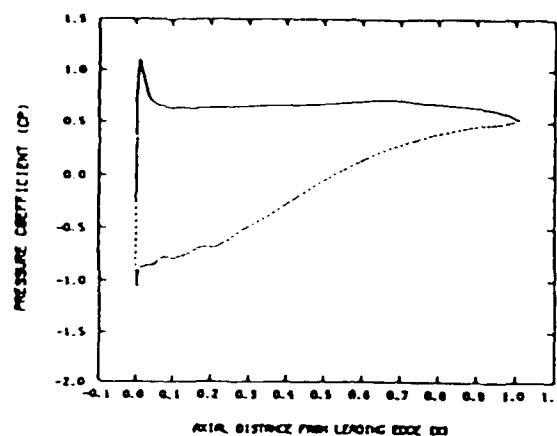
(a) $\alpha_1 = 57.0°$
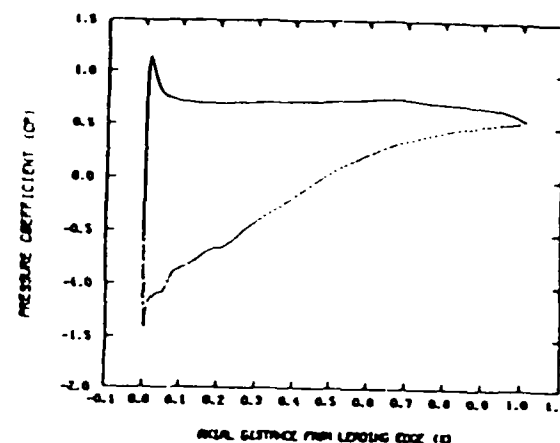
(b) $\alpha_1 = 58.5°$
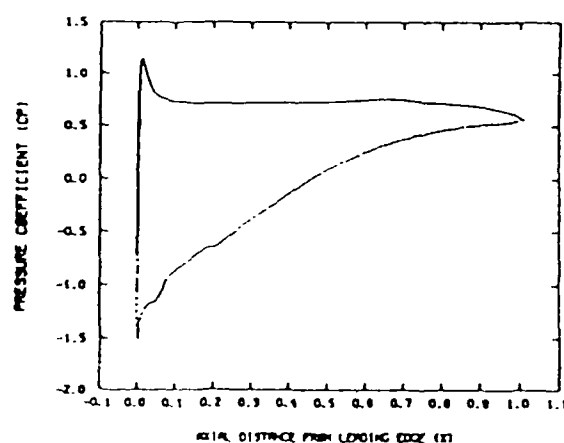
(c) $\alpha_1 = 59.0°$
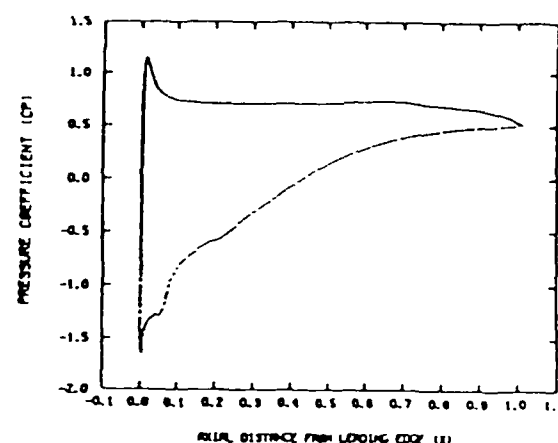
(d) $\alpha_1 = 60°$

Fig. 25 — Surface Pressure Distribution
at Different Inflow Angles

(a) $\alpha_1 = 57.0°$
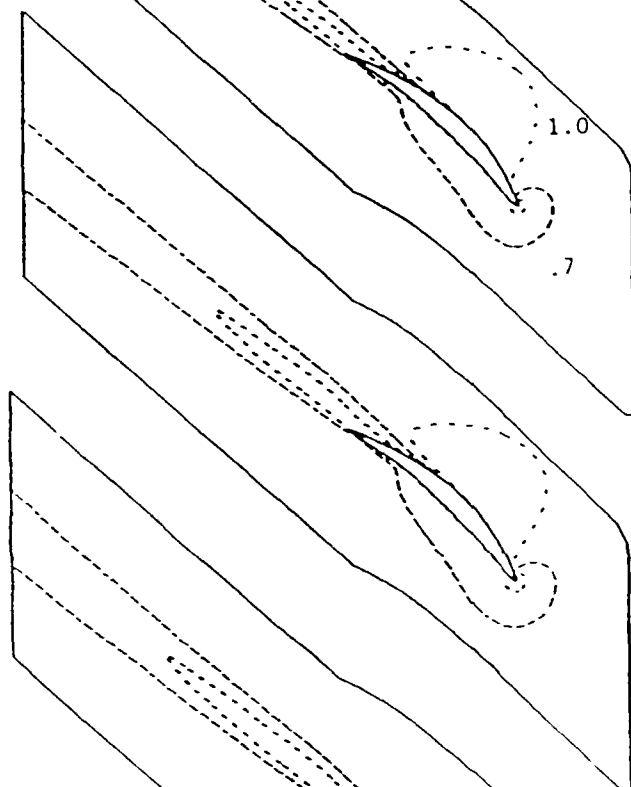
(b) $\alpha_1 = 58.5°$
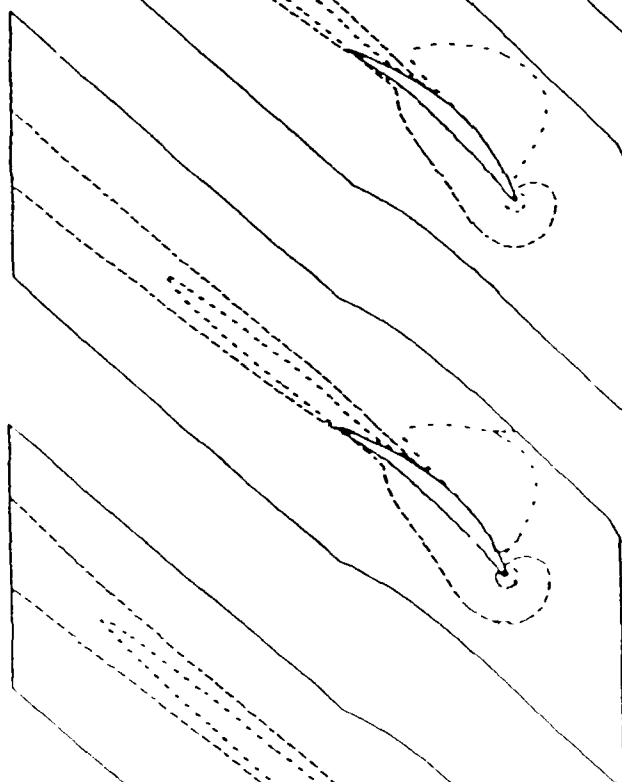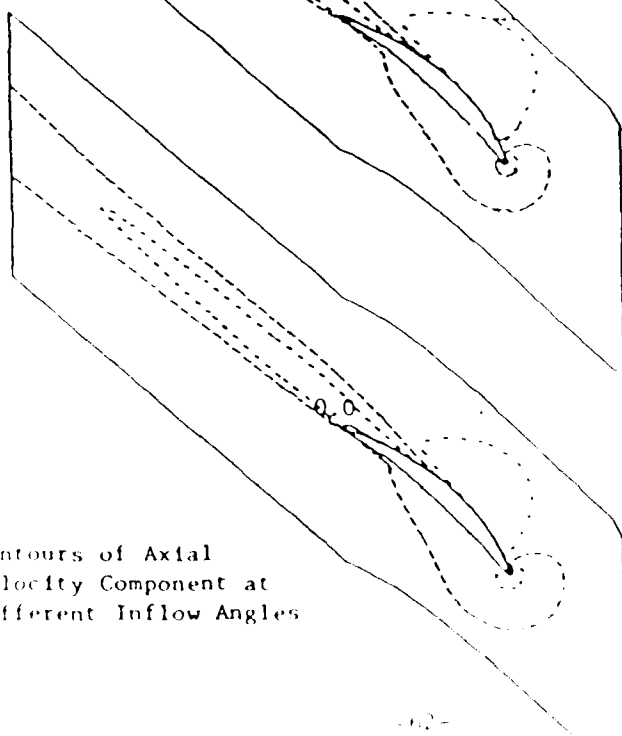
(c) $\alpha_1 = 59.0°$

Fig. 26 - Contours of Axial
Velocity Component at
Different Inflow Angles

(d) $\alpha_1 = 60.0°$
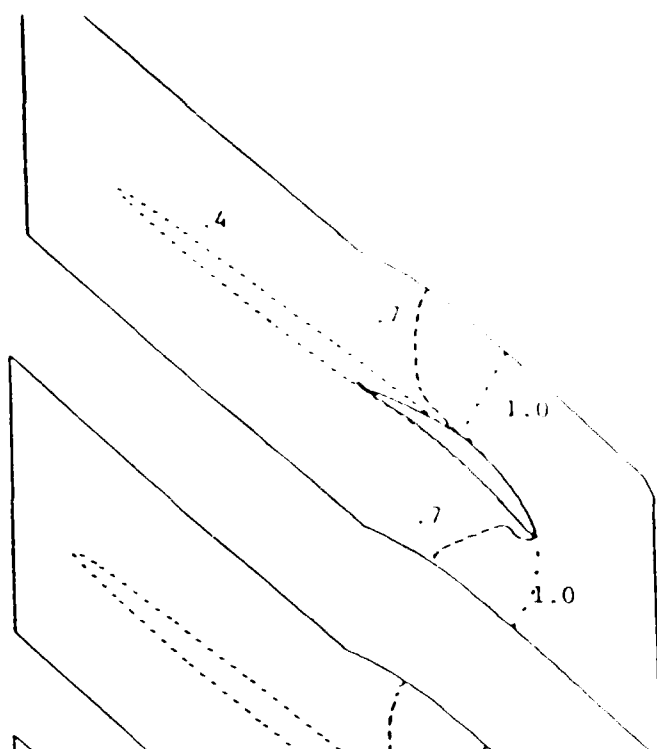
(a) $\alpha_1 = 57°$
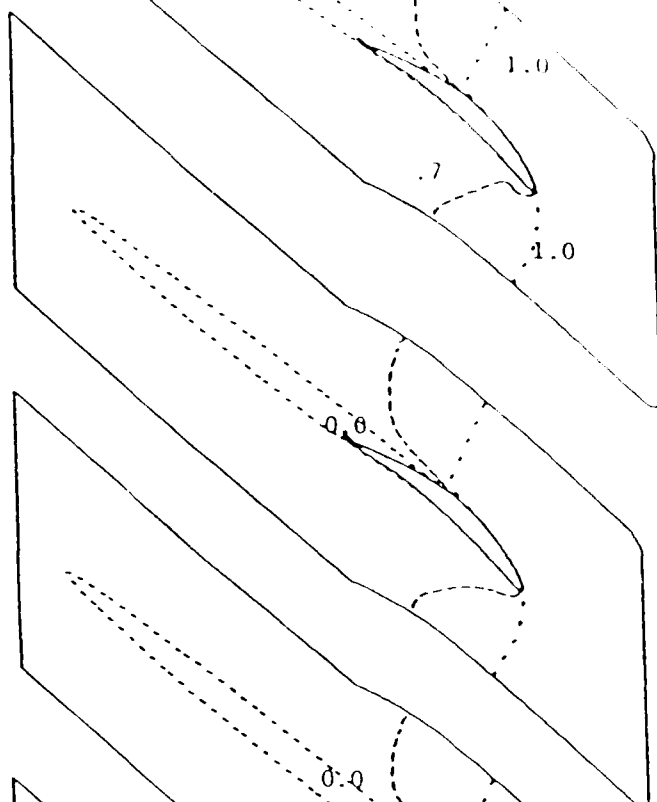
(b) $\alpha_1 = 58.5°$
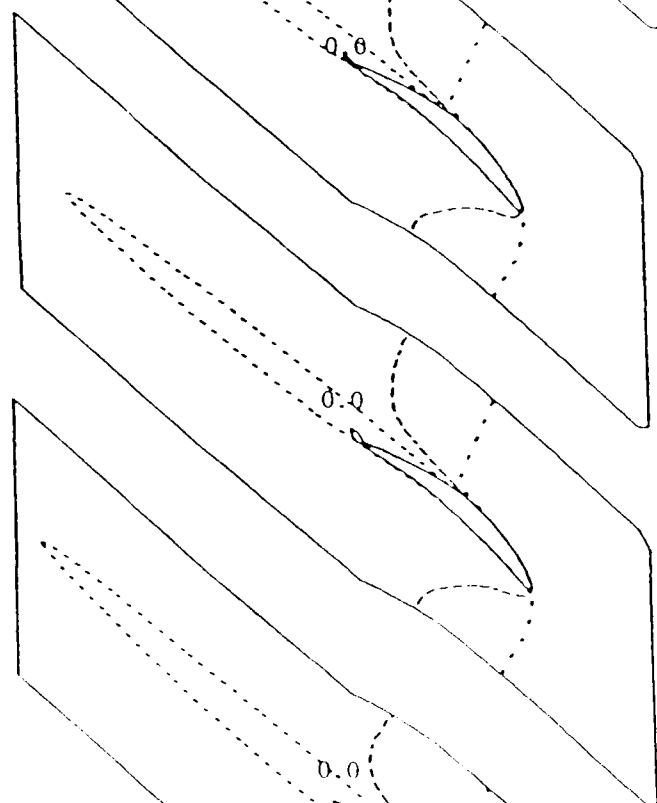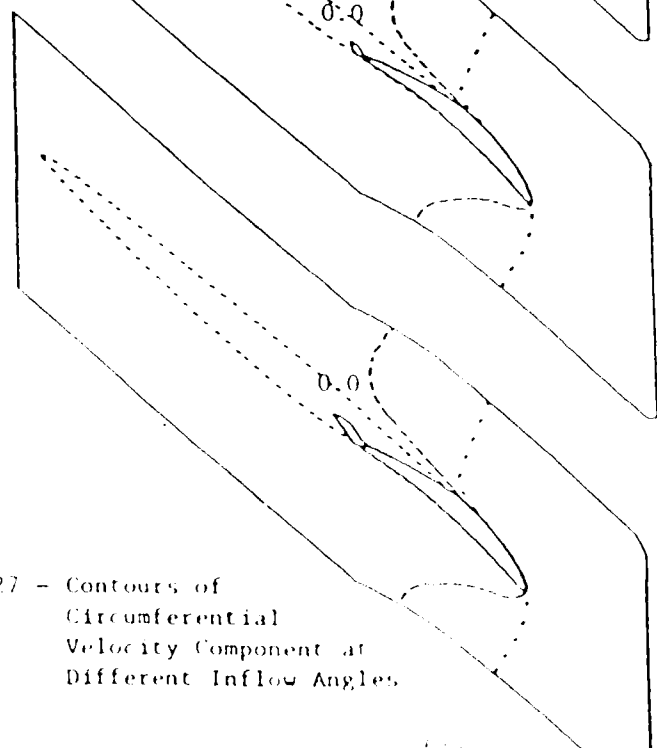
(c) $\alpha_1 = 59.0°$

Fig. 27 — Contours of
Circumferential
Velocity Component at
Different Inflow Angles.

(d) $\alpha_1 = 60°$
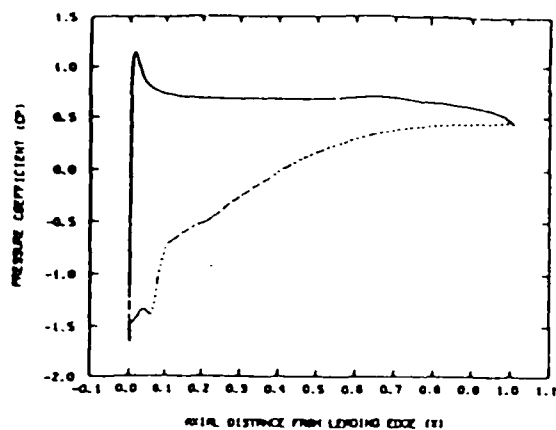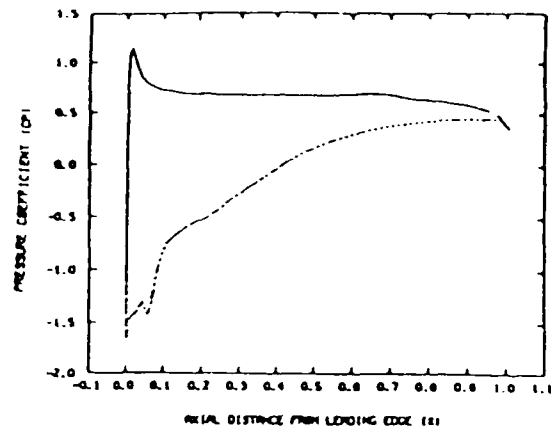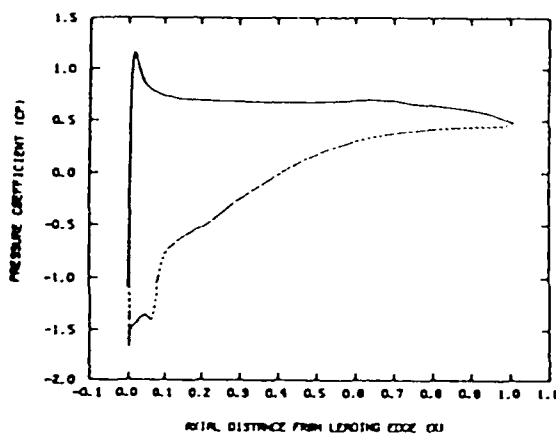
(a) $\alpha_1 = 61°$, $t = 0$

(b) $\alpha_1 = 61°$, $t = 6.36$

(c) $\alpha_1 = 61°$, $t = 10.35$
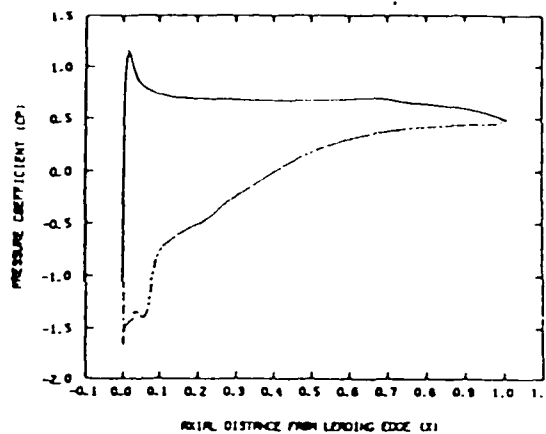
(d) $\alpha_1 = 61°$, $t = 14.35$
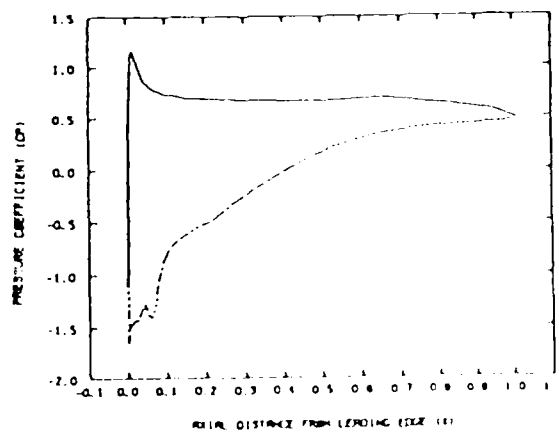
(e) $\alpha_1 = 61°$, $t = 18.35$

Fig. 28 — Surface Pressure Distribution at Different Times
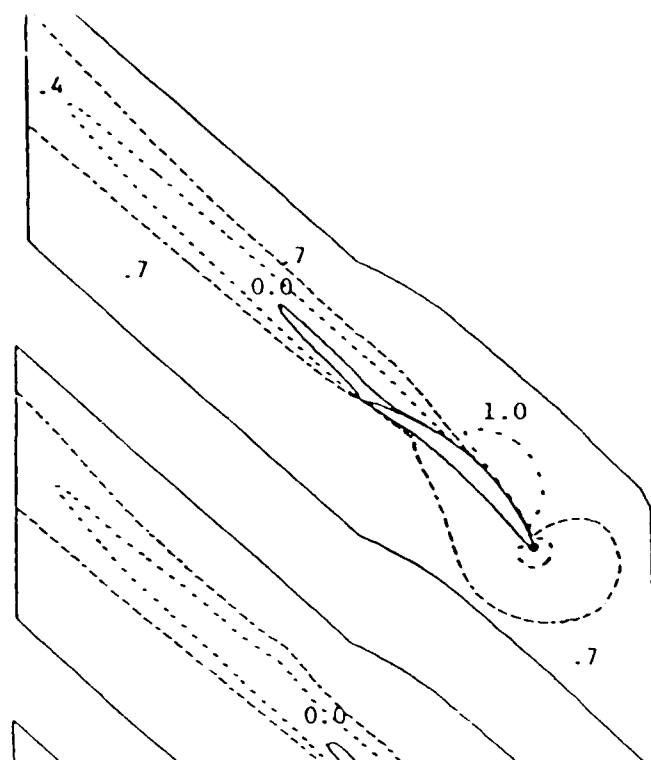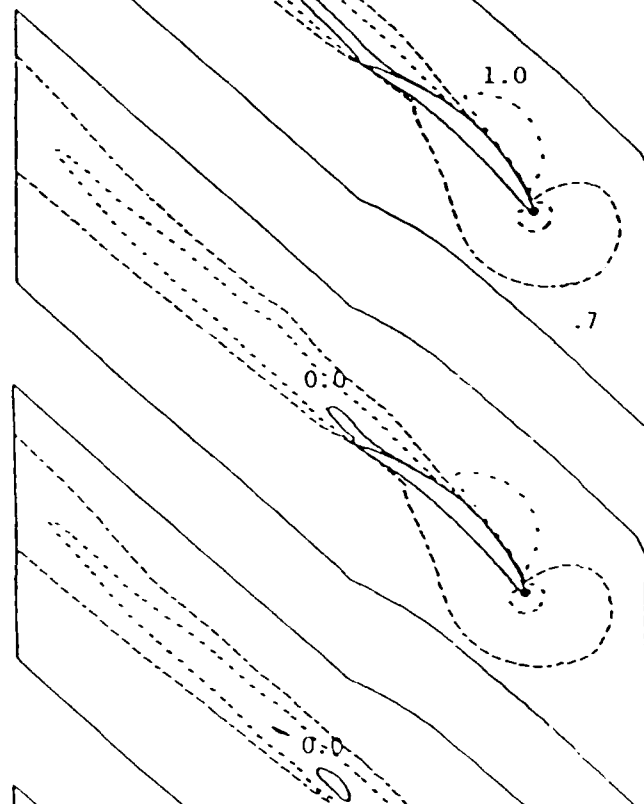
(a) $\alpha_1 = 61.0°$
$t = 0$

(b) $\alpha_1 = 61.0°$
$t = 6.36$
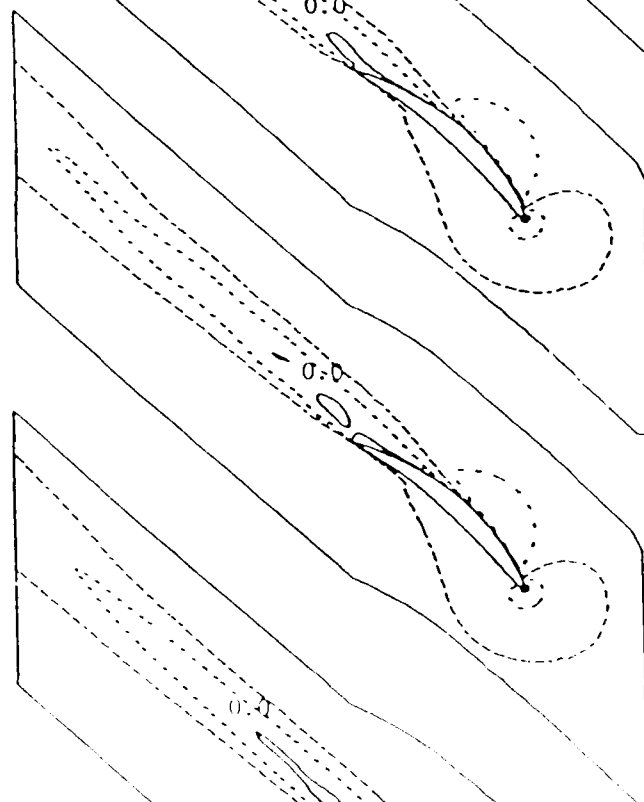
(c) $\alpha_1 = 61.0°$
$t = 10.35$
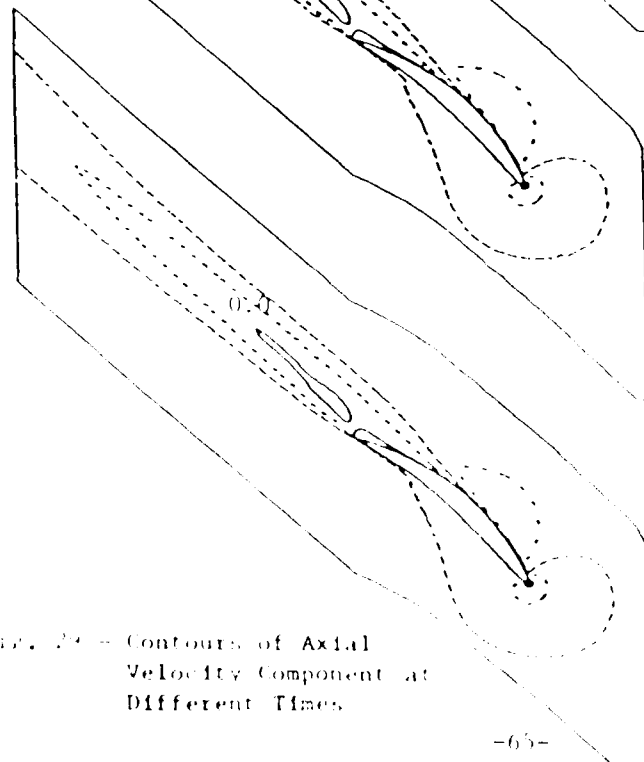
(d) $\alpha_1 = 61.0°$
$t = 14.35$

Fig. 24 - Contours of Axial
Velocity Component at
Different Times.
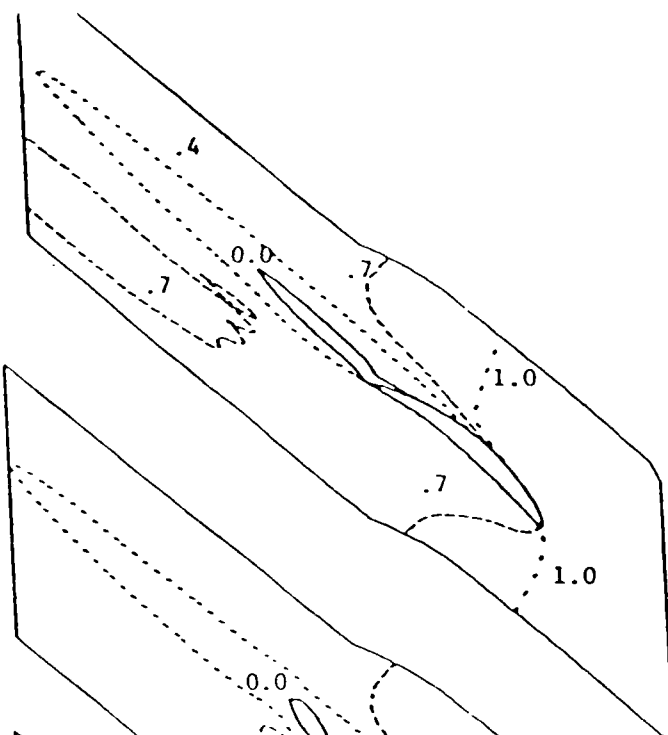
(a) $\alpha_1 = 61.0°$
t = 0.0
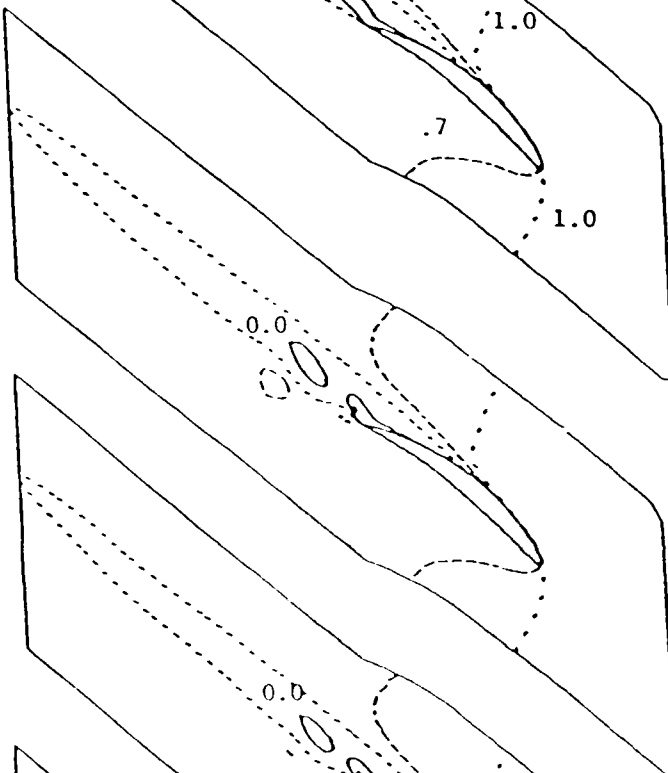
(b) $\alpha_1 = 61.0°$
t = 6.36
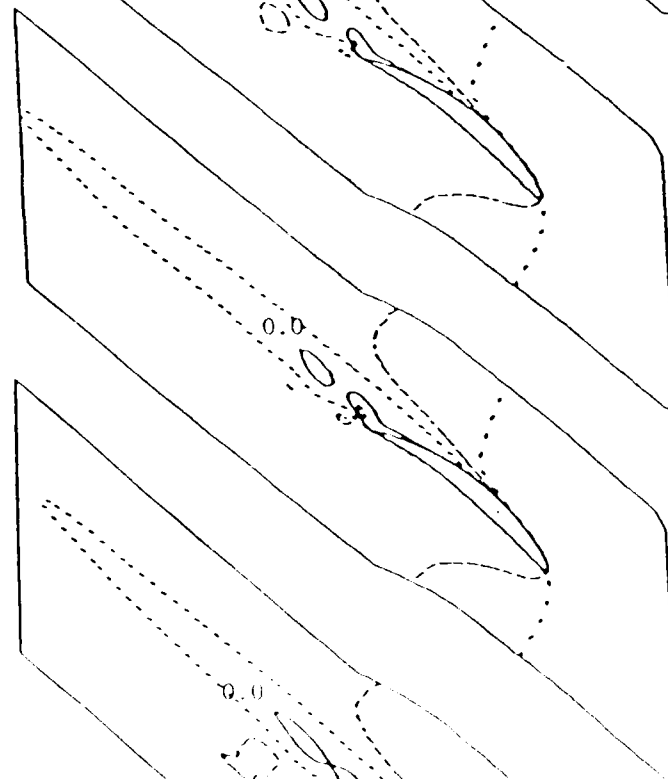
(c) $\alpha_1 = 61.0°$
t = 10.35
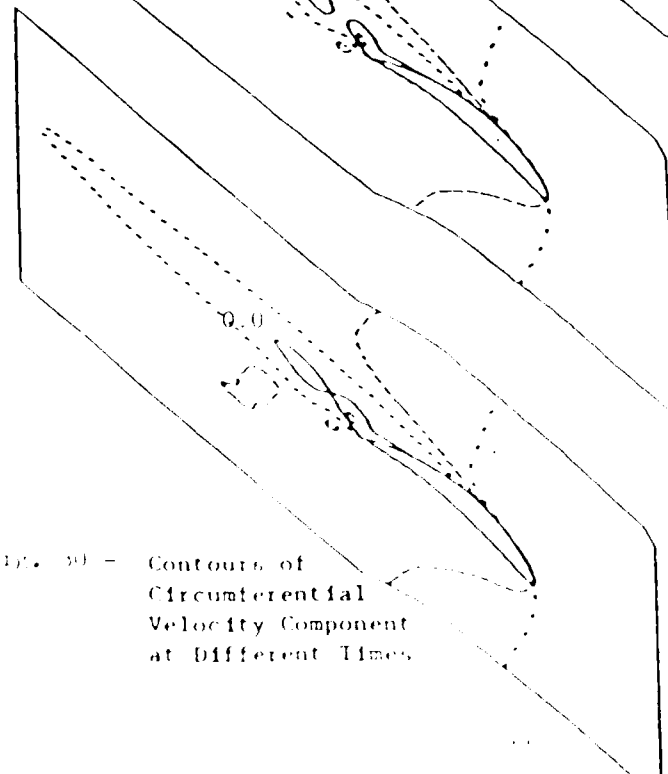
(d) $\alpha_1 = 61.0°$
t = 14.35

Fig. 59 — Contours of Circumferential Velocity Component at Different Times
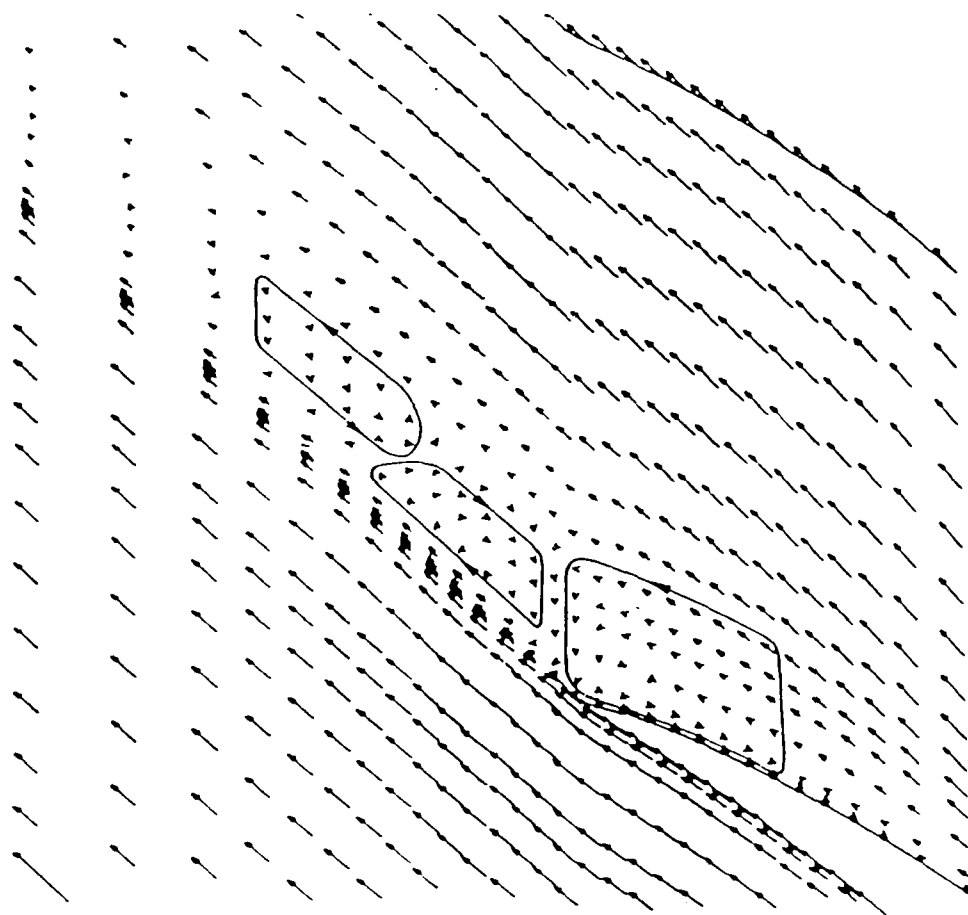
Fig. 31 — Velocity Vector Field at t = 14.35 (α = 61°)

simulation, the intent is to first obtain a five passage flow in which each
passage contains an identical flow field. The intent is then to introduce a
disturbance, locally create a stalled passage and then follow the flow
development in time. An obvious question arises in terms of how to introduce
the disturbance; three obvious possibilities exist. The first possibility
would introduce a disturbance in total pressure and/or flow incidence at the
inflow boundary; such a calculation has been demonstrated in the relaxation
calculation previously discussed (Figs. 16-22). The second approach would
introduce a static pressure disturbance at the outflow boundary. The final
approach, which is the one used, would introduce a disturbance in the flow
field. The disturbance chosen was suction surface wall transpiration over the
aft 50 percent of the axial chord.

Prior to introducing the disturbance for a multiple passage calculation,
the effect of a wall transpiration disturbance on a single passage flow field
was considered. Two series of time accurate unsteady calculations were
performed for single passage cascade flows. In the first series of
calculations, the baseline flow is the steady-state solution for inflow angle
of 57°. In the second series of calculations, the baseline flow is the
steady-state solution for inflow angle of 60°. At some instant, a disturbance
was then applied to these baseline flows through the specification of the wall
boundary condition on the suction side of the blade. More specifically, an
injection toward the upstream direction was introduced (Uwall = -0.05,
Wwall = 0) in the trailing edge region. The spatial extent of the injection is
about 50 percent of the axial chord length.

The first case considered is that of 57° inflow. A steady calculation was
obtained at 57° via the Navier-Stokes solver using a matrix preconditioning
technique suitable for steady solutions (e.g., Ref. 22 and 23). The solution
was then continued in real time to t = 4.0 when a wall jet was applied. The
inclusion of a wall jet led to a change in the flow field, however, a new
steady state was reached by t = 8.0. This adjustment time of 4.0 units
corresponds roughly to that due to relaxation of an upstream distortion shown
in Figs. 16-22. The surface pressure distribution is shown in Fig. 32. A
careful examination shows considerable change between t = 4.0 and t = 8.0
and little change thereafter. Contours of velocity components are shown in
Figs. 33 and 34. Again, the major adjustment occurs between t = 4.
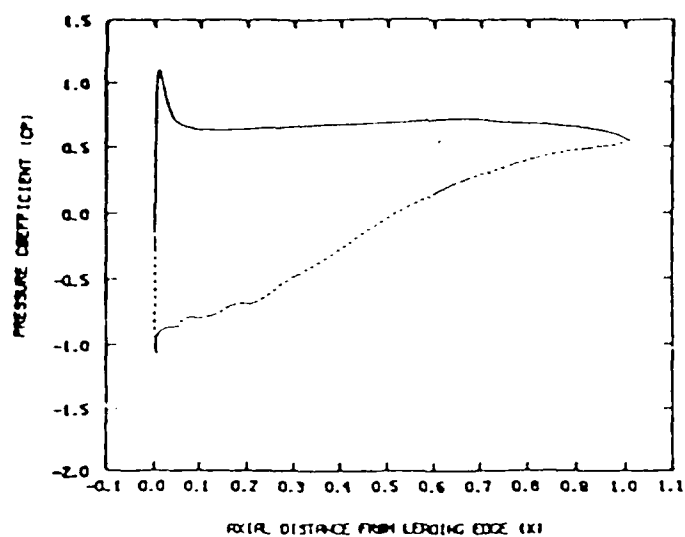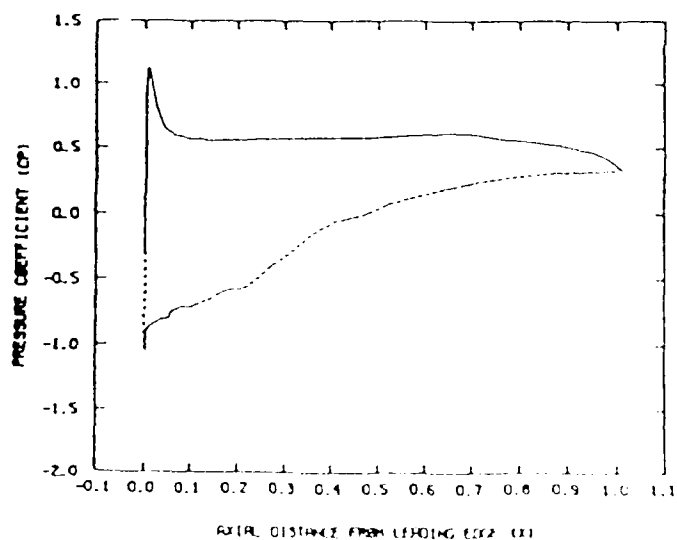
(a) No Wall Jet, t=4

(b) With Wall Jet, t=8
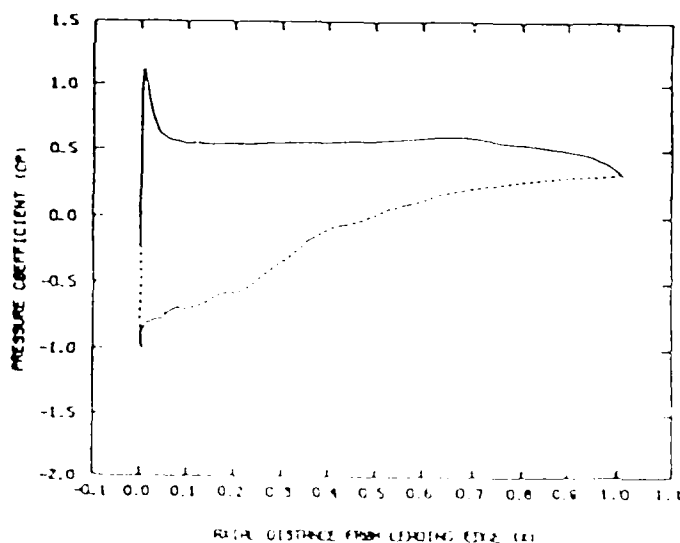
(c) With Wall Jet, t 12

(d) With Wall Jet, t 16

Fig. 32 — Pressure Coefficient Distribution on Blade Surface at Different
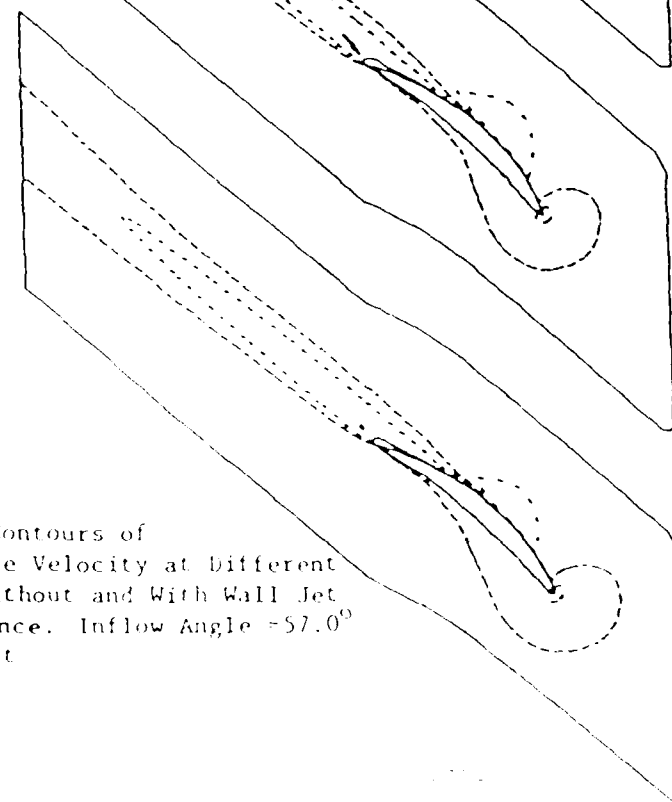Times, without and with Wall Jet Disturbance. Inflow Angle = 57.0°
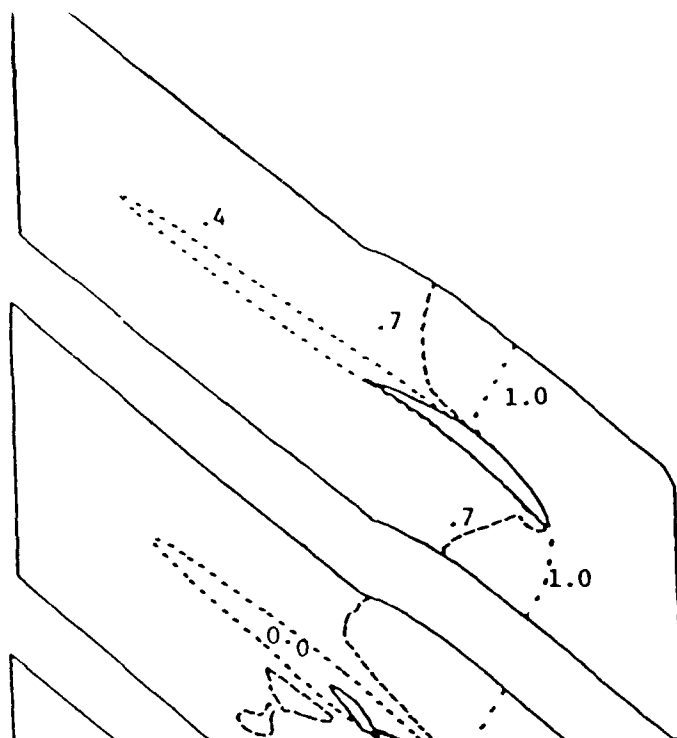Throughout
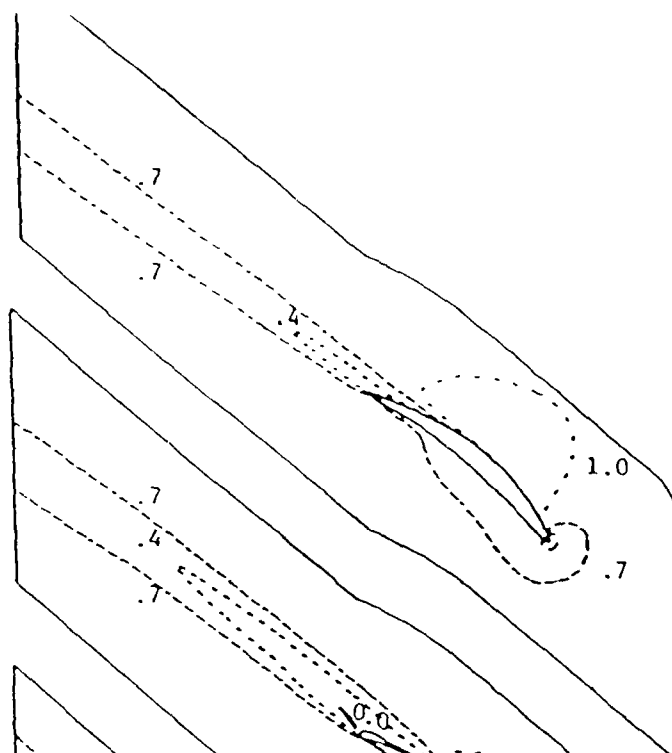
(a) No Wall Jet, t=4
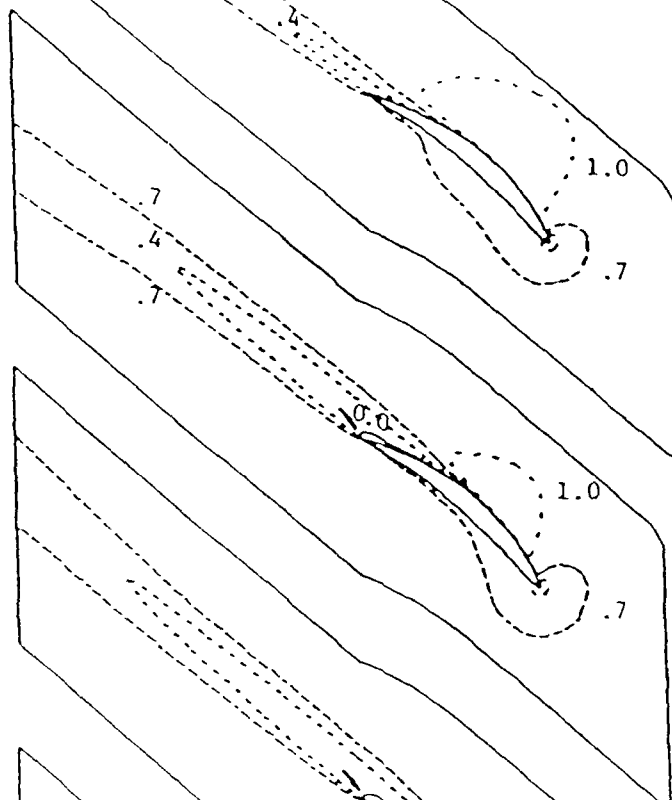
(b) With Wall Jet, t=8
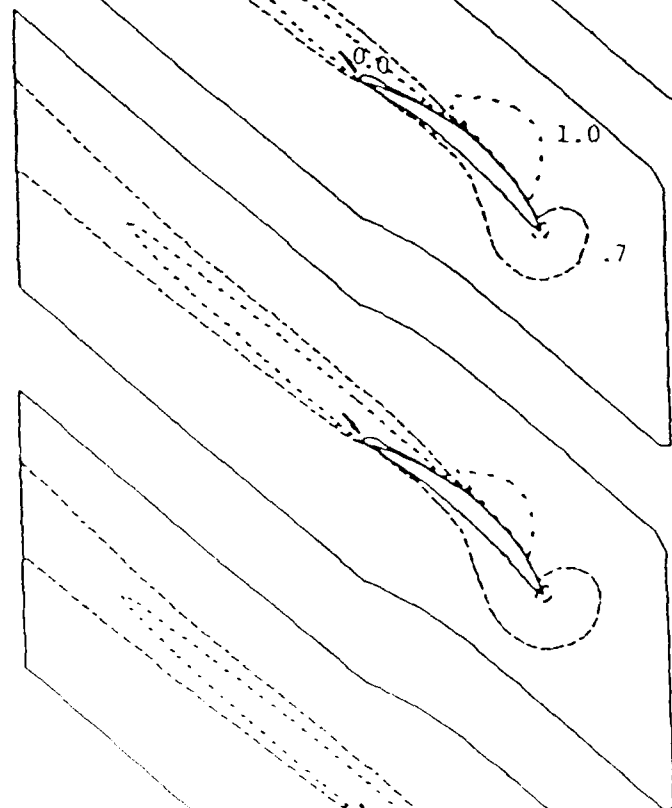
(c) With Wall Jet, t=1

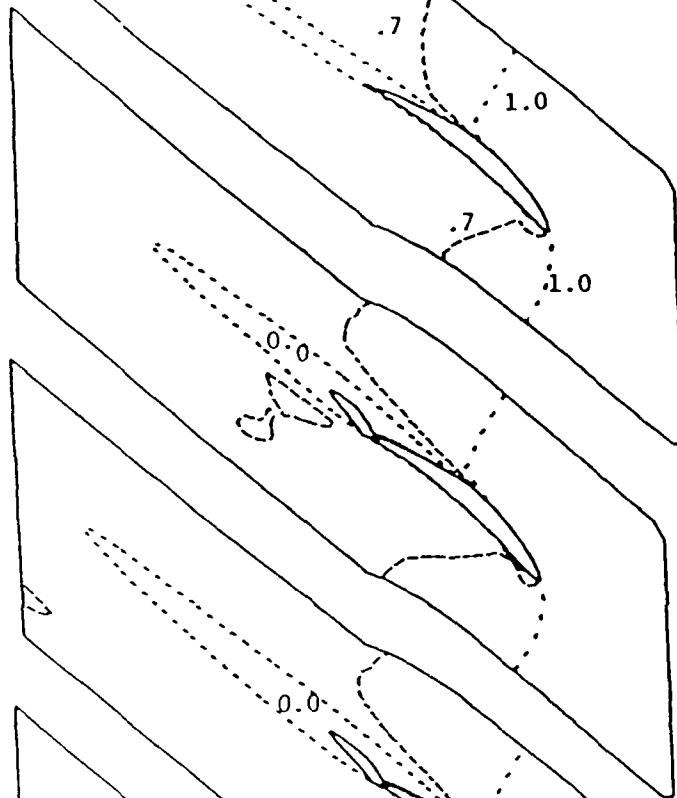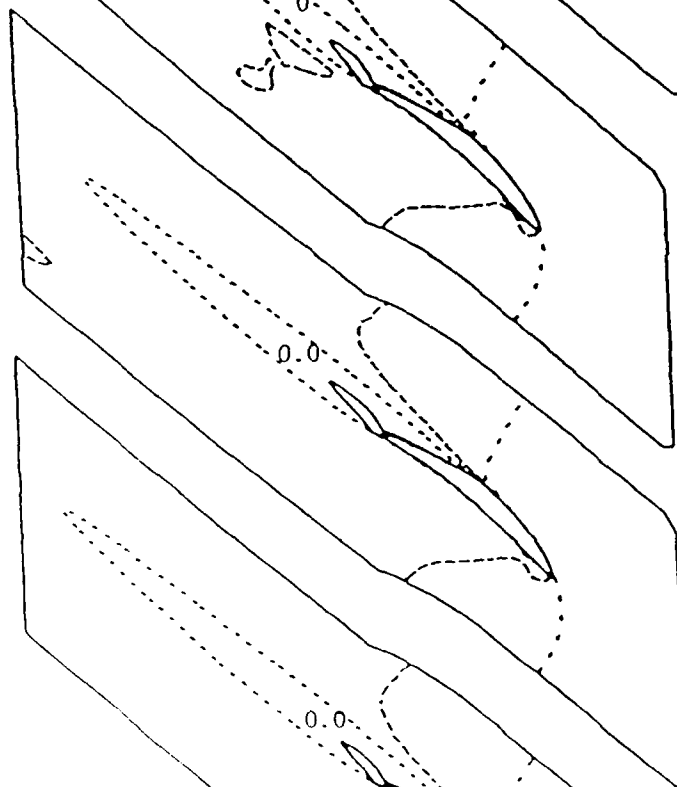Fig. 33 — Contours of
Streamwise Velocity at Different
Times, Without and With Wall Jet
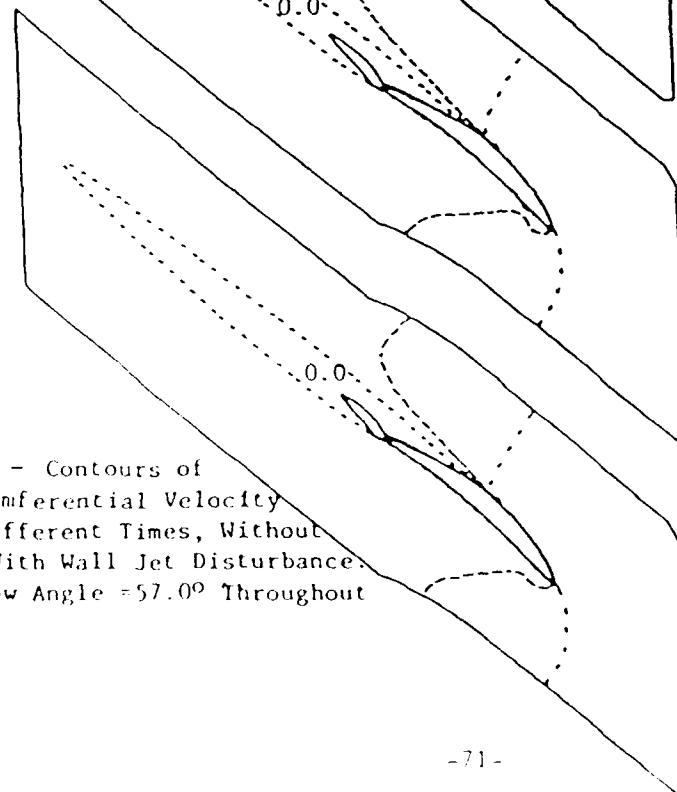Disturbance. Inflow Angle =57.0°
Throughout

(d) With Wall Jet, t=1

(a) No Wall Jet, t=4

(b) With Wall Jet, t=8

(c) With Wall Jet, t=12

Fig. 34 - Contours of
Circumferential Velocity
at Different Times, Without
and With Wall Jet Disturbance,
Inflow Angle =57.0° Throughout

(d) With Wall Jet, t=16

and t = 8.0. After t = 8.0 the only significant changes occur in the wake
region where the disturbance is continuing to move downstream.

The second case considered is that of 60° inflow. In this case, the wall
jet is applied from a converged solution at t = 0.0. In contrast to the 57°
case, introduction of the wall jet led to a solution which exhibited periodic
shedding and did not reach a steady state. Computed pressure distributions for
the wall jet on calculations are given in Figs. 35a - 35j. The calculation was
also run with the jet removed at t = 24.0 and the surface pressure returned to
its original state as shown in Figs. 35h' and 35i'. Velocity contours of the U
and W velocity components are presented in Figs. 36 and 37. Contours of
streamwise velocity at different times with wall jet disturbance and without
are shown in Fig. 36 a-i'. At t = 0.0 (Fig 36a) the flow is attached and there
is no reversed flow region; at t = 4.0 (Fig. 36b), after the disturbance has
been in effect for 4.0 non-dimensional time span, a large separation zone is
developed. The zero contour line is shown by a solid line which delineates
the reversed flow regions at t = 8.0, 12.0, 16,...36.0 (Figs. 36c-j). The
large separation zone, started at t = 4.0, split into two or more separation
zones floating into downstream. Figs. 36h'-i' show the contours after the
disturbance has been removed. It can be seen that the flow returns to its
initial flow field implying the uniqueness of the solution under the given
inflow angle of 60.0 degrees. Contours of transverse velocity for this series
of calculations are shown in Figs. 37a-i'. It should be noted that once the
wall jet problem is established the unsteadiness does not propagate upstream of
the blade (see Figs 36e-j).

Multiple Passage Calculations

The final set of calculations considered were made for a multiple passage
configuration. The configuration used was a five passage configuration in
which each passage was that of stator No. 1 of Ref. 33. This stator blade was
geometrically identical to that of the fifth stage stator blade of a J-79
compressor but with size reduced by a factor of 1.67. The tests of Ref. 33
were run at relatively low Mach number, $M_\infty \approx 0.075$. Calculations were run at
a higher Mach number, $M_\infty \approx 0.4$, to avoid very small time increments which are
required at lower Mach numbers due to stiffness of the equations at low Mach
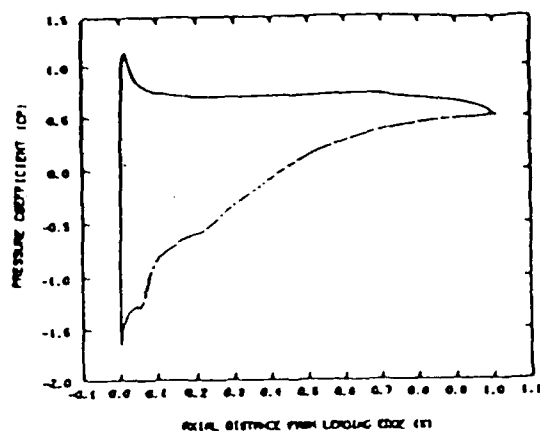
(a) No Disturbance Applied,
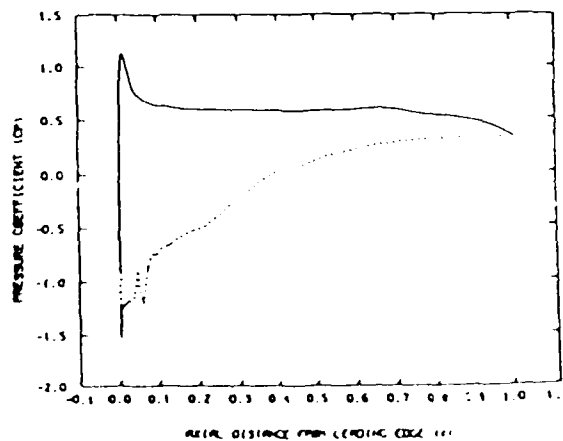Steady State, t=0
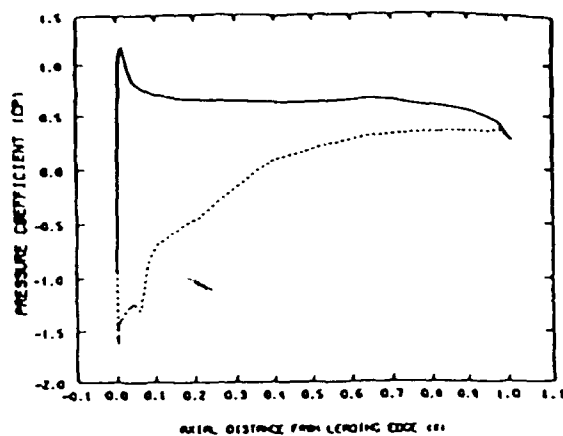
(b) With Jet Disturbance,
t=4.0
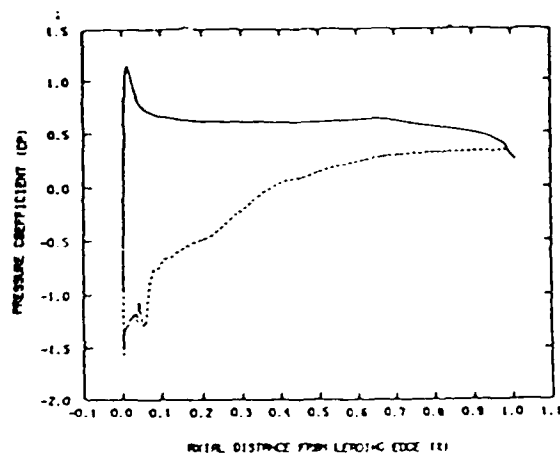
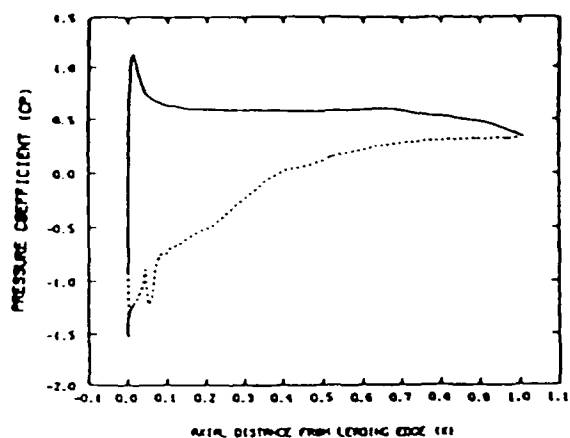(c) With Jet Disturbance,
t=8.0
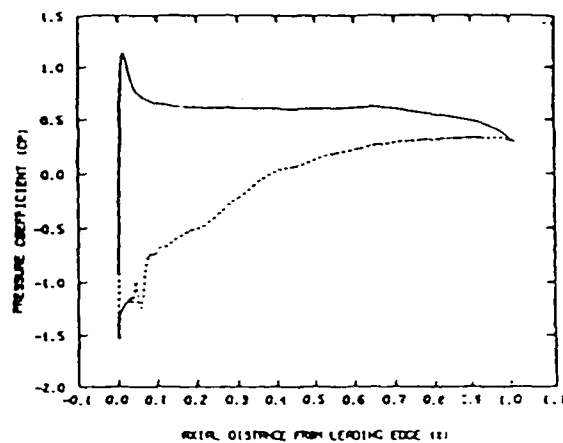
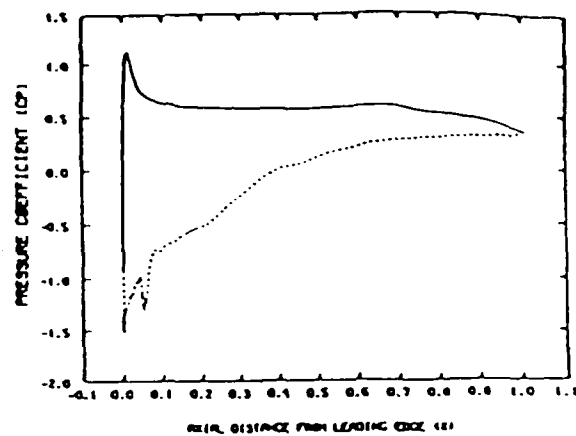(d) With Jet Disturbance,
t=12.0
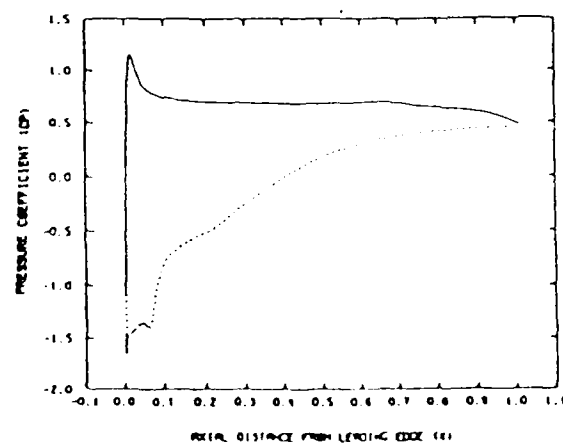
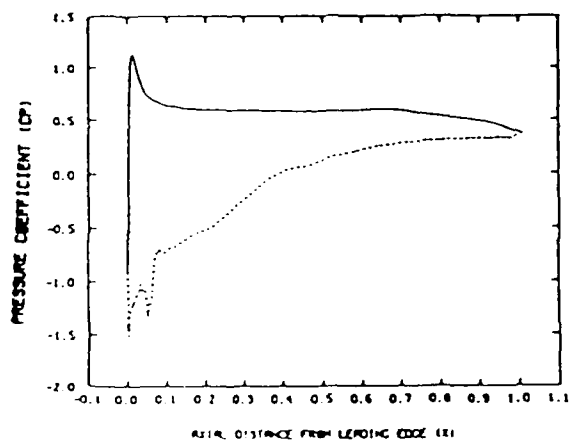(e) With Jet Disturbance,
t=16.0

(f) With Jet Disturbance,
t=20.0

Fig. 35 - Pressure Coefficient Distribution on Blade Surface at Different Times
During Jet Disturbance and after Jet Disturbance is Removed. Inflow
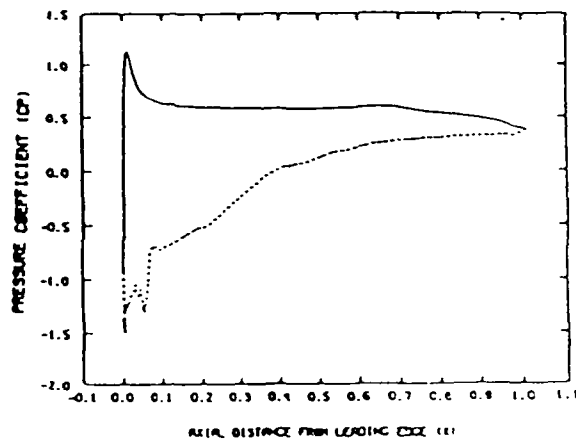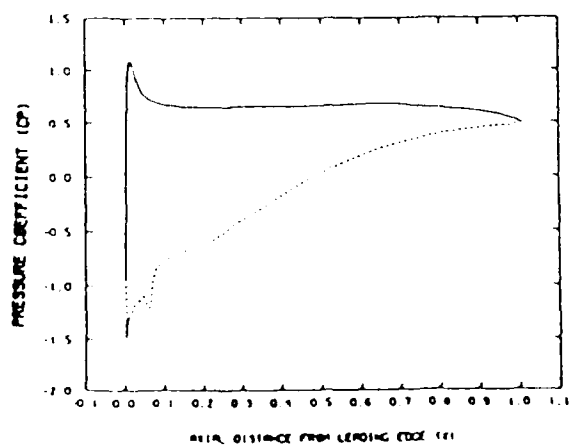Angle = 60.0° Throughout. (Continued)

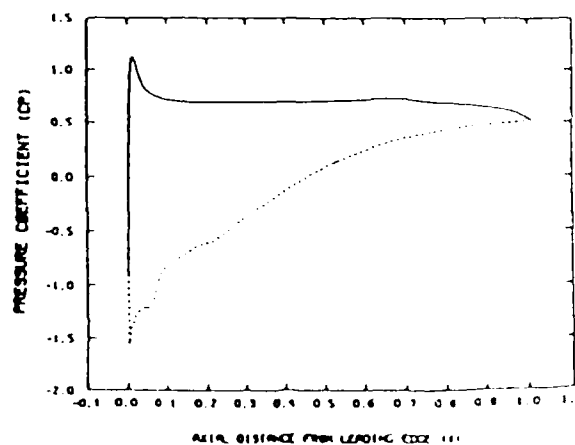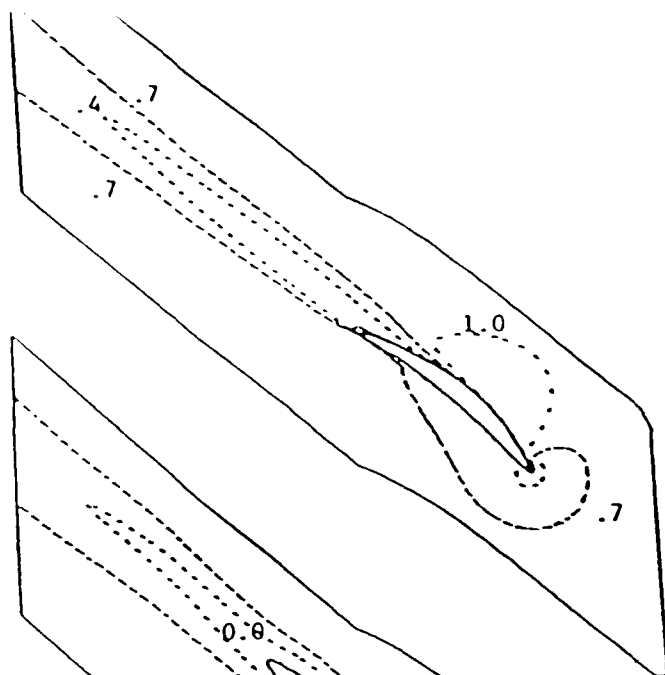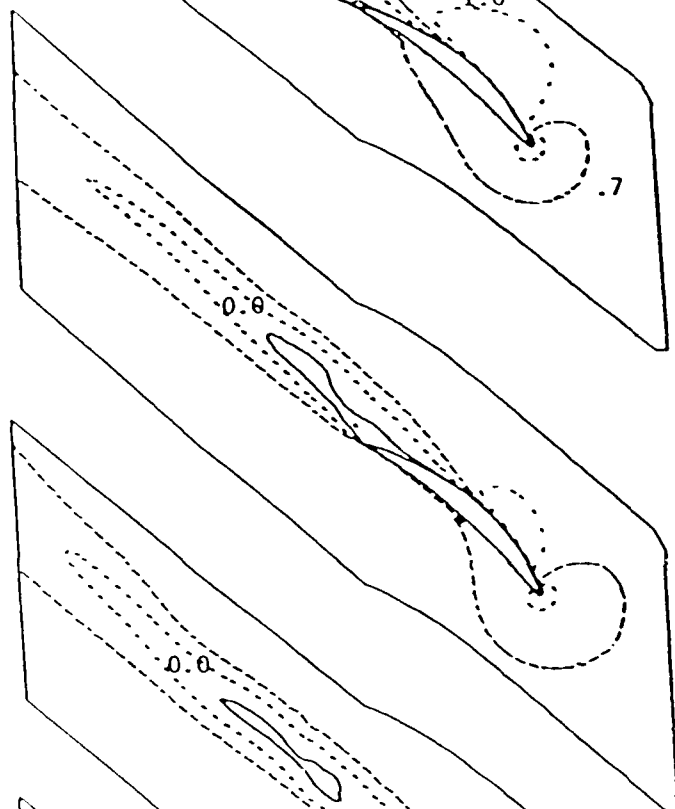(g) With Jet Disturbance,
t=24.0

(h) With Jet Disturbance,
t=28.0

(i) With Jet Disturbance,
t=32.0

(j) With Jet Disturbance,
t=36.0

(h') Jet Disturbance Removed,
T=28.0

(i') Jet Disturbance Removed,
t=32.0

Fig. 35 Concluded

-74-

(a) No Wall Jet, t=0.0
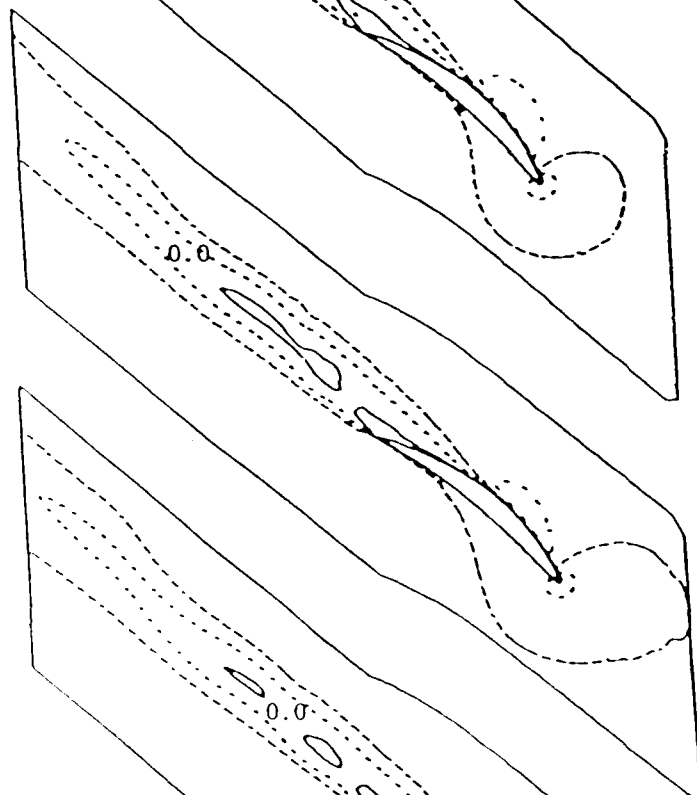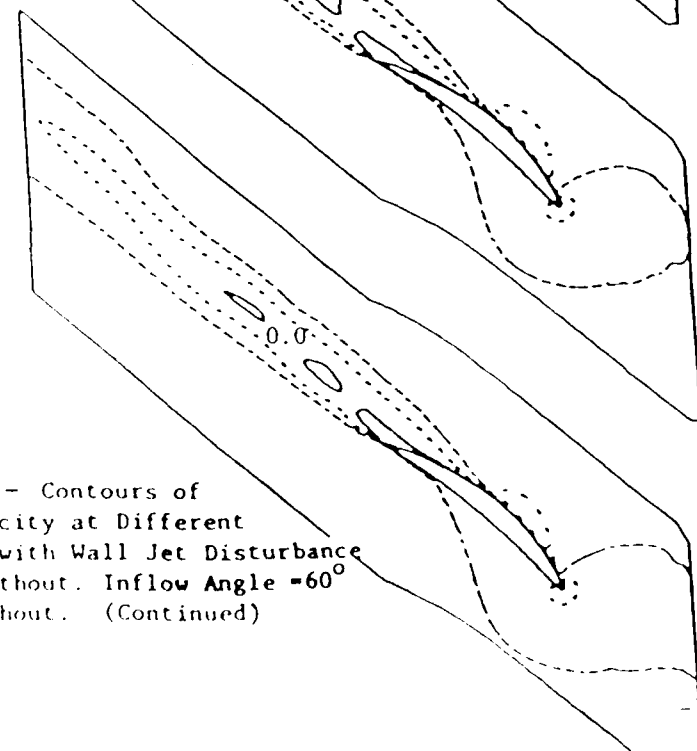
(b) With Wall Jet, t=4.

(c) With Wall Jet, t=8.

Fig. 36 — Contours of
U-Velocity at Different
Times with Wall Jet Disturbance
and Without. Inflow Angle -60°
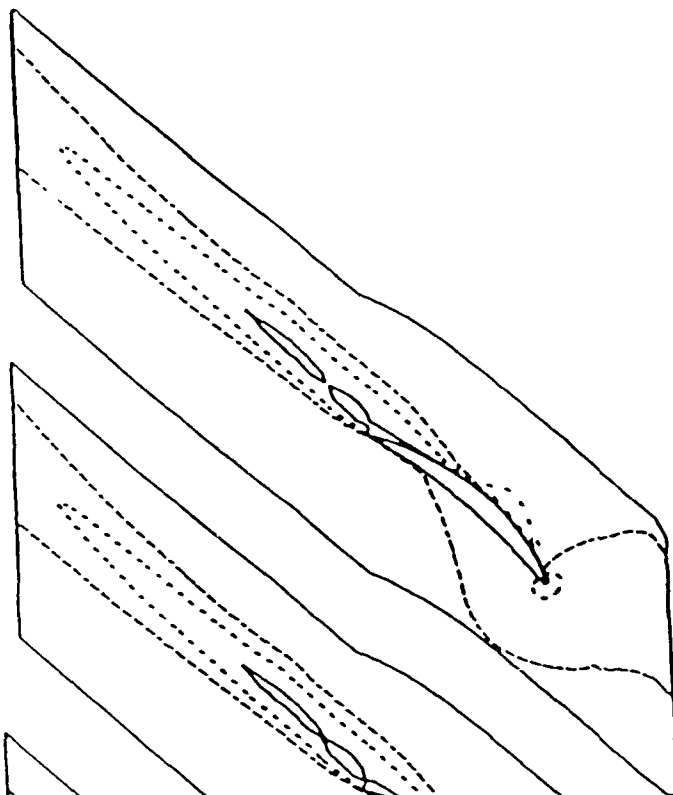Throughout. (Continued)
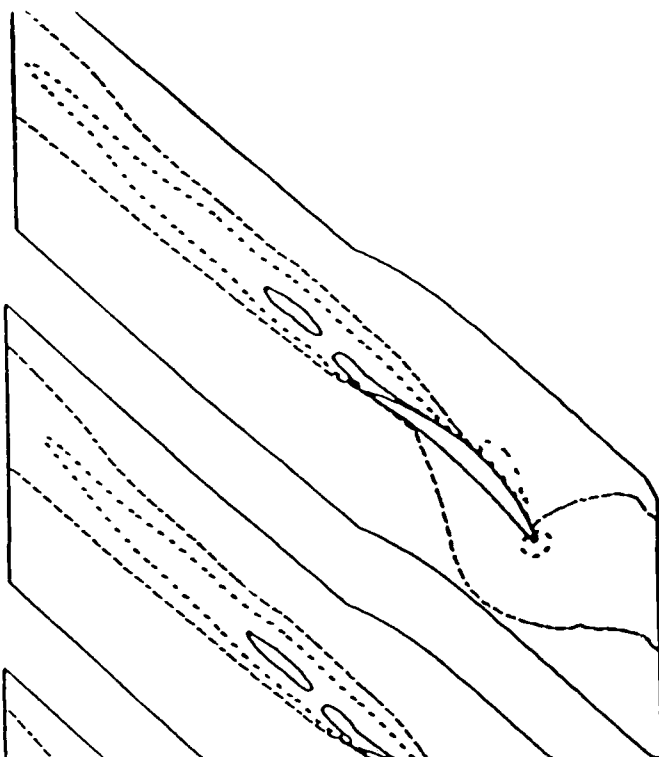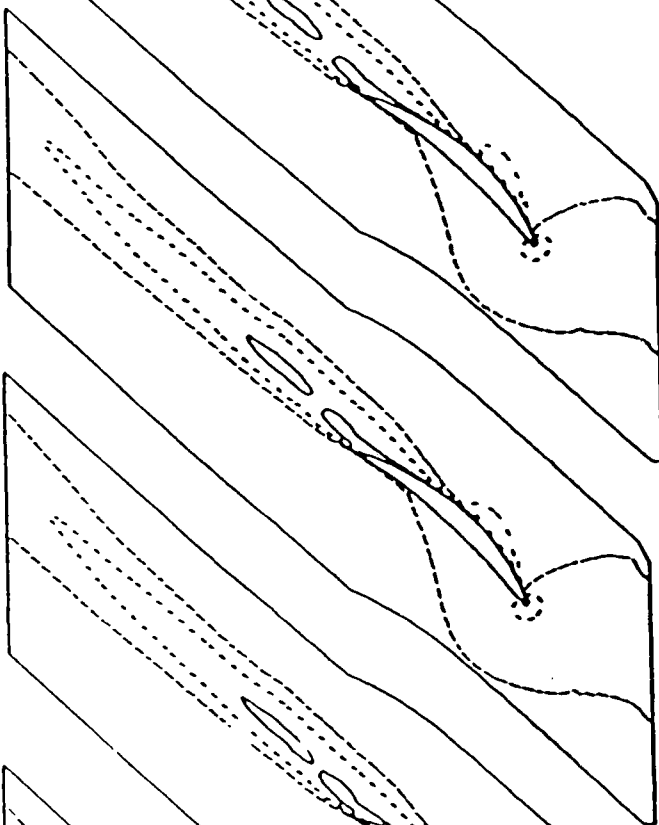
(d) With Wall Jet, t=12
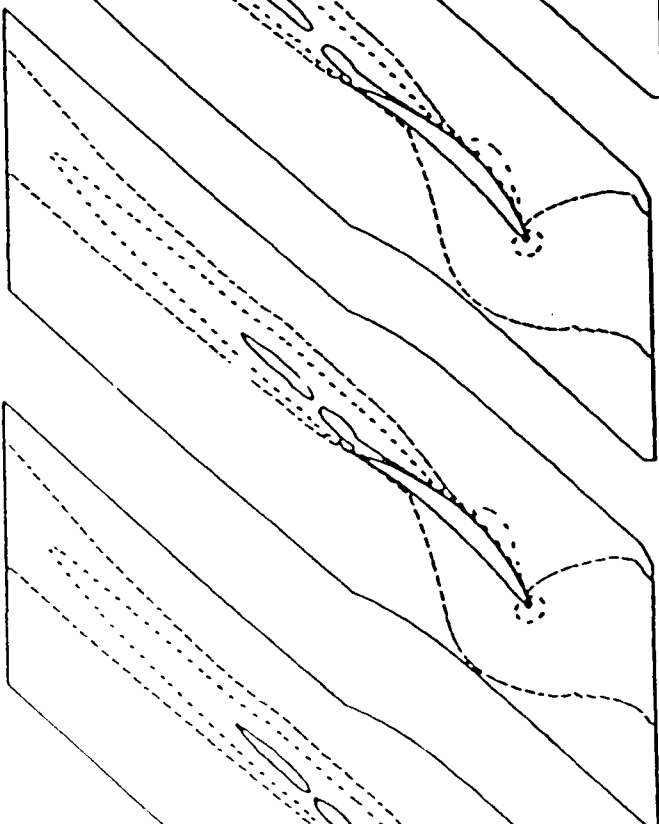
(e) With Wall Jet, t=16
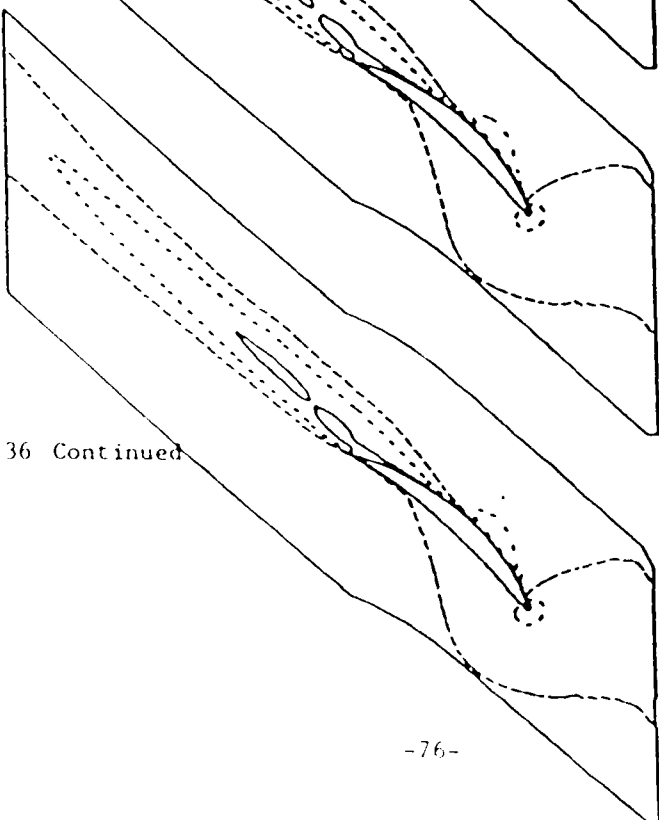
(f) With Wall Jet, t=20.

(g) With Wall Jet, t=24.

Fig. 36 Continued
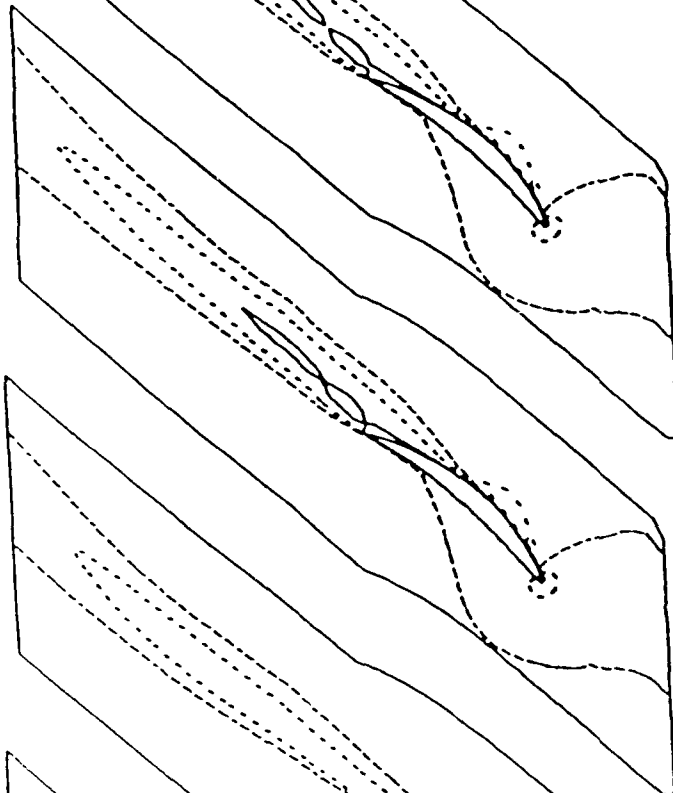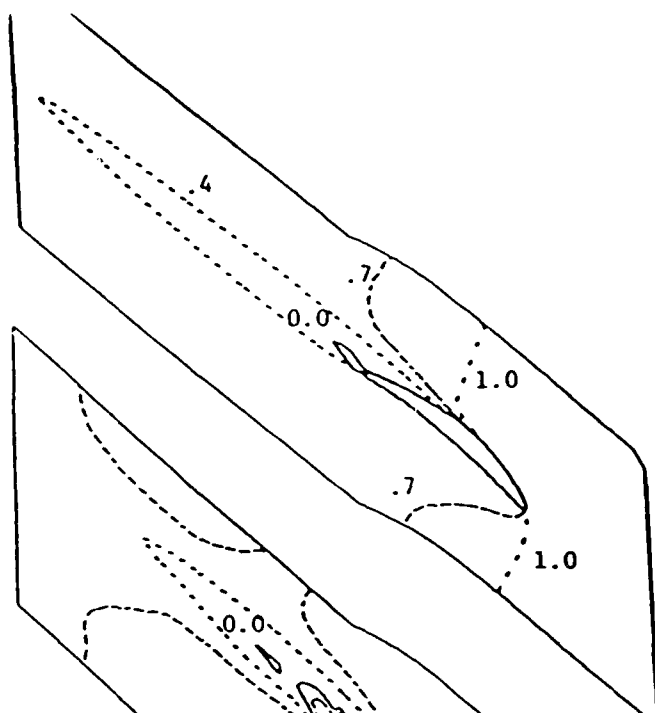
(h) With Wall Jet, t=28.
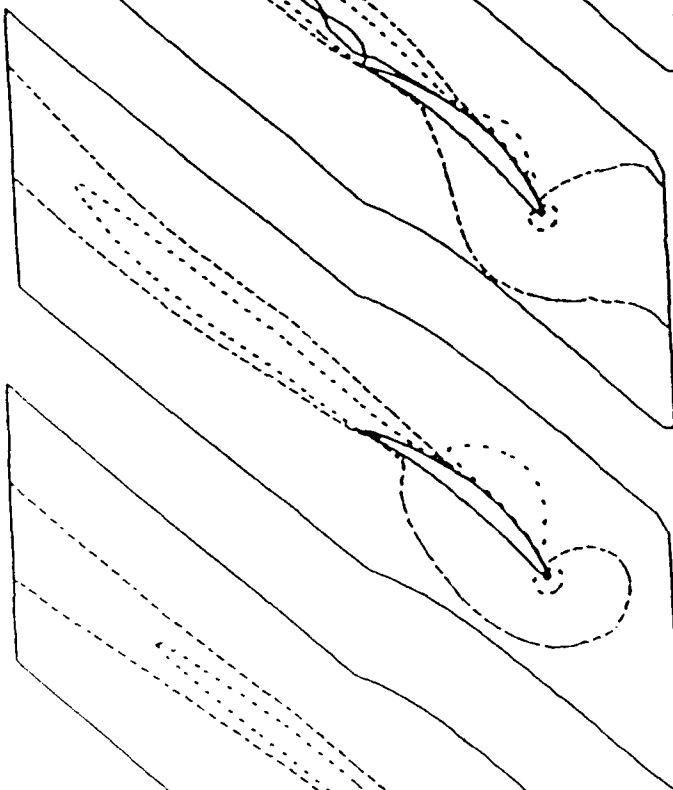
(i) With Wall Jet, t=32.

(j) With Wall Jet, t=36.
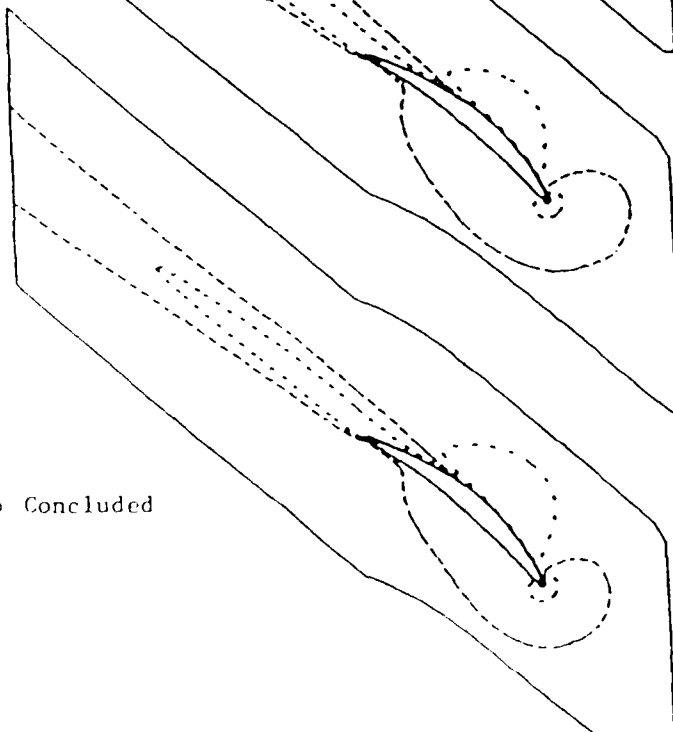
(h') Wall Jet Removed, t=28.

Fig. 36 Concluded

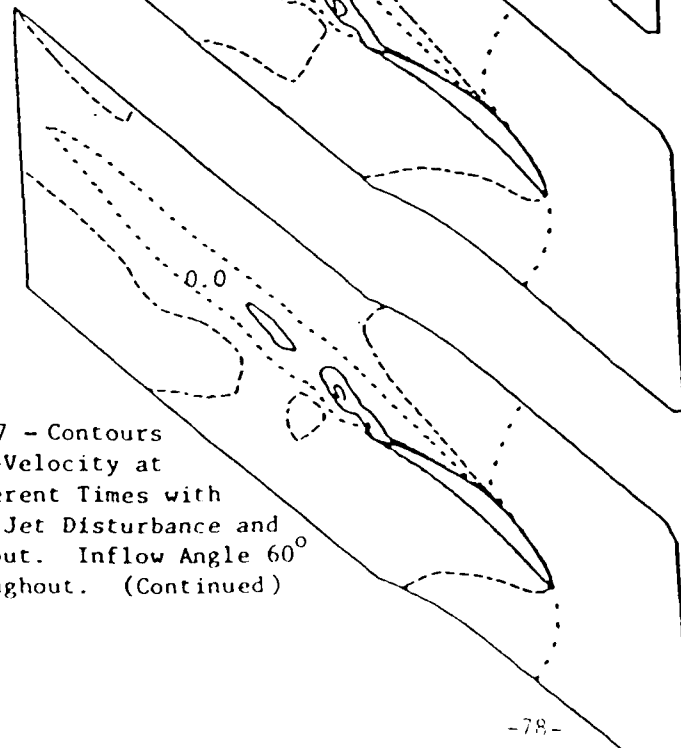(i') Wall Jet Removed, t=32.

(a) No Wall Jet, t=0.0
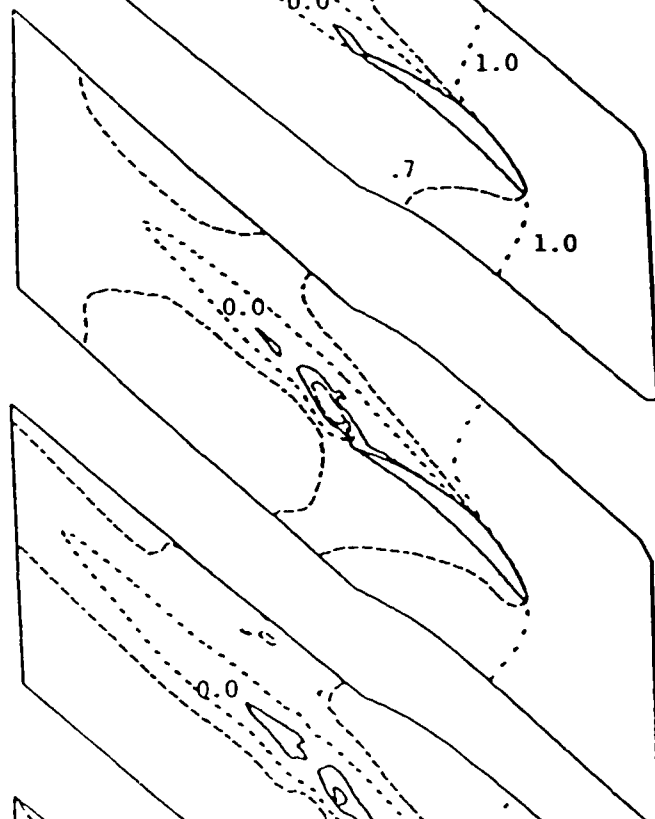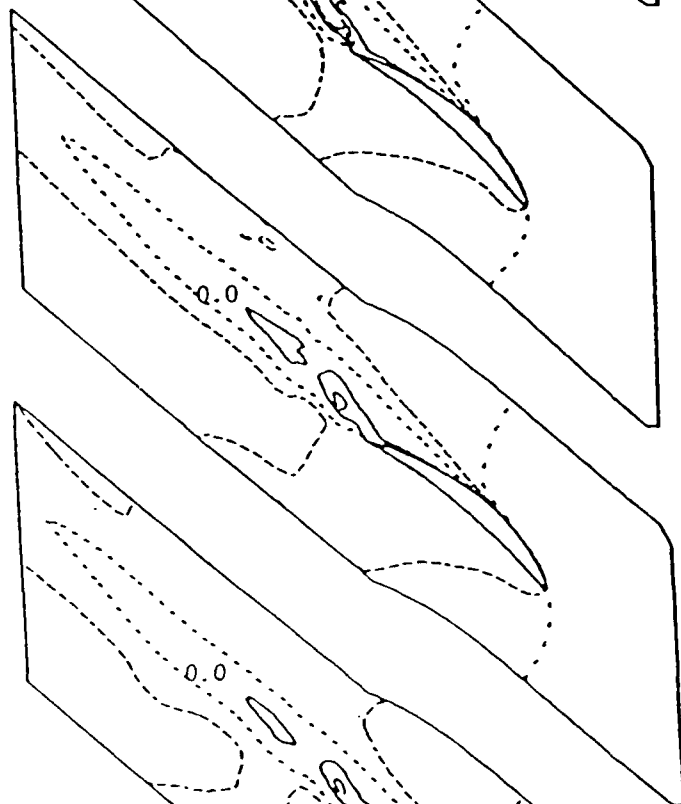
(b) With Wall Jet, t=4.

(c) With Wall Jet, t=8.

Fig. 37 – Contours
of W–Velocity at
Different Times with
Wall Jet Disturbance and
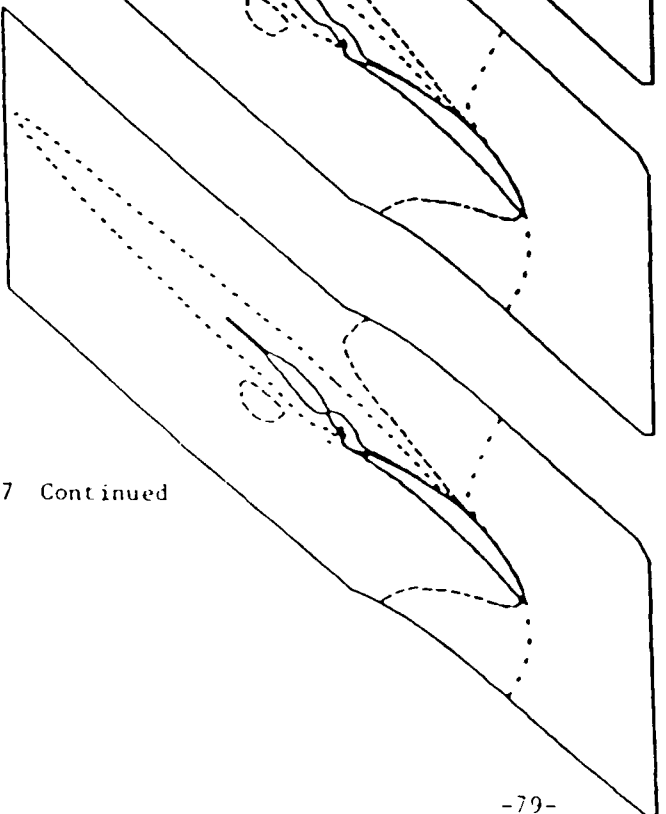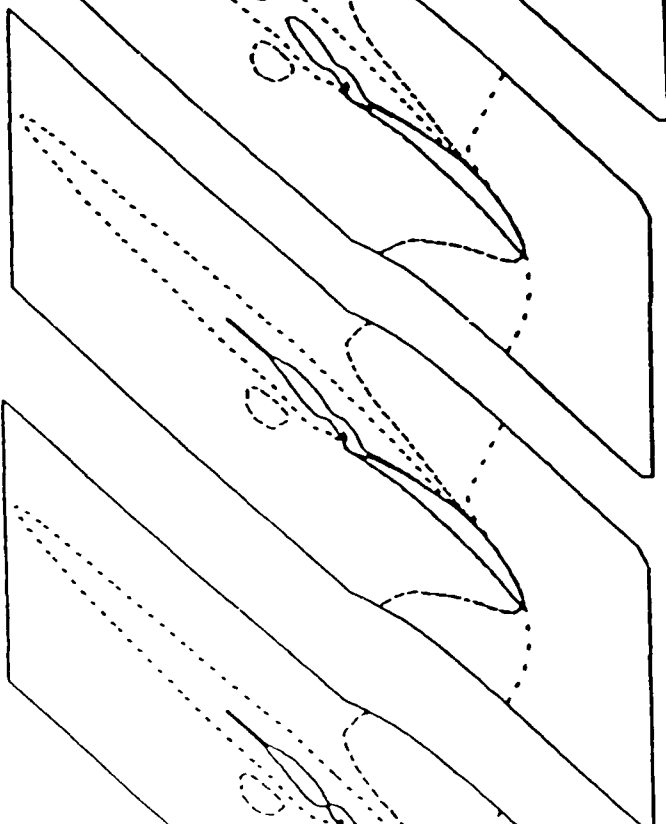Without. Inflow Angle 60°
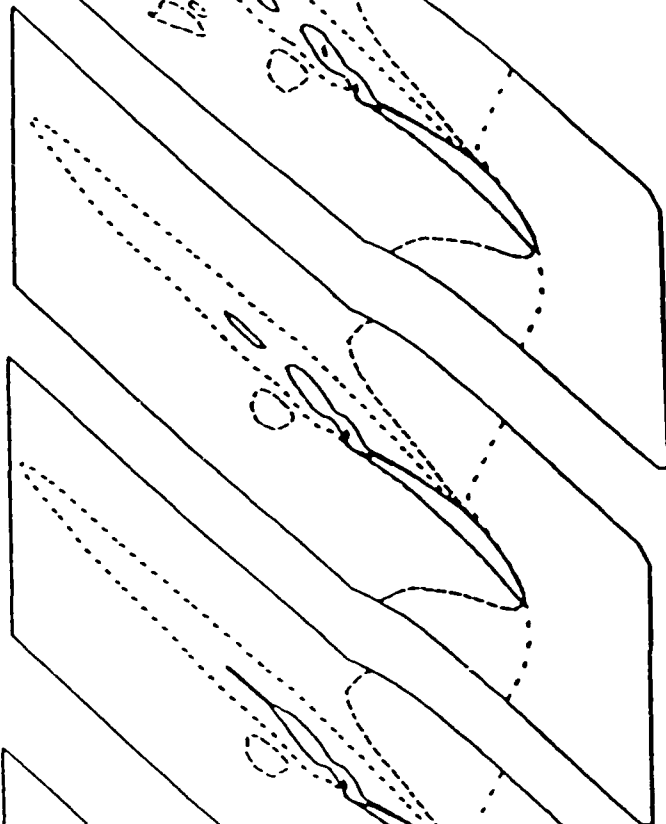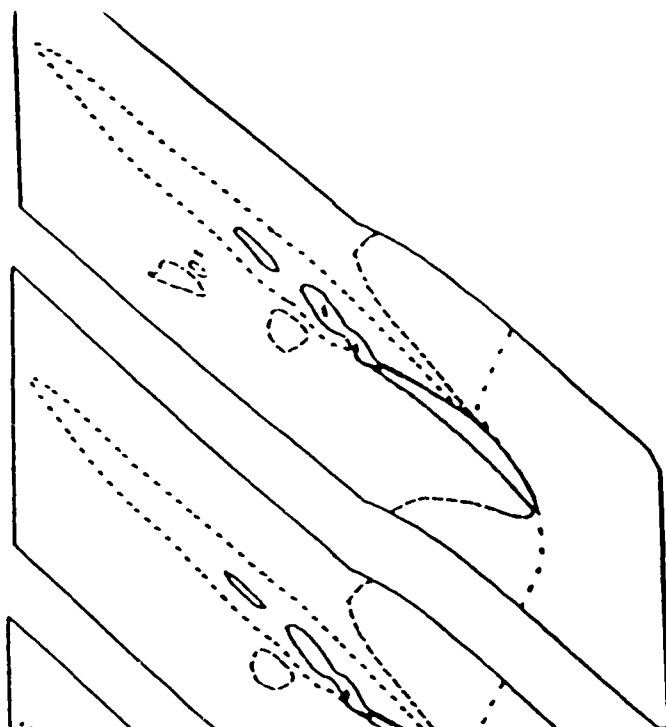Throughout. (Continued)

(d) With Wall Jet, t=12.

(e) With Wall Jet, t=16.

(f) With Wall Jet, t=20.

(g) With Wall Jet, t=24.

Fig. 37 Continued

(h) With Wall Jet, t=28.

(i) With Wall Jet, t=32.

(j) With Wall Jet, t=36.

(h') Wall Jet Removed, t=28.

Fig. 37 Concluded

(i') Wall Jet Removed, t=32.
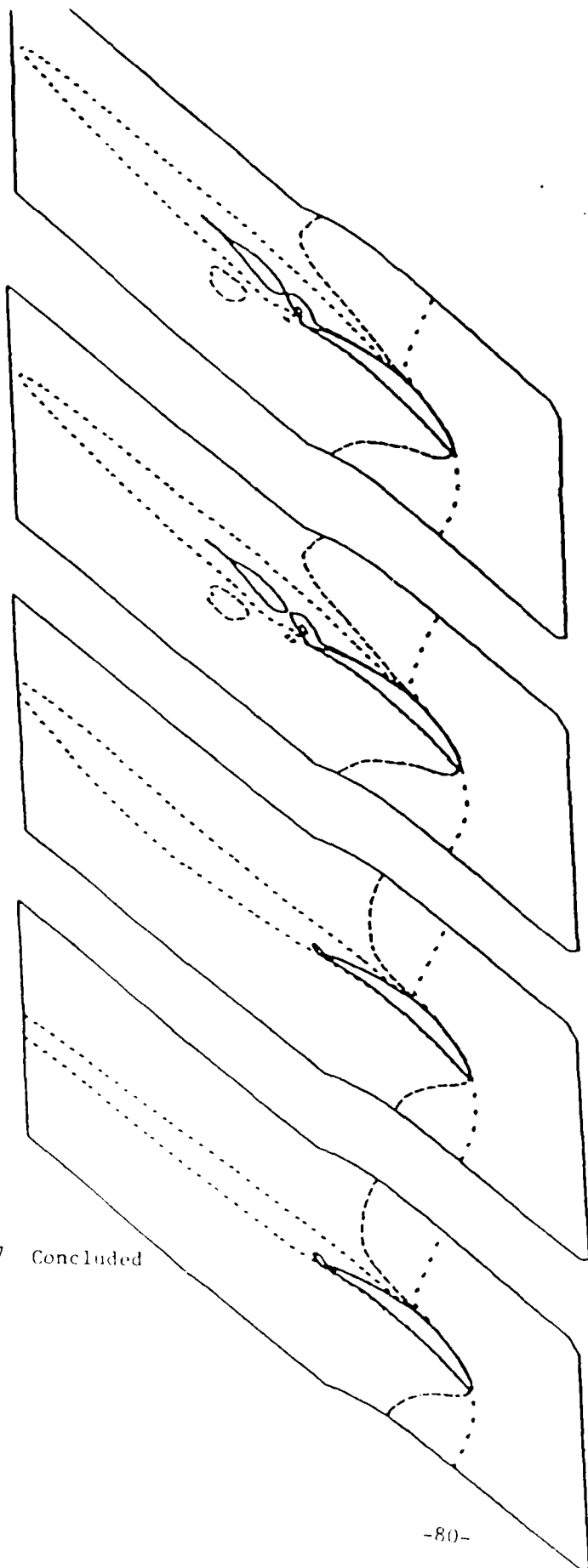
numbers. At $M_\infty = 0.4$, time increments of 0.02 were taken where a unit time increment is based upon axial chord and upstream axial velocity. In this regard, it should be noted that typical inlet Mach number conditions for actual operation are found in the high subsonic or low supersonic regime. Therefore, in practice, the restriction to moderate Mach numbers or above, if reasonable time steps are to be taken, does not represent a practical drawback. In regard to the comparison with data in the present effort, the difference in inflow Mach number condition should not be significant since the calculation was performed for flow conditions where the compressibility effects were of minor importance.

Calculations were run for a solidity of 0.85 and a stagger angle of $40°$ over a range of inflow angles. The experimental data for this configuration is shown in Fig. 24. As can be seen in this figure, at $40°$ stagger, no stall was observed for inflow below $58.5°$ and steady rotating stall was observed for inflow above $60°$. In addition, at this inflow angle stall was observed to occur experimentally in a sharp and definite manner. Calculations were performed at various inflow angles by first obtaining a steady solution at that inflow angle, if such a solution existed. If a time periodic solution existed, the solution was run until a time periodic solution was obtained. In either case, a wall jet disturbance was then introduced along the suction surface of the second blade in the manner discussed in the single passage calculation. Subsequently, a stall zone appeared and if the stall zone propagated, the disturbance was removed and the evolving flow field observed. These results were then analyzed; details of cases considered follow.

Case No. 1 - 57°

The first case considered is that of $57°$ inflow. As can be seen in Fig. 24, no rotating stall should be observed under these conditions. The calculation was initiated, run to steady flow and then a disturbance introduced into the second passage. The disturbance consisted of wall blowing at a rate of 5 percent of the upstream velocity over the aft fifty percent of the suction surface. The steady solution prior to introduction of the disturbance is shown in Fig. 38. Figure 38a gives U-velocity contours, Fig. 38b gives W-velocity contours and Fig. 38c gives surface pressure coefficient. Identical flow was found in each passage.
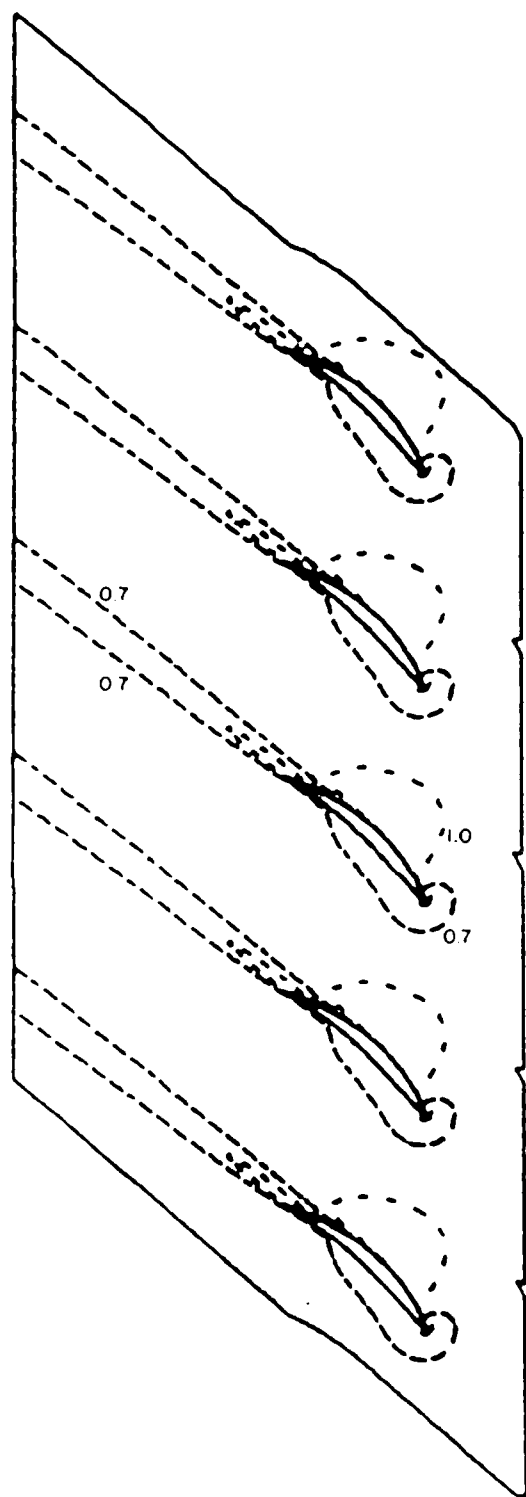
Fig. 38a. U-Velocity Contours,
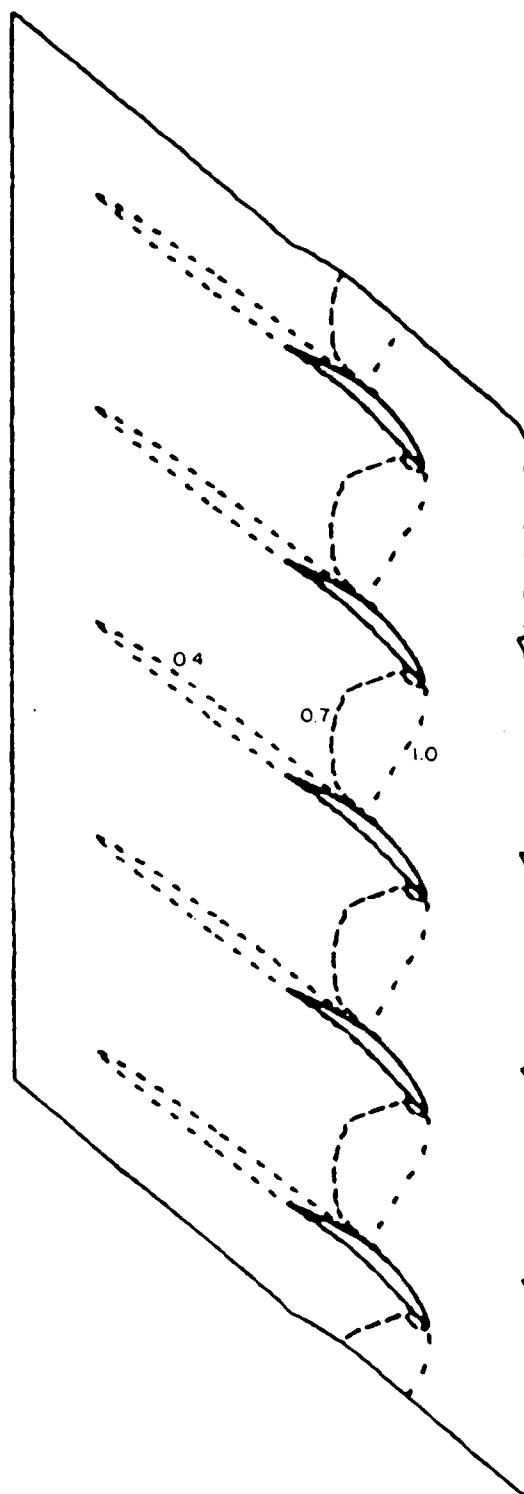57° Inflow,
Initial Flow Field.

Fig. 38b. W-Velocity Contours,
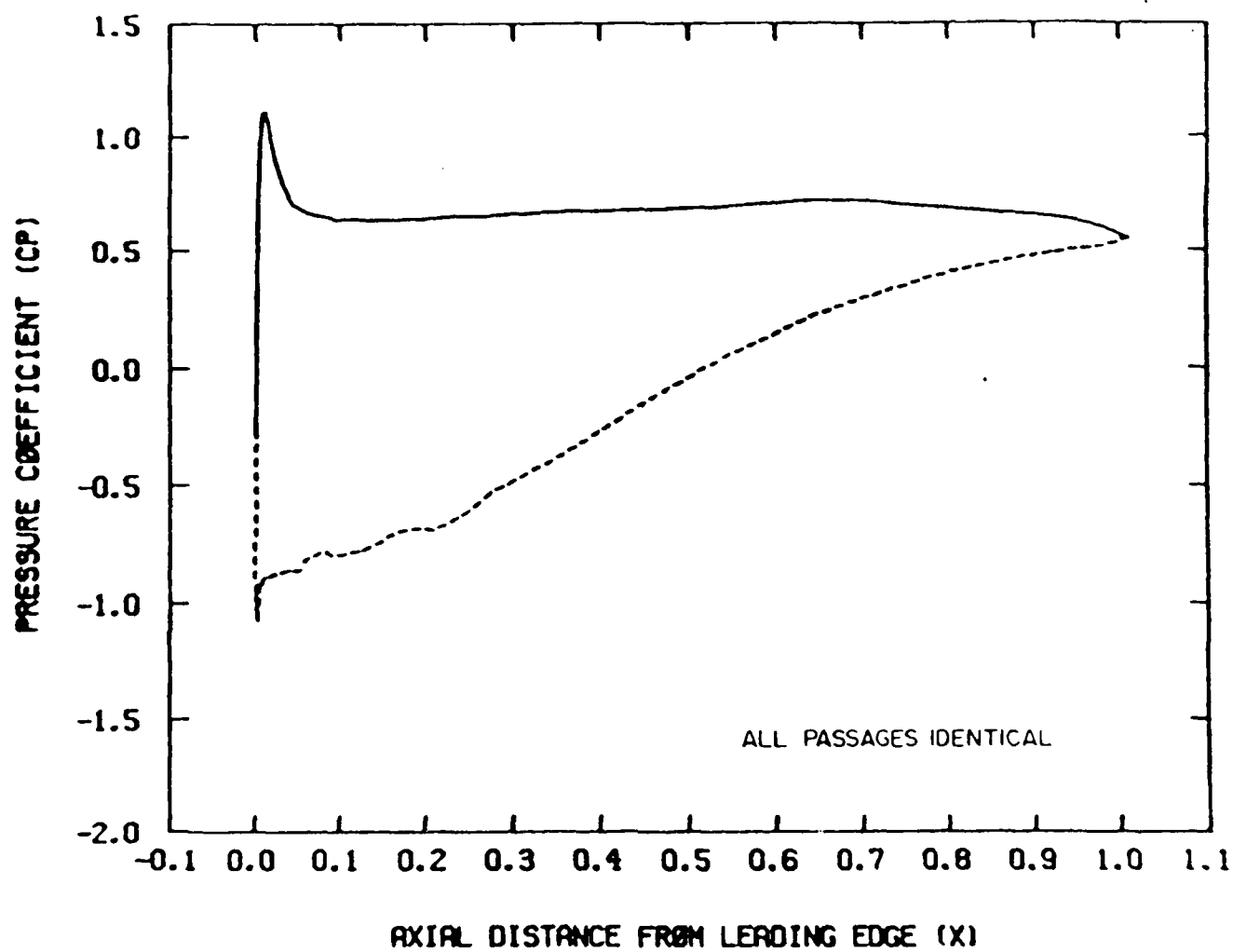57° Inflow,
Initial Flow Field.

Fig. 38c. Surface Pressure Coefficient, 57° Inflow, : .· ·
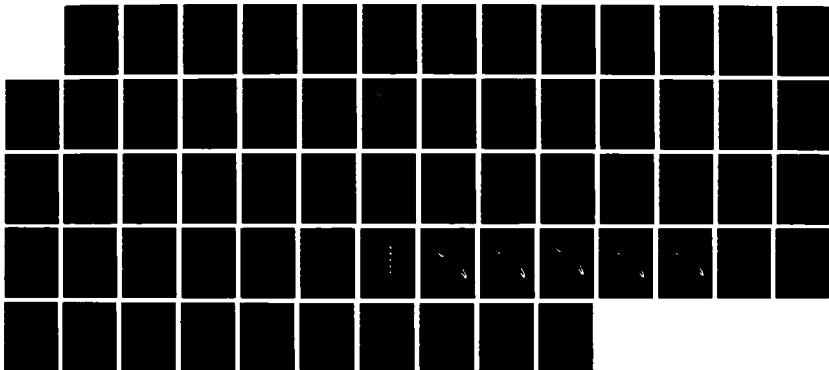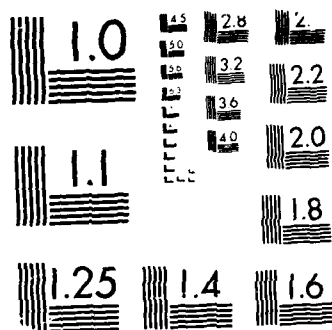
A jet was then introduced on the second blade suction surface and within eight time units a new steady solution was obtained. This new flow was not periodic on a passage-by-passage basis. Contours of the U-velocity component and the W-velocity component are shown in Fig. 39a and 39b, respectively. Clearly, a disturbance is present. The major disturbance is on the second blade, however, changes are also noted on both the first and third blade flow fields. A distinct and observable separation zone appears in the aft region of the second blade suction surface. In addition, the leading edge regions of both the first and third blades are affected. The effective incidence on the first passage is decreased and that on the third is increased. This is consistent with the usual explanation of the rotating stall process occurring due to change in incidence of neighboring passages. This increase in incidence of the third passage will tend to stall the third passage. This third passage stall tends to relieve the second passage stall and, therefore, after some time period the stall zone originally observed on the second blade will proceed to the third blade (e.g., Ref. 1) Although this basic flow disturbance pattern is clearly observed in Figs. 39a and 39b, no propagation was observed and a new steady flow pattern was attained. This is consistent with the data as shown in Fig. 24. The calculation was continued for an additional eight time units; no significant change was noted. Surface pressures relating to the new flow state are given in Fig. 39c.

Case No. 2 - 61°

The second case considered was for an inflow of 61°. Again, a five passage configuration was used. With the exception of the flow inflow angle, conditions were identical to that of Case No. 1. A solution without any disturbance present is shown in Fig. 40. As in the case of the single passage 60° calculation, a separated zone was observed. It should be noted that all passages had nearly identical flows. Since the periodicity conditions were set at both pitchwise boundaries, since the geometry and computational grid of all passages were identical and since inflow and outflow boundary conditions were uniform along the entire domain, identical solutions would be expected in the absence of roundoff error. Such a set of solutions is shown in Figs. 40a-c. It is possible that with continuing running of the solution, roundoff error
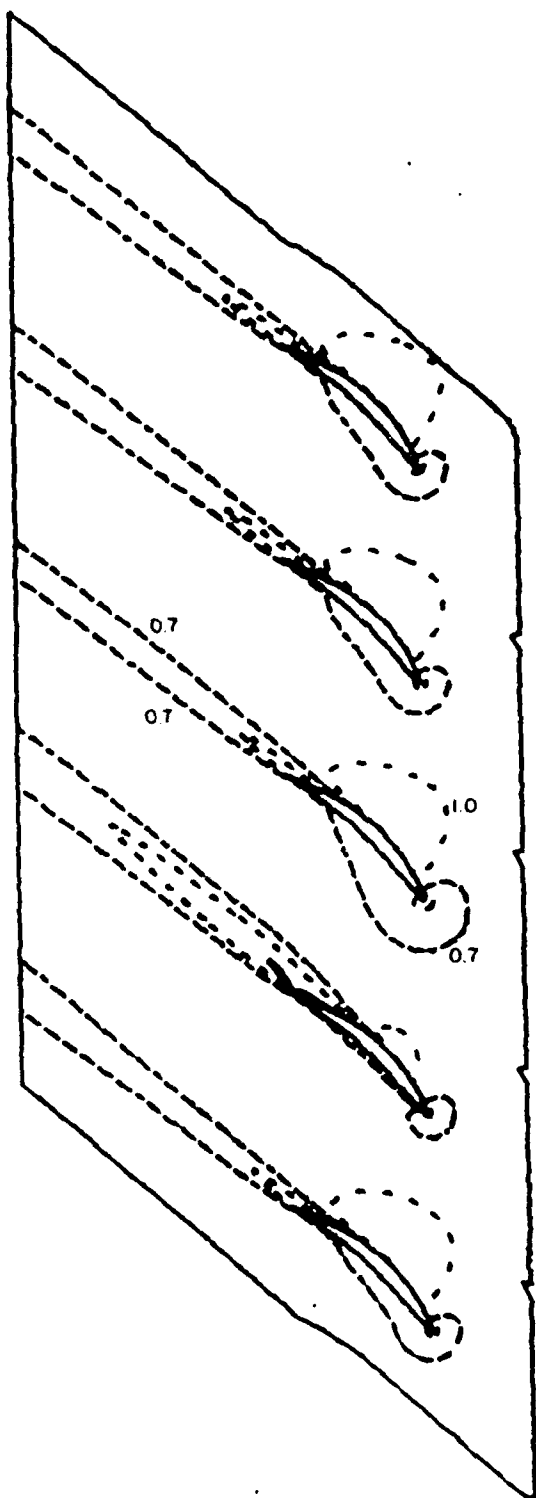
Fig. 39a. U-Velocity Contours,
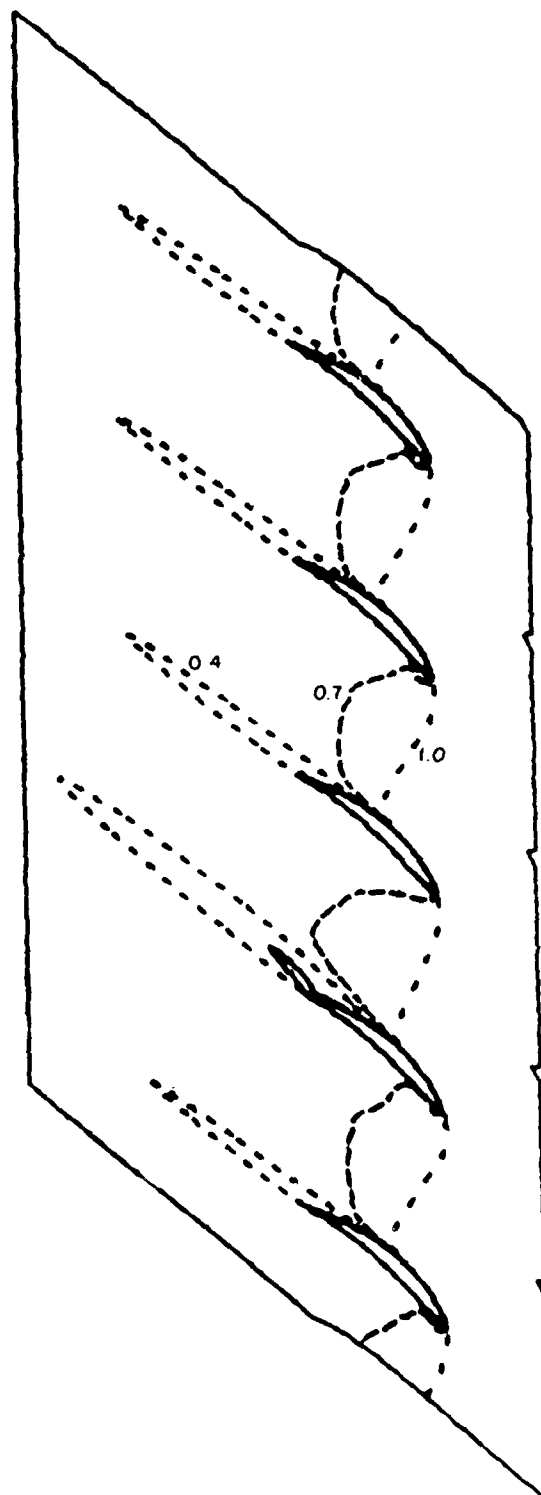57° Inflow,
New Flow Field with
Disturbance Applied.

Fig. 39b. W-Velocity Contours,
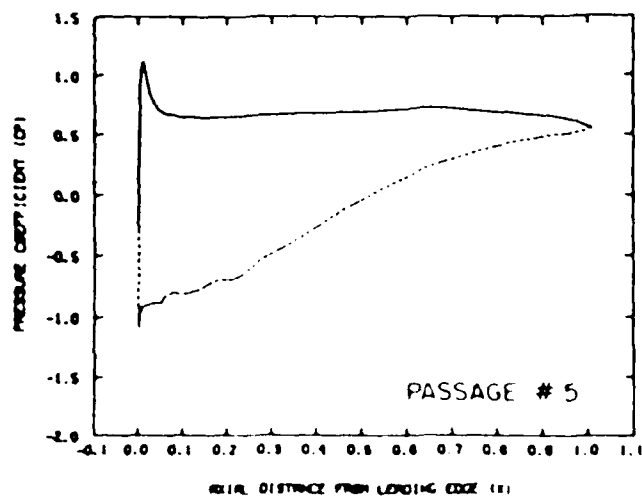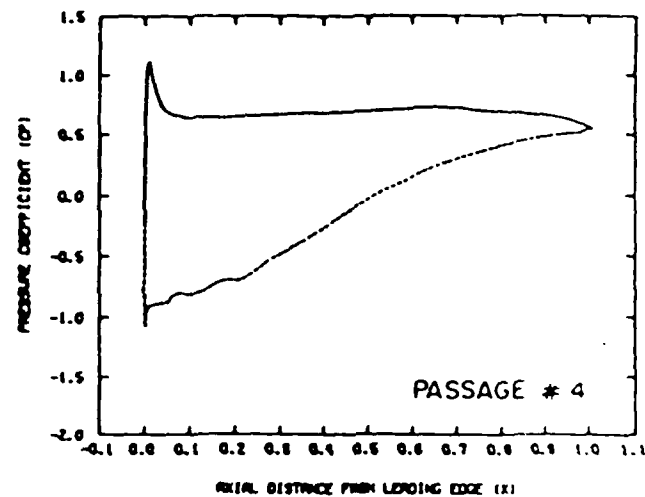57° Inflow,
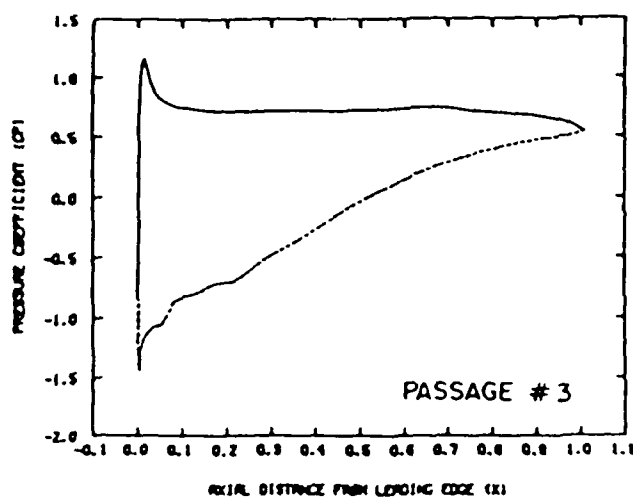New Flow Field with
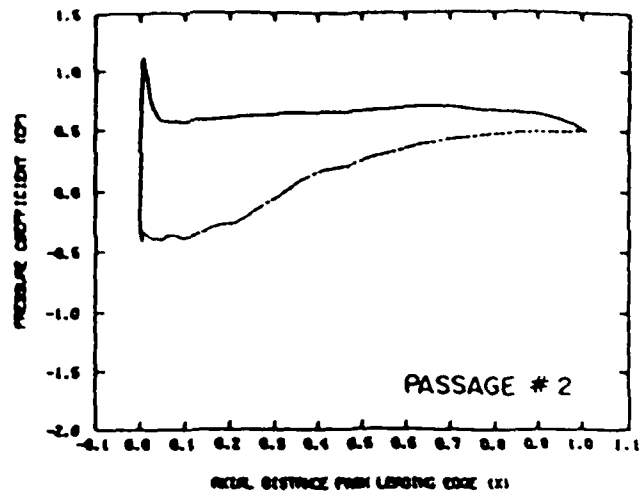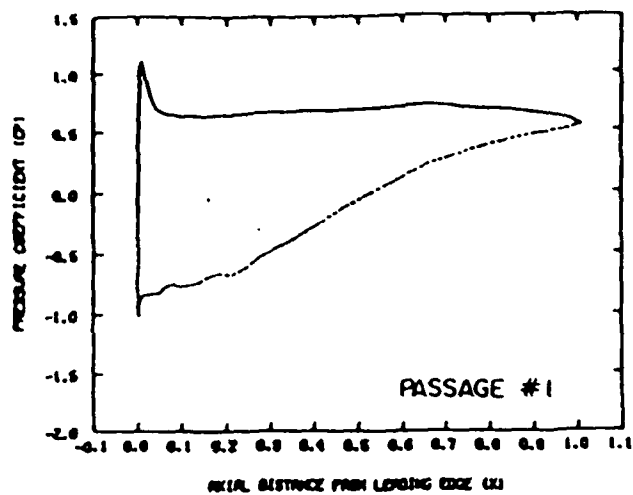Disturbance Applied

Fig. 39c   Surface Pressure Coefficient, 57° Inflow,
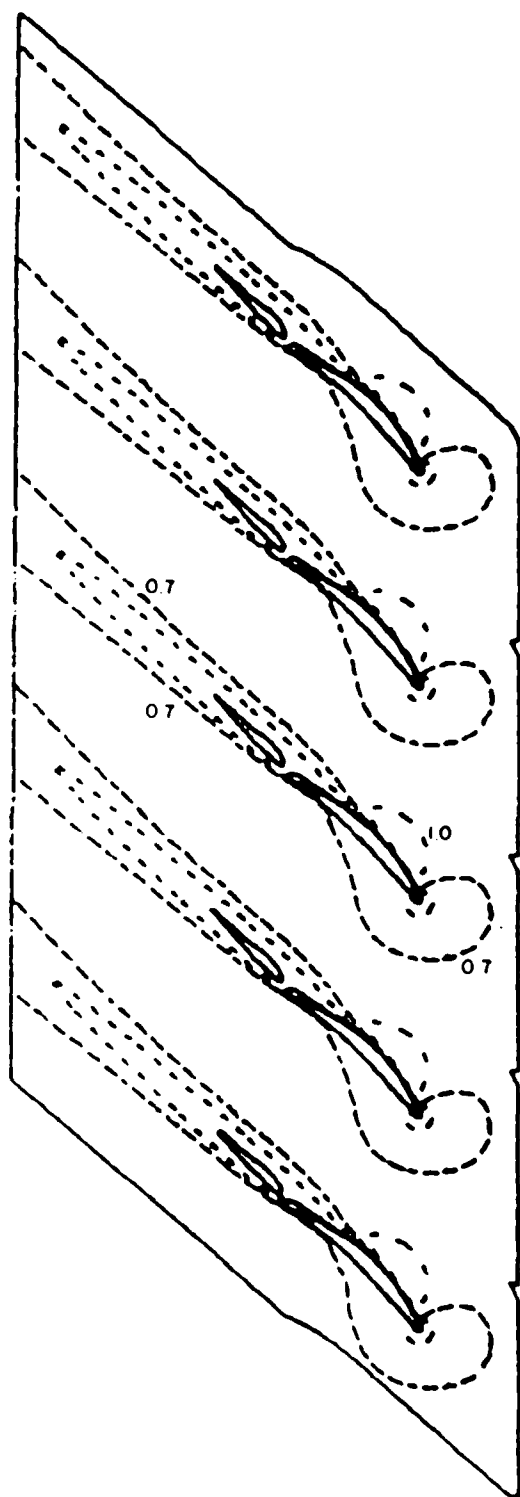New Flow Field with Disturbance Applied

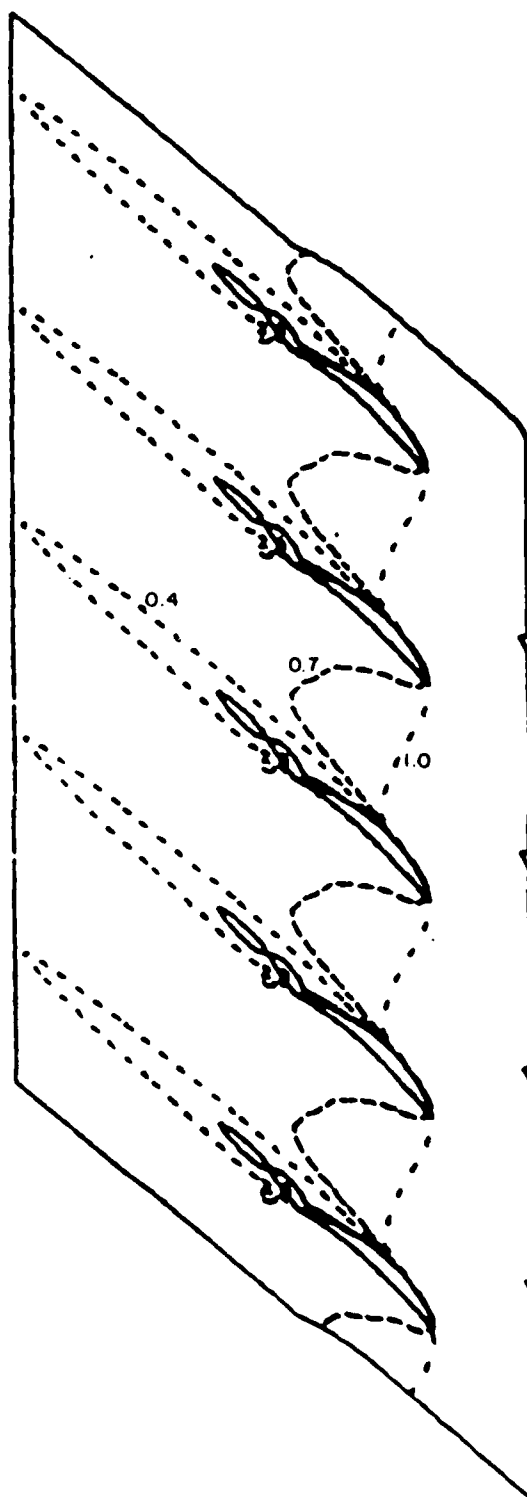Fig. 40a. U-Velocity Contours,
61° Inflow,
Undisturbed Flow

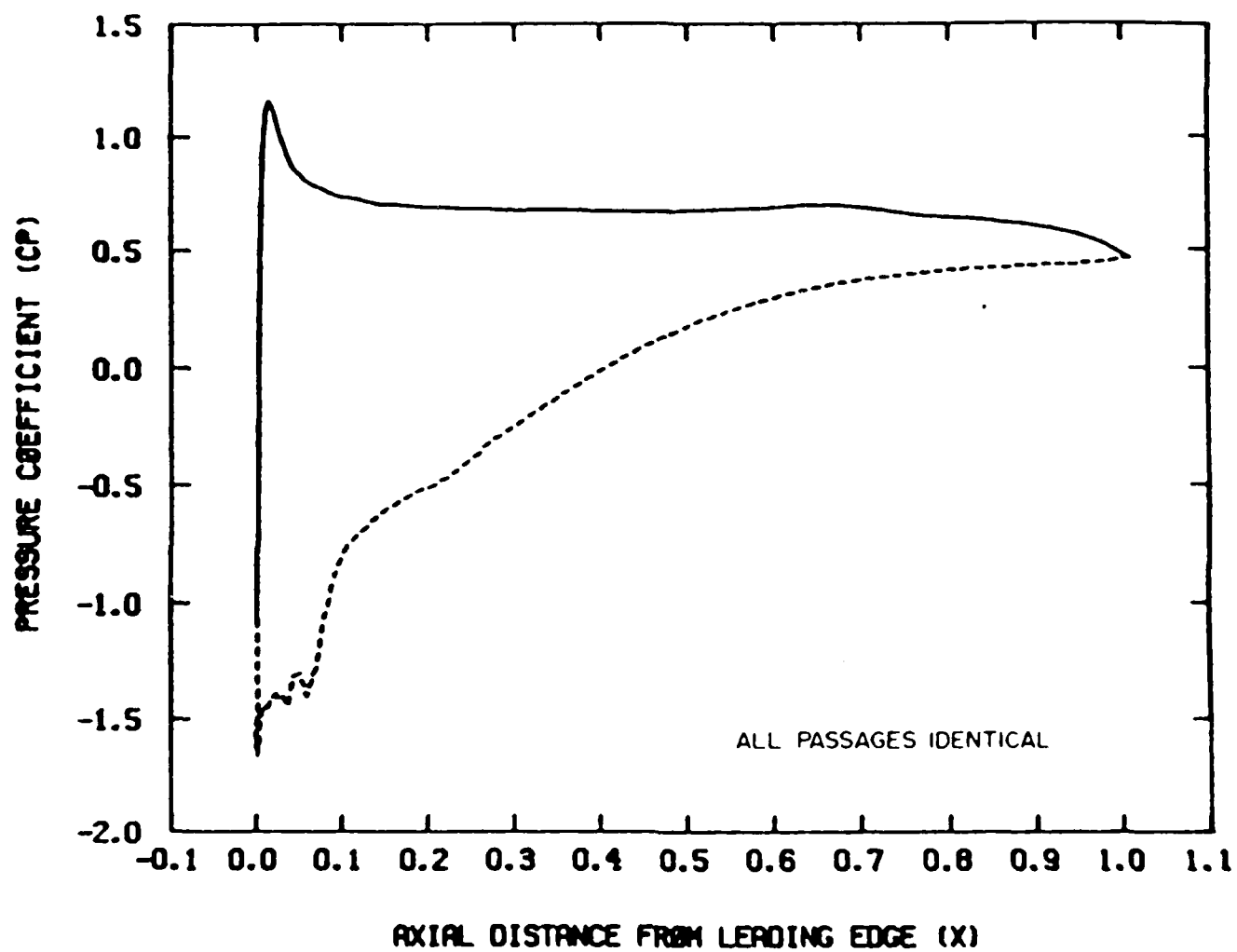Fig. 40b. W-Velocity Contours,
61° Inflow,
Undisturbed Flow

-87-

Fig. 40c. Surface Pressure Coefficient, 61° Inflow, Undisturbed Flow.

would develop passage-to-passage differences. However, this question was not pursued in the present study. At t = 4.0 a disturbance in terms of a 0.02 suction surface blowing was introduced on the second blade. This was maintained until t = 8.0, when it was removed.

Table 1 presents the developing pattern between t = 12 and t = 36. As can be seen, the large separation region propagates in the direction from blade 1 to blade 5. A representative flow pattern is shown in Figs. 41a and 41b. It is clear that each passage at all times does contain separated flow and although the region of most intense flow separation does propagate, passages do not fully recover. This is not usually the behavior associated with rotating stall.

Case No. 3 - 60° Inflow

Based upon the previous two cases, the third case was chosen at an intermediate inflow angle. Clearly, 57° inflow does not lead to any propagation whereas 61° leads to a definite propagation. However, in this latter case no complete recovery was ever attained in any passage. Therefore, the third case

Table 1 - Blade flow properties for 61° case; X indicates large separation zone, O indicates small separation zone.

BLADE NUMBER

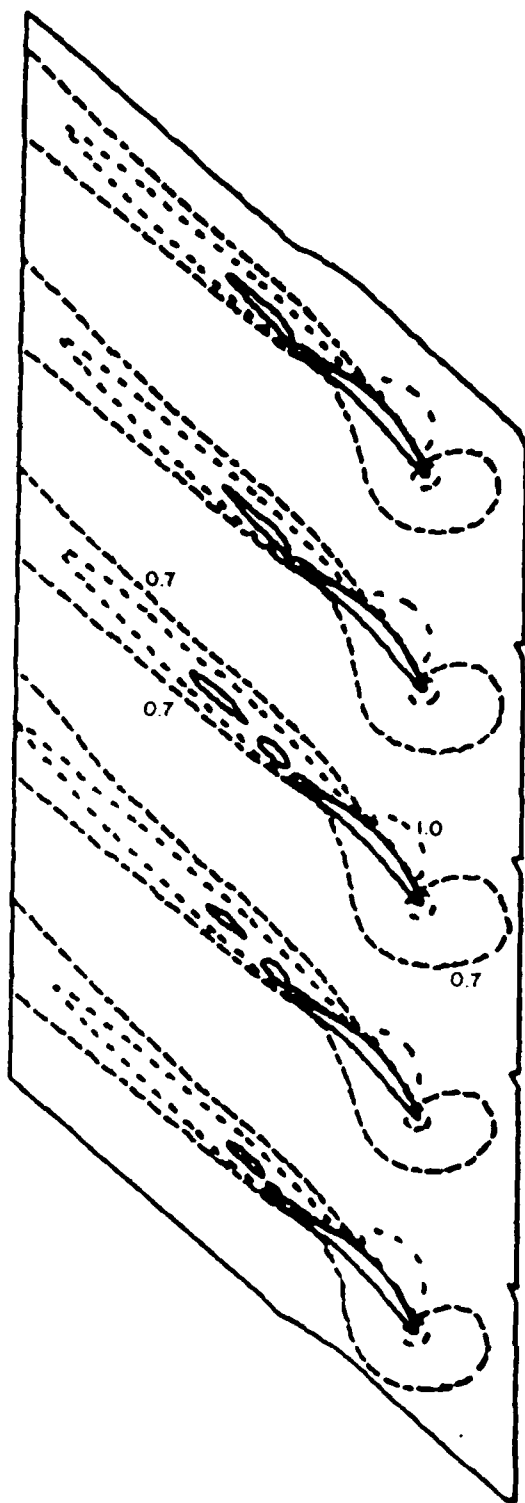| t	1	2	3	4	5
12	O	O	O	X	X
16	X	O	O	X	X
20	X	X	O	O	X
24	X	X	X	O	O
28	O	O	X	X	O
32	O	O	X	X	O
36	O	O	O	X	X

Fig. 41a.   U-Velocity Contours,
            61° Inflow,
            Flow After 12 Units
            of Time.

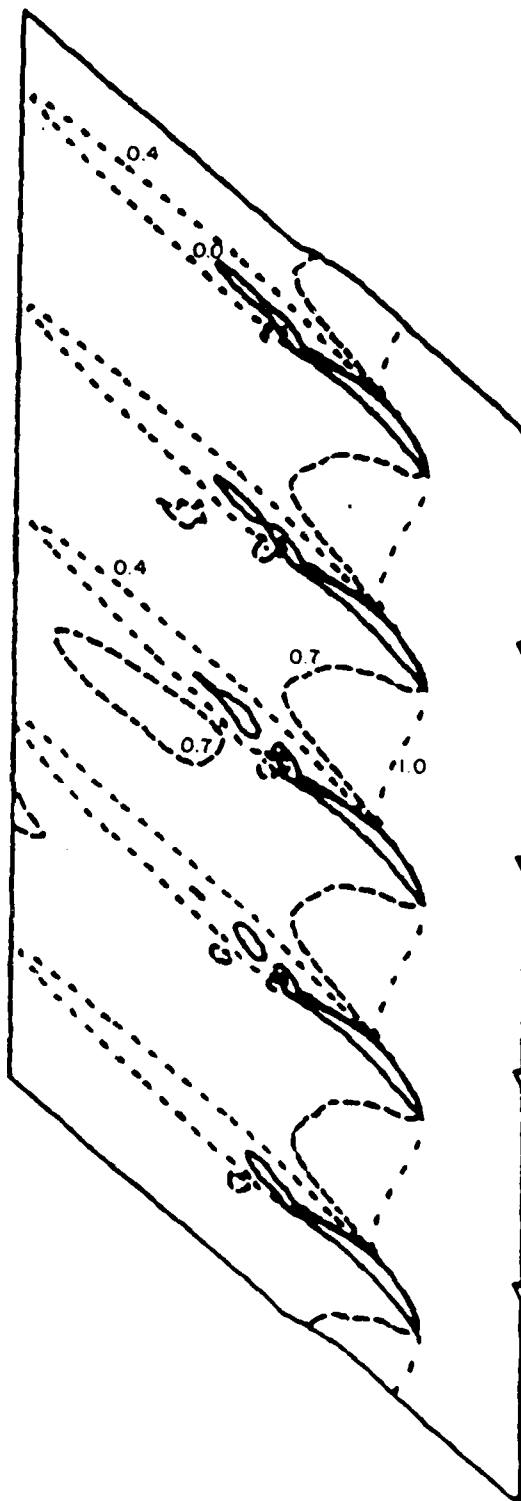Fig. 41b.   W-Velocity Contours,
            61° Inflow,
            Flow After 12 Units
            of Time.

-90-

was run at 60° inflow. At 60° inflow no significant separation zone existed
with no disturbance applied. The velocity contours for this steady undisturbed
flow are shown in Figs. 42a and 42b. The disturbance again was introduced as a
wall blowing disturbance on the suction surface of the second blade. In brief,
upon introduction of the wall disturbance a significant separation zone
appeared and in this case propagated toward blade 3. The wall disturbance was
maintained until the separation zone reached blade 3 with some effect noted on
blade 4. At that point the disturbance was removed and though some propagation
continued, the disturbance rapidly died. Contours of the flow development with
the wall disturbance on are shown in Figs. 43a and 43b. As can be seen, the
upstream incidence of blades 1, 2 and 3 are affected by the blade 2 wall
blowing disturbance, however, the stall propagation was limited. Surface
pressure plots for the five blades are shown in Fig. 43c. Furthermore, as
shown in Figs. 44a and 44b, upon removal of the disturbance the separation zone
disappears.

Case No. 4a - 60.5°

The final case considered was for an inflow of 60.5°. As will be
described, three separate cases were run at this inflow angle. All cases were
initiated from a solution obtained by first performing a 60.5° inflow five
passage calculation and then introducing a wall blowing effect on the aft
portion of the second passage. The flow pattern prior to the initiation of
wall blowing is shown in Figs. 45a and 45b. As can be seen, even in the
absence of any wall blowing disturbance, a small separation region is clearly
visible. In addition, the flow is essentially identical on a passage-to-
passage basis. The Case 4a calculation was then initiated by introducing a
disturbance in the second passage. The disturbance was held until t = 24 (see
Figs. 45c and 45d), when it was removed. The calculation was then allowed to
proceed. The time step taken in all runs was 0.02. The results at t = 32.0
are shown in Figs. 46c and 46d. These results show separated flow on the first
and fourth blades. As time proceeded, the pattern changed as shown in Figs.
46c-46p. Although the pattern did show a propagation of the separation zone(s)
from passage to passage, the propagating pattern was in continuous change.
Although the strength of the separated zone did not decrease with time as was
the case for 60° inflow, an unchanging propagating pattern did not emerge.
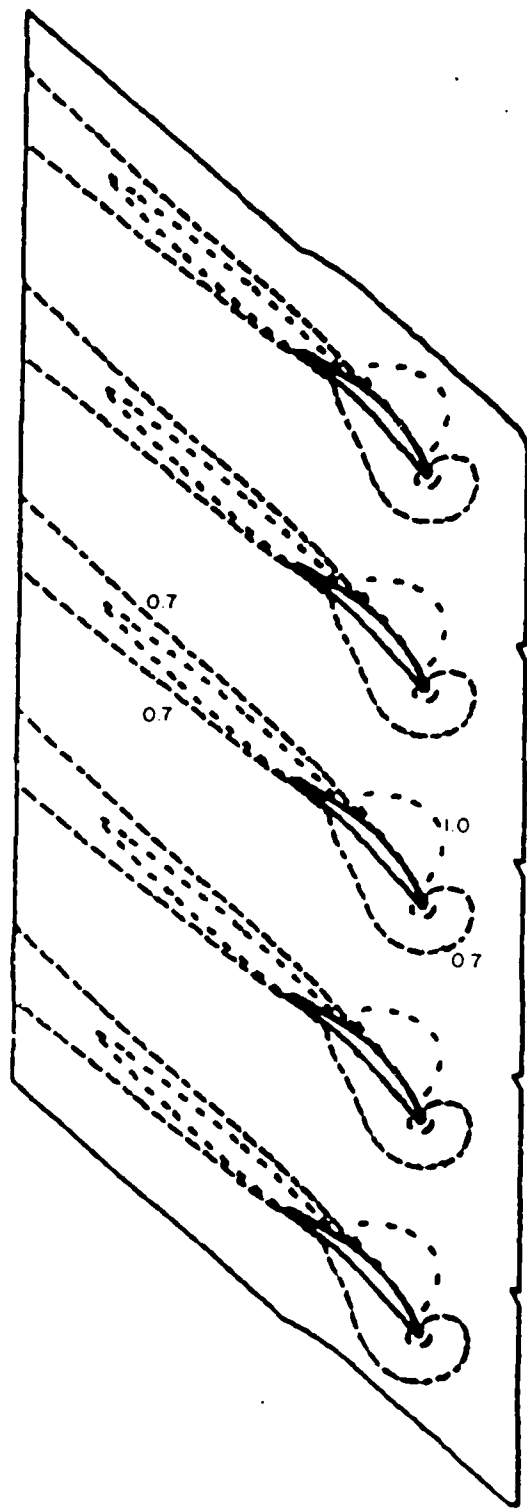
Fig. 42a.   U-Velocity Contours,
            60° Inflow,
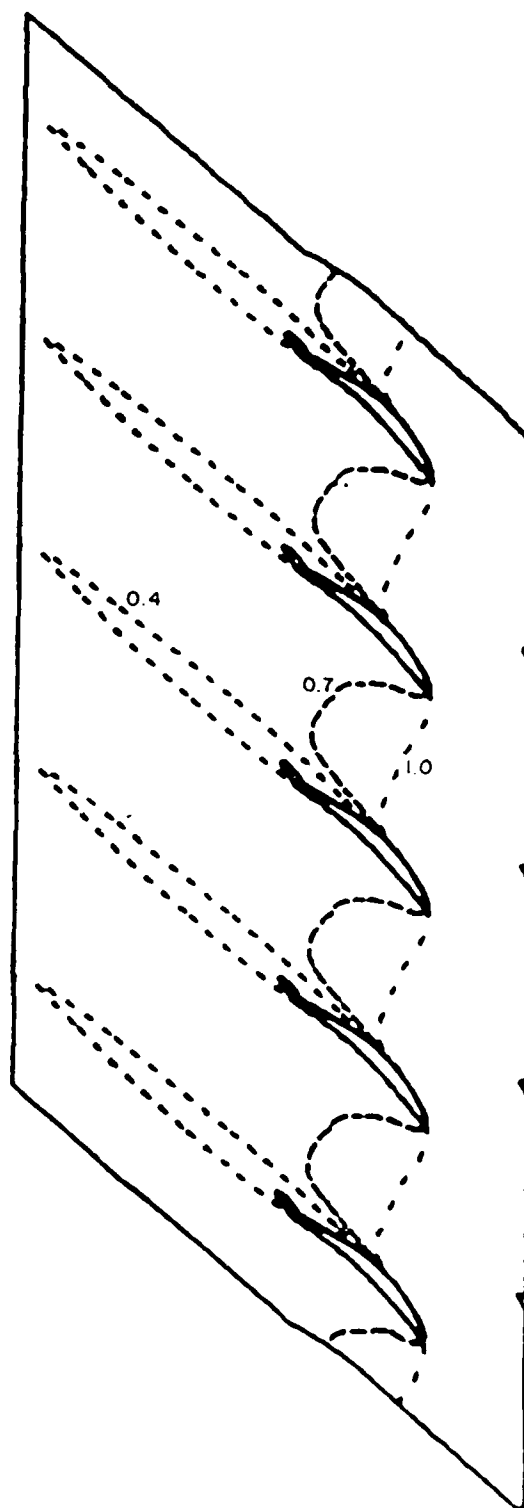   Initial Flow Field.

Fig. 42b.   W-Velocity Contours,
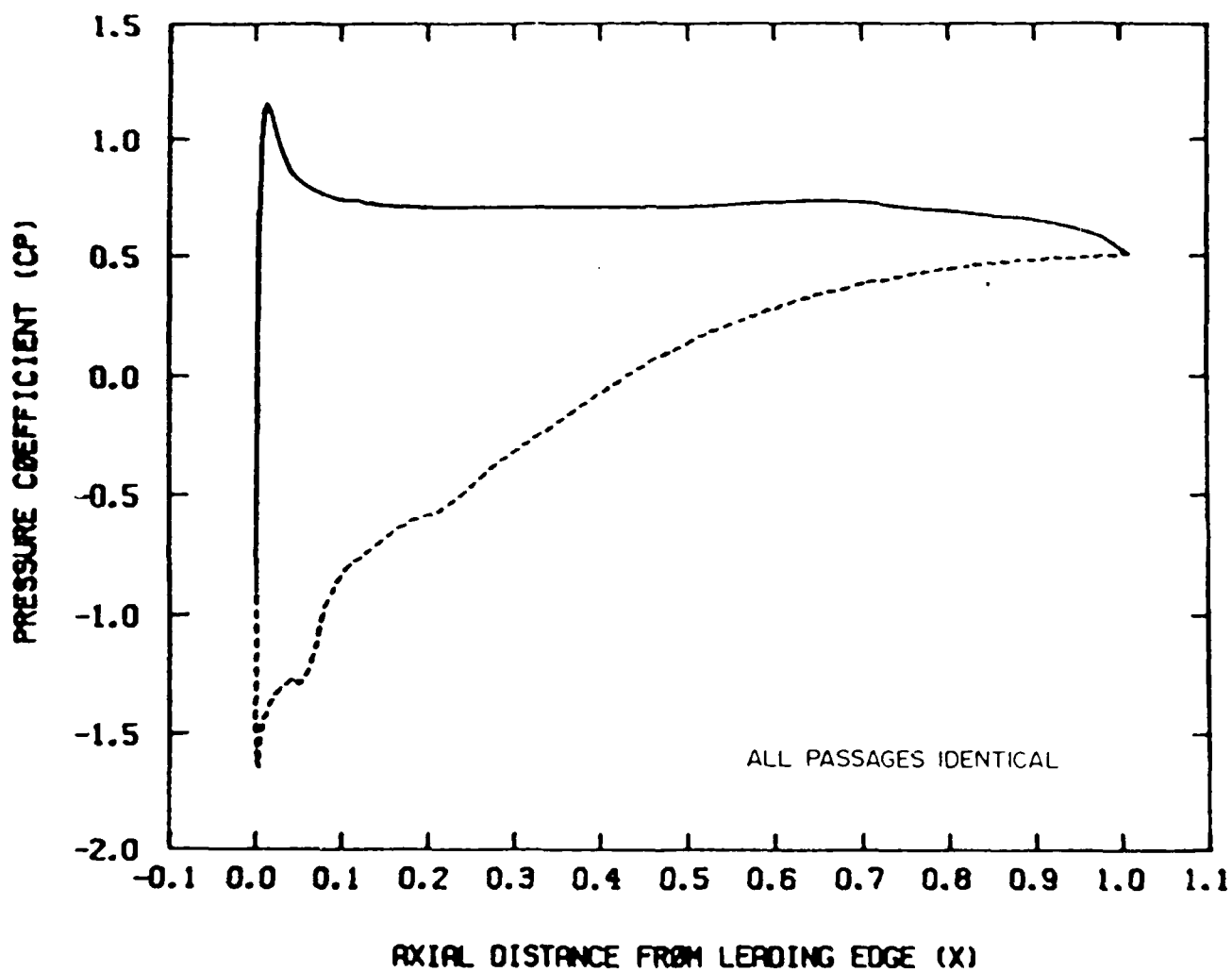   60° Inflow,
            Initial Flow Field.

Fig. 42c. Surface Pressure Coefficient, 60° Inflow, Initial Flow Field.
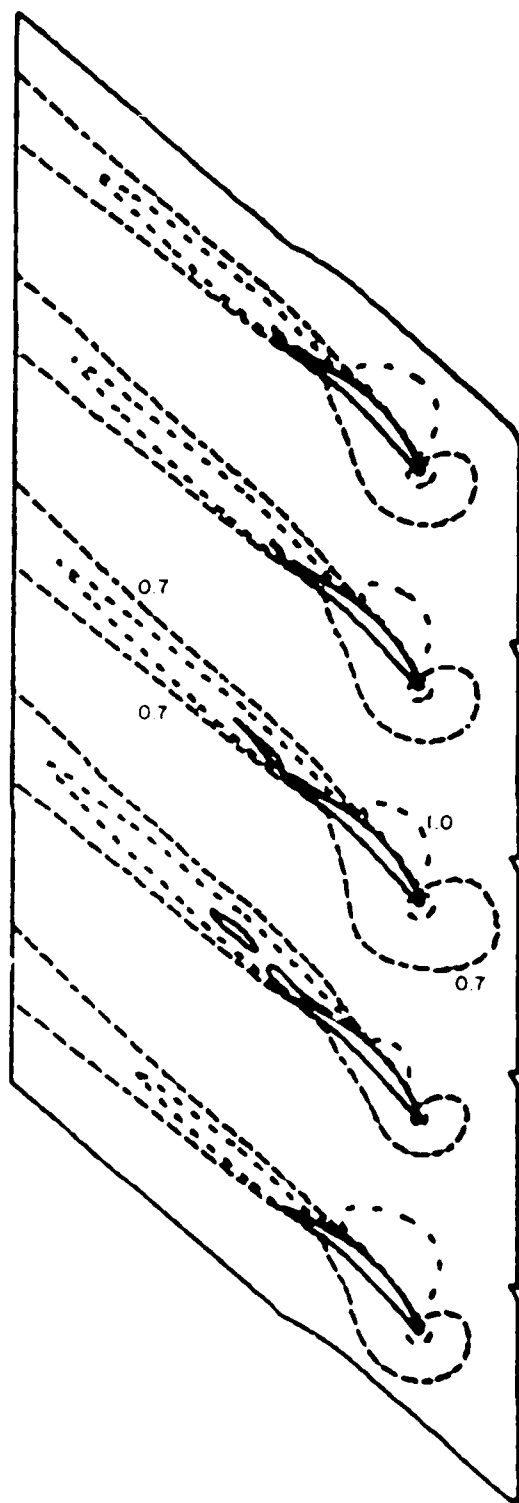
Fig. 43a   U-Velocity Contours,
            40° Inflow,
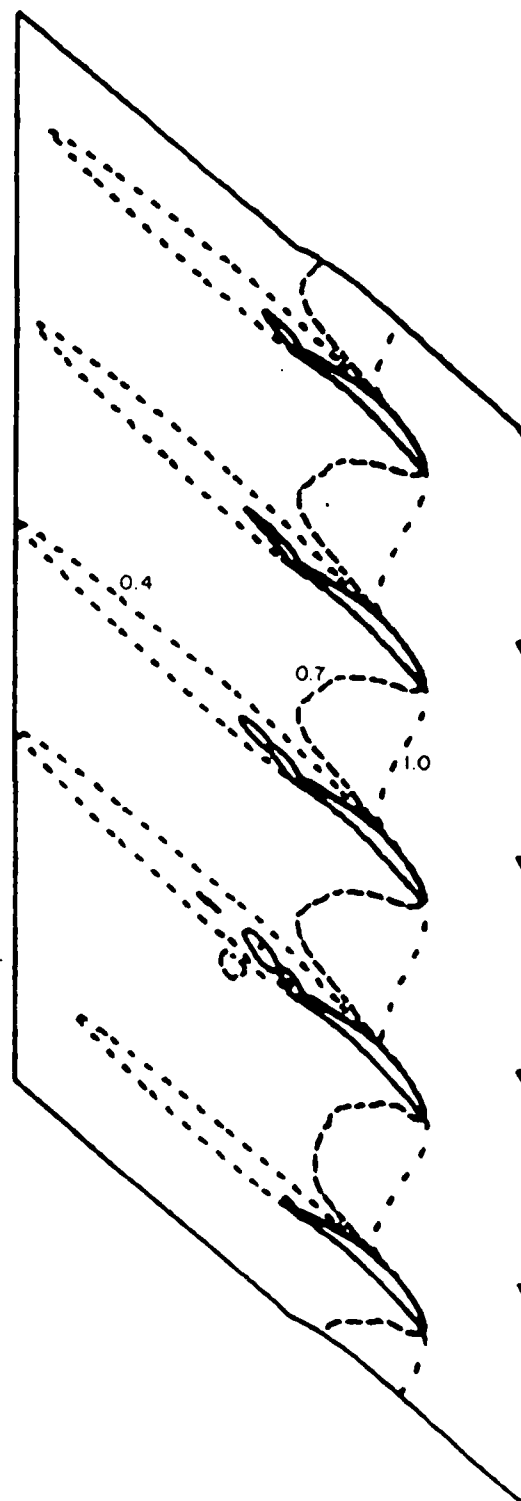   Disturbance Applied.

Fig. 43b.   W-Velocity Contours,
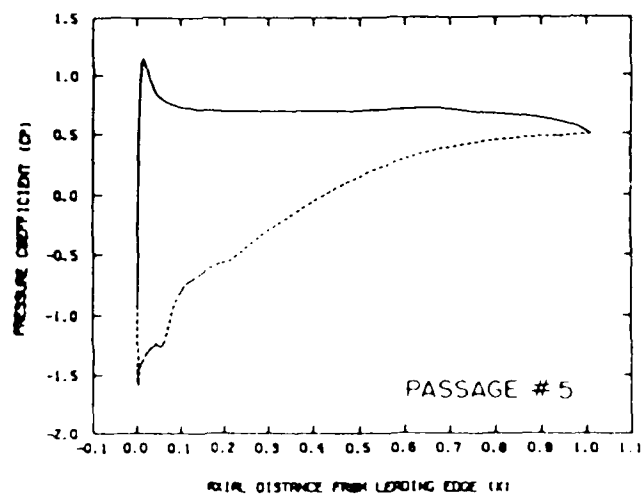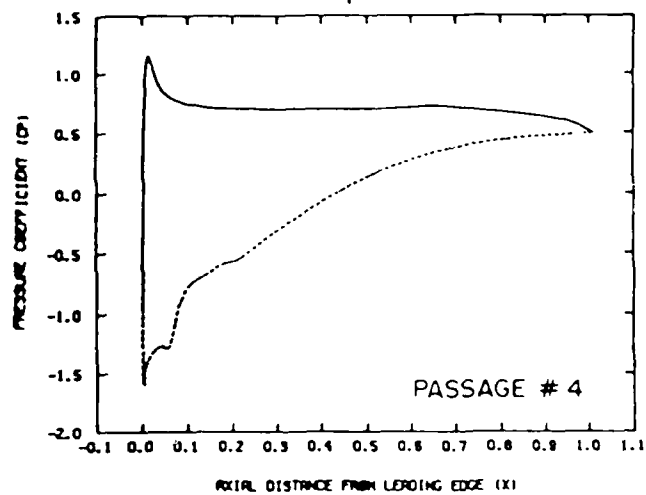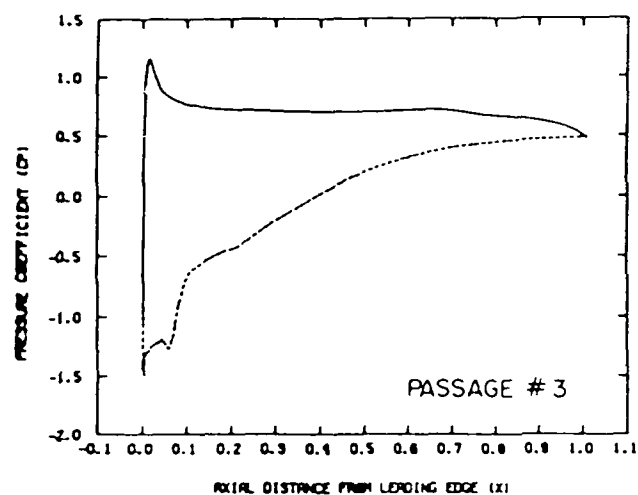   60° Inflow,
            Disturbance Applied
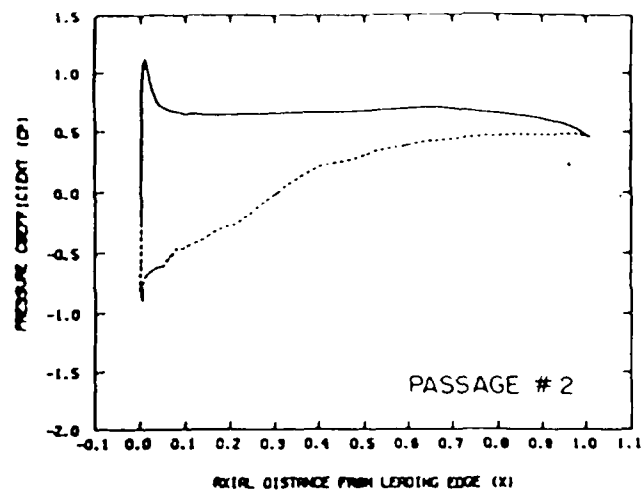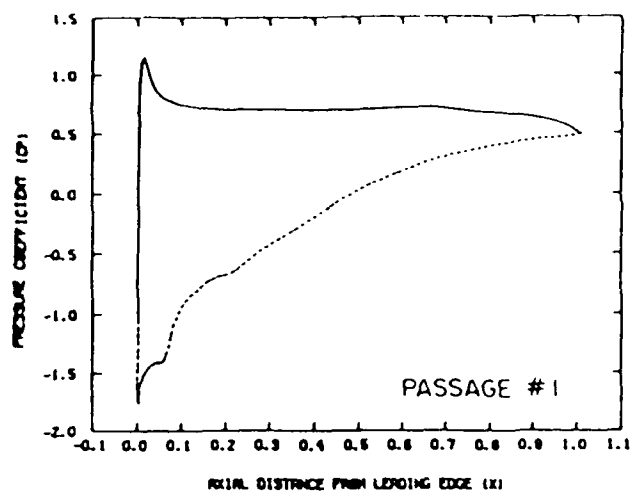
Fig. 43c. Surface Pressure Coefficient, 60° Inflow, Disturbance Applied
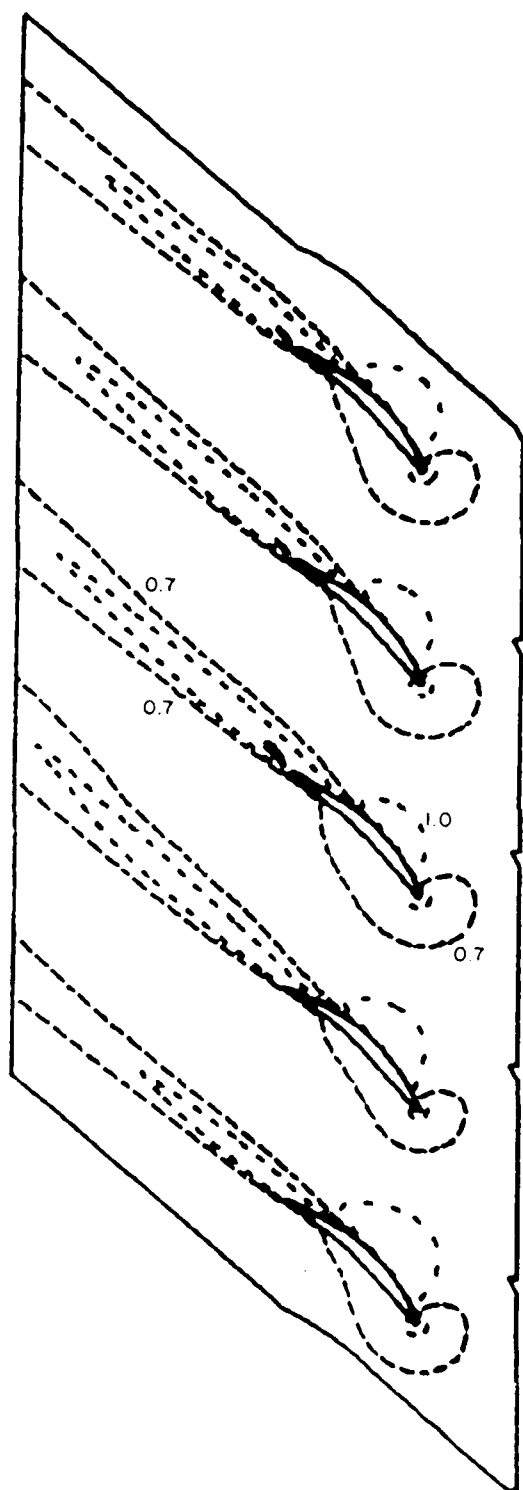
Fig. 44a U Velocity Contours,
          6° Inflow,
          Disturbance Removed
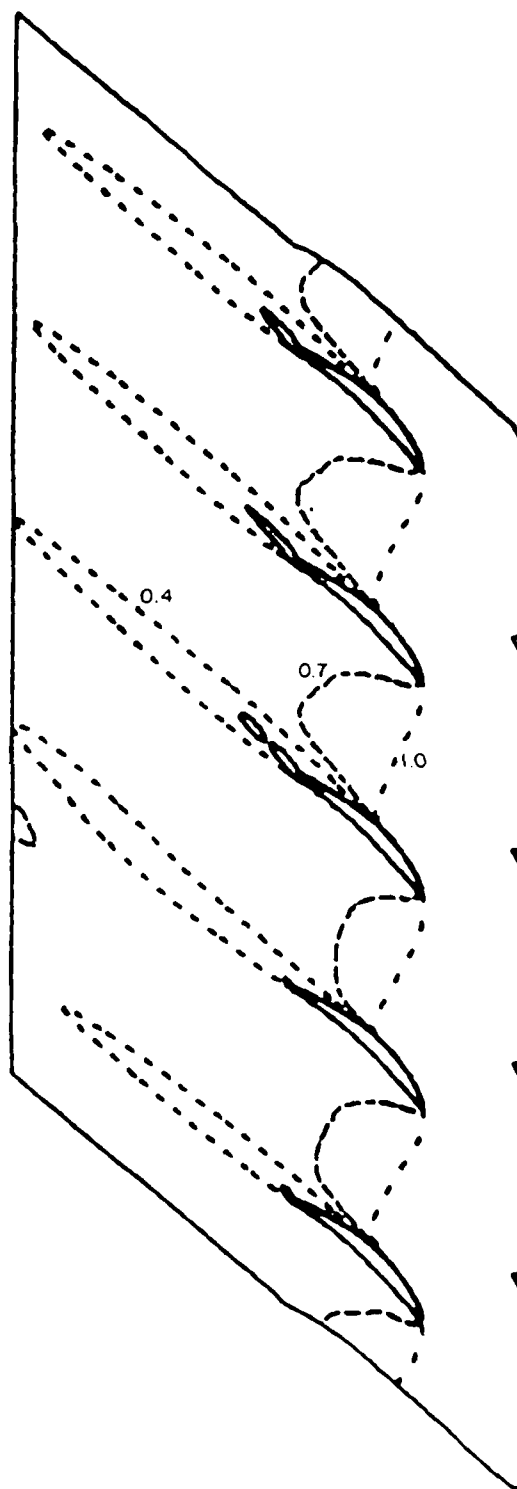
Fig. 44b. W Velocity Contours,
           6° Inflow,
           Disturbance Removed
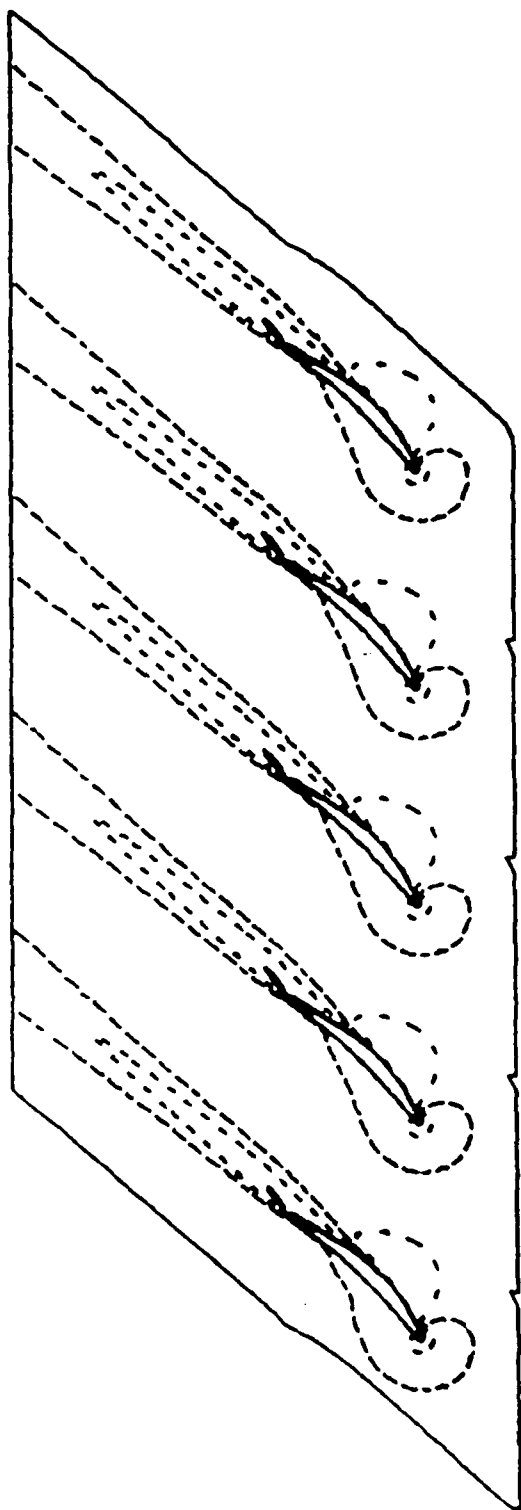
Fig. 45a. U-Velocity Contours,
           60.5° Inflow,
           Initial Flow Field
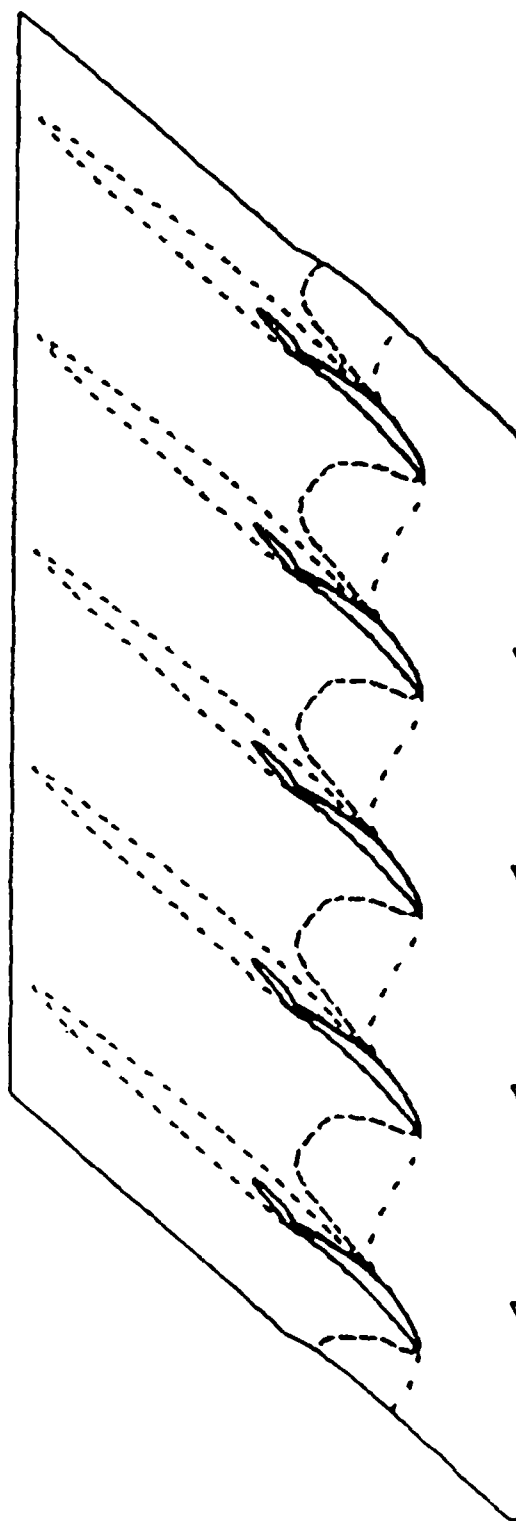
Fig. 45b. W-Velocity Contours,
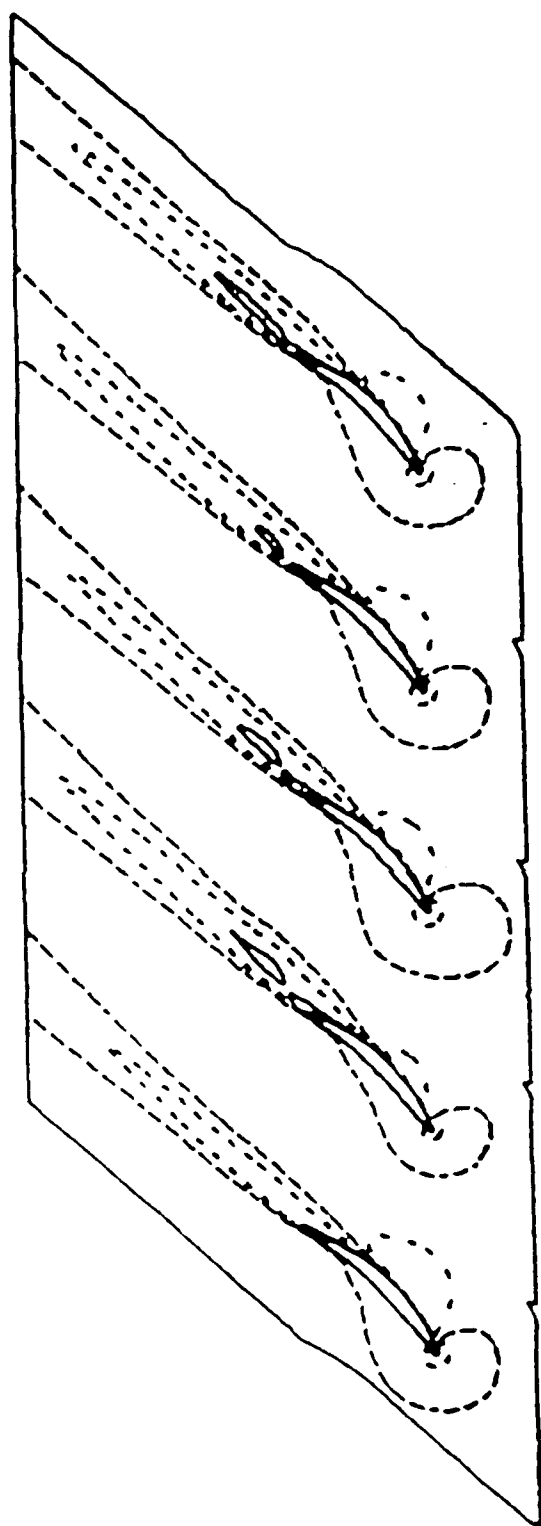   60.5° Inflow,
           Initial Flow Field.

Fig. 45c. U-Velocity Contours,
60.5° Inflow,
Disturbance on Blade
No. 2, t=24

Fig. 45d. W-Velocity Contours,
60.5° Inflow,
Distubance on Blade
No. 2, t = 24

Fig. 46a. U-Velocity Contours,
60.5° Inflow,
Disturbance Removed,
Case 4a, t = 28.

Fig. 46b. W-Velocity Contours,
60.5° Inflow,
Disturbance Removed,
Case 4a, t = 28

Fig. 46c. U-Velocity Contours,
          60.5° Inflow,
          Disturbance Removed,
          Case 4a, t = 32

Fig 46d   W-Velocity Contours,
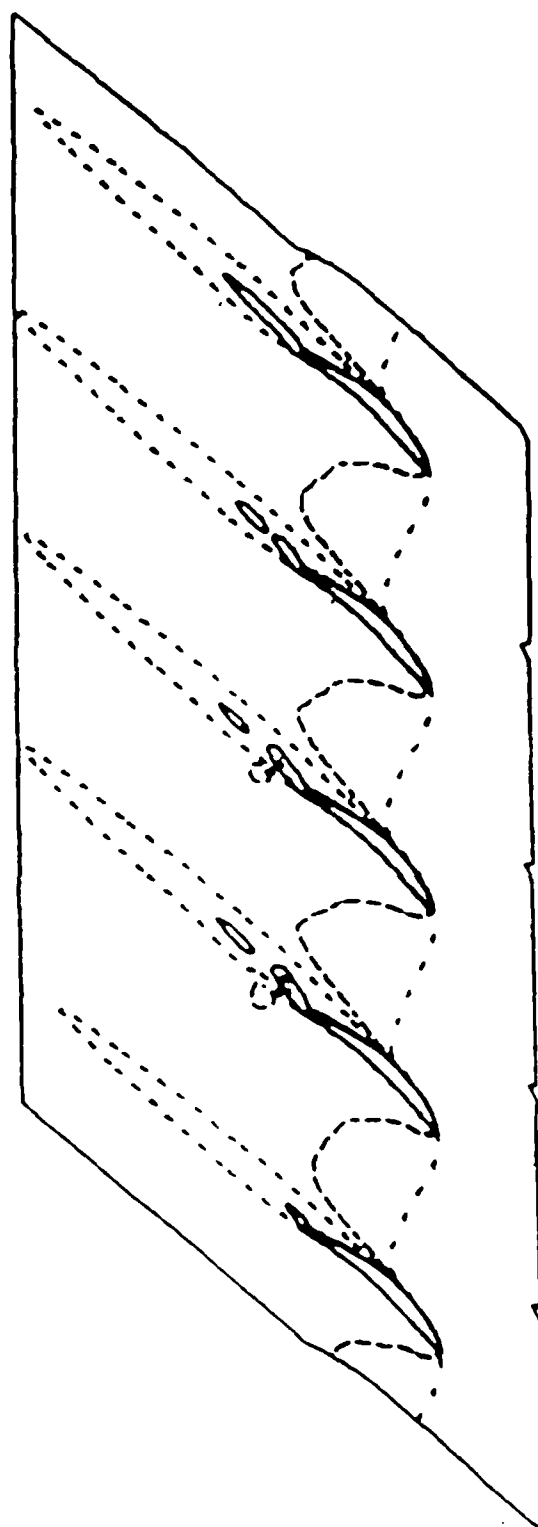   60.5° Inflow,
          Disturbance Removed,
          Case 4a, t = 3.

-1-

Fig. 46e.   U-Velocity Contours,
             60.5° Inflow,
             Disturbance Removed,
             Case 4a, t = 36.

Fig. 46f.   W-Velocity Contours,
             60.5° Inflow,
             Disturbance Removed,
             Case 4a, t = 36.
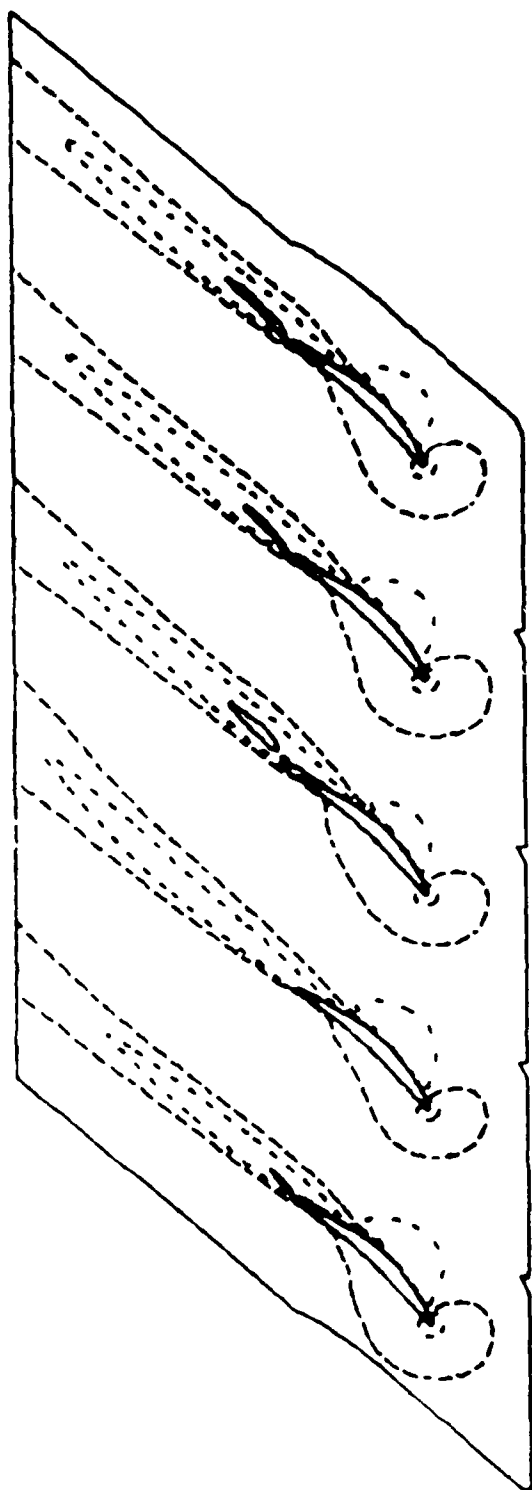
Fig. 46g. U-Velocity Contours,
60.5° Inflow,
Disturbance Removed,
Case 4a, t = 40.
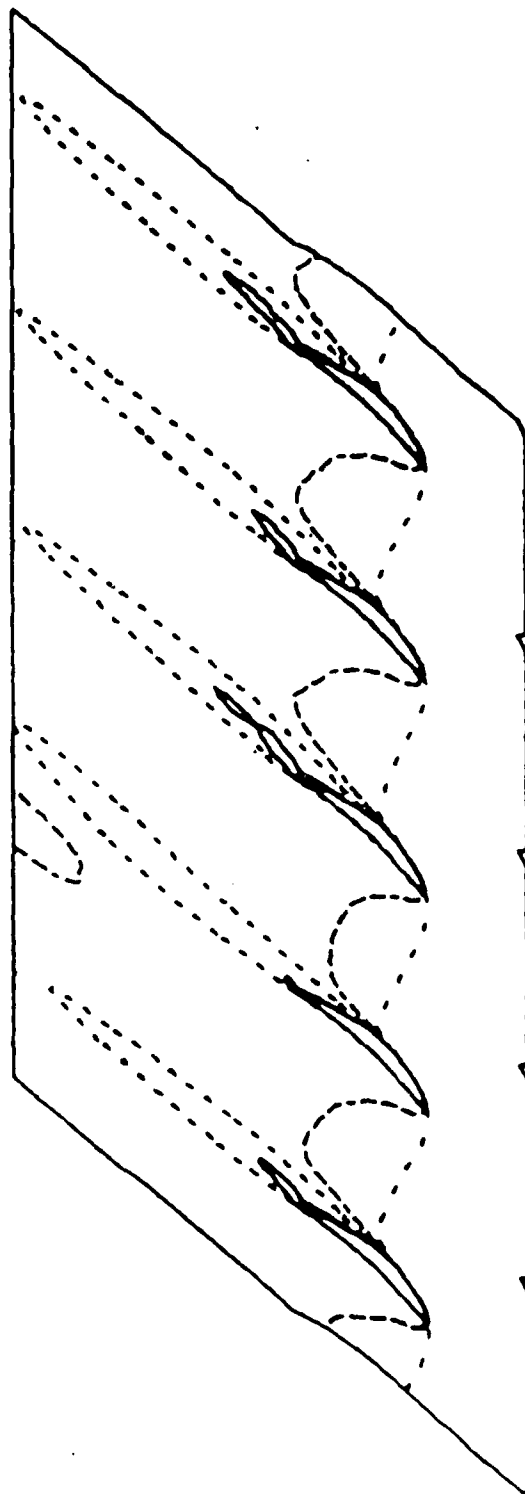
Fig. 46h. W-Velocity Contours,
60.5° Inflow,
Disturbance Removed,
Case 4a, t = 40.

Fig. 46i. U-Velocity Contours,
60.5° Inflow,
Disturbance Removed,
Case 4a, t = 44

Fig. 46j. W-Velocity Contours,
60.5° Inflow,
Disturbance Removed,
Case 4a, t = 44

Fig. 46k. U Velocity Contours,
60.5° Inflow,
Disturbance Removed,
Case 4a, t = 48.

Fig. 46l. W-Velocity Contours,
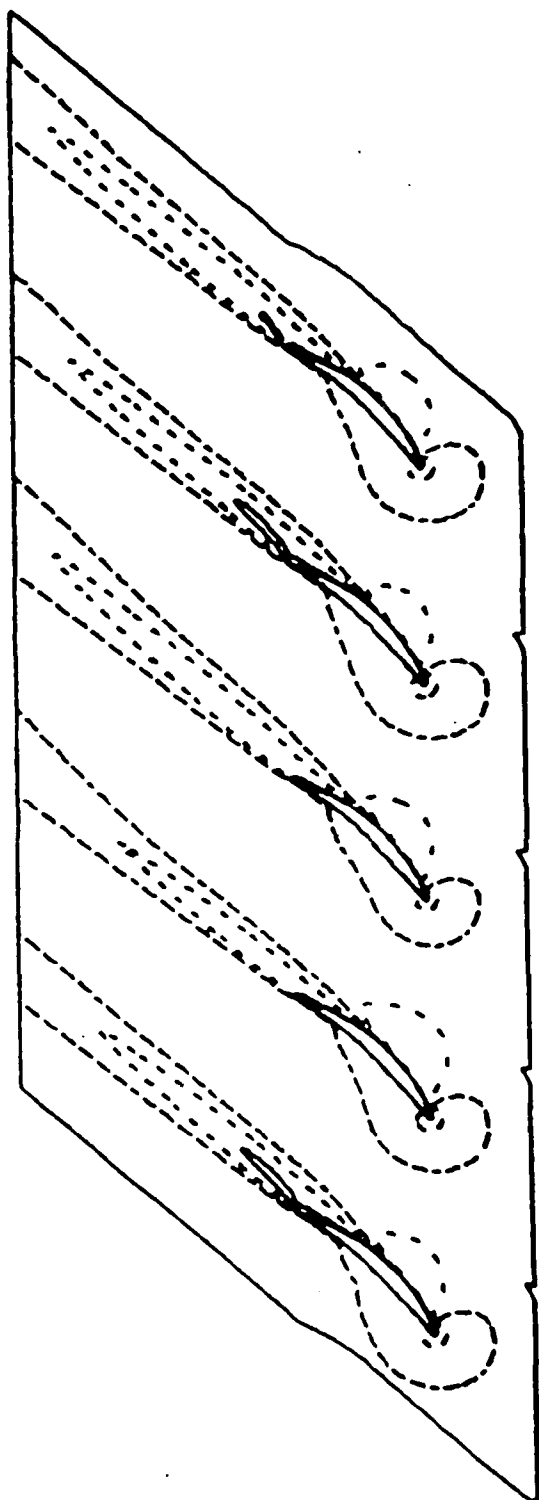60.5° Inflow,
Disturbance Removed,
Case 4a, t = 48.

Fig. 46m. U-Velocity Contours,
           60 5° Inflow,
           Disturbance Removed,
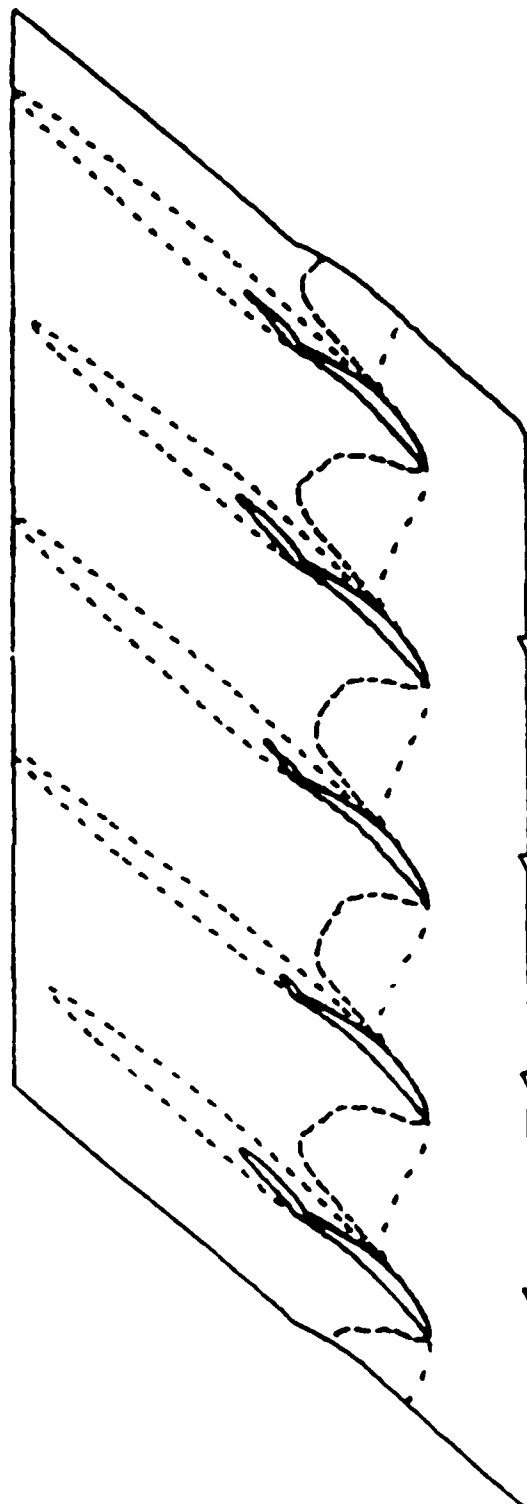   Case 4a, t = 52

Fig. 46n. W-Velocity Contours,
           60.5° Inflow,
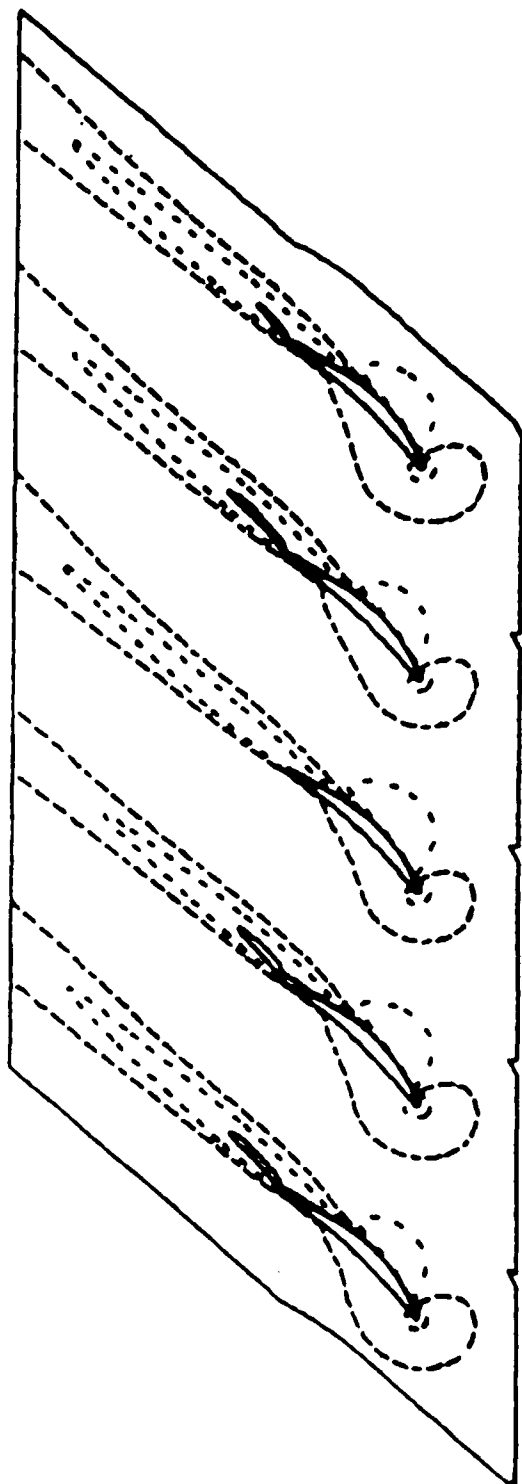   Disturbance Removed,
           Case 4a, t = 52

Fig. 46o. U-Velocity Contours,
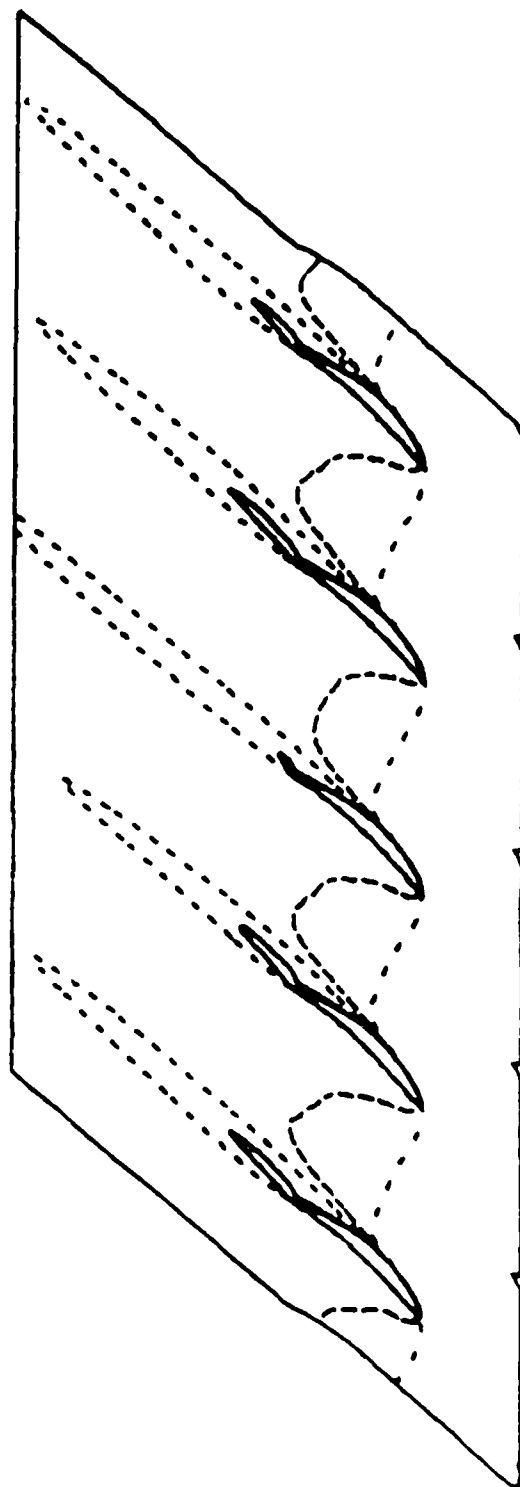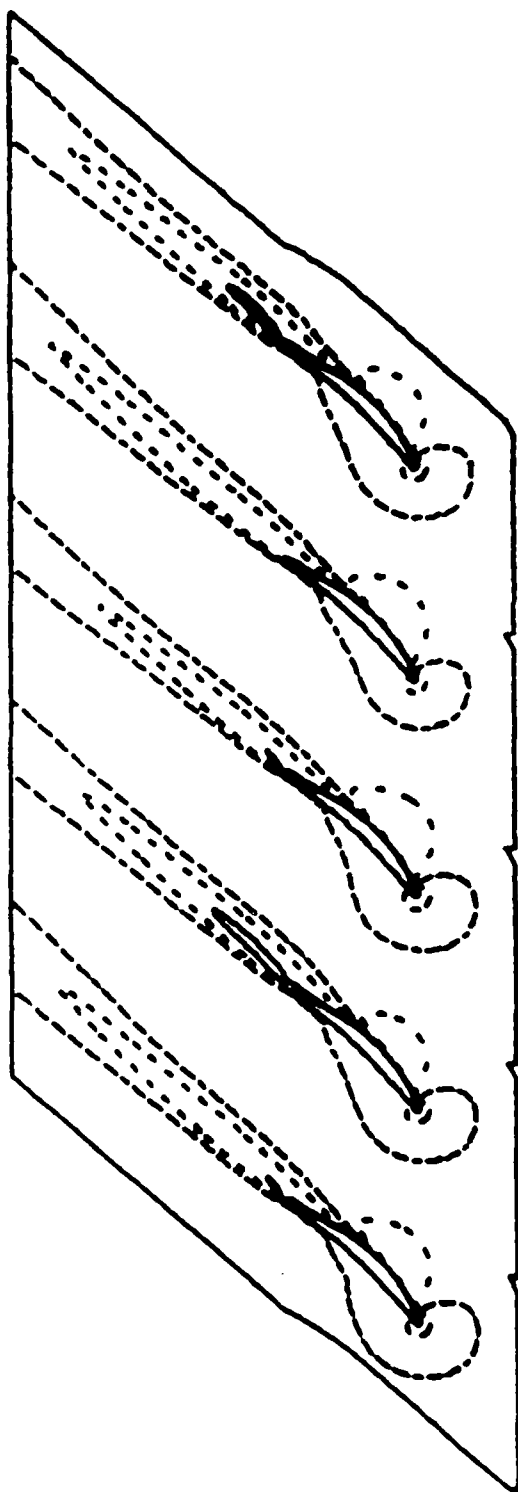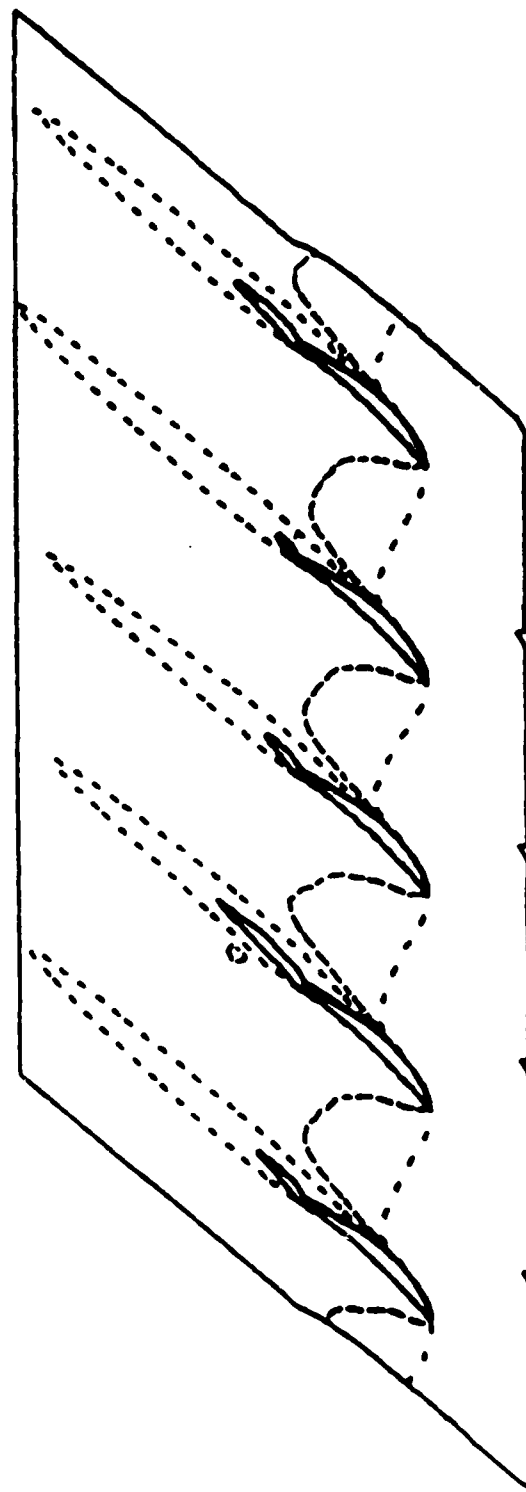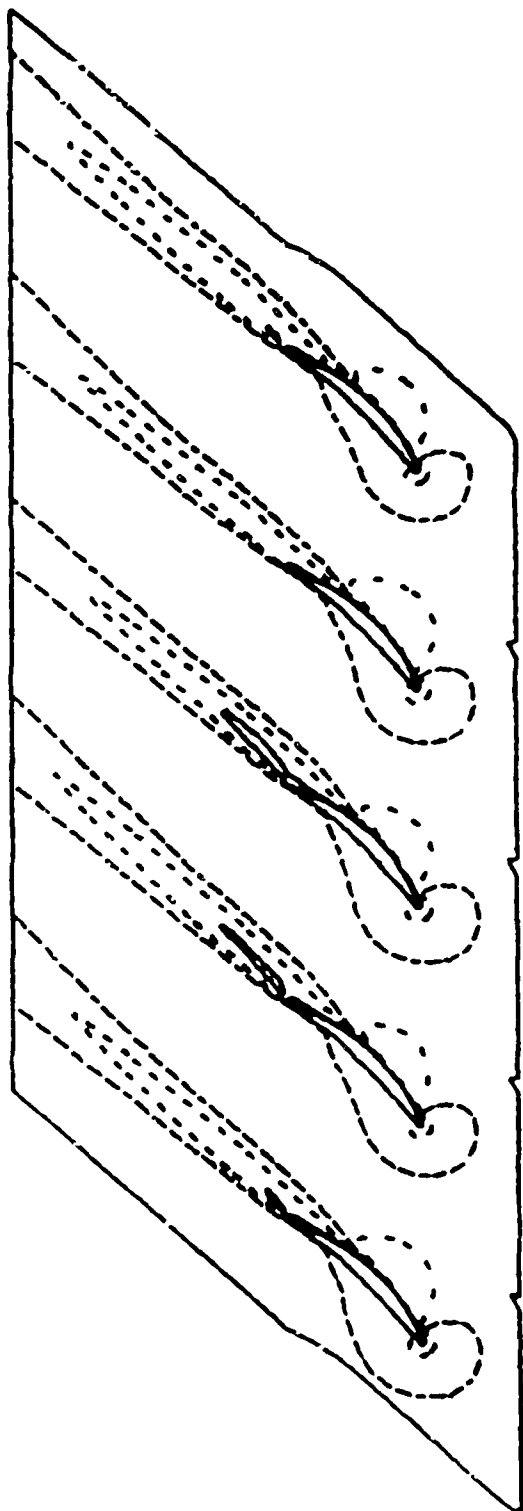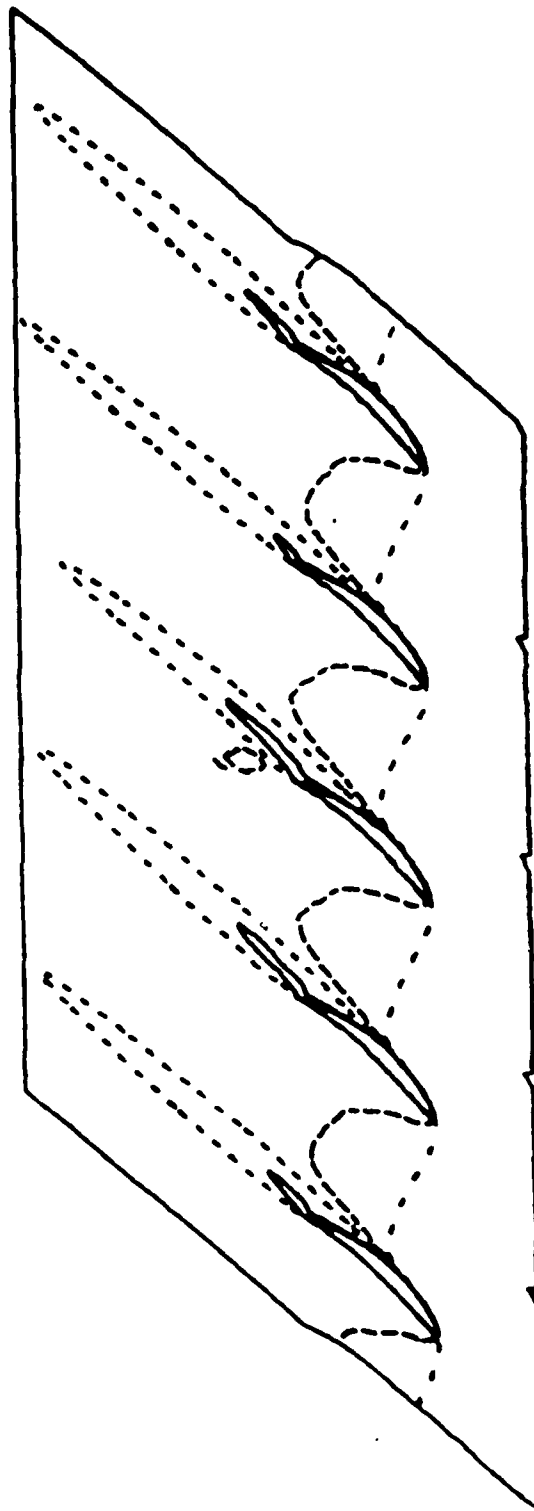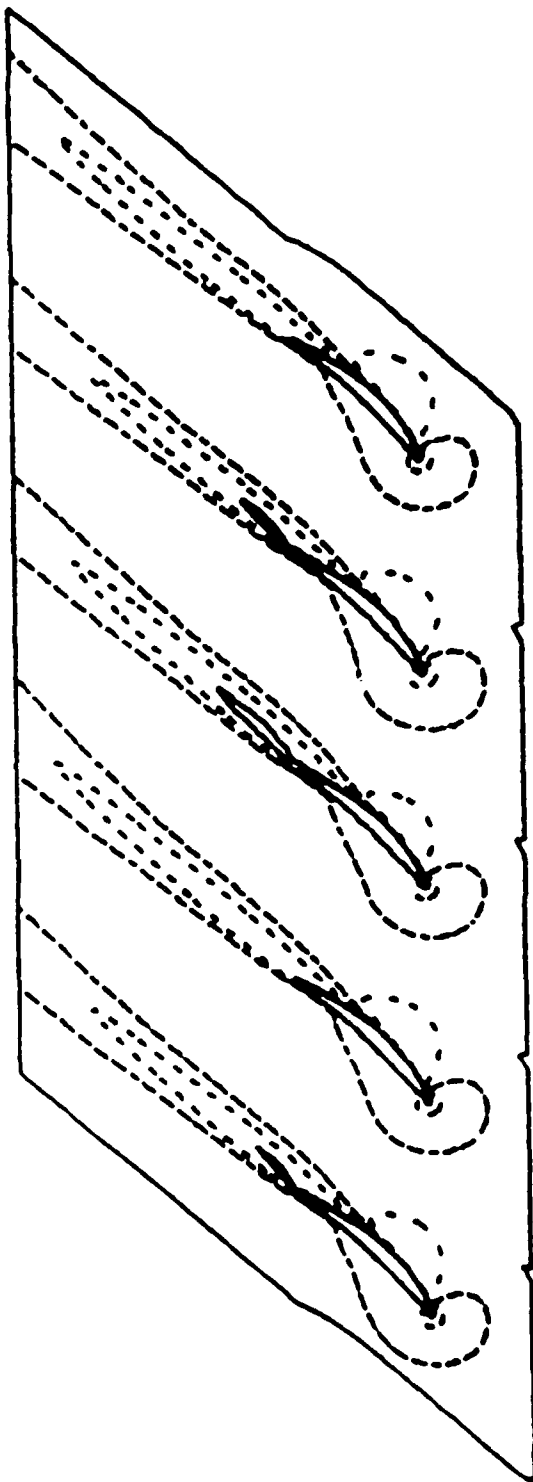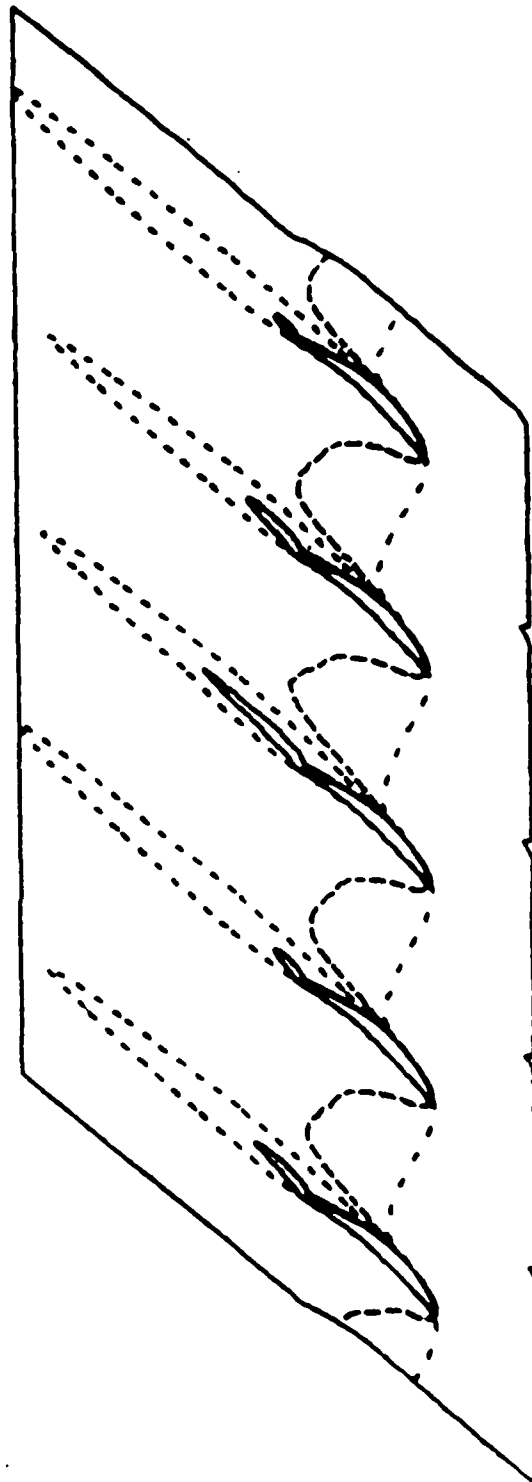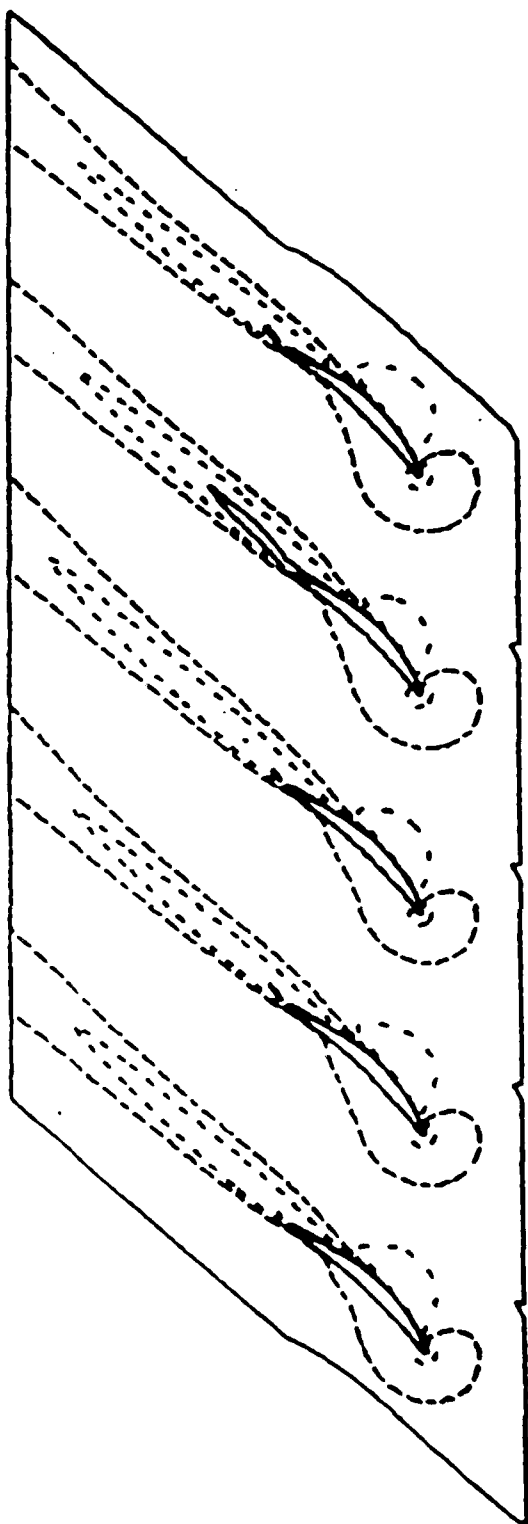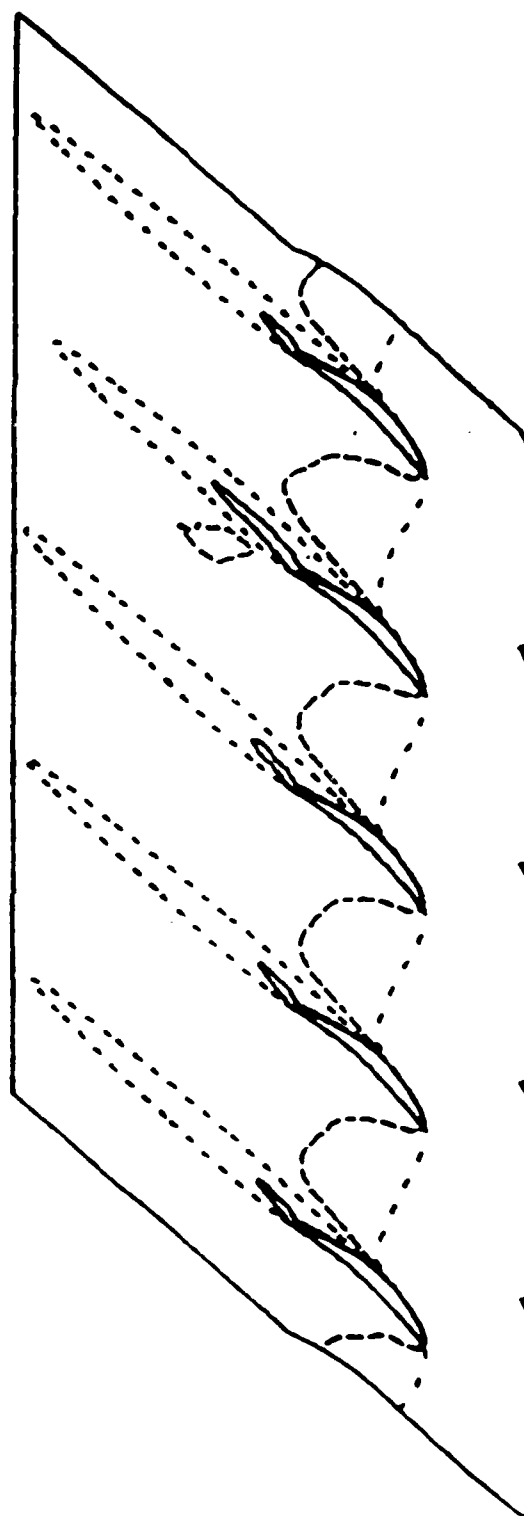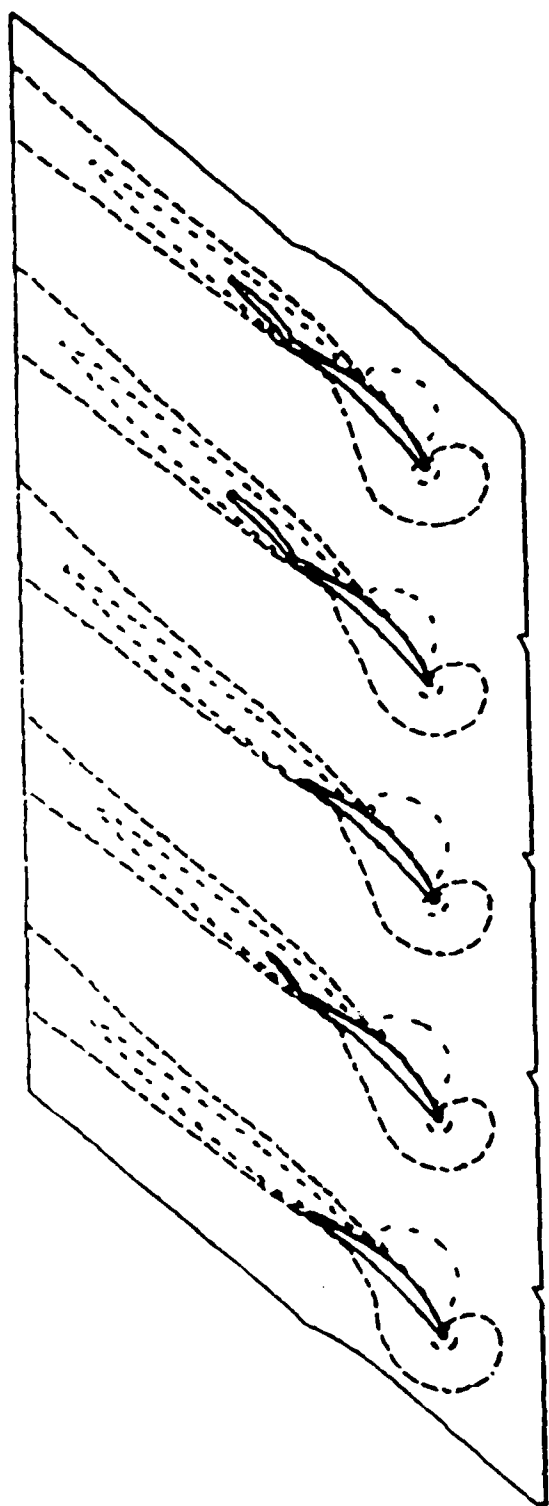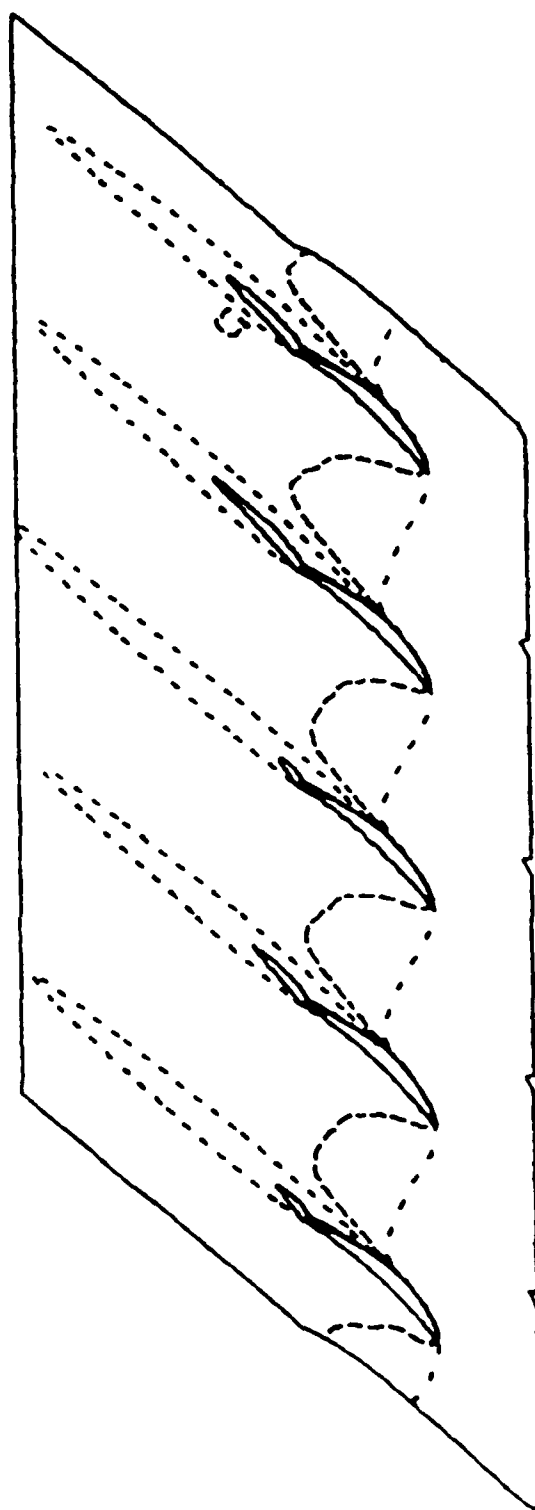60.5° Inflow,
Disturbance Removed,
Case 4a, t = 56.

Fig. 46p. W-Velocity Contours,
60.5° Inflow,
Disturbance Removed,
Case 4a, t = 56.

-196-

The calculation was run for nearly two cycles. Rather than continue this case, two other cases were run at the same flow conditions but with different initial disturbances. This was done to ascertain the dependence of the developed flow on the initial disturbance and in particular to try to reinforce the initial disturbance so as to obtain a single coherent propagating pattern. One of the cases, Case 4b, was continued for more than three cycles of propagation. These other two cases are now described.

Case No. 4b - 60.5°

As previously discussed, Case 4a showed development of a propagating stall region, however, an unchanging coherent pattern was not obtained. In Case 4b, the initial disturbance was reinforced at time t = 24.0, by removing the wall blowing in the second passage and introducing wall blowing in the fourth passage. The fourth passage wall blowing was maintained for 8 units of time and then was removed at t = 32.0. The flow field at t = 24.0, which was the last time step having second passage wall blowing, is given in Figs. 47a and 47b. At this time, passages 2 through 5 show some separation due to the passage number 2 disturbances, whereas the effect of this disturbance is to unload the first blade and have this passage flowing without separation.

The flow pattern at t = 32.0, which is eight time units after the jet has been removed from the second blade and imposed on the fourth blade, is shown in Figs. 47c and 47d. As can be seen, the separation zone has been strengthened considerably and is particularly strong at the fourth passage. The disturbance then is removed; results at successive times are presented in Figs. 47e-47rr. As can be seen, the separated flow region propagates from blade to blade for approximately three complete cycles, where each cycle represents propagation through the entire computational domain. For example, Figs. 47q and 47r (t = 60) represent an approximate cycle of propagation past the flow represented at Figs. 47e and 47f. It should be noted that at 60.5°, Case 4b conditions, the disturbance continues to propagate with undiminished strength. This clearly shows a rotating stall behavior. In addition, the pattern remained essentially identical as it propagated, in contrast to the changing propagating pattern of Case 4a.

To show a more complete picture of the flow at a specific instance of time, static pressure contours and velocity vector plots at t = 76.0 are given

Fig. 47a. U-Velocity Contours,
60.5° Inflow,
Disturbance on Blade
No. 2, t=24.

Fig. 47b. W-Velocity Contours,
60.5° Inflow,
Disturbance on Blade
No. 2, t = 24.

Fig. 47c. U-Velocity Contours,
60.5° Inflow,
Disturbance on Blade
No. 4, t = 32.

Fig. 47d. W-Velocity Contours,
60.5° Inflow,
Disturbance on Blade
No. 4, t = 32

Fig. 47e. U-Velocity Contours,
60.5° Inflow,
Disturbance Removed,
τ = 76

Fig. 47f. W-Velocity Contours,
60.5° Inflow,
Disturbance Removed,
τ = 76

Fig. 47g   U-Velocity Contours,
           60.5° Inflow,
           Disturbance Removed,
           t = 40.

Fig. 47h. W-Velocity Contours,
           60.5° Inflow,
           Disturbance Removed,
           t = 40.

Fig. 47i. U-Velocity Contours,
60.5° Inflow,
Disturbance Removed,
t = 44

Fig. 47j. W-Velocity Contours,
60.5° Inflow,
Disturbance Removed,
t = 44.

Fig. 47k. U-Velocity Contours,
60.5° Inflow,
Distu bance Removed,
r = 4P

Fig. 47l. W-Velocity Contours,
60.5° Inflow,
Disturbance Removed,
r = 4P

-113-
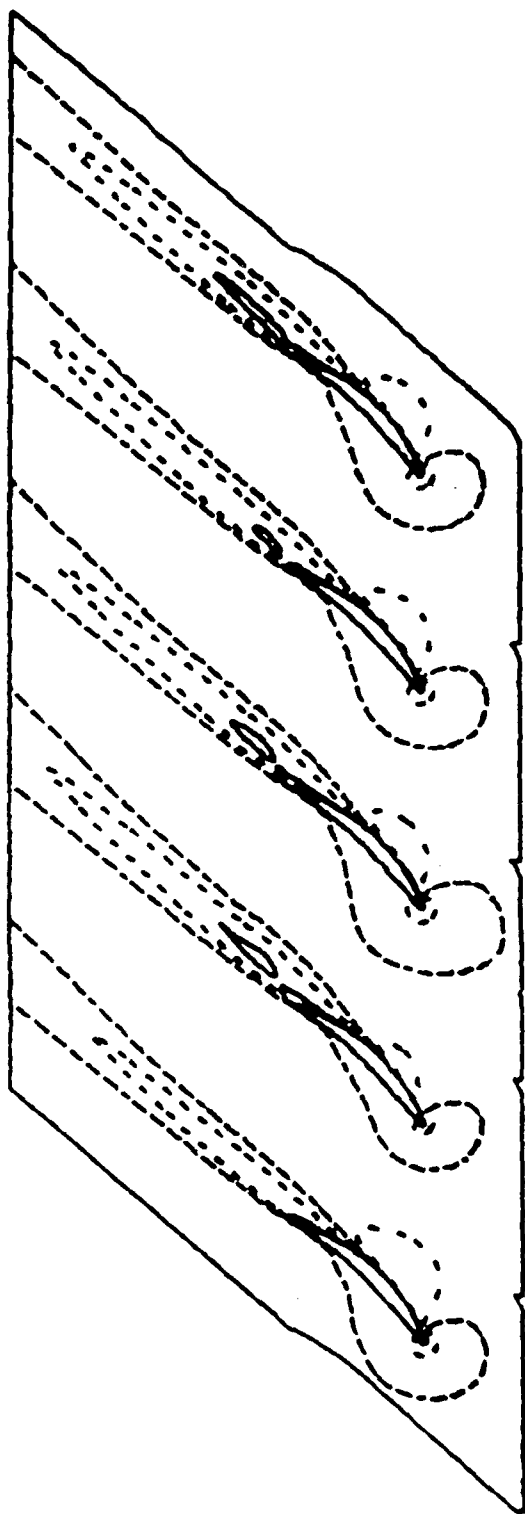
Fig. 47m   U-Velocity Contours,
           60.5° Inflow,
           Disturbance Removed,
           t = 5?

Fig. 47n. W-Velocity Contours,
           60.5° Inflow,
           Disturbance Removed,
           t = 52.

-114-

Fig. 47o   U-Velocity Contours,
            60.5° Inflow,
            Disturbance Removed,
            t = 56.
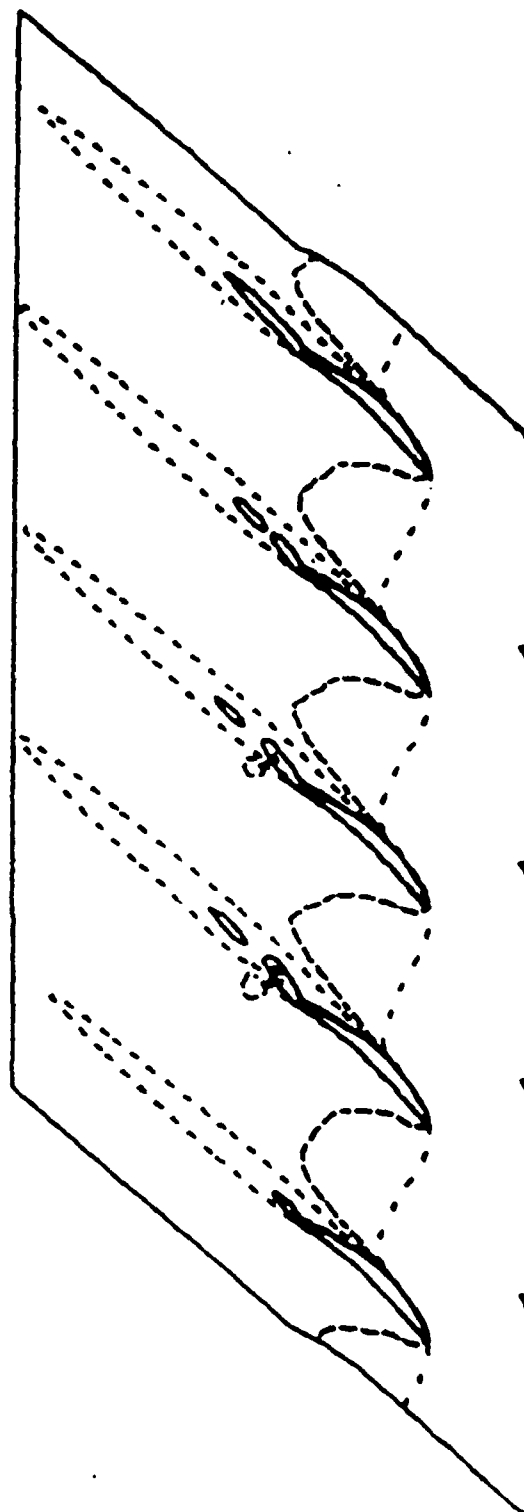
Fig. 47p.   W-Velocity Contours,
            60.5° Inflow,
            Disturbance Removed,
            t = 56.

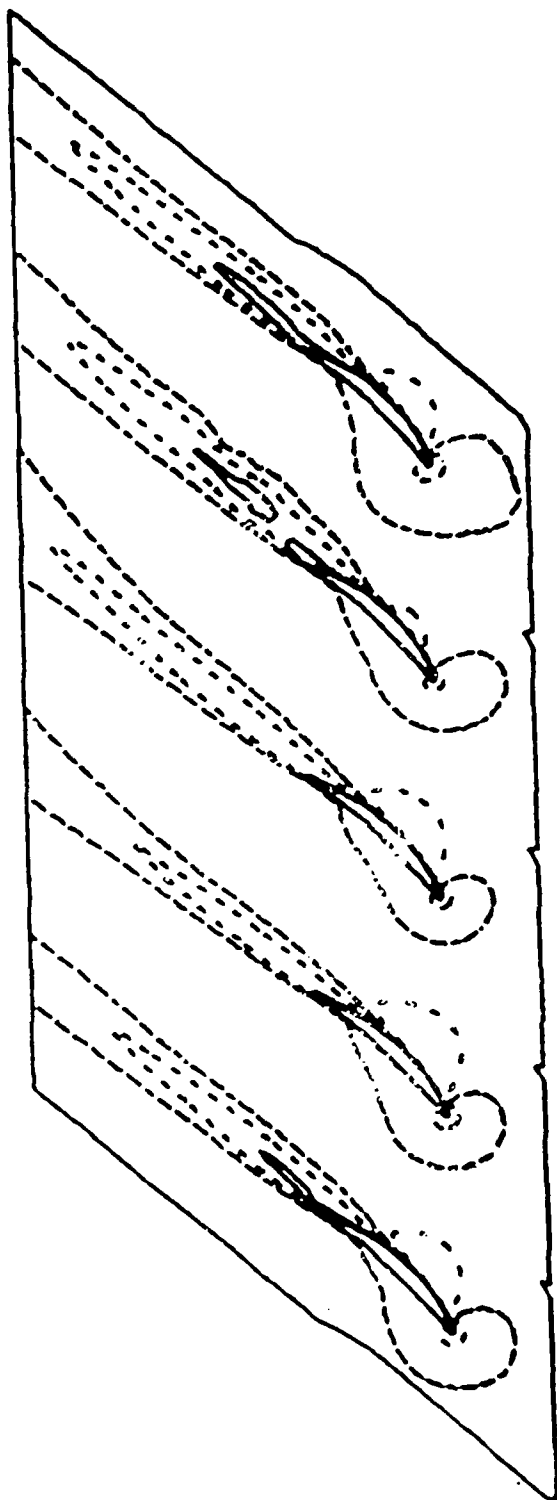Fig. 47q   U-Velocity Contours,
           60.5° Inflow,
           Disturbance Removed,
           t = 0.
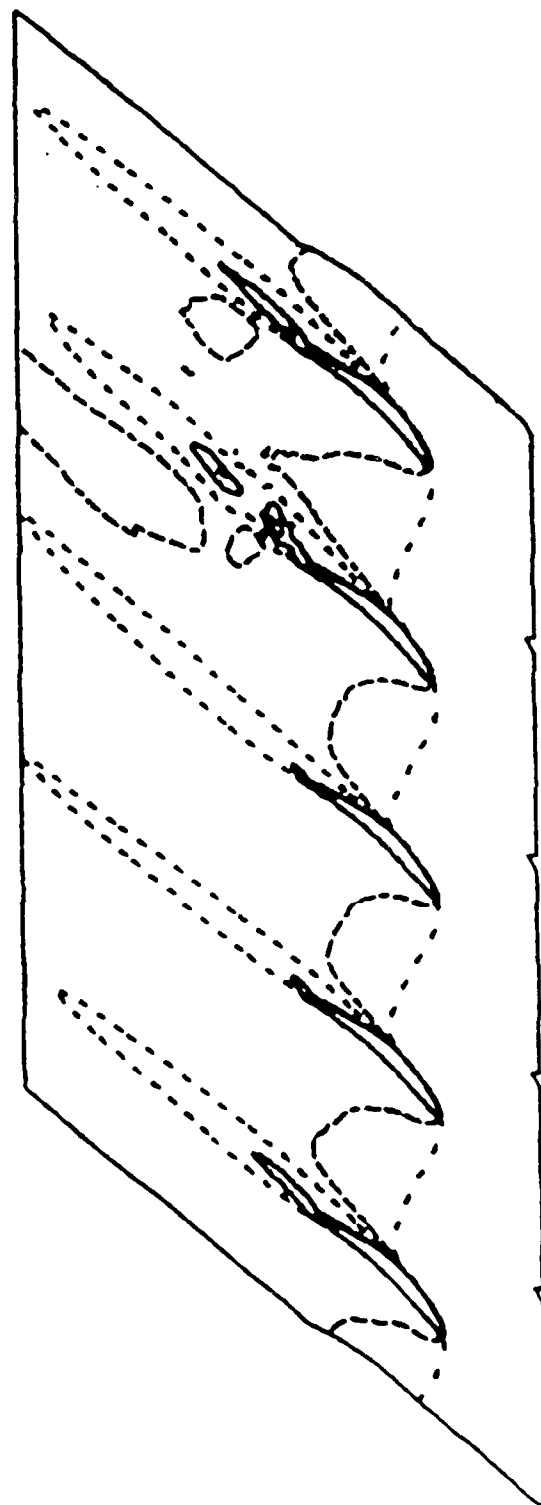
Fig. 47r.   W-Velocity Contours,
            60.5° Inflow,
            Disturbance Removed,
            t = 60.
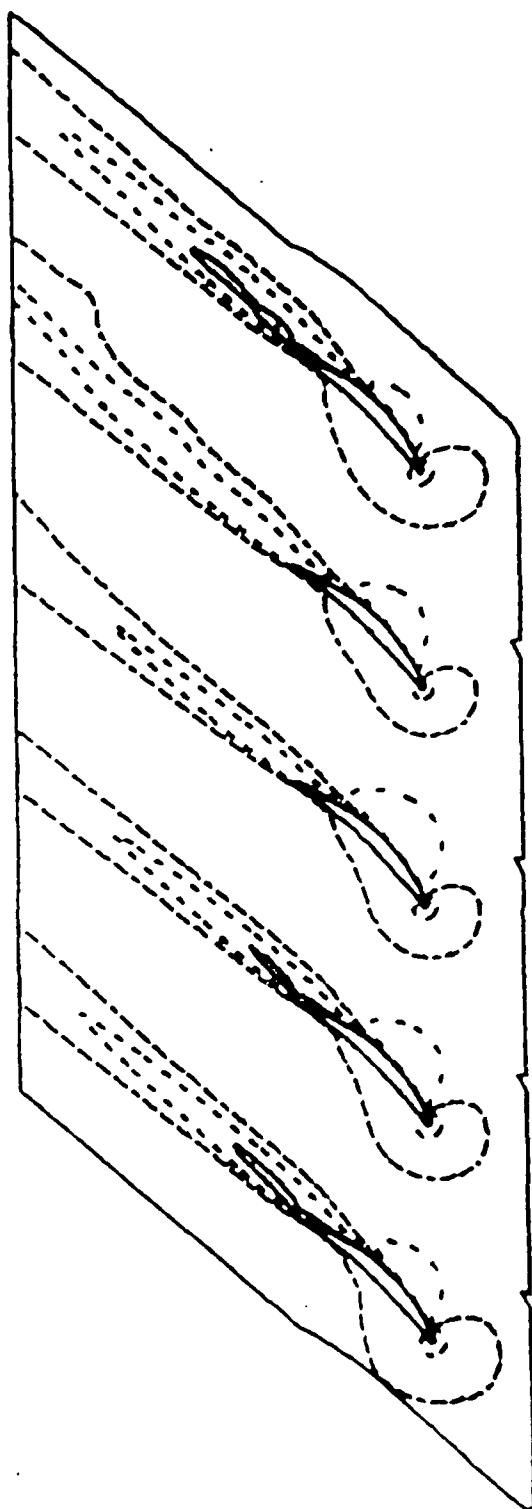
Fig. 47s. U-Velocity Contours,
60.5° Inflow,
Disturbance Removed,
t = 64
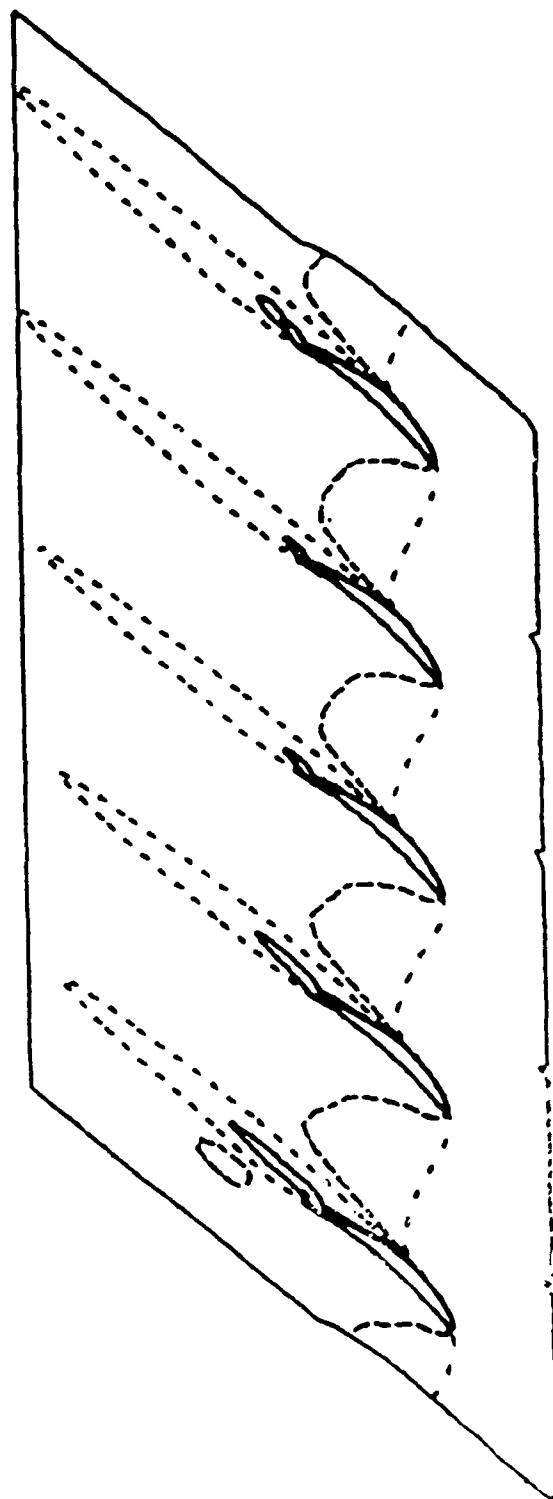
Fig. 47t. W-Velocity Contours,
60.5° Inflow,
Disturbance Removed,
t = 64.
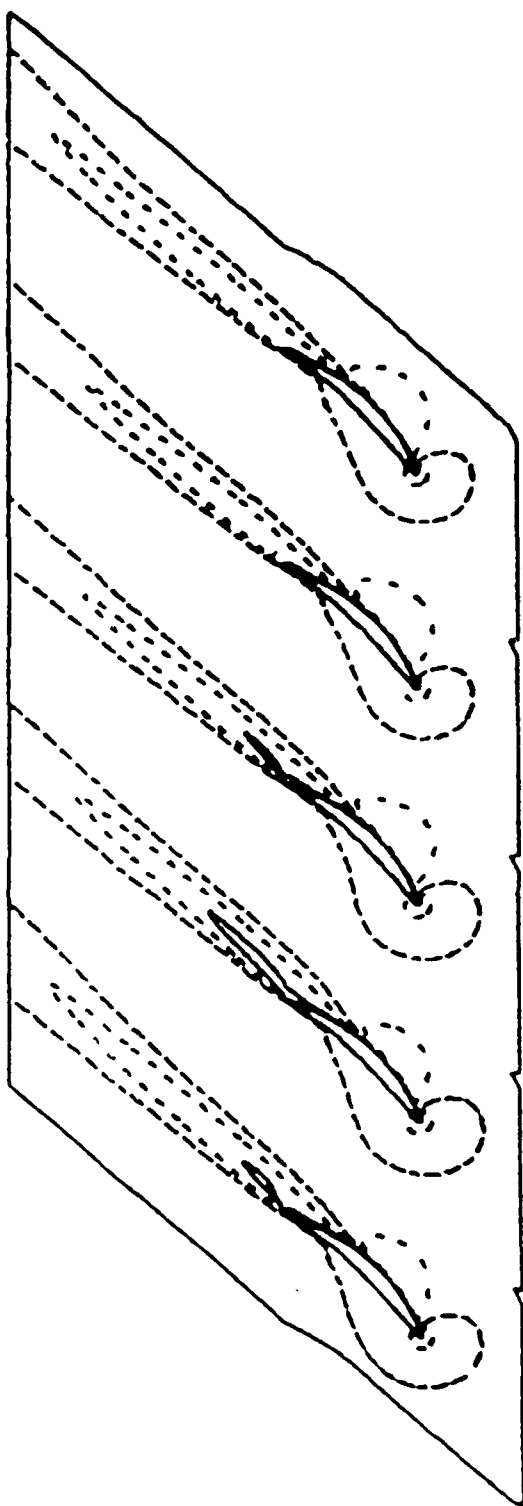
Fig. 47u. U-Velocity Contours,
           60.5° Inflow,
           Disturbance Removed,
           t = 68.
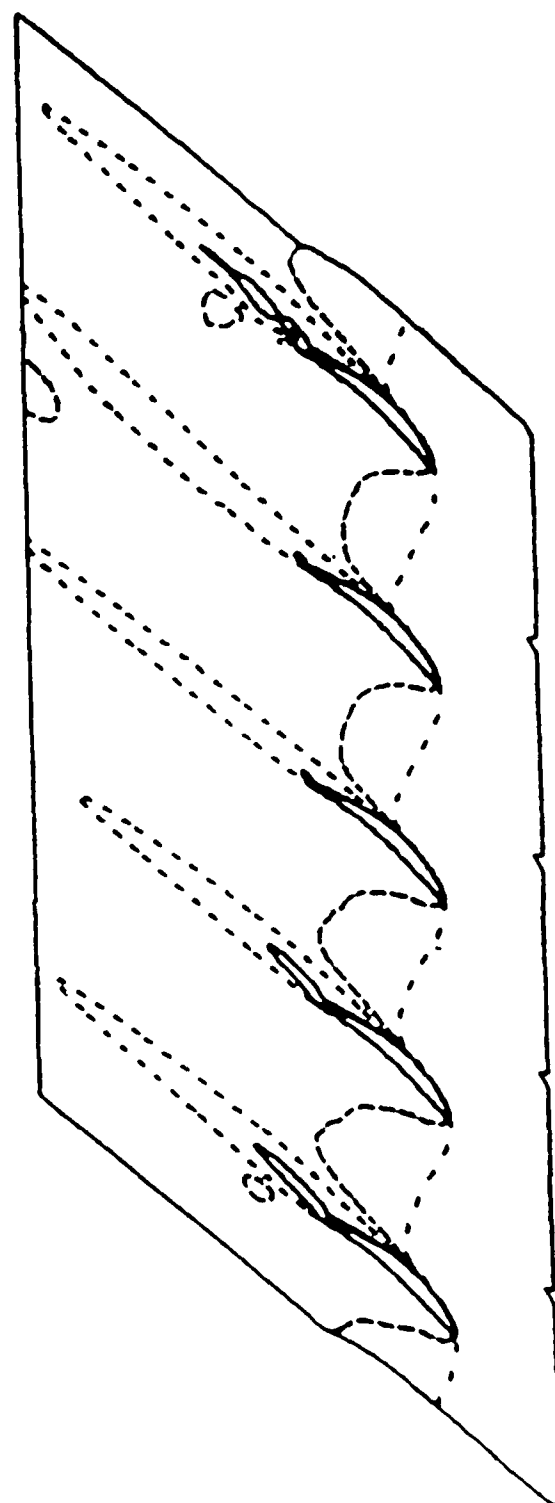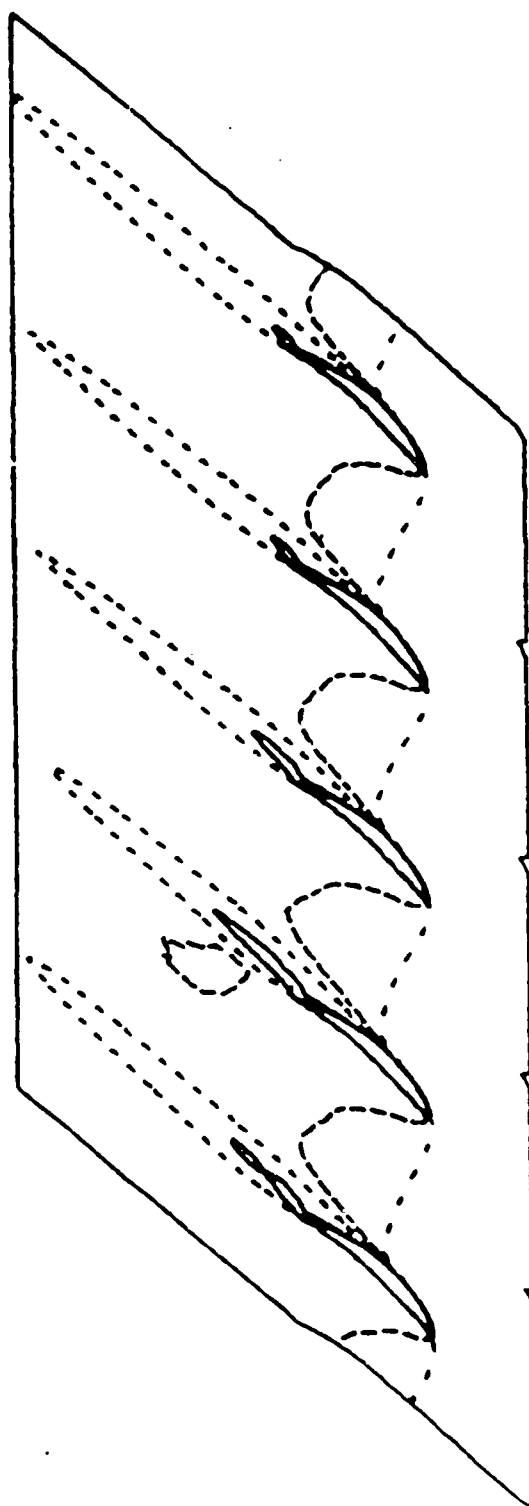
Fig. 47v. W-Velocity Contours,
           60.5° Inflow,
           Disturbance Removed,
           t = 68.
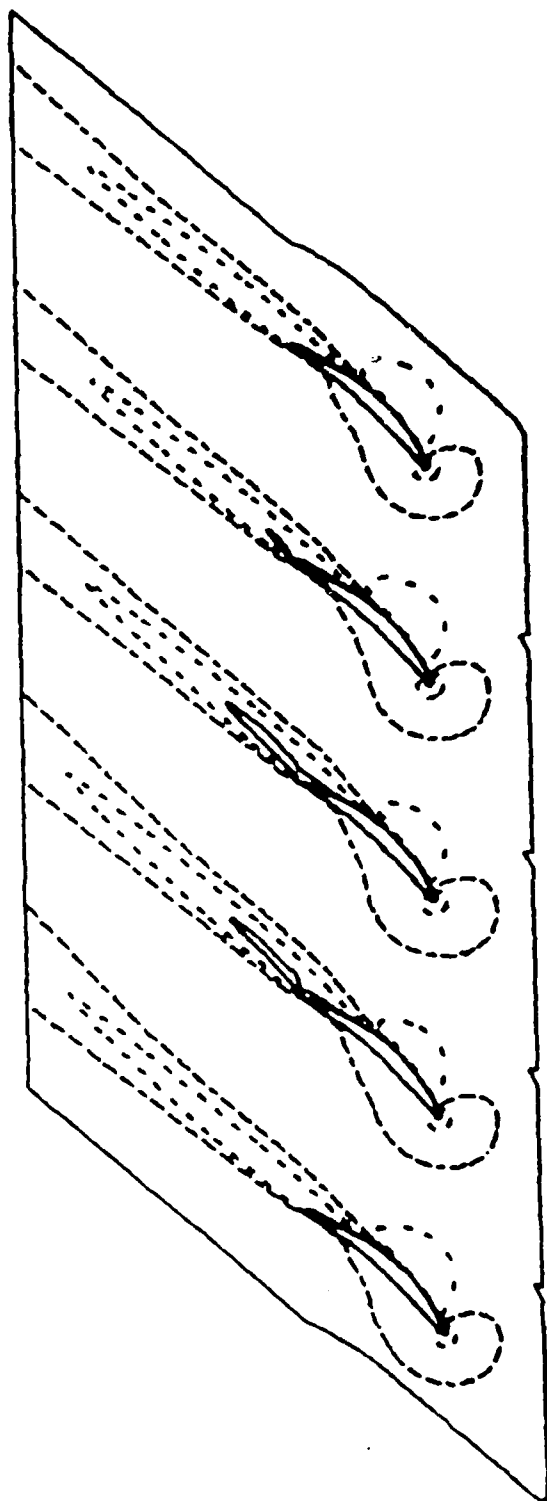
Fig. 47w.   U-Velocity Contours,
            60.5° Inflow,
            Disturbance Removed,
            t = 72.
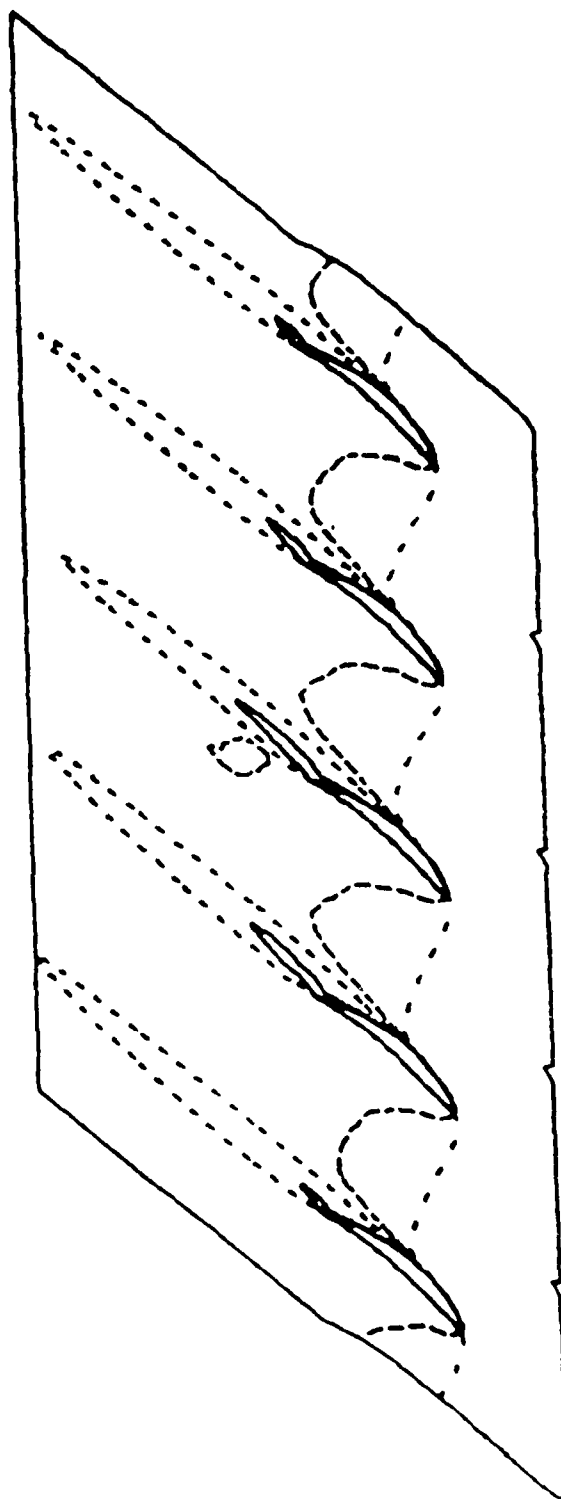
Fig. 47x.   W-Velocity Contours,
            60.5° Inflow,
            Disturbance Removed,
            t = 72.
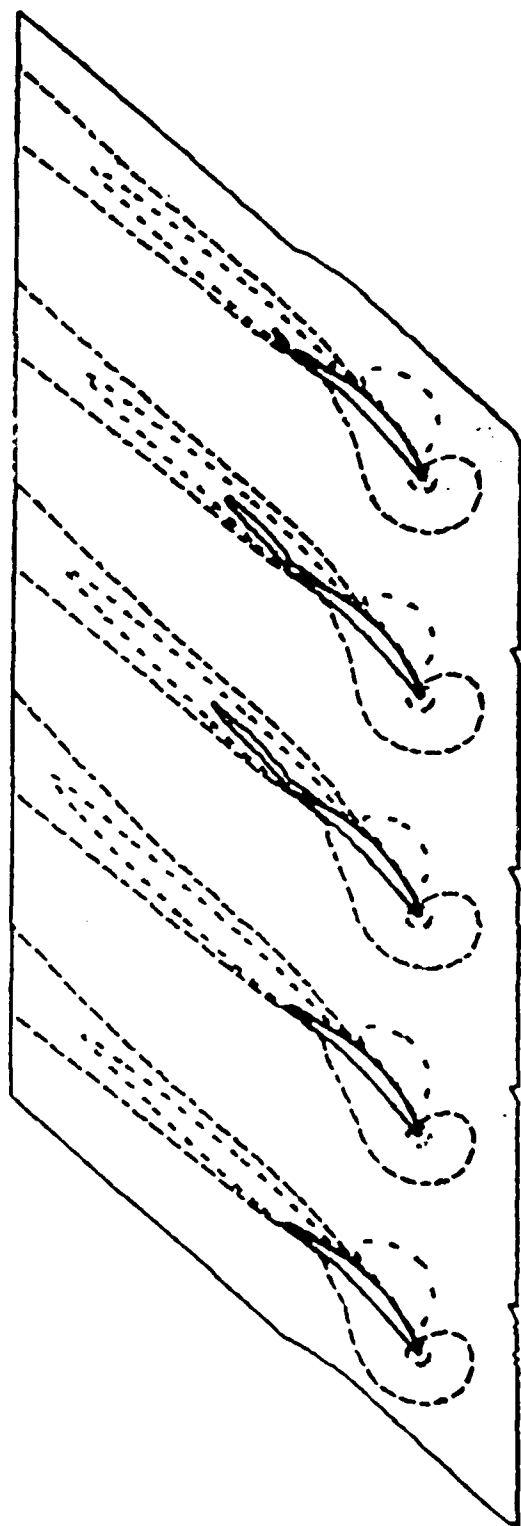
Fig. 47y. U-Velocity Contours,
60.5° Inflow,
Disturbance Removed,
t = 76.
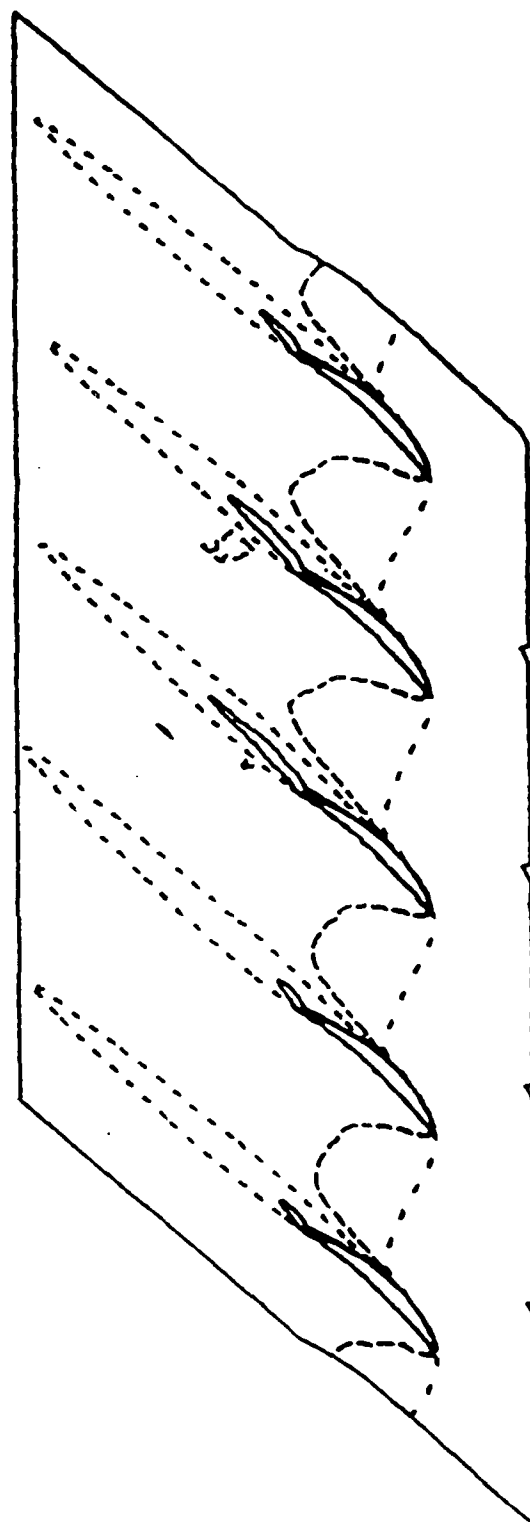
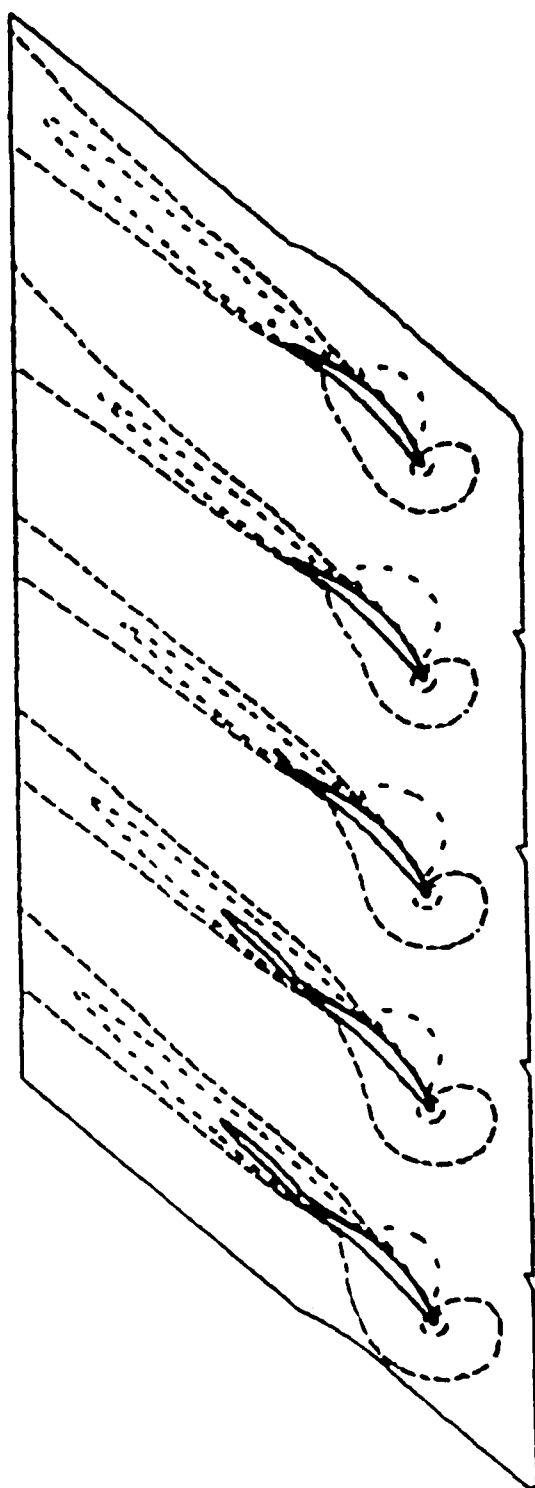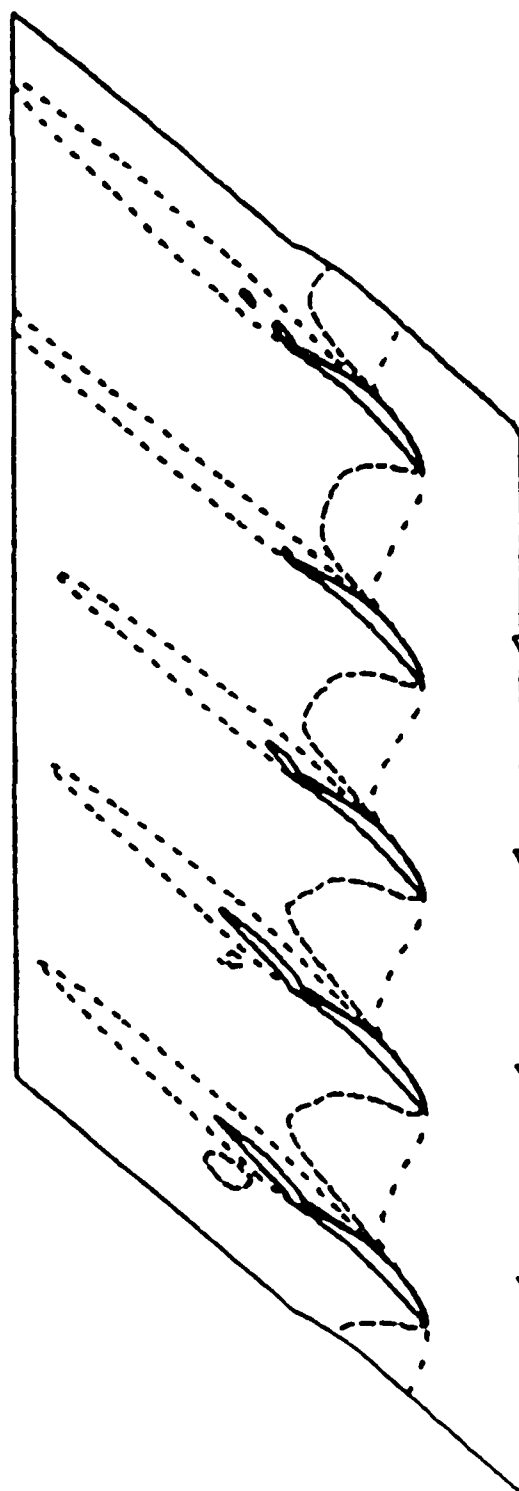Fig. 47z. W-Velocity Contours,
60.5° Inflow,
Disturbance Removed,
t = 76.
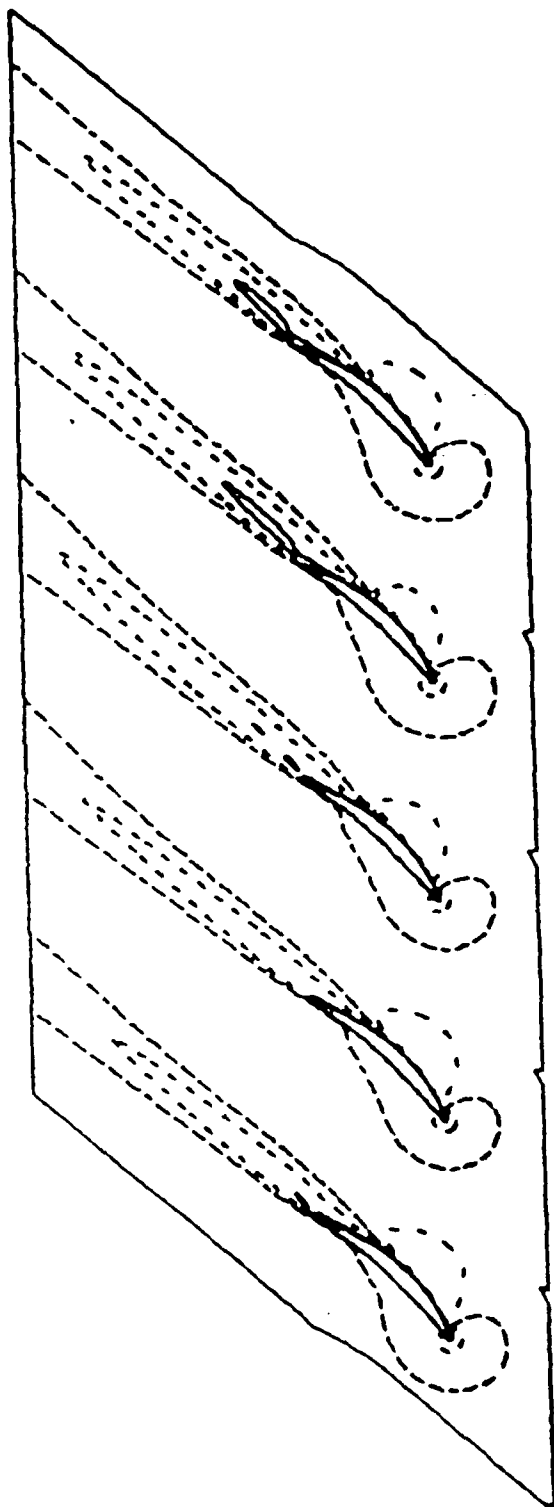
Fig. 47aa. U-Velocity Contours,
60.5° Inflow,
Disturbance Removed,
t = 80.
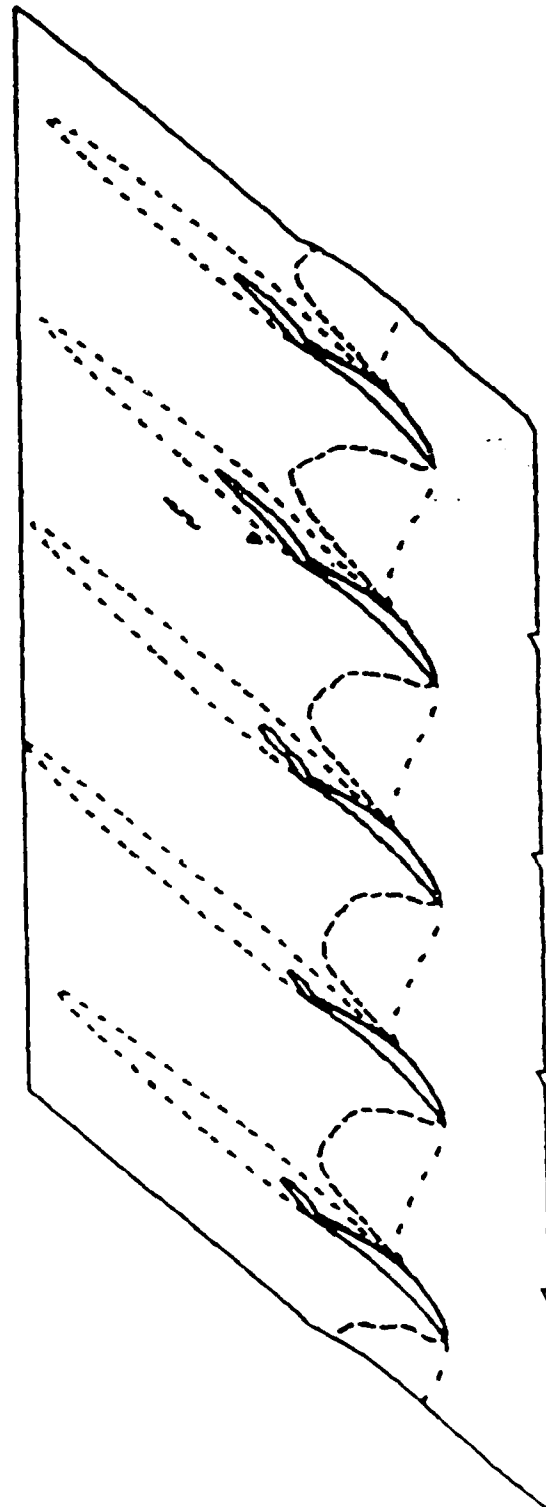
Fig. 47bb. W-Velocity Contours,
60.5° Inflow,
Disturbance Removed,
t = 80
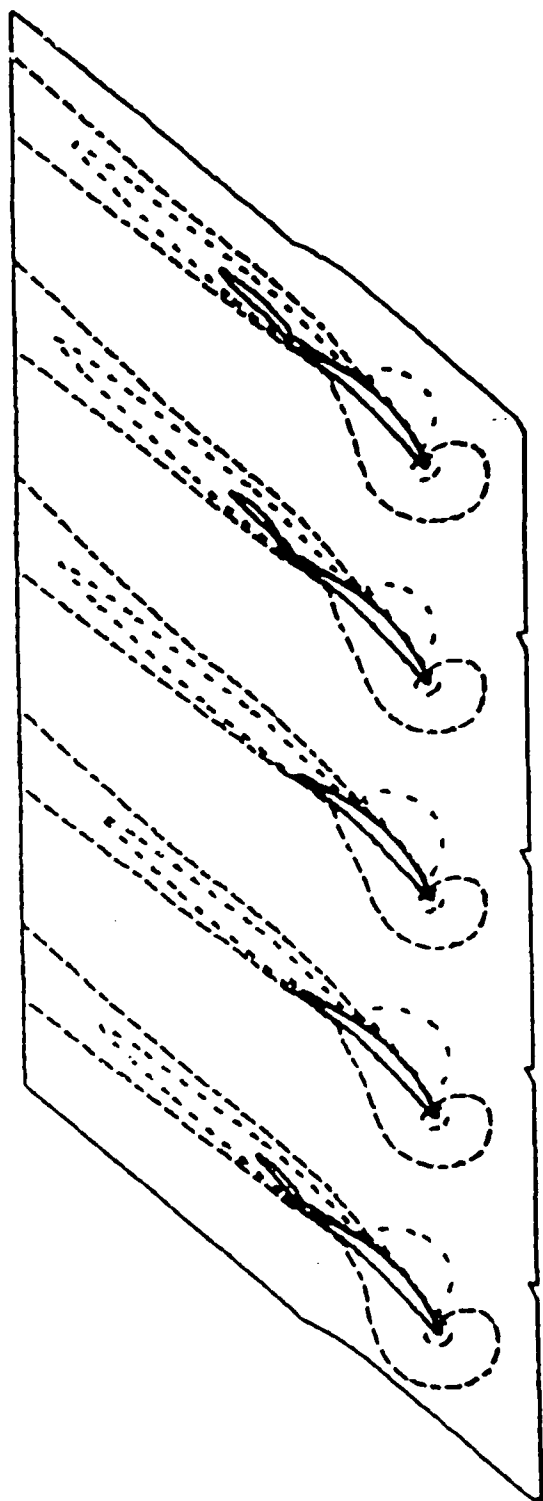
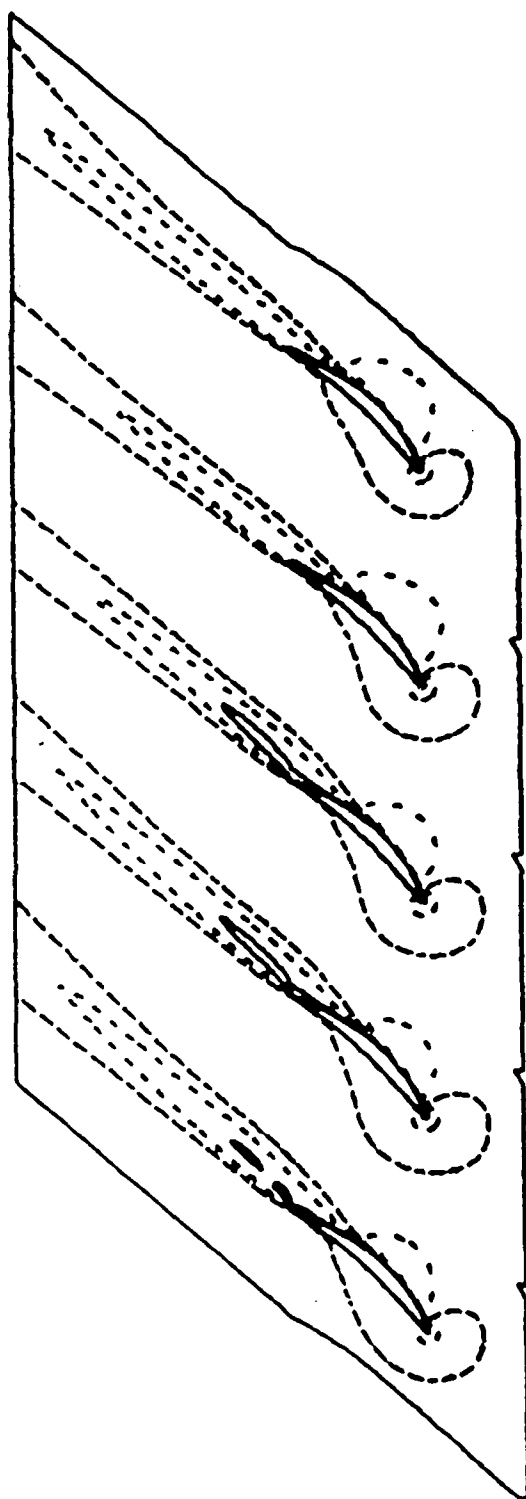Fig. 47cc. U-Velocity Contours,
            60.5° Inflow,
            Disturbance Removed,
            t   84.
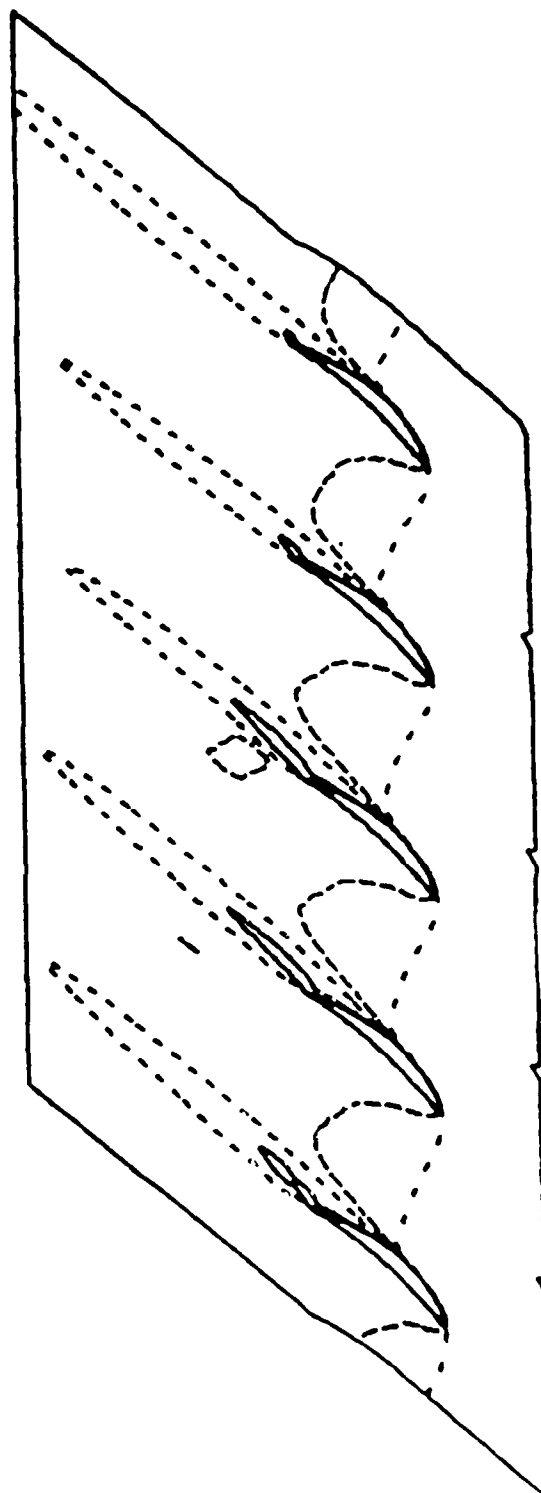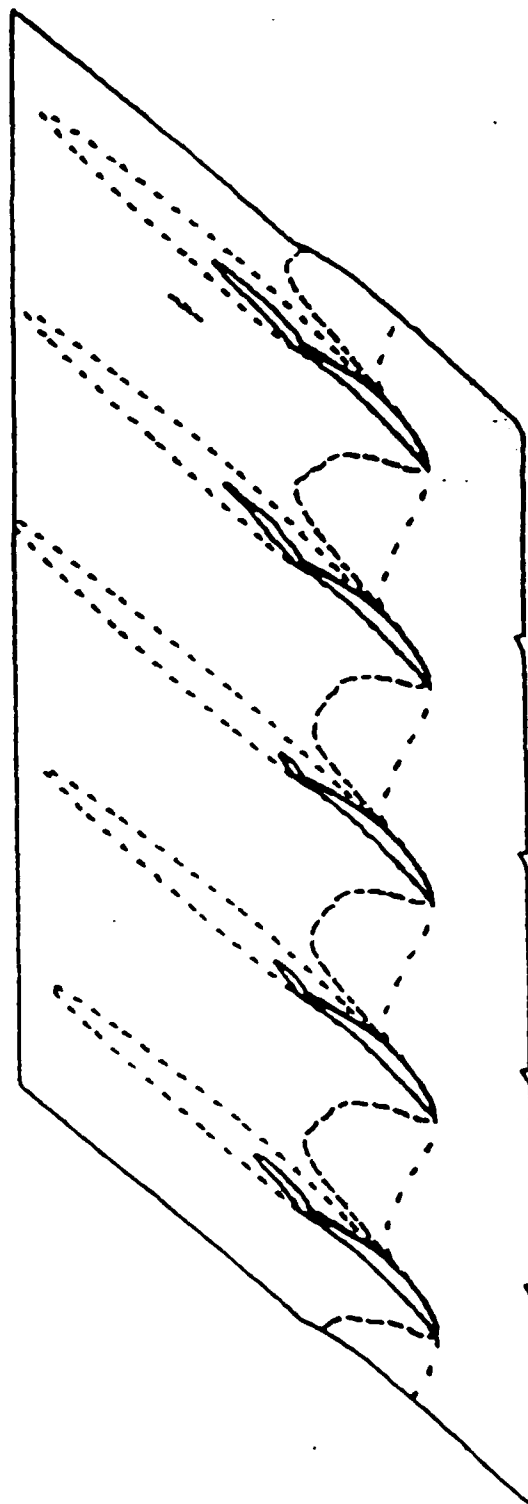
Fig. 47dd. W-Velocity Contours,
            60.5° Inflow,
            Disturbance Removed,
            t   84
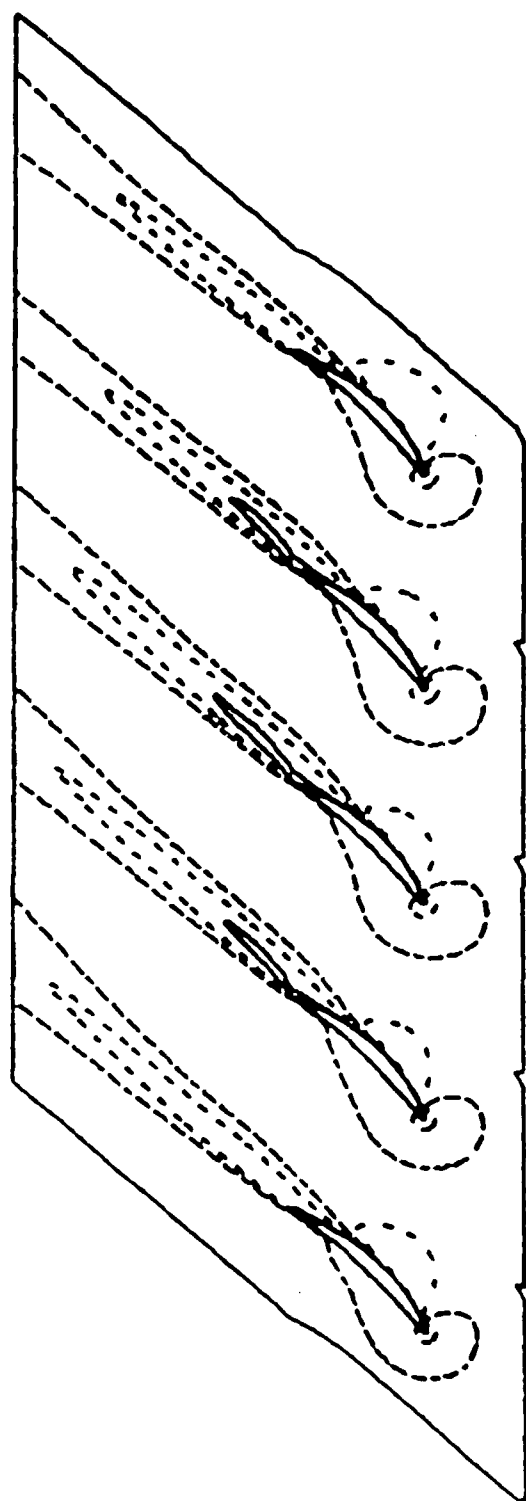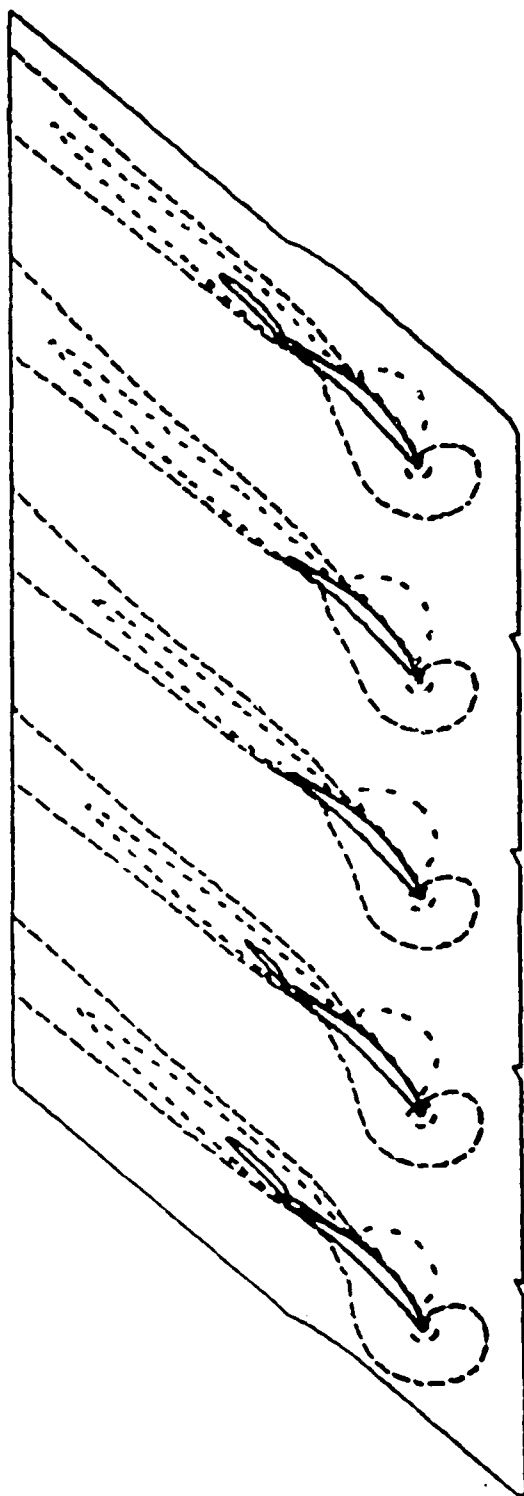
Fig. 47ee. U-Velocity Contours,
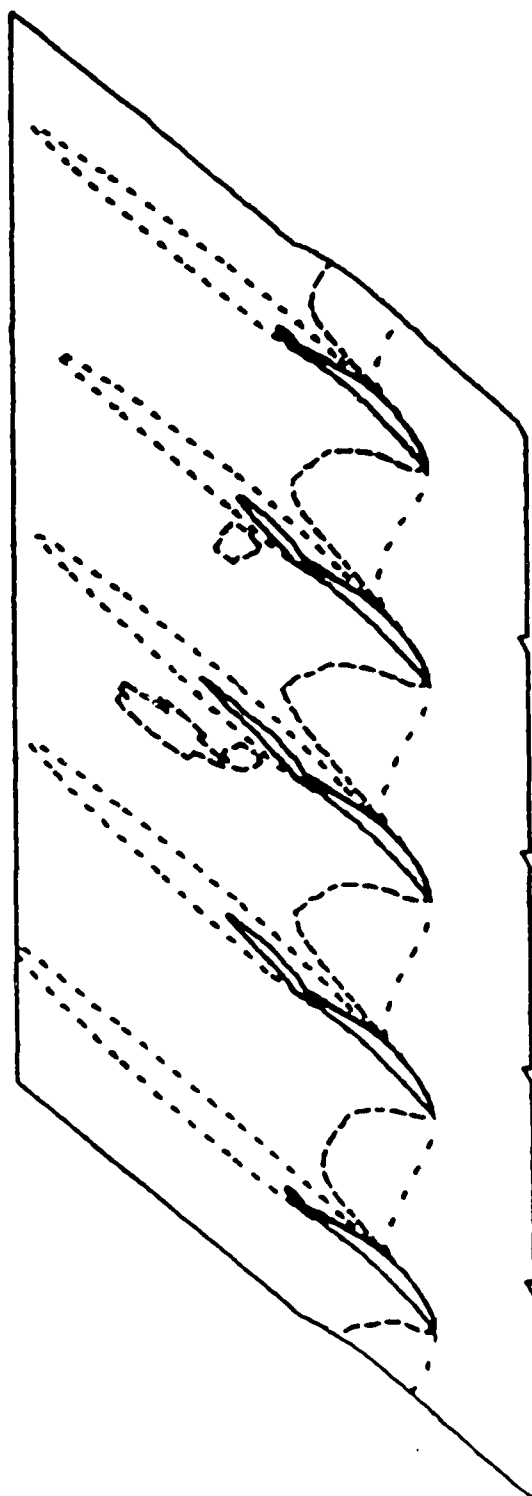60.5° Inflow,
Disturbance Removed,
t = 88.
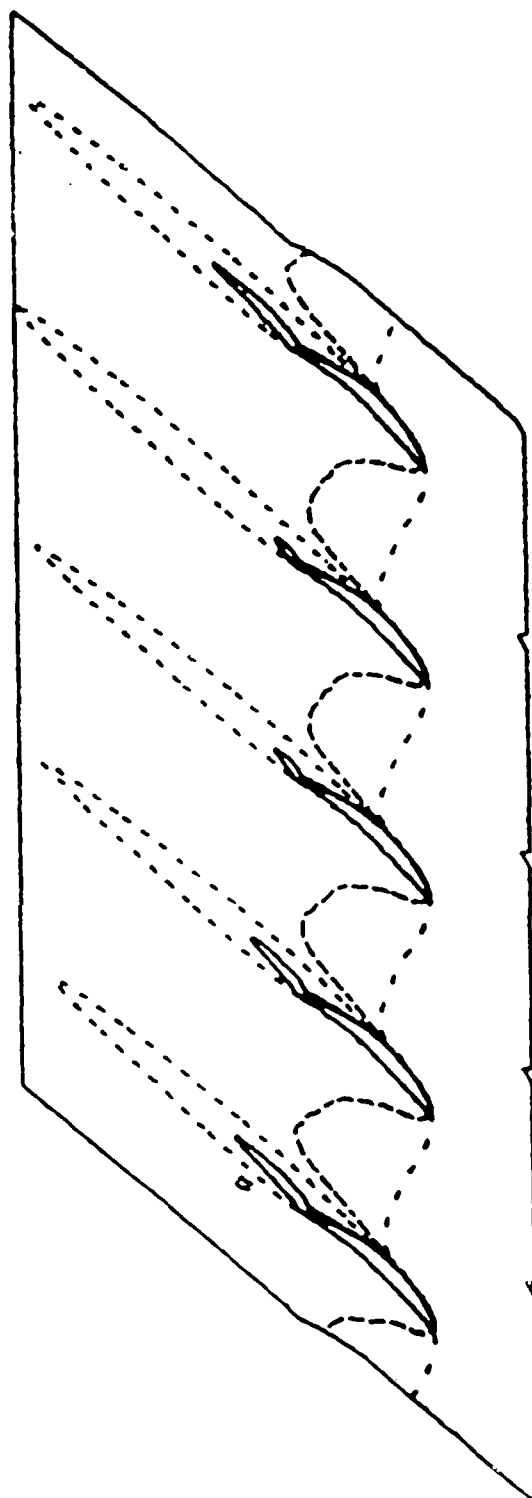
Fig. 47ff. W-Velocity Contours,
60.5° Inflow,
Disturbance Removed,
t = 88.
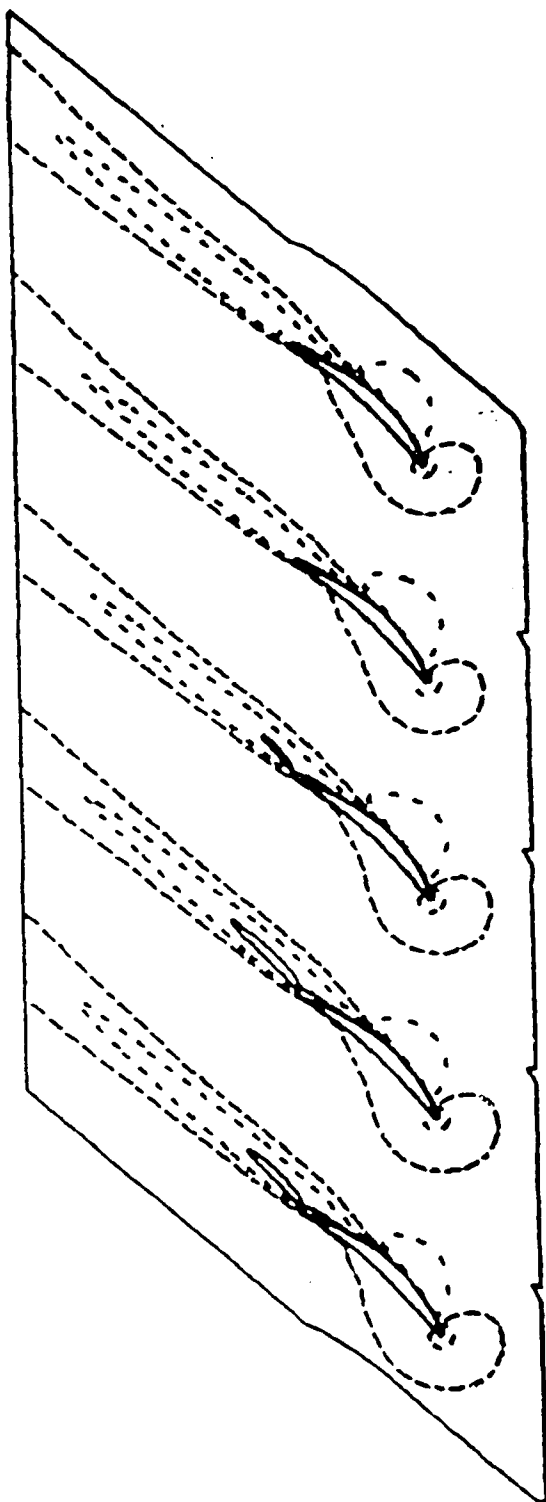
Fig. 47gg. U-Velocity Contours,
60.5° Inflow,
Disturbance Removed,
t = 92
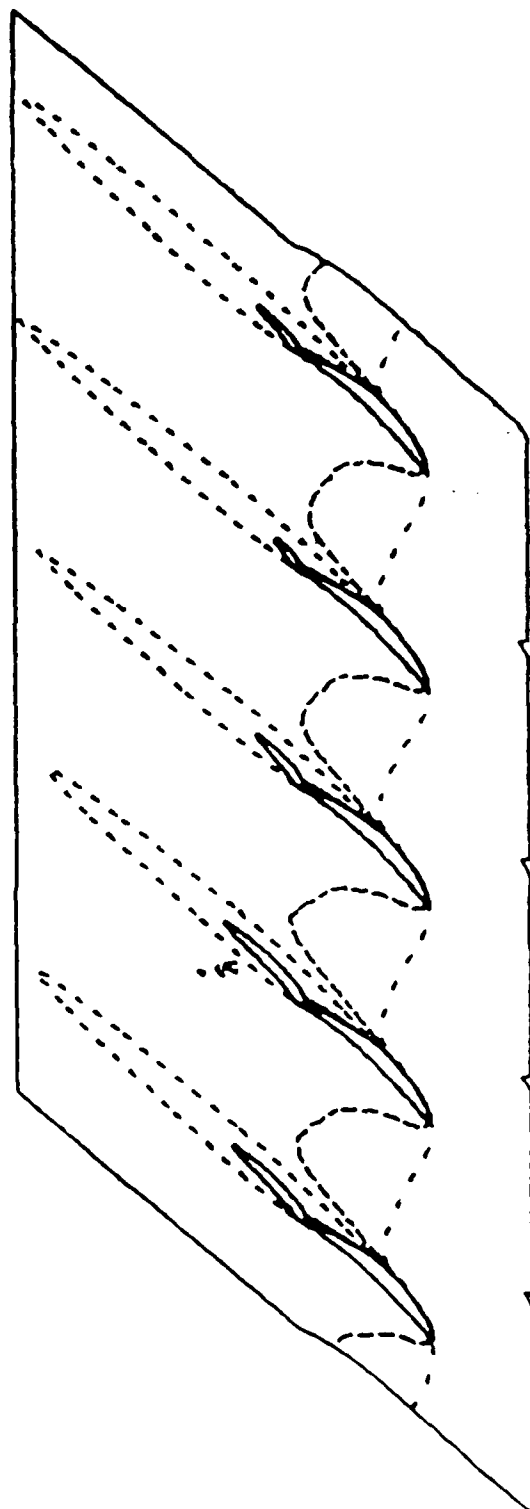
Fig. 47hh. W-Velocity Contours,
60.5° Inflow,
Disturbance Removed,
t = 92

-124-
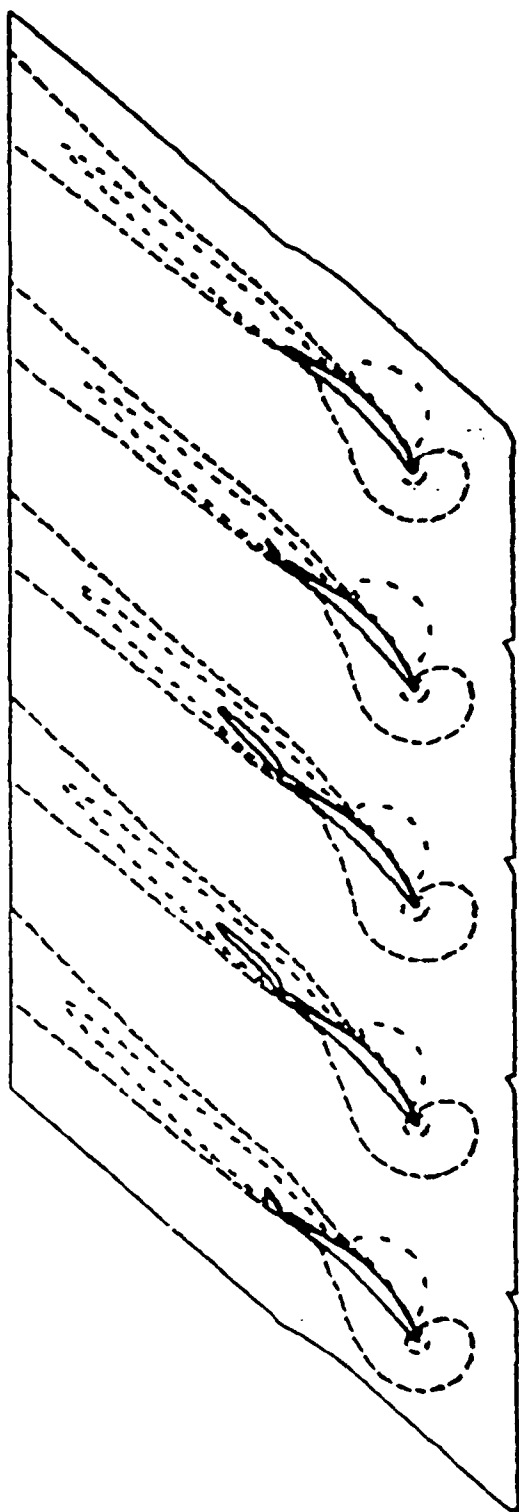
Fig. 47ii. U-Velocity Contours,
60.5° Inflow,
Disturbance Removed,
: . . .
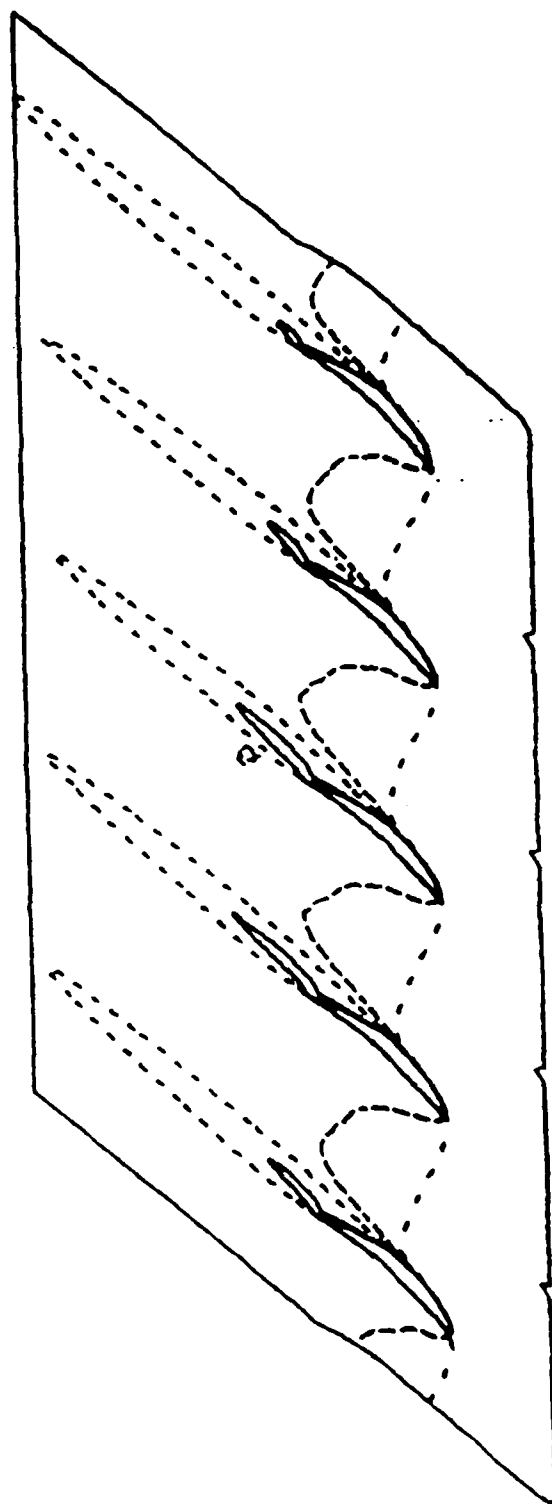
Fig. 47jj. W-Velocity Contours,
60.5° Inflow,
Disturbance Removed,
: . 96
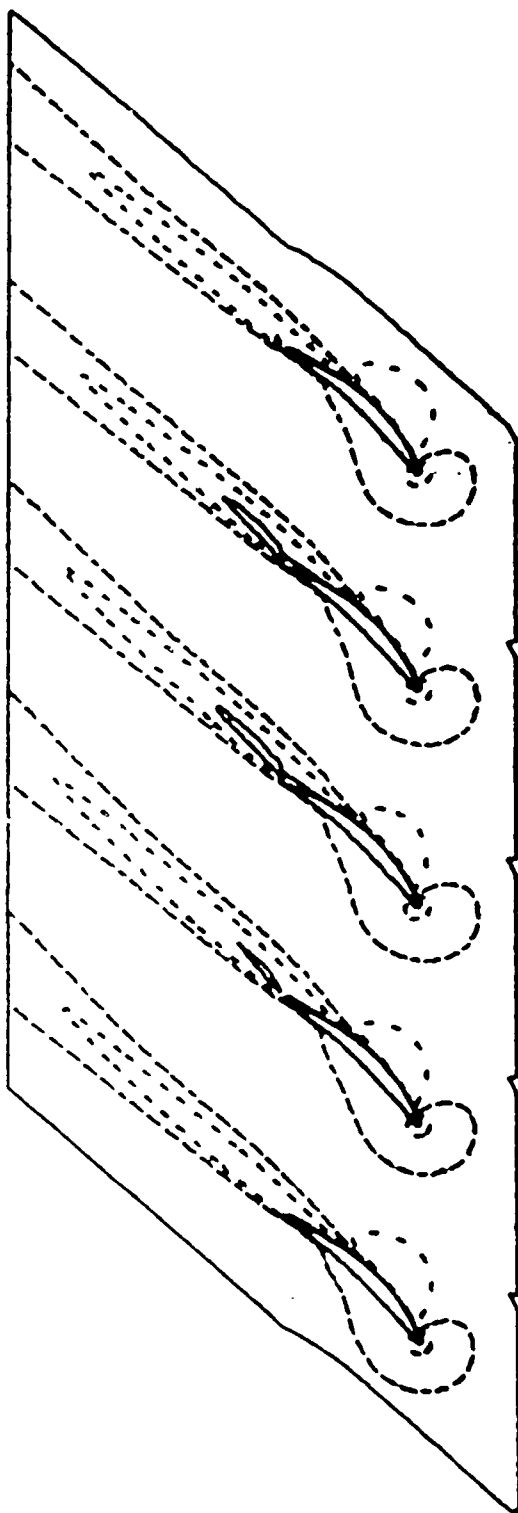
Fig. 47kk. U-Velocity Contours,
60.5° Inflow,
Disturbance Removed,
t = 100
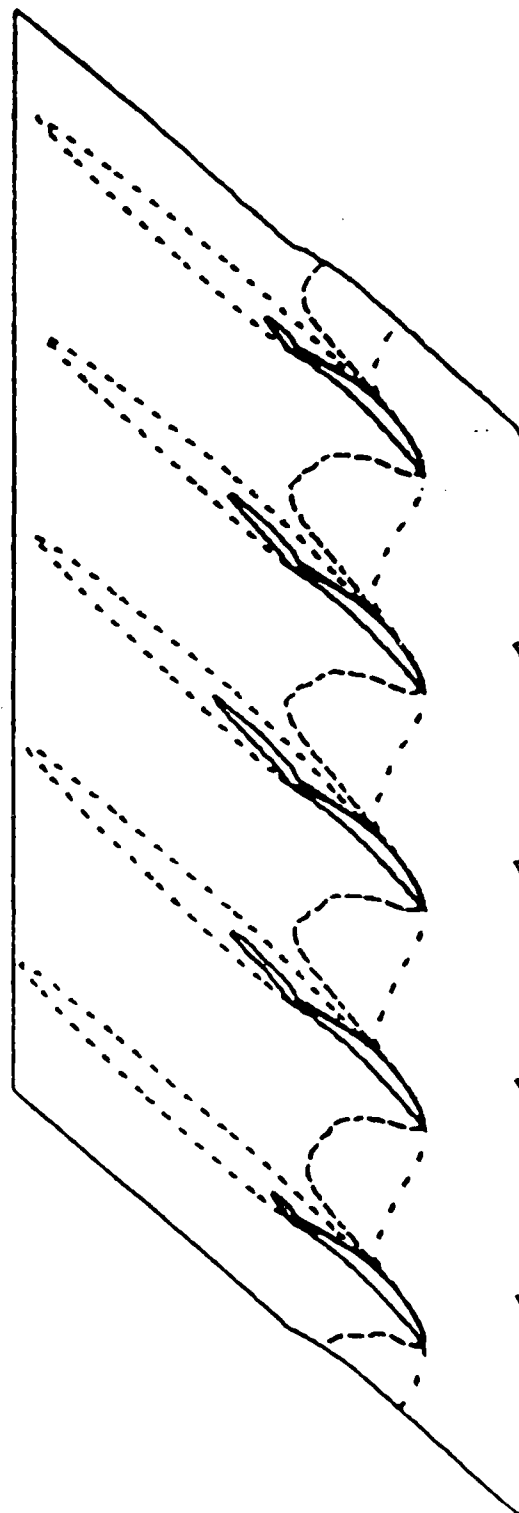
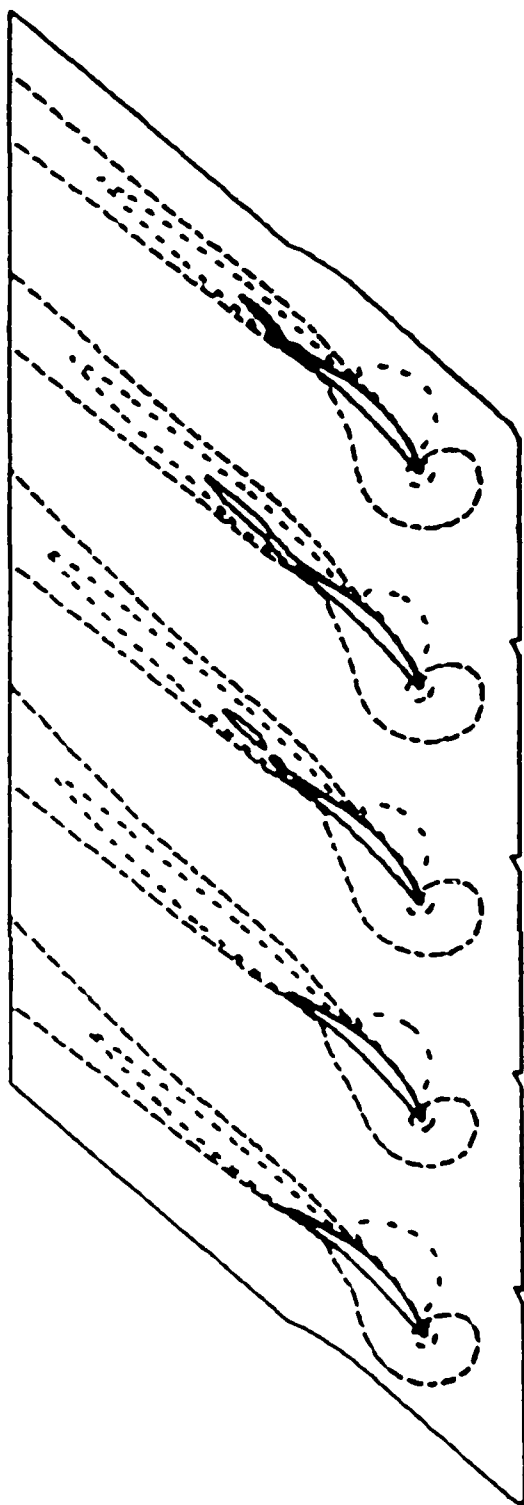Fig. 47ll. W-Velocity Contours,
60.5° Inflow,
Disturbance Removed.
t = 100.
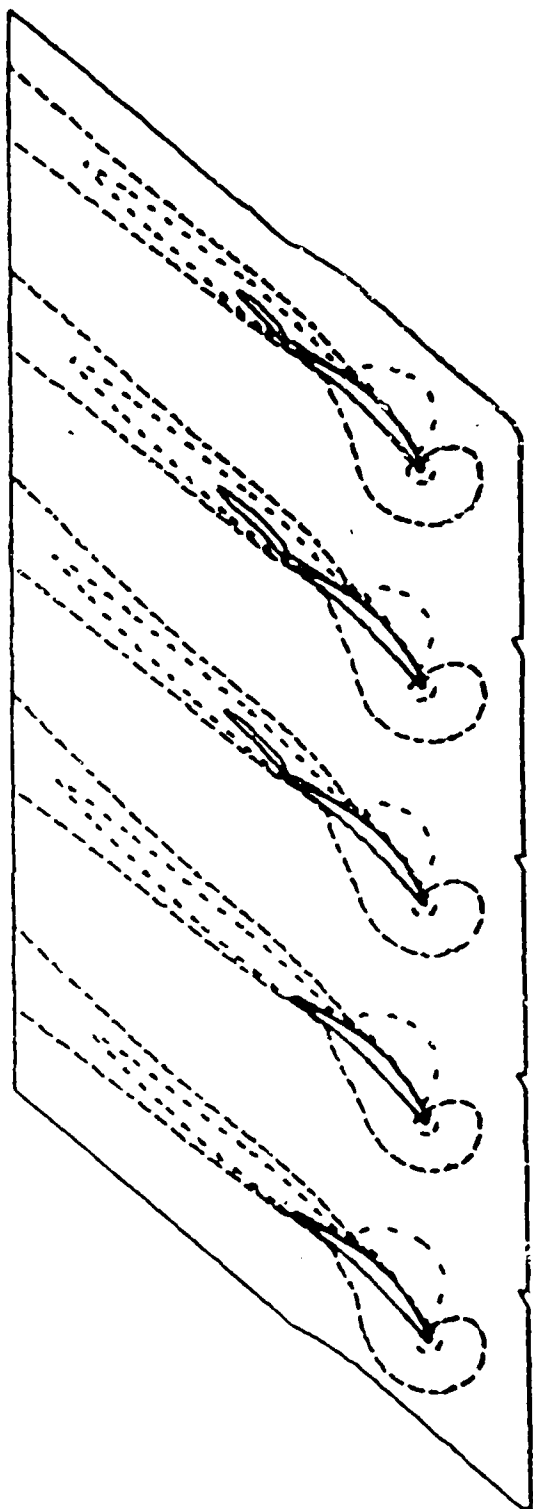
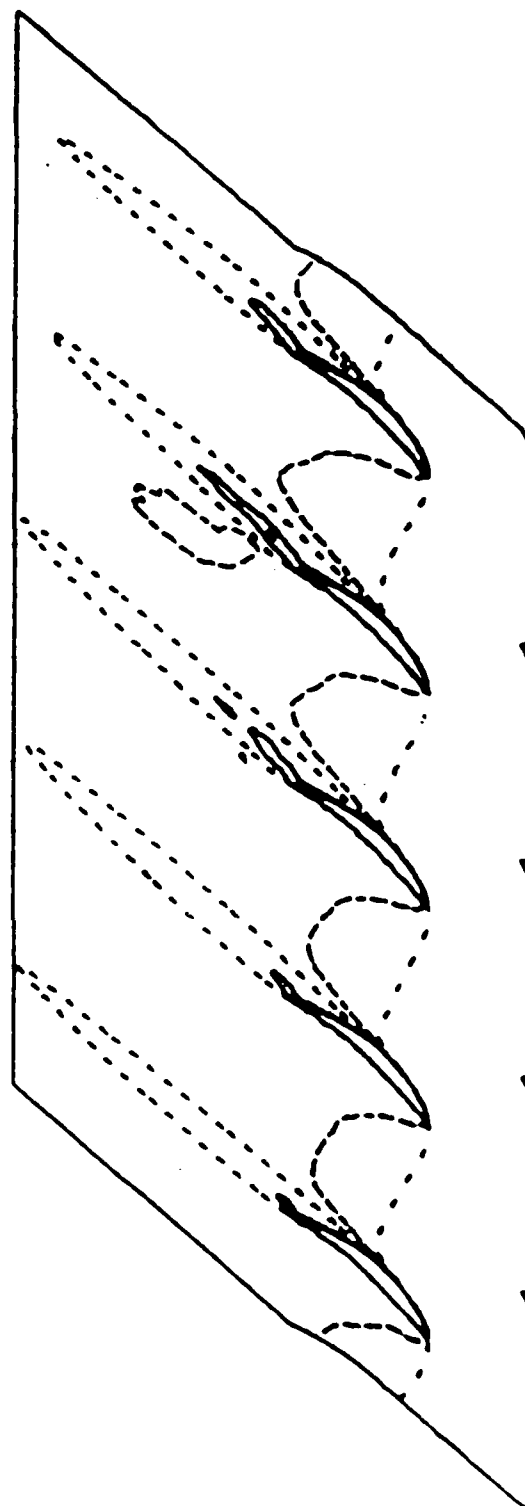Fig. 47mm. U-Velocity Contours,
60.5° Inflow,
Disturbance Removed,
t - 104.
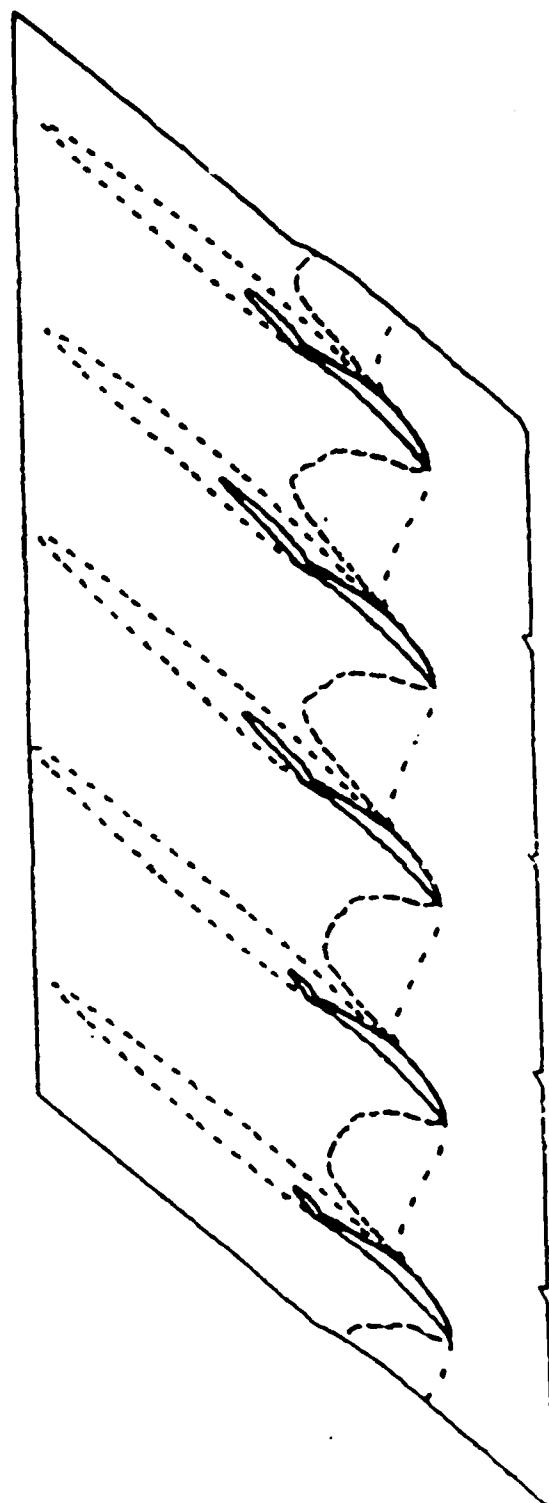
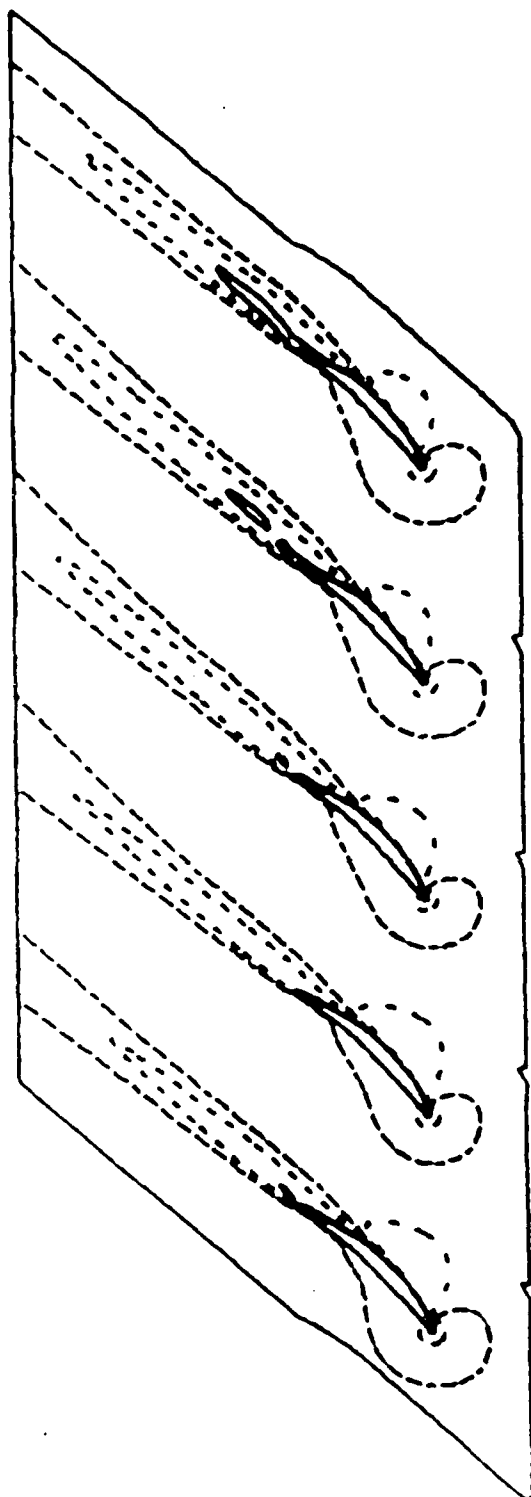Fig. 47nn. W-Velocity Contours,
60.5° Inflow,
Disturbance Removed,
t - 104
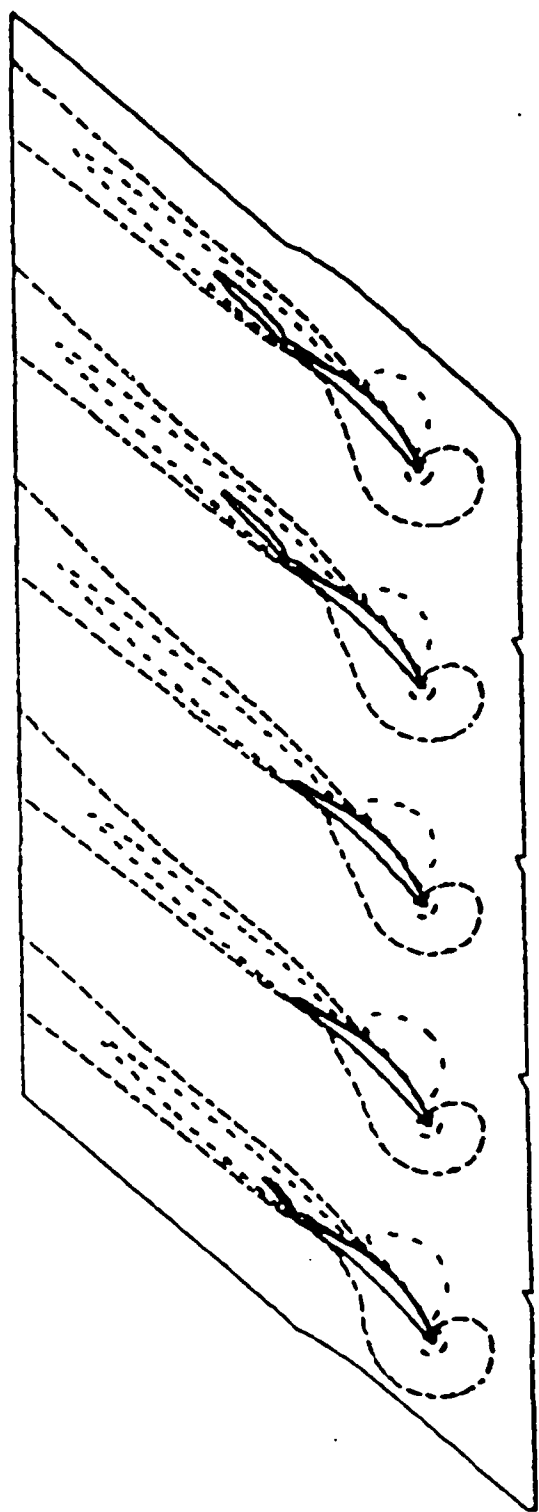
Fig. 47oo. U-Velocity Contours,
           60.5° Inflow,
           Disturbance Removed,
           t - 108.
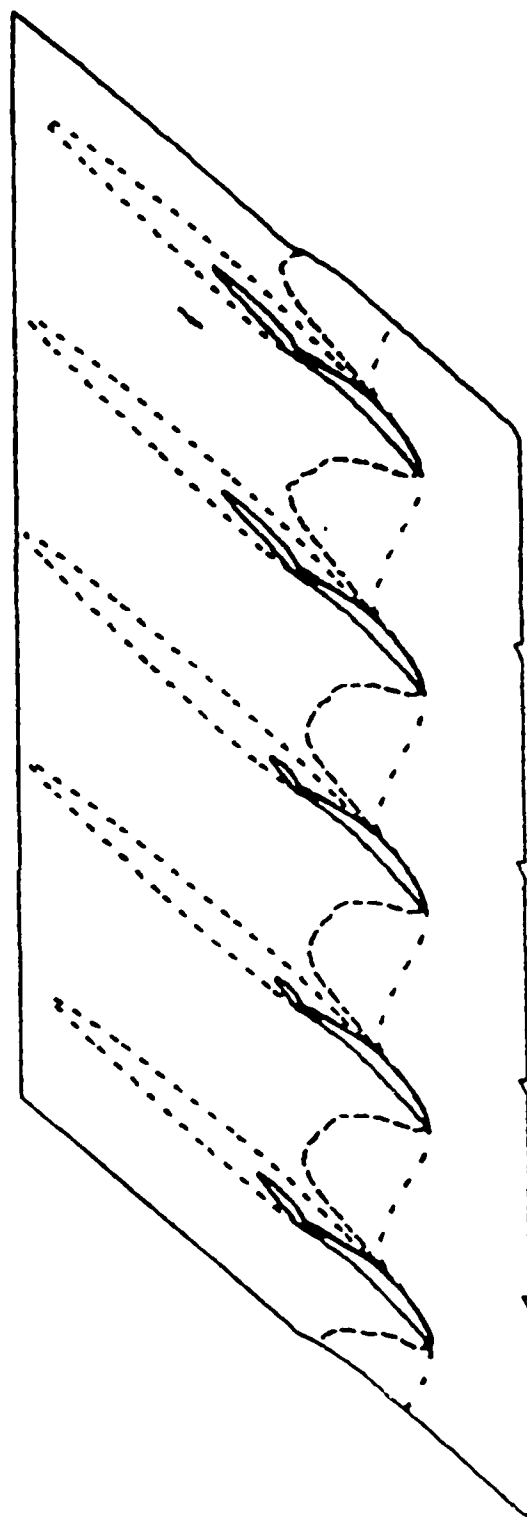
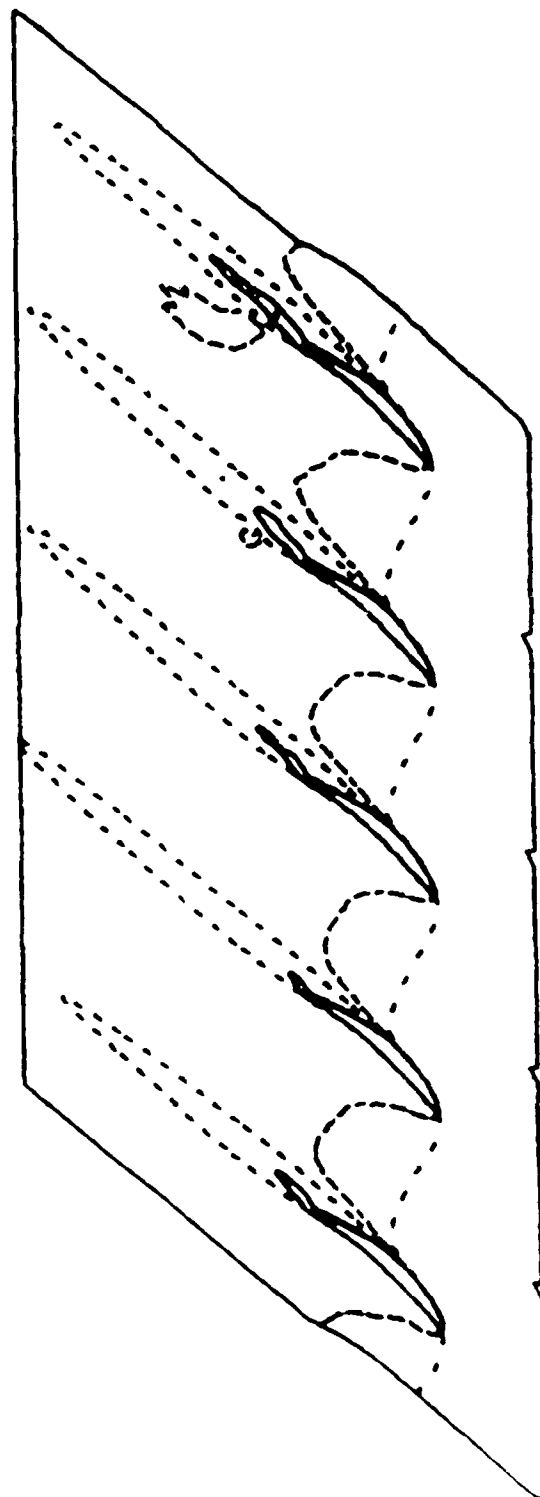Fig. 47pp. W-Velocity Contours,
            60.5° Inflow,
            Disturbance Removed,
            t - 108.
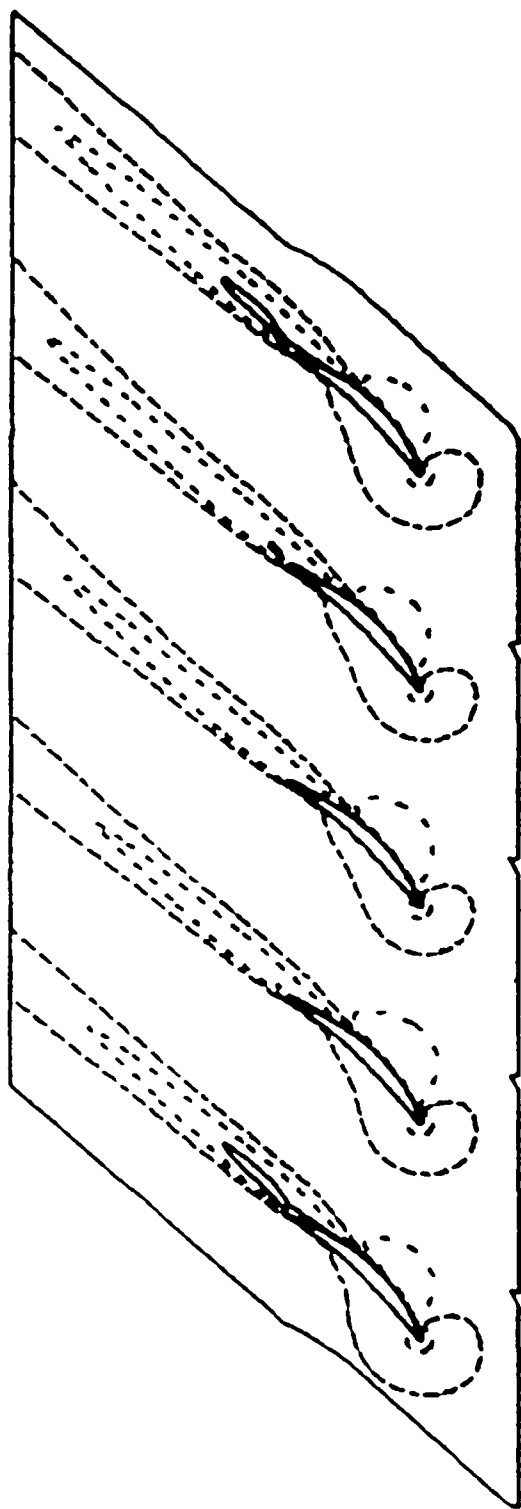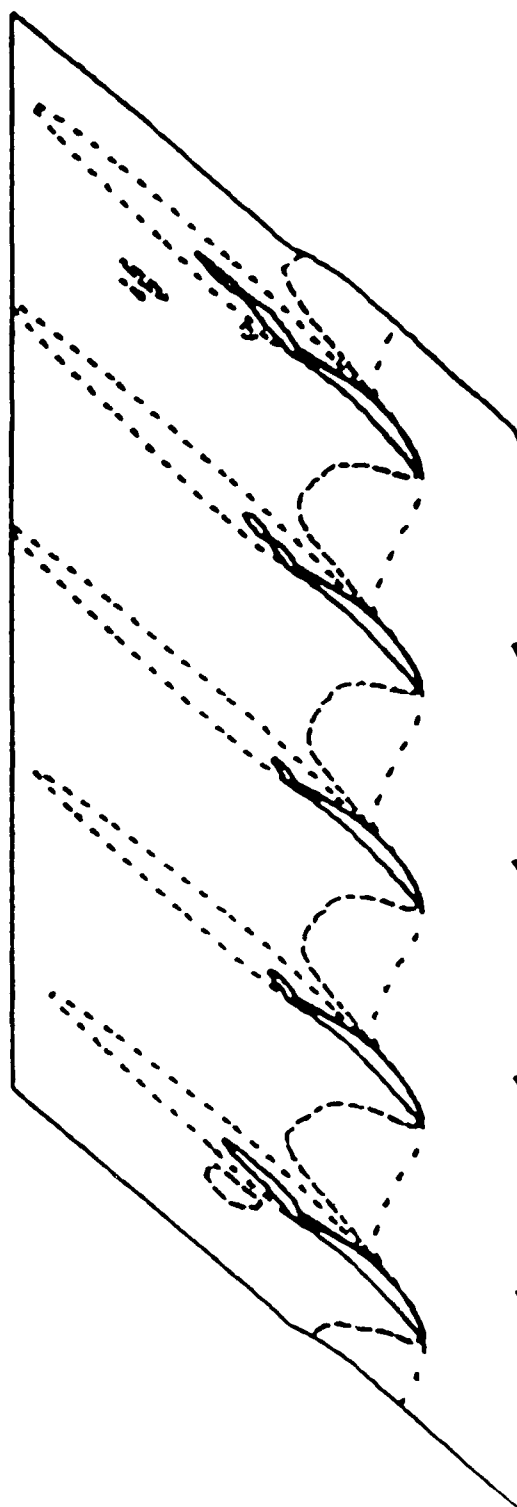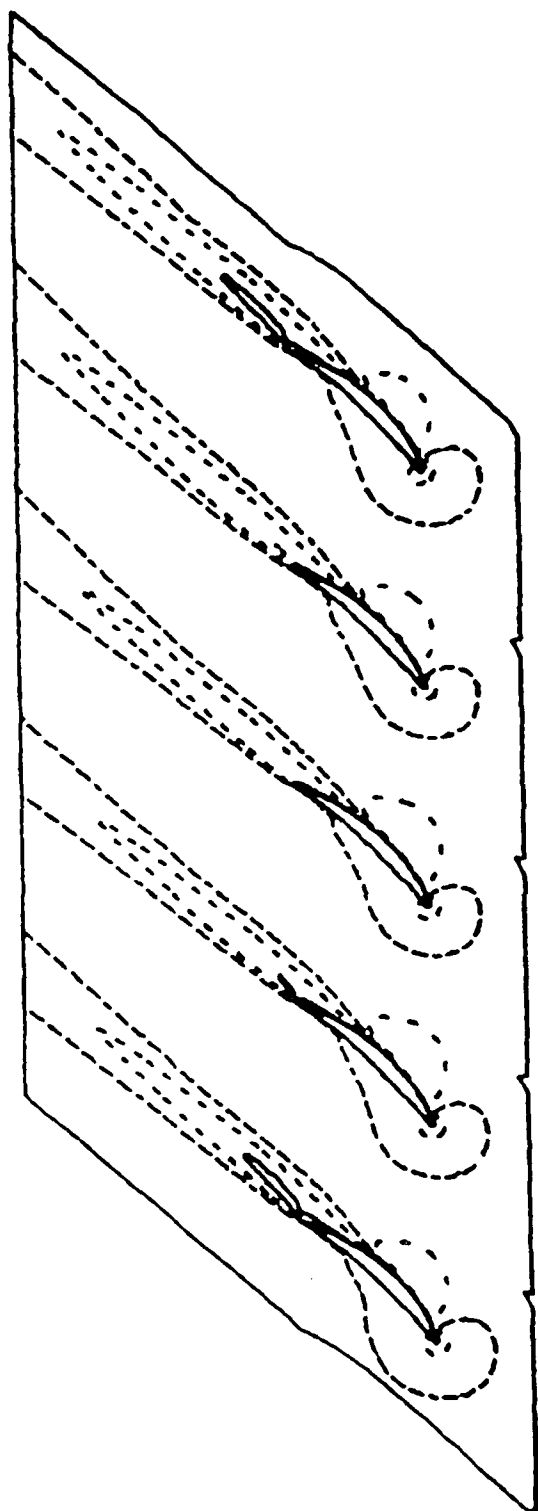
Fig. 47qq. U-Velocity Contours,
60.5° Inflow,
Disturbance Removed,
t = 112.

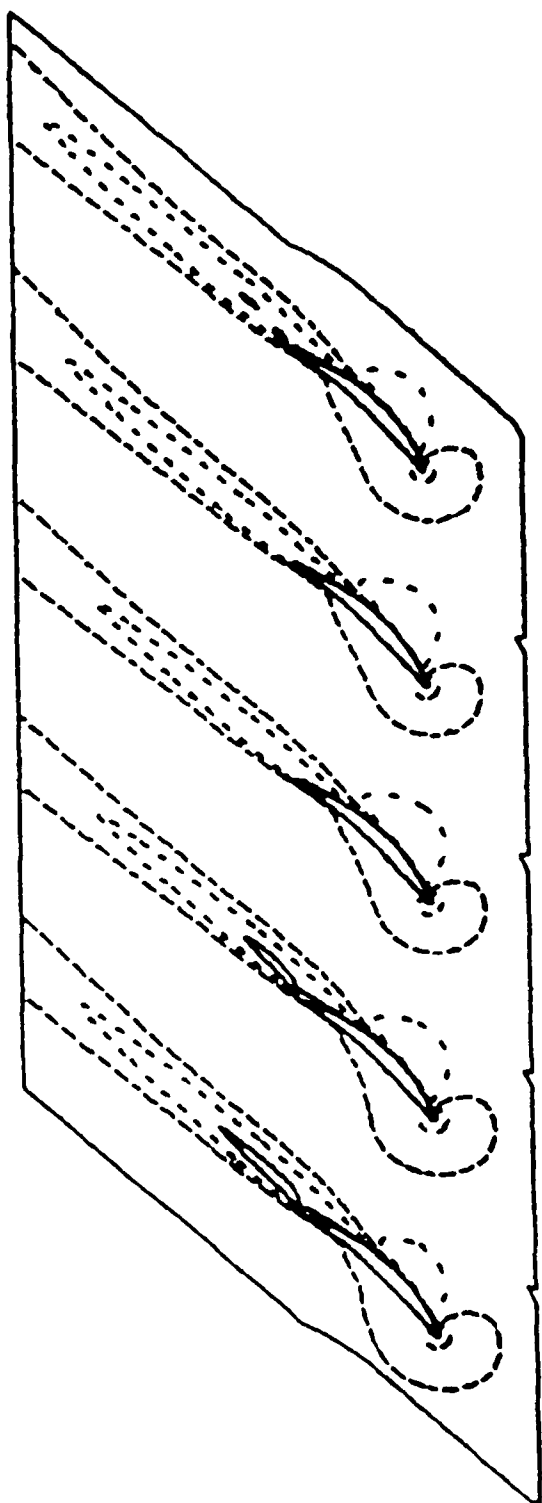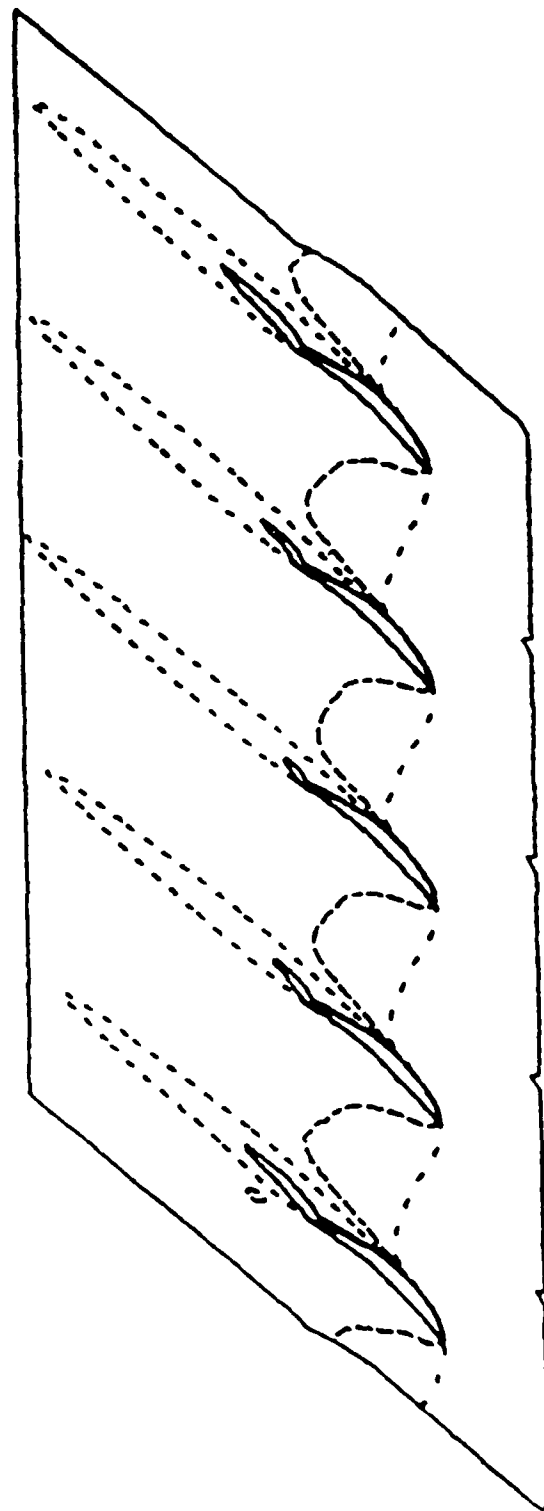Fig. 47rr. W-Velocity Contours,
60.5° Inflow,
Disturbance Removed,
t = 112.
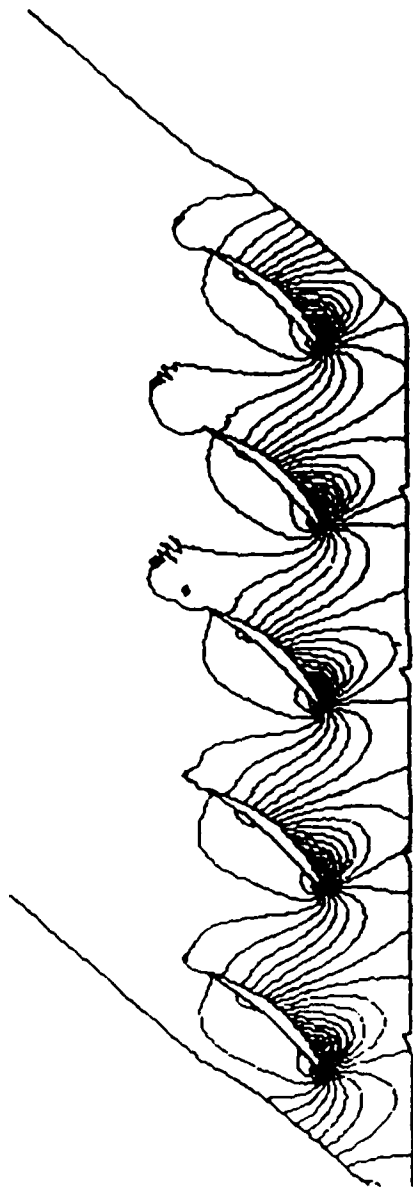
Fig. 47ss. C_p Contours, 60.5° Inflow, Disturbance Removed, t - 72.
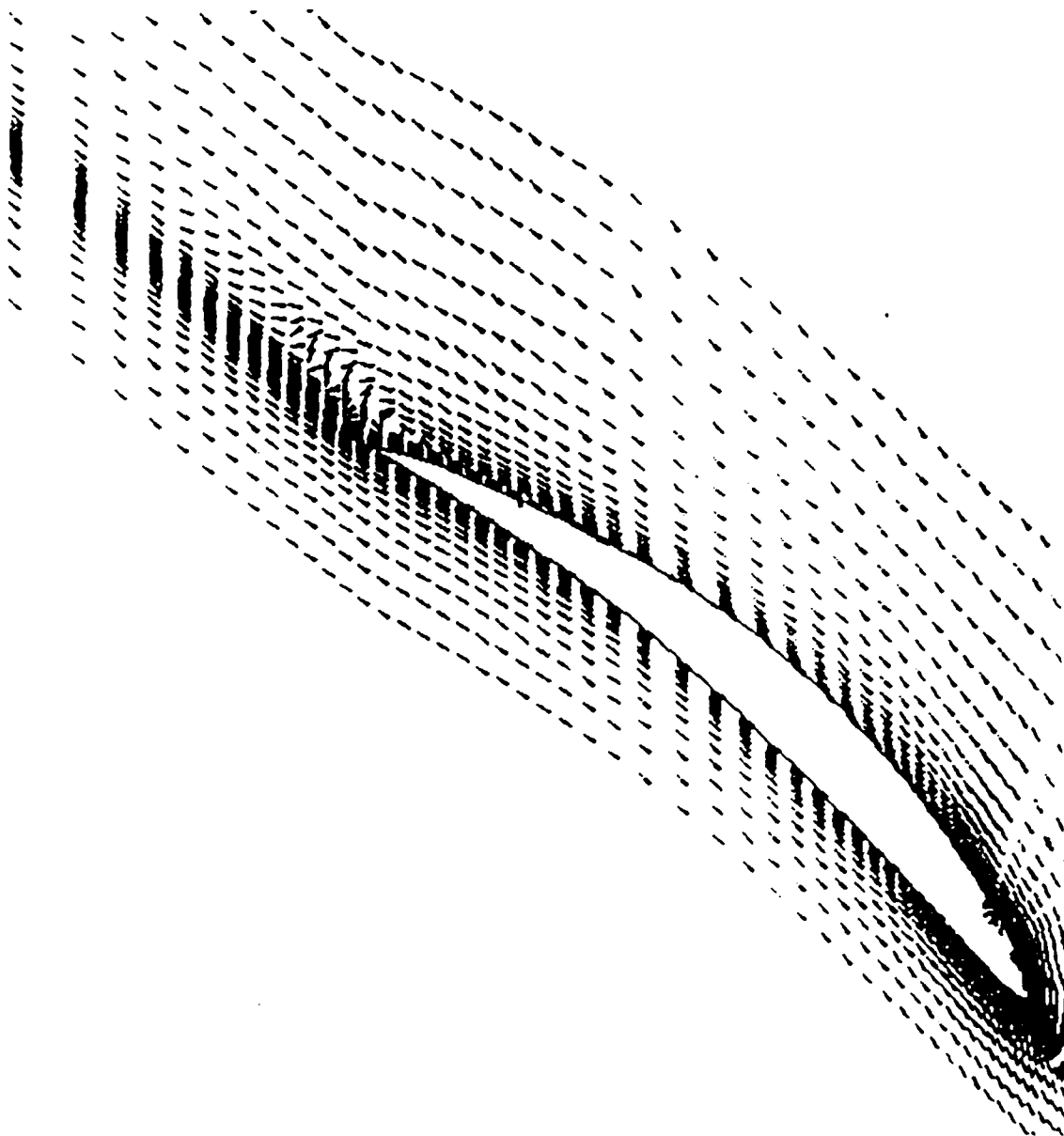
Fig. 47tt. Velocity Vector Plots, Blade No. 1, 60.5° Inflow,
Disturbance Removed, t - 72.
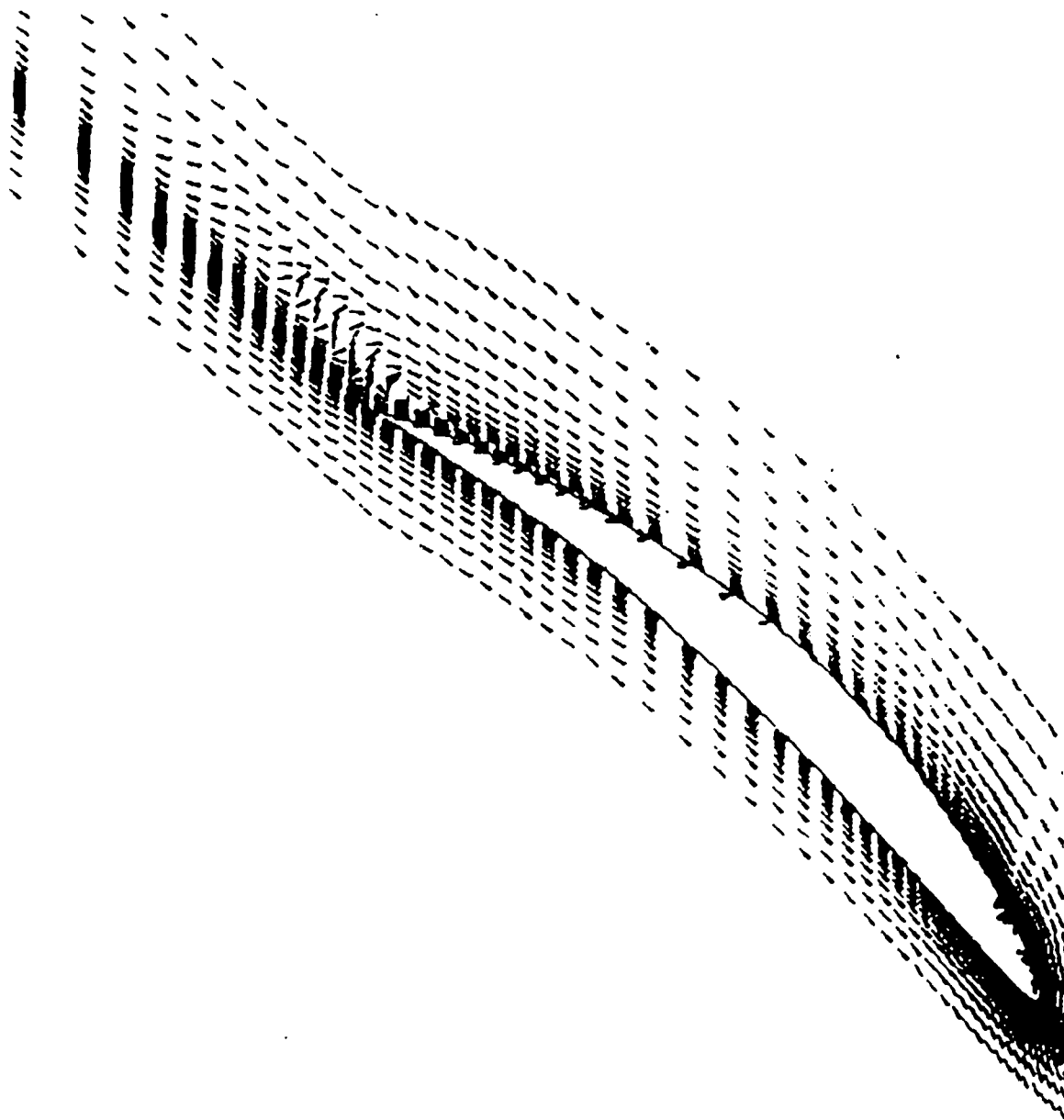
Fig. 47uu. Velocity Vector Plots, Blade No. 2, 60.5° Inflow,
Disturbance Removed, t - 72.
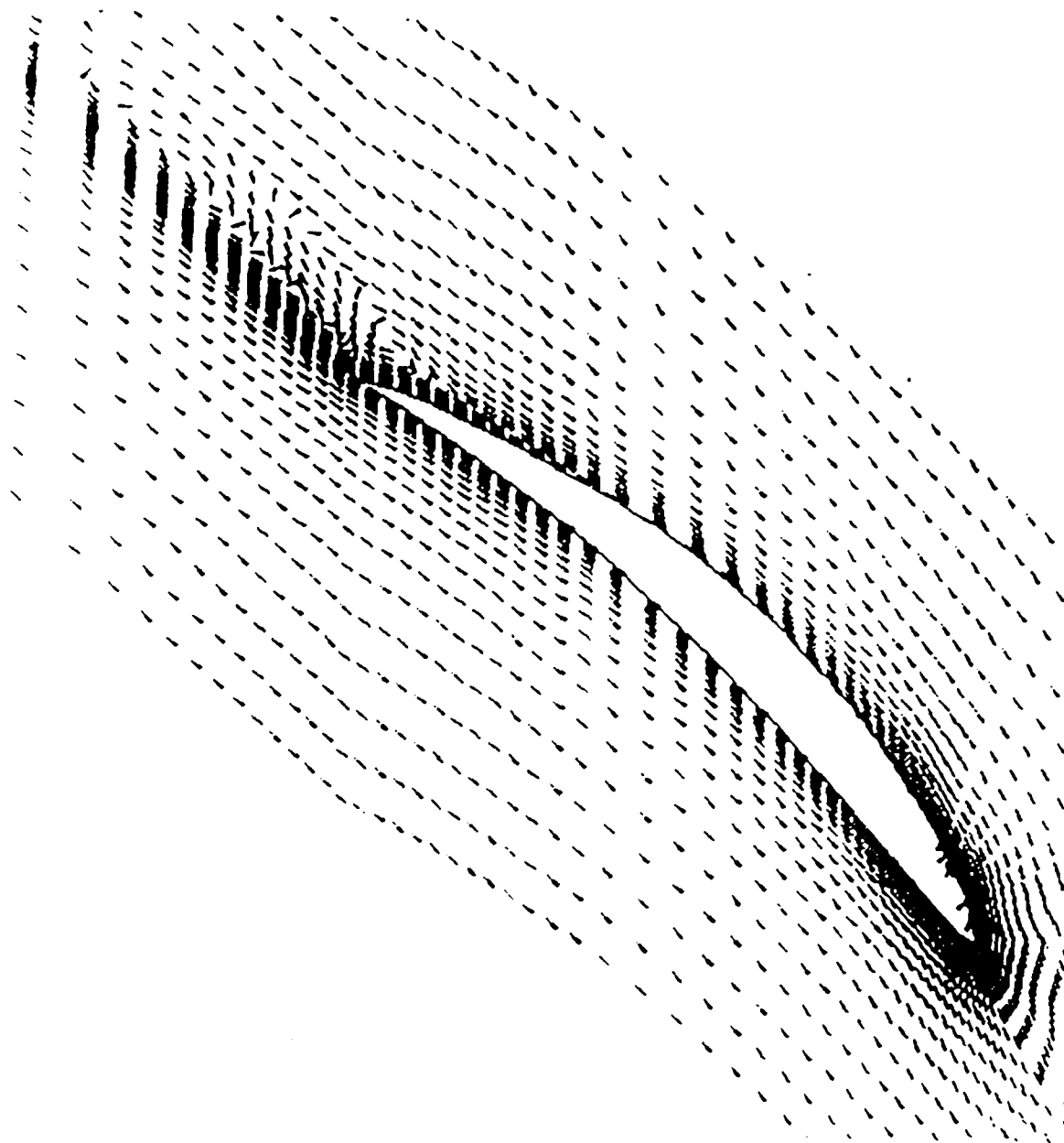
Fig. 47vv. Velocity Vector Plots, Blade No. 3, 60.5° Inflow,
Disturbance Removed, t - 72.
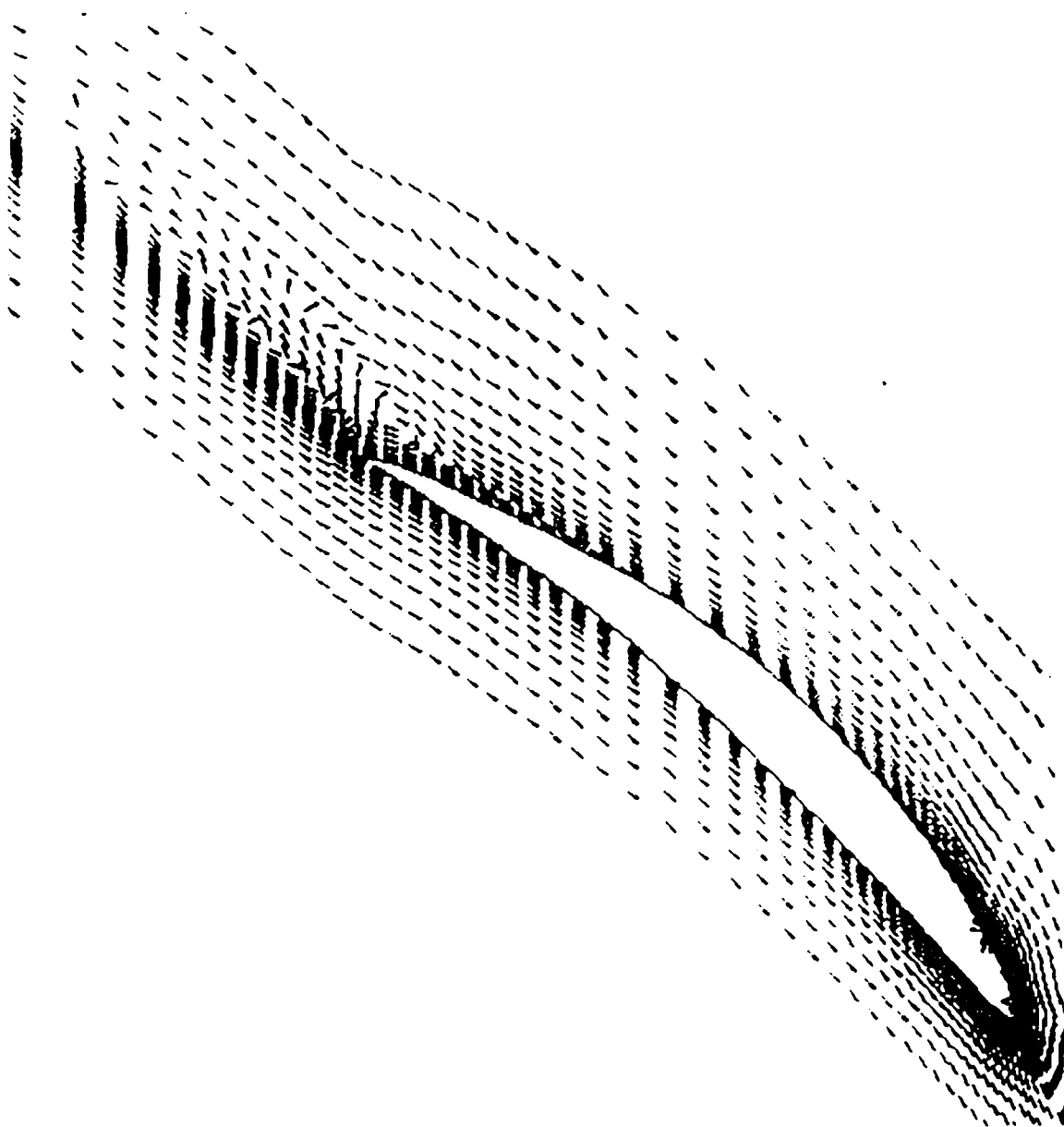
Fig. 47ww. Velocity Vector Plots, Blade No. 4, 60.5° Inflow,
Disturbance Removed, t - 72.
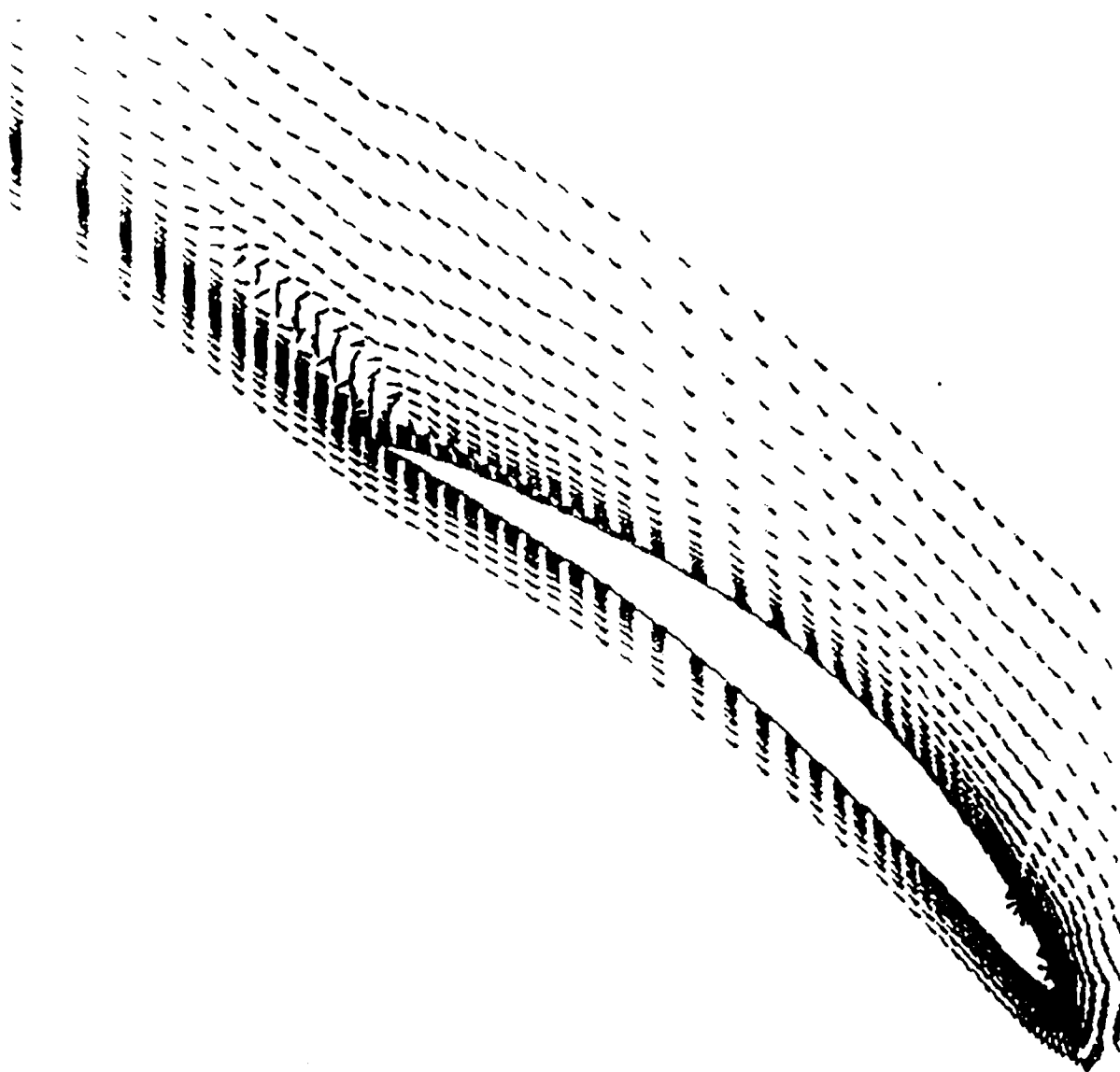
Fig. 47xx. Velocity Vector Plots, Blade No. 5, 60.5° Inflow,
Disturbance Removed, t = 72.

in Figs. 47ss-47xx. The velocity component contours for this flow are given in Figs. 47y and 47z. Figure 47ss shows the static pressure contours; the distortion in the upper passages due to the separated zones is evident. Distortion also appears on the inlet plane. Vector plots for each of the blades are presented in Figs. 47tt-47xx. The larger separation zones for blades 4 and 5 are clearly evident.

Case No. 4c - 60.5°

The final case, Case 4c, was a continuation of the sensitivity of the resulting pattern to the initial disturbance. The calculation was initiated from the flow shown in Figs. 47a and 47b. The disturbance was then reinforced by continuing the wall blowing on blade 2 and adding wall blowing on blades 3 and 4. The wall blowing was then removed and the resulting flow field showed a propagation disturbance field. The results were very similar to those of Case No. 4b with the same flow patterns and propagation speed, so these results will not be repeated here. A typical flow pattern is shown in Figs. 48a and 48b. The main conclusion is the similar pattern to Case 4b which was developed from a very different initial disturbance.

Rotating Stall Cases - Summary

Cases 1-4 present a variety of calculations for Stator Set No. 1 of Ref. 33. All cases were run at 40° stagger and a solidity of 0.85 with the inflow varied between 57° and 61°. The limitations of the present two-dimensional modeling have been addressed in the Background section. It is clear that the present two-dimensional approach does not address important three-dimensional effects which are present in fully developed stall. In addition, there are the usual problems associated with turbulence models for complex flows. Nevertheless, it is reasonable to expect that the present approach would simulate conditions at which rotating stall first occurs.

The cases considered were at 57°, 61°, 60° and 60.5°. As has been shown, these relatively small changes in incidence showed dramatic changes in flow behavior. Considering first the experimental data shown in Fig. 24, at 40° stagger no rotating stall was observed below 58.5° inflow angle and steady rotating stall was observed at approximately 60° inflow. Therefore, the
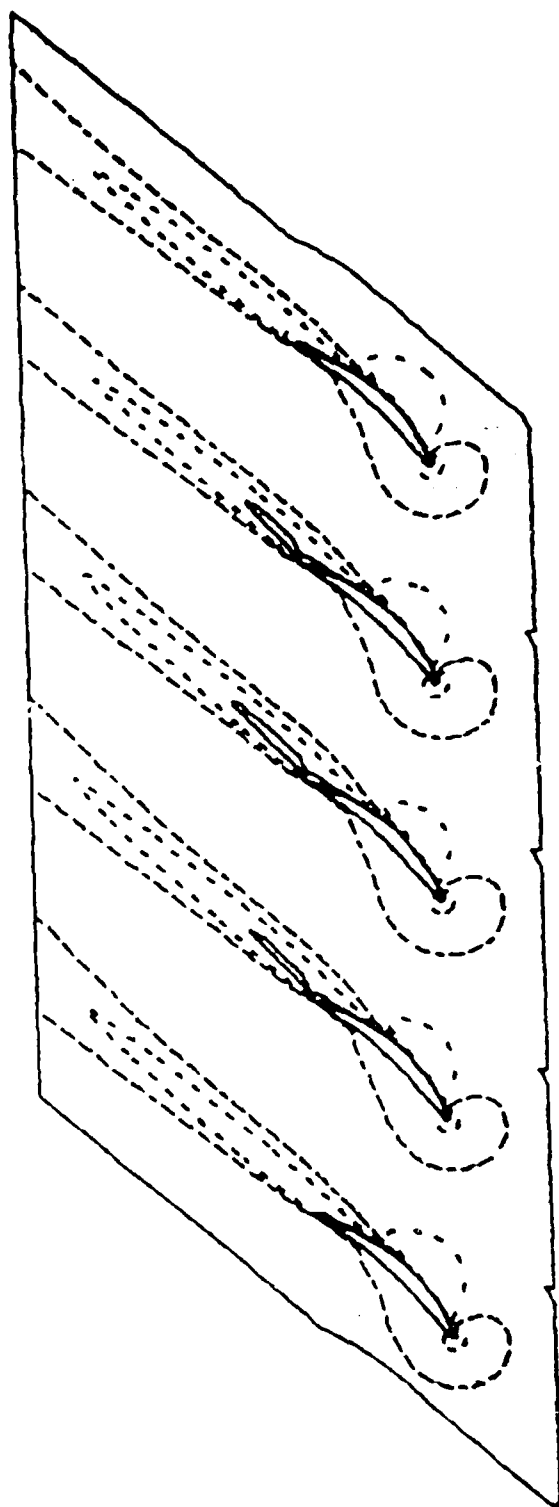
Fig. 48a. U-Velocity Contours, 60.5° Inflow, Case 4c.
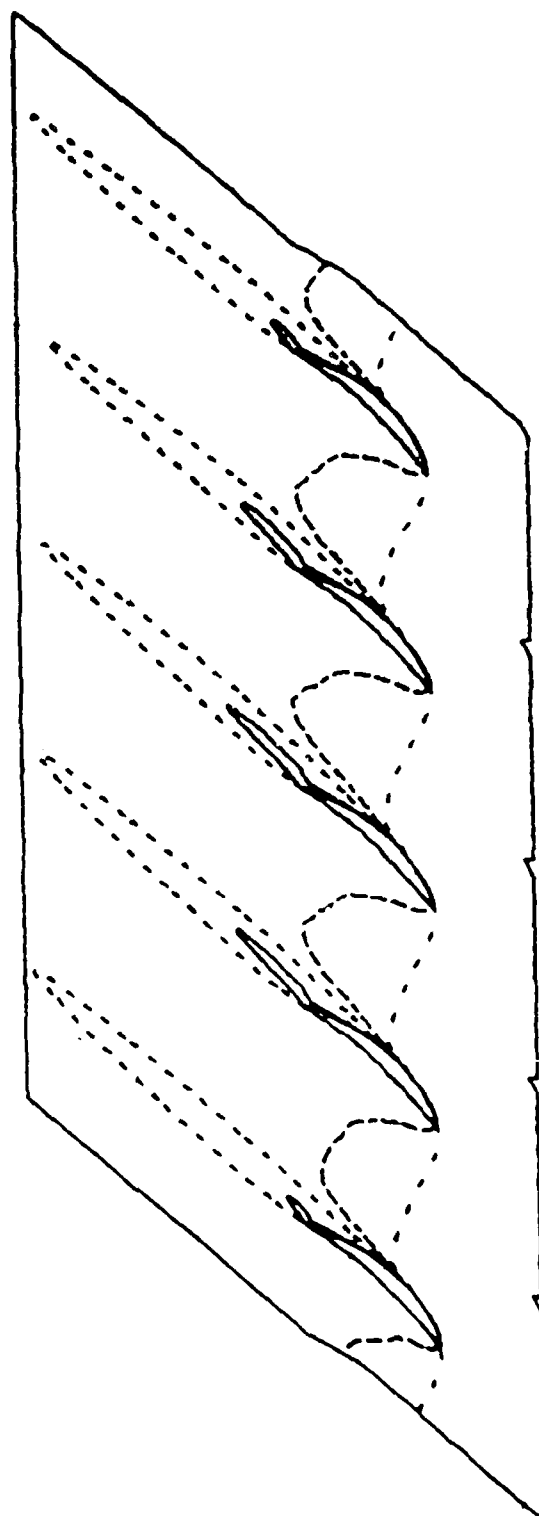
Fig. 48b. W-Velocity Contours, 60.5° Inflow, Case 4c.

experiments show the region $57° < \alpha < 61°$ to be a region of rapid flow behavior change.

The results at $57°$ showed that introduction of a disturbance gave significant change in the passage-to-passage flow but no propagation of the disturbance from passage to passage was noted. At $60°$ introduction of a disturbance again led to a loss of passage-to-passage symmetry and development of a flow separation region. Although the region did progress in the passage-to-passage direction, once the disturbance was removed the flow returned to its original state; the propagating region generated by the disturbance was not self sustaining.

The $60.5°$ case showed a markedly different behavior. Introduction of the disturbance led to a passage-to-passage asymmetry and propagation of the stalled region. However, in contrast to the $60°$ case, propagation continued even when the disturbance was removed. Three different types of disturbance were introduced and all showed propagation; two of the three showed the same flow pattern as the stall region propagated through the set of blades. One of the calculations followed the propagation over three complete cycles, during which time the disturbance showed no significant attenuation. This would associate $60.5°$ inflow with the inception of rotating stall for five passage periodicity. This is in good agreement with the inception noted experimentally in Fig. 24. Of course it must be noted that the present calculation assumes five passage periodicity and the effect of this assumption must be explored, nevertheless, the results give very good correspondence to the stall inception data.

The $61°$ case showed all passages to be separated prior to introduction of a disturbance. The calculation did not converge to a steady flow but showed vortex shedding from the blade trailing edge. When a disturbance was introduced and then removed, a difference in the size of the separation zone on a passage-to-passage basis appeared and this pattern propagated through the five blade cascade passage. However, all passages showed some separation at all times.

In regard to the flow physics, the calculations do show that rotating stall can be initiated by a local disturbance imposed within a single passage. Under appropriate conditions, this local disturbance will amplify and lead to a large scale separated zone that will propagate through the cascade. The present results show this to occur both for a case where no separation is

present prior to the introduction of the disturbance, 60.5° inflow, and for a case where all passages contain separated flow prior to introduction of a disturbance, 61° inflow. The present study has not progressed far enough to make an assessment of the effect of the type of disturbance, the size of the separation zone prior to propagation, etc. upon the stability boundary. The calculations do confirm the stall propagation mechanism to be a change in effective incidence due to blockage, as it is the induced change in upstream incidence which causes recovery of the initially stalled passage and appearance of the stalled region in an adjacent passage. In all of the previously discussed numerical simulations, the static pressure at the quarter-chord point on the suction side of the blade has been stored for each time step on the five blades. A comparison between these pressure-time records and the corresponding flow patterns in terms of the contours of the velocity components indicates that the blade immediately ahead of the propagating stall at first experiences an increase in the static pressure at the suction side quarter chord point. Subsequently, such an increased pressure is associated with the stall of this blade. Later, when the stall region starts to shrink, the pressure in the leading edge region also begins to decrease, until the stall region is propagated to the next blade. A typical pressure-time variation during the onset-development-decay cycle of the stalled region is illustrated in Fig. 49. Since the variation of the pressure in the leading edge region is directly related to the angle of attack, passages ahead of the propagating stall experience an increased incidence leading them to stall, whereas passages behind the propagating stall region experience a reduced incidence leading to recovery from stall. Although not as clear, the increase in incidence for the passages showing trailing edge separation can also be inferred from the u and w velocity component contour plots. Finally, as shown in Fig. 50, the decreased loading on blades having trailing edge separation is obvious from the surface pressure plots. Figure 50 compares surface pressure on blades 1 and 3 for the 60.5° inflow case corresponding to Figs. 47g and 47h. Furthermore, the propagation velocity appears to be approximately 0.23 times the undisturbed upstream tangential velocity. This can be interpreted as 0.23 times the wheel speed. In comparison with the results of the vortex method (Refs. 14 and 15), this propagation speed seems somewhat low. For example, the vortex method calculations of Spalart (Ref. 14) and Speziale et al. (Ref. 15) appeared to give propagation speed values of 0.38 times the wheel speed and between 0.28
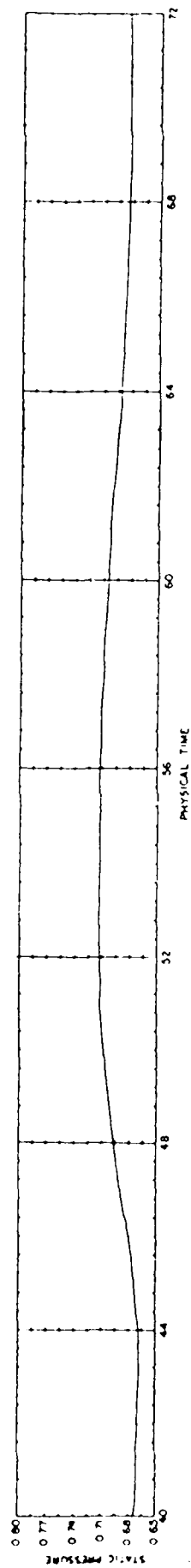
Fig. 49. Typical Pressure Variation at the Quarter-Chord Point During the Onset-Development-Decay Cycle of the Stalled Region
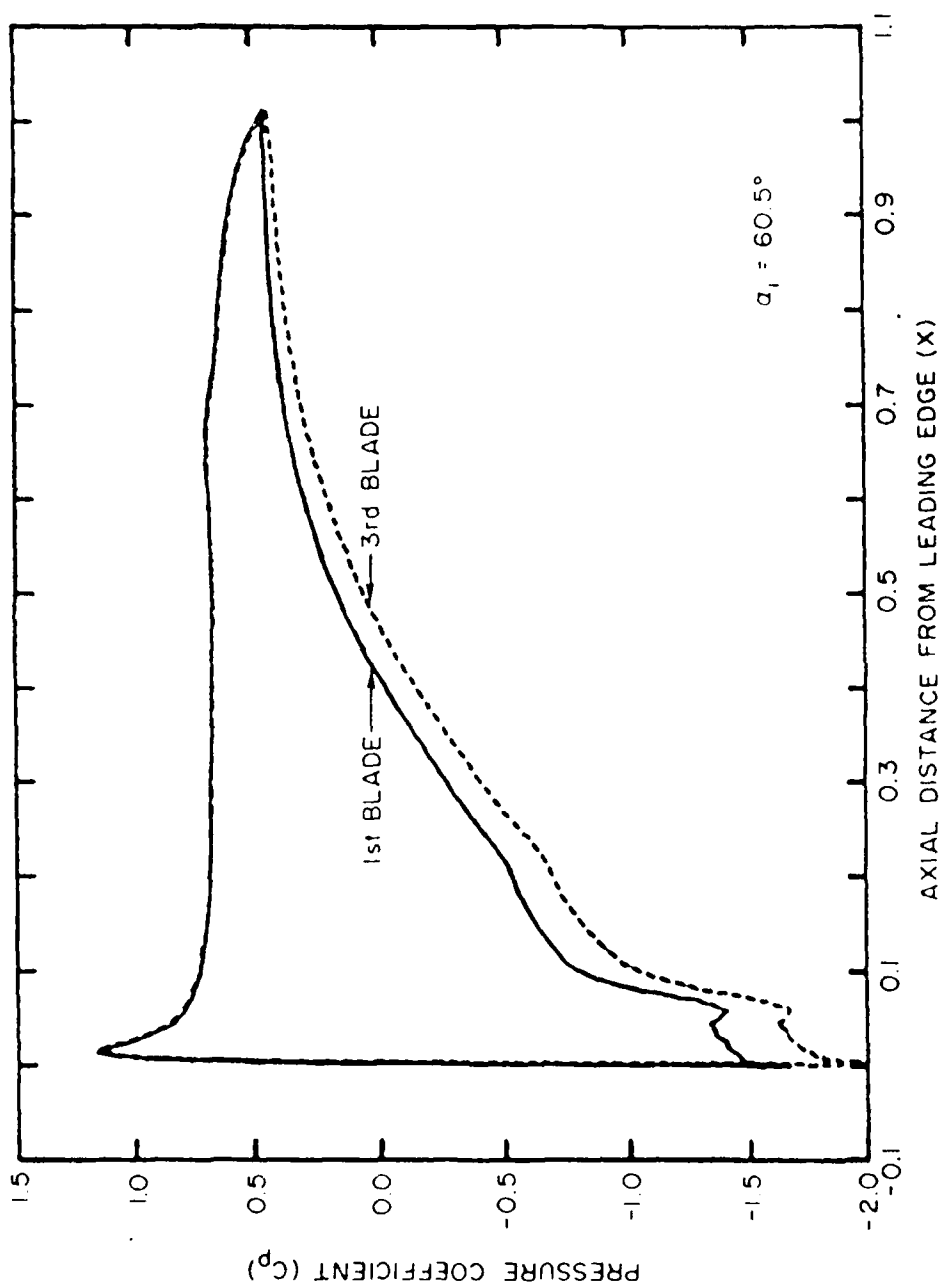
Fig. 50. Surface Pressure Distribution on Blades Stalled (1st Blade) and Unstalled Regions (3rd Blade) of the Five Passage Cascade

and 0.47 times the wheel speed, respectively. The present results are lower, however, the results of Ref. 14 were for a cascade of cambered NACA009 airfoils and those of Ref. 15 were for cascades of cambered and uncambered NACA0012 airfoils. Another analysis is that of Takata and Nagano (Ref. 3) which gives propagation velocity of approximately 0.35 times the blade speed.

Experimental data for stall propagation shows a wide range of results. For example, a compilation of early data given in Ref. 2 shows propagation speeds between 0.3 and 0.7 of the wheel speed with a significant dependence on disturbance wavelength, blade row geometry, flow conditions, etc. Day and Cumpsty (Ref. 35) took detailed flow measurements for stalled axial flow compressors having one to four stages. For the single stage compressors tested, the rotational speed varied between 19 percent and 66 percent rotational speed; obviously, the ratio of propagation speed to wheel speed does show considerable variation.

The separation zones of the present simulation are significant but do not dominate the entire passage. Results showing velocity vector plots which clearly delineate the separated zones have been presented on Figs. 47tt-47xx. Obviously, none of the passages are fully stalled under these flow conditions, therefore, the results represent an incipient rotating stall case.

CONCLUDING REMARKS

An existing two-dimensional Navier-Stokes cascade analysis has been rewritten for effective use on the CRAY series of computers. The resulting vectorized code represents a very efficient cascade code which for two momentum and a continuity equation requires approximately 1×10^{-4} CPU seconds per grid point per time step. In conjunction with the code vectorization, the code has been extended to allow multiple passage calculations without requiring passage-to-passage periodicity. Rather, in its present form the code allows periodic boundary conditions to be set for an arbitrary number of blade passages. This capability allows phenomena which are not periodic on a passage-to-passage basis, such as inlet distortion and rotating stall, to be simulated. In addition, an 'H-grid' capability and axial velocity density ratio (AVDR) effects were incorporated into the code.

Cases were run demonstrating both inlet distortion and propagating stall capability. Demonstration inlet distortion cases were made for both two blade

-142-

and five blade periodicity. Distortion in terms of both inflow total pressure and inflow angle was considered. The propagating stall calculations were run for a J-79 compressor stator set which had been the subject of extensive experimental investigation. A stagger angle of 40° and a solidity of 0.85 was chosen and a series of calculations run over a range of inflow angles between 57° and 61°. In each case a steady solution which was blade-to-blade periodic was obtained and a disturbance was introduced. The disturbance consisted of a small amount of wall transpiration on the aft portion of the second blade suction surface. The results showed no propagating stall at 57°. At 60° inflow a propagating stall cell could be initiated by introducing wall transpiration on the suction surface of one of the blades. However, when this disturbance source was removed, the propagating stall cell disappeared. When the inflow angle was increased to 60.5°, the disturbance initiated a propagating stall pattern which continued even after the disturbance was removed. The zone propagation continued for three complete cycles without any significant decrease in intensity; the calculation then was discontinued.

The present results represent to the best of the authors' knowledge the first simulation of rotating stall from a finite difference solution of the Navier-Stokes equations. Although certain approximations in regard to two-dimensional flow, turbulence modeling, etc., are obviously present, the results show good agreement with data for rotating stall inception and show the physical features of the process.

REFERENCES

1.   Marble, F.E.: Propagation of Stall in a Compressor Blade Row. Journal of
     the Aeronautical Sciences, Vol. 22, 1955.

2.   Emmons, H.W., Kronauer, R.E. and Rockett, J.A.: A Survey of Stall
     Propagation - Experiment and Theory. Journal of Basic Engineering, Vol.
     81, 1959.

3.   Takata, H. and Nagano, S.: Nonlinear Analysis of Rotating Stall. Journal
     of Engineering for Power, Vol. 84, 1972.

4.   Adamczyk, J.J.: Unsteady Fluid Dynamic Response of an Isolated Rotor with
     Distorted Inflow. AIAA Paper No. 74-49, 1974.

5.   Nenni, J.P. and Ludwig, G.R.: A Theory to Predict the Inception of
     Rotating Stall in Axial Flow Compressors. AIAA Paper 74-528, 1974.

6.   Ludwig, G.D., Nenni, J.P. and Erickson, J.C., Jr.: Investigation of
     Rotating Stall Phenomena in Axial Flow Compressors, Vol. I - Basic Studies
     of Rotating Stall. AFAPL-TR-76-48, Vol. I, June 1976.

7.   Ludwig, G.R. and Nenni, J.P.: Basic Studies of Rotating Stall in Axial
     Flow Compressors. AFAPL-TR-79-2083, September 1979.

8.   Nenni, J.P., Homicz, G.F. and Ludwig, G.R.: Rotating Stall
     Investigations, Vol. I - Theoretical Investigations. AFWAL-TR-83-2002,
     1983.

9.   Greitzer, E.M.: Review - Axial Compressor Stall Phenomena. Journal of
     Fluids Engineering, Vol. 102, 1980.

10. Greitzer, E.M.: The Stability of Pumping Systems. Journal of Fluids
     Engineering, Vol. 103, 1981.

11. Cunpsty, N.A. and Greitzer, E.M.: A Simple Model for Compressor Stall
     Propagation. Journal of Engineering for Power, Vol. 104, 1982.

12. Moore, F.K. and Greitzer, E.M.: A Theory of Post-Stall Transients in
     Axial Compression Systems: Part I - Development of Equations. Journal of
     Engineering for Gas Turbines and Power, Vol. 108, 1986.

13. Moore, F.K. and Greitzer, E.M.: A Theory of Post-Stall Transients in
     Axial Compression Systems: Part II - Application. Journal of Engineering
     for Gas Turbines and Power, Vol. 108, 1986.

14. Spalart, P.R.: Two Recent Extensions of the Vortex Method. AIAA Paper
     84-0343, 1984.

15. Speziale, C.G., Sisto, F. and Jonnavithula, S.: Vortex Simulation of
     Propagating Stall in a Linear Cascade of Airfoils. Journal of Fluids
     Engineering, Vol. 108, 1986.

REFERENCES (Continued)

16. Chorin, A.J.: Numerical Study of Slightly Viscous Flows. Journal of Fluid Mechanics, Vol. 57, 1973.

17. Spalart, P.R. and Leonard, A.: Computation of Separated Flows by a Vortex Tracing Algorithm, AIAA Paper 81-1246, 1981.

18. Shamroth, S.J., Gibeling, H.J. and McDonald, H.: A Navier-Stokes Solution of Laminar and Turbulent Flow Through a Cascade of Airfoils, AIAA Paper No. 89-1426, 1980. (Also SRA Report R79-920004-F, 1982).

19. Shamroth, S.J., McDonald, H. and Briley, W.R.: Prediction of Cascade Flow Fields Using the Averaged Navier-Stokes Equations, ASME Journal of Eng. for Gas Turbines and Power, Vol. 106, No. 2, pp. 383-390, April 1984.

20. Weinberg, B.C., Yang, R.-J., McDonald, H. and Shamroth, S.J.: Calculation of Two- and Three-Dimensional Transonic Cascade Flow Fields Using the Navier-Stokes Equations, Journal of Eng. for Gas Turbines and Power, Vol. 108, pp.93-102, 1986.

21. McDonald, H., Shamroth, S.J. and Briley, W.R.: Transonic Flows with Viscous Effects, Transonic Shock and Multi-Dimensional Flows: Advances in Scientific Computing, Academic Press, New York, 1982.

22. McDonald, H. and Briley, W.R.: Computational Fluid Dynamic Aspects of Internal Flows, AIAA Paper 79-1445, July 1979.

23. Briley, W.R., McDonald, H. and Shamroth, S.J.: A Low Mach Number Euler Formulation and Application to Time Iterative LBI Schemes, AIAA Journal, Vol. 21, No. 10, p. 1467-1469, October 1983.

24. Briley, W.R. and McDonald, H.: An Implicit Numerical Method for the Multi-Dimensional Compressible Navier-Stokes Equations, United Aircraft Research Laboratories Report M911363-6, November 1973.

25. Briley, W.R. and McDonald, H.: Solution of the Multidimensional Compressible Navier-Stokes Equations by a Generalized Implicit Method, Journal of Comp. Physics, Vol. 24, pp. 372-397, August 1977.

26. Briley, W.R. and McDonald, H.: On the Structure and Use of Linearized Block Implicit Schemes, Journal of Comp. Physics, Vol. 34, No. 1, pp. 54-72, January 1980.

27. Briley, W.R. and McDonald, H.: Computation of Three-Dimensional Horseshoe Vortex Flow Using the Navier-Stokes Equations, Seventh International Conference on Numerical Methods in Fluid Dynamics, Stanford University, June 1980.

28. Rudy, D.H. and Bushnell, D.M.: A Rational Approach to the Use of Prandtl's Mixing Length in Free Turbulent Shear Flow Calculations. Conferenec on Free Turbulent Shear Flows at Langley Research Center, NASA SP-321, 1973.

REFERENCES (Concluded)

29. Shamroth, S.J., Gibeling, H.J. and McDonald, H.: A Navier-Stokes Solution for Laminar and Turbulent Flows Through a Cascade of Airfoils. SRA Report R79-920005-f, 1979.

30. Shamroth, S.J. and McDonald, H.: Development of a Design-Oriented Navier-Stokes Cascade Analysis, Report AFWAL 84-2036, 1984.

31. Hobbs, D.E., Wagner, J.H., Dannenhoffer, J.F. and Dring, R.P.: Experimental Investigation of Compressor Cascade Wakes, ASME Paper 82-GT-299, 1982.

32. Erdos, J.F., Alzner, E. and McNally, W.: Numerical Solution of Periodic Transonic Flow Through a Fan Stage. AIAA Journal, Vol. 15, 1977.

33. Ludwig, G.R., Nenni, J.P. and Arendt, R.H.: Investigation of Rotating Stall in Axial Flow Compressors and Development of a Prototype Rotating Stall Control System. AFAPL-TR-73-45, 1973 (See. Also Ref. 7).

34. Smith, L. and Suo, M.: Personal Communication.

35. Day, J.J. and Cumpsty, N.A.: The Measurement and Interpretation of Flow Within Rotating Stall Cells in Axial Compressors, J. Mech. Eng. Science., Vol. 20, 1978.

END

DATE

FILMED

DTIC

JULY 88